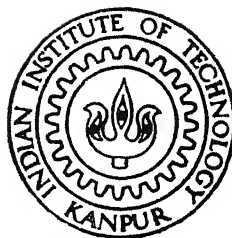


# GROWTH AND STRUCTURAL CHARACTERIZATION OF DIAMOND AND DIAMONDLIKE CARBON FILMS

by  
**MANJU MALHOTRA**



PHY  
1996  
D  
MAL  
GRO

DEPARTMENT OF PHYSICS  
**INDIAN INSTITUTE OF TECHNOLOGY KANPUR**  
DECEMBER, 1996

# **GROWTH AND STRUCTURAL CHARACTERIZATION OF DIAMOND AND DIAMONDLIKE CARBON FILMS**

*A Thesis Submitted*  
in Partial Fulfillment of the Requirements  
for the Degree of  
Doctor of Philosophy

*by*  
**MANJU MALHOTRA**

*to the*  
**DEPARTMENT OF PHYSICS**  
**INDIAN INSTITUTE OF TECHNOLOGY, KANPUR**  
**December, 1996**

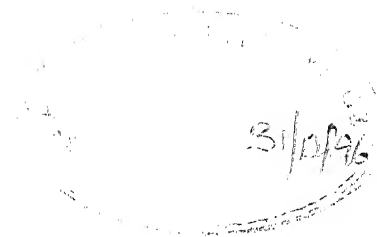
13 JUL 1998

CENTRAL LIBRARY  
I. I. T., KANPUR

---

Acc. No. **A** 125699

PHY-1996-D-MAL-GRC



## CERTIFICATE

It is certified that the work contained in this thesis entitled *Growth and structural characterization of diamond and diamondlike carbon films* by *Manju Malhotra* has been carried out under my supervision and that this work has not been submitted elsewhere for a degree.

A handwritten signature in cursive script, reading "Satyendra Kumar".

---

Satyendra Kumar  
Department of Physics  
Indian Institute of Technology  
Kanpur

December, 1996



*Dedicated to....*

*my parents & teachers*

## Acknowledgments

I feel pleasure in expressing my gratitude to Dr. Satyendra Kumar, my worthy guide and mentor, for his valuable contribution to my research work. He has not only provided intellectual inputs to my Ph.D. thesis but has been a constant source of encouragement and inspiration to me. His ceaseless quest for perfection has helped me a lot in learning new things and honing my abilities.

This has been a process of learning by doing for me. The period of six and a half years has been quite a pleasant, though arduous at times, experience. The most important achievement of mine, I feel, in this course has been learning the methodology of research and development. At a more general level, I have developed the ability and confidence to meet any new challenges thrown up by life, squarely.

I am thankful to Dr. S.C. Agarwal for his encouragement and for extending me the facilities of his laboratory. Dr. V.N. Kulkarni was kind enough to go through the preprint of some chapters and suggest appropriate modifications. I am very much grateful to him for extending the ERDA facility also at a very crucial stage of this work. My sincere thanks are due for Dr. Y.N. Mohapatra for useful discussions. Also, my thanks are due for Drs. Deshdeep Sahdev, A.K. Majumdar and O.P. Katyal for discussions and suggestions. I am also thankful to Dr. L. Sarkar for helping me by providing gases.

I would like to extend my sincere thanks to the technical staff of Physics workshop Mr. Ram Singh, Mr. B. Singh, Mr. R.M. Singh and Mr. Raghunath Singh for their sincere and hard work in making numerous experimental workpieces used in this work. I sincerely thank the staff of the Glass Blowing unit for making various job pieces. My thanks are due for staff of Central Workshop also for their help.

I am very grateful to Dr. B.D. Malhotra, BECPRL, National Physical Laboratory, New Delhi for providing me with their FTIR spectrometer for measurements on a number of samples. I am also thankful to Dr. P.N. Dixit, Dr. R.N. Bhattacharya and members of

film group, NPL for discussions and also for providing me with the thickness data of the samples.

Dr. P.T. Rajgopalan, Scientist 'F', DMSRD, Kanpur kindly extended to me the use of SEM and helped me in taking SEM micrographs.

I am grateful to the Department of Advance Center for Material Science (ACMS), Kanpur for extending to me different facilities used for characterization of films. I am thankful to Mr. Uma Shanker for doing XRD and Mr. P. Paul for SEM measurements. I availed the facility of Vickers micro indentation in Material Testing Laboratory, IIT Kanpur.

I am also thankful to Mr. A. Trivedi for helping me troubleshoot the problems with the SEM.

I express my thanks to all my friends, colleagues and lab mates who helped me in various ways in the course of this work. I would particularly like to thank Dr. Ram bilas, Dr. A.K. Khulbe, Dr. S.K. Tripathi, S. Bhargava, Subhash, Saurabh, Nivedita, Nazrul, Mr. T. Som, Sandhya, Navneet, Gautam, Anil, Pratima, Chaitali, Subhashish, Anshu, Asha, Vandana, Irina, Anjali and Debashish.

I would like to thank the staff of Physics department – especially Mr. L. Singh, Mr. R. Panda, Mr. D.P. Pant, Mr. Ghanshyam and Mr. A.K. Srivastava – for their help in various matters. I am thankful to Mr. R.C. Vishwakarma for typing the thesis and Mr. R. Jain for preparing neat tracings.

I wish to express my gratitude to my parents, my brother Ravindra, Bhabi, nephew Avinav and sister Sangeeta whose affection and active assistance has indeed been invaluable. All of them have stood by me through my smiles and tears. Their affection and unflinching faith in me have kept me happy all along.

*Manju Malhotra*  
Manju Malhotra

## SYNOPSIS

**Name of Student:** MANJU MALHOTRA      **Roll No:** 9010974

**Degree for which submitted:** Ph.D.      **Department:** Physics

**Thesis Title:** Growth and structural characterization of diamond and diamondlike carbon Films.

**Name of thesis supervisor:** Dr. Satyendra Kumar  
Department of Physics  
I.I.T. Kanpur- 208 016

**Month and year of thesis submission:** December, 1996.

Thin films of diamond and diamondlike carbon have gained increasing importance due to their numerous useful properties such as high hardness, optical transparency for visible and infrared light, good electrical insulation, high dielectric strength, high thermal conductivity, and chemical inertness. However, tailoring the combination of these properties requires special efforts as carbon can assume various structures. Multiplicity in configurations of C-C and C-H bonding leads to complex microstructures, and plays a vital role in determining properties of thin films of carbon. Carbon can participate in  $sp^3$ ,  $sp^2$  or even  $sp^1$  bonds in thin films. In addition, hydrogen may bond to carbon in mono-, di- or trihydride groups in solid networks. This leads to thin films of carbon ranging from soft graphitic films to the extreme case of hard polycrystalline diamond. In between lies an interesting range of hydrogenated amorphous carbon (a-C:H) films having properties from polymeric (electrically insulating, high optical bandgap, and soft) to diamond like (insulating, large bandgap and hard). It is this later category called diamondlike carbon (DLC), which has attracted much attention in recent years. In general, DLC films exhibit properties which are combination of graphite, diamond and polymer-like nature of their constituents. Hence, a correlation of film properties with microstructure and growth conditions is important from both basic and technological point of view.

In this work, we have carried out systematic studies on the growth of hydrogenated amorphous carbon (a-C:H) films with a view to understand the inter-relationships between growth parameters and film microstructure. In particular, the role of hydrogen, which influences both growth conditions and properties of the deposited films, is investigated using a variety of characterization techniques. A correlation between hydrogen incorporation, microstructure of the films, and their physical properties is established. Based on information obtained from the effects of deposition conditions on the plasma and film properties, a phenomenological model is presented to explain the nucleation and growth of a-C:H films. In addition, growth of square faceted polycrystalline diamond films has been accomplished by using a simple and inexpensive oxy-acetylene flame technique.

Two different deposition techniques, namely, dc glow discharge decomposition and combustion flame were employed. Acetylene was the source of carbon species in both cases. A simple dc glow discharge reactor was designed and fabricated. The electrical discharge parameters of the system were characterized by measuring the starting voltages ( $V_{st}$ ) required to initiate the plasma as a function of the interelectrode gap spacing ( $d$ ) and the total gas pressures ( $p$ ). Plotting the  $V_{st}$  vs  $p \cdot d$  product over a large parameter range, it was found to follow Paschen's law. Mass spectroscopic analysis of the plasma in the two branches of this curve shows marked differences in the plasma species. Atomic and molecular hydrogen were found to be significant byproducts of the plasma dissociation of acetylene. In particular, gas phase polymerization, as evident from the presence of  $C_xH_y$  ( $x > 1, y > 2$ ) species, dominates the discharge operated at higher  $p \cdot d$  branch of the curve. Addition of hydrogen to the acetylene shifts the minimum in the Paschen curve to higher operating pressures and reduces the polymerization.

It is clear that hydrogen participates in the growth of carbon films and plays a crucial role in determining their properties. Hydrogen provides to the carbon atoms  $sp^3$ ,  $sp^2$  bonding, which in turn affects the hybridization of carbon-carbon atoms during growth leading to graphitic or diamond like character. The total amount of hydrogen in the films may also vary from fraction of a percent in polycrystalline diamond films to several tens of percent in a-C:H films. It is therefore essential to obtain reliable information on the total hydrogen content and type of C-C and C-H bonding

configurations to understand the microstructure and the physical properties of the films. We have applied three complementary techniques viz. infrared spectroscopy (IR), elastic recoil detection analysis (ERDA), and mass spectroscopic thermal effusion (MSTE) to characterize hydrogen in a-C:H films and explore their microstructural features. It is shown that a careful analysis of IR data can yield reliable values of  $sp^3$  and  $sp^2$  bonding fractions of C-C bonds in a-C:H films. Further,  $sp^3/sp^2$  ratio, as popularly quoted in literature, is not necessarily a good indicator of the film quality. However, we have found that detailed information on hybridization fractions, total hydrogen content ( $C_H$ ) as well as fractions of  $CH_3$ ,  $CH_2$ , and  $CH_1$  is required to correlate the measured film properties such as microhardness and optical bandgap etc. ERDA is known to produce total atomic hydrogen concentration (bonded and unbonded) in carbon films. We have shown that the hydrogen content from ERDA should be estimated with caution because of the ion induced migration of hydrogen from the samples. Further, hydrogen depth profiles using ERDA show a non-uniform distribution of hydrogen in soft a-C:H films.

The MSTE technique, though destructive, provided useful microstructural information. Threshold temperature for hydrogen effusion is found to be about 400 °C and two major peaks are observed at around 600 °C and 750 °C in our dc glow discharge a-C:H films. MSTE spectra show the evolution of hydrogen along with a variety of hydrocarbons ( $CH_3$ ,  $C_2H_2$ ,  $C_2H_4$ ,  $C_3H_3$  and  $C_4H_3$  etc.) for soft films. However, the hydrogen evolution at high temperature was found to dominate the effusion spectra in case of hard films with methane being the only hydrocarbon species evolved. The analyses of hydrogen effusion peaks by studying the peak positions as a function of heating rates and sample thickness suggest bond breaking or thermal desorption to be the rate limiting step. Study of as-deposited and annealed samples shows that the nature of hydrogen incorporation is different in polymeric and diamondlike films. In DLC, hydrogen is found to be homogeneously distributed as contrast to the case in polymeric films.

Having established the methodology for characterization of hydrogen, a detailed variation in suitably chosen growth parameters was carried out and their effects on film properties were studied to obtain an insight into the mechanism of film growth. Parameters influencing homogeneous gas phase plasma reactions such as total working

is pressure, gas composition and electric fields as well as those influencing the heterogeneous surface based reactions such as substrate temperature ( $T_s$ ) and negative bias as to the substrates were varied. The physical properties of the films were found to have a complex dependence on deposition conditions. At a fixed substrate temperature and discharge power, increasing the total acetylene gas pressure decreases the film microhardness and increases the hydrogen content. Harder films ( $\sim 2000 \text{ kgf/mm}^2$ ) were obtained at lower growth pressures (in lower branch of the Paschen curve). Substrate temperature mainly affects the  $sp^3$  and  $sp^2$  fractions in the film and resultant optical properties. Film properties could be further modified by mixing acetylene with hydrogen. By increasing the degree of dilution, the total hydrogen content in the samples decreases and microhardness increases.

Keeping the substrate temperature at  $250^\circ\text{C}$  and hydrogen dilution of 50 %, surface based reactions could be further controlled by applying a negative bias ( $V_b$ ) to the substrate. Consistent with earlier results, ion energy is found to have a strong effect on film properties. At an applied  $V_b$  of  $-250 \text{ V}$ , we are able to make DLC films having high microhardness ( $\sim 2500 \text{ Kgf/mm}^2$ ), large optical bandgap ( $\sim 2.5 \text{ eV}$ ) and low hydrogen content ( $\sim 6 \text{ at.}\%$ ). These films contain  $sp^3$  C-C bonding fraction of 0.71 along with a significant fraction of  $sp^2$  (0.23) bonding. Micro-Raman analysis shows Raman peaks at  $1353 \text{ cm}^{-1}$  and  $1287 \text{ cm}^{-1}$  indicating the presence of nanocrystallites of hexagonal diamond polytypes in these plasma CVD deposited samples. These results demonstrate that the films are comparable to so called tetrahedrally bonded hydrogenated amorphous carbon (ta-C:H) produced by more exotic ion beam methods.

In addition to the growth of amorphous carbon films using dc glow discharge plasma CVD, we have also studied the growth of polycrystalline diamond films by using combustion flame method. Here, key issues concerning the deposition technique involve the ability to deposit smooth diamond films on metallic substrates of practical importance. We have used molybdenum and stainless steel substrates for this purpose.

The reactive nature of oxy-acetylene flame varies with the flow ratio of constituent gases and the geometry of the flame. Acetylene rich flame consists of three distinct

reactive zones: inner cone, reducing middle zone and oxidizing outer flame. The homogeneous reactions in the combustion flame produce various hydrocarbon species. The species formed in the middle zone of flame are found to be growth precursors of diamond. Exposing the substrates to diamond forming species, the surface based reactions are controlled by the variations in  $T_s$ . The nature of substrate surface also influences the film growth. A short duration pretreatment of Mo substrates by outer zone of the oxy-acetylene flame at lower  $T_s$  results in the improvements in quality and adherence of the diamond films. Films with predominantly (100) square faceted diamond crystallites were deposited on Mo. Using a similar surface modification technique, we are able to overcome the problem of carbon diffusion in steel. Good quality diamond films were deposited on stainless steel substrates. Formation of interfacial layers and their effects on the subsequent diamond growth is studied. ERDA and MSTE measurements show a low hydrogen content and higher thermal stability of diamond films.

The thesis is organized as follows:

After a brief review of the properties of diamond and DLC films, the motivation and objective of this work are introduced in chapter I. Next chapter describes the experimental techniques used by us to characterize the amorphous carbon and polycrystalline diamond films. Our glow discharge reactor and deposition methodology of films is presented in chapter III. The parameterization of reactor and identification of glow discharge characteristics are also dealt with in the same chapter. The characterization of hydrogen and microstructure in a-C:H films has been established in chapter IV using three complementary techniques IR, ERDA and MSTE. The dependence of film properties on growth parameters and a growth model based on these results are the subject matter of chapter V. Chapter VI deals with the growth and structural characterization of oxy-acetylene flame deposited diamond films. Summary, conclusions and scope of future work are outlined in chapter VII.



## LIST OF PUBLICATIONS

1. Study of hydrogen in diamondlike carbon films, Manju Malhotra, T. Som, V.N. Kulkarni and Satyendra Kumar, Vacuum, 1996 (In Press)
2. Deposition of diamond films on metal substrates, Manju Malhotra, S.C. Agarwal and Satyendra Kumar, Bull. Mater. Science, 19 (1996) 455.
3. Subband gap absorption in hydrogenated amorphous silicon by constant photocurrent method, Anil K. Sinha, M. Malhotra, E. Bhattacharya, S. Kumar and S.C. Agarwal, Indian Journal of Pure and Applied Physics, vol 31, (1993) 548.
4. Thermal gas effusion from diamondlike carbon films, Manju Malhotra and Satyendra Kumar, accepted for presentation in 7<sup>th</sup> European Conference on Diamond, Diamondlike and Related Materials (DIAMOND 1996) held in France, 8-13 September 1996. (To appear in Diamond and Related Materials 1997).
5. Plasma chemical vapor deposition of diamondlike carbon films, Manju Malhotra and Satyendra Kumar, Proceedings of the National Symposium on Plasma Science 1995, IIT Kanpur, ed. By P.K. Ghosh. P89.
6. Growth of polycrystalline diamond films on stainless steel substrates without external buffer layers using oxy-acetylene flame, Satyendra Kumar and Manju Malhotra, Diamond and Related Materials (submitted).
7. Deposition of hydrogenated amorphous carbon films using DC glow discharge of acetylene, Manju Malhotra and Satyendra Kumar, J. Vac. Sci. Technol (Submitted).
8. Ion beam induced migration and analysis of hydrogen in a-C:H films, (in preparation).
9. Evidence of nanocrystallinity in plasma deposited highly tetrahedral hydrogenated amorphous carbon films. (To be submitted)
10. Role of surface pretreatments on the growth of diamond films on metal substrates using oxy-acetylene flames. (To be submitted).

# CONTENTS

Acknowledgments	vii
Synopsis	ix
List of publications	xiv
Contents	xv
List of Tables	xix
List of Figures	xxi

## CHAPTER I

INTRODUCTION.....	1
1.1 FORMS OF CARBON.....	2
1.2 THIN FILMS OF DAMOND AND DIAMOND-LIKE CARBON .....	4
1.2.1 <i>Diamond Films</i> .....	4
1.2.2 <i>Diamond-like Carbon Films</i> .....	5
1.3 APPLICATIONS OF DIAMOND AND DLC FILMS.....	9
1.4 REVIEW OF DEPOSITION TECHNIQUES.....	10
1.4.1 <i>Physical Vapor Deposition (PVD)</i> .....	14
1.4.2 <i>Chemical Vapor Deposition (CVD)</i> .....	16
1.4.3 <i>Hybrid Techniques</i> .....	21
1.4.4 <i>Combustion Flame Method</i> .....	23
1.5 MOTIVATION AND OBJECTIVES .....	24
1.6 THESIS PLAN .....	26

## CHAPTER II

<b>CHARACTERIZATION TECHNIQUES.....</b>	<b>27</b>
2.1 THICKNESS MEASUREMENT .....	27
2.2 STRUCTURE .....	28
2.2.1 <i>X-ray Diffraction</i> .....	28
2.2.2 <i>Scanning and Transmission Electron Microscopy</i> .....	29
2.2.3 <i>Raman Spectroscopy</i> .....	30
2.2.4 <i>Composition Analysis</i> .....	30
2.3 HYDROGEN BONDING AND CONTENT .....	31
2.3.1 <i>Infrared Spectroscopy</i> .....	31
2.3.2 <i>Mass Spectroscopic Thermal Effusion</i> .....	33
2.3.3 <i>Elastic Recoil Detection Analysis (ERDA)</i> .....	34
2.4 OPTICAL PROPERTIES .....	36
2.4.2 <i>Dielectric Constant and Optical Gap</i> .....	38
2.5 MECHANICAL PROPERTIES .....	39
2.5.1 <i>Microhardness</i> .....	39
2.5.2 <i>Stress Measurement</i> .....	41

## CHAPTER III

### LOW GLOW DISCHARGE DEPOSITION OF DIAMOND-LIKE CARBON FILMS

3.1 INTRODUCTION .....	42
3.2 PREPARATION OF DLC FILMS .....	42
3.2.1 <i>Design and Fabrication of the Reactor</i> .....	43
3.2.2 <i>Deposition Methodology</i> .....	44
3.3 DISCHARGE CHARACTERISTICS.....	47
3.3.1 <i>Initiation and Maintenance of the Discharge</i> .....	47
3.3.2 <i>Plasma Confinement</i> .....	49
3.3.3 <i>Electrode Separation</i> .....	49
3.3.4 <i>Floating and Bias Potentials</i> .....	50

3.4 MASS SPECTROMETRY OF THE DISCHARGE .....	51
3.5 DISCUSSION AND SUMMARY .....	54
<b>CHAPTER IV</b>	
<b>ANALYSIS OF HYDROGEN IN A-C:H FILMS.....</b>	<b>59</b>
4.1 INTRODUCTION .....	59
4.2 INFRARED SPECTROSCOPY .....	61
4.2.1 <i>Sp<sup>3</sup>/Sp<sup>2</sup> Ratio</i> .....	65
4.2.2 <i>Hydrogen Content</i> .....	68
4.3 ELASTIC RECOIL DETECTION ANALYSIS .....	69
4.4 THERMAL GAS EFFUSION .....	72
4.4.1 <i>Theory</i> .....	72
4.4.2 <i>Hydrogen Effusion</i> .....	75
4.4.4 <i>Hydrocarbon Effusion</i> .....	78
4.5 EFFECTS OF ANNEALING .....	81
4.6 SUMMARY AND CONCLUDING REMARKS .....	84
<b>CHAPTER V</b>	
<b>GROWTH AND PROPERTIES OF A-C:H FILMS.....</b>	<b>86</b>
5.1 INTRODUCTION .....	86
5.2 RESULTS .....	86
5.2.1 <i>Effect Of Acetylene Pressure</i> .....	87
5.2.2 <i>Effect Of Hydrogen Dilution</i> .....	90
5.2.3 <i>Effect Of Substrate Temperature</i> .....	92
5.2.4 <i>Effect Of Substrate Bias</i> .....	95
5.3 PROCESSES IN GROWTH OF A-C:H FILMS .....	98
5.3.1 <i>Homogeneous Processes</i> .....	99
5.3.2 <i>Heterogeneous Processes</i> .....	100
5.4 GROWTH MODEL .....	102
5.5 DISCUSSION .....	107

5.5.1 Average Coordination Number.....	107
5.5.2 Effects of Hydrogen On Film Properties .....	109
5.5.3 Role of Ion Energies .....	111
5.6 CONCLUDING REMARKS.....	113
<b>CHAPTER VI</b>	
<b>DIAMOND SYNTHESIS BY COMBUSTION FLAME CVD .....</b>	<b>114</b>
<b>INTRODUCTION.....</b>	<b>114</b>
6.2 PREPARATION OF DIAMOND FILMS .....	117
6.2.1 Experimental.....	117
6.2.2 Oxy-Acetylene Flame: Structure and Compositions.....	117
6.2.3. Optimization of flame: .....	119
6.3 RESULTS AND DISCUSSION.....	120
6.3.1 DIAMOND GROWTH ON MO .....	120
6.3.2 DIAMOND GROWTH ON STEEL.....	125
6.3.3 Diamond Growth on W and Ni.....	128
6.4 CONCLUSIONS.....	129
<b>CHAPTER VII</b>	
<b>SUMMARY, CONCLUSIONS AND SCOPE OF FURTHER WORK.....</b>	<b>130</b>
<b>REFERENCES.....</b>	<b>134</b>

## LIST OF TABLES

1.1	Properties of cubic diamond, lonsdaleite and graphite ( After Ref. 6 and 7).....	3
1.2	Applications of diamond and diamondlike carbon films.....	11
1.3	Comparison of various deposition techniques used for preparation of diamond and diamondlike carbon films.....	12
3.1	Deposition Parameter space scanned.....	46
4.1	Growth parameters and some of the physical properties of the samples on which hydrogen and microstructural analysis is presented in this chapter.....	61
4.2	Peak assignments for various bonding configurations observed in the infrared spectra.....	63
4.3	Microstructural and physical properties of a-C:H films. $Sp^3$ and $sp^2$ are hybridization fractions calculated from the conventional analysis of IR data. $Sp^{3*}$ and $sp^{2*}$ are fractions of C-C bonds bonded in $sp^3$ and $sp^2$ hybridization, respectively. Percentages of $CH$ , $CH_2$ and $CH_3$ are from the bonded hydrogen content ( $C_H$ ).....	67
4.4	Values of the thickness for two typical type A and B samples, as deposited and after heating to $600^\circ C$ and $1000^\circ C$ as measured by stylus method and estimated from thermal effusion data.....	81
4.5	Peak position of D and G bands ( $cm^{-1}$ ) and integrated intensity ratios of ( $I_D/I_G$ ) obtained after the deconvolution of Raman spectra of the sample (DLC49) after heating up to $600$ and $1000^\circ C$ .....	84
5.1	The deposition parameters used for the preparation of films.....	87
5.2	Effect of gas pressure on the properties of a-C:H films. $Sp^{3*}$ and $sp^{2*}$ are the percentages of C-C bonds bonded in $sp^3$ and $sp^2$ hybridizations, respectively. Percentages of $CH$ , $CH_2$ and $CH_3$ are from the bonded hydrogen content ( $C_H$ ). .....	89
5.3	Effect of hydrogen dilution on the properties of a-C:H films.....	91
5.4	Effect of substrate temperature on the properties of a-C:H films. DLC33A is the sample #DLC33 after heating to $600^\circ C$ at $\sim 20^\circ C/min$ . heating rate.....	93

5.6	Peak positions ( $\text{cm}^{-1}$ ), and their assignments of a sample (DLC51) deposited with acetylene-hydrogen mixture (50%) at $250^\circ\text{C}$ substrate temperature with a bias of $-250\text{V}$ , observed in the Raman spectrum. ....	97
6.1	Lattice parameters, crystal structures and solid surface energies ( $\text{ergs}/\text{cm}^2$ ) of various substrate materials.....	115

## LIST OF FIGURES

Fig. 1.1	(a) The atomic arrangements in graphite, lonsdaleite and cubic diamond (b) Unit cells of graphite, lonsdaleite and diamond.	2
Fig. 1.2	(a) Schematic representation of $sp^3$ , $sp^2$ and $sp^1$ hybridized atoms. (b) A two-dimensional representation of a structure for a diamond-like hydrogen (After ref. 34). $\bullet$ = $sp^2$ carbon atoms, $\bigcirc$ = $sp^3$ carbon atoms, O = hydrogen atoms. Nominal hydrogen fraction is 0.33; nominal fraction of carbon sites with $sp^3$ coordination is 0.28.	6
Fig. 1.3	Schematic diagram of some physical vapor deposition techniques (a) single beam sputtering (b) dual beam sputtering (c) laser ablation (d) laser ion beam (e) mass selected ion beam and (f) laser plasma hybrid.	14
Fig. 1.4	Schematic diagram of thermal CVD techniques (a) HFCVD and (b) EACVD	16
Fig. 1.5	Schematic of electric discharges (a) direct current (b) radio frequency (capacitive coupling) and (c) radio frequency (inductive coupling).	17
Fig. 1.6	Schematic diagram of (a) Microwave plasma and (b) Electron cyclotron resonance (ECR) Plasma CVD techniques.	20
Fig. 1.7	Schematic flowchart of growth-property relationship for diamond and DLC films.	24
Fig. 2.1	Schematic diagram of the back scattering process. Target of mass M is initially at rest.	31
Fig. 2.2	Schematic diagram of the thermal gas effusion system.	33
Fig. 2.3	A typical ERDA geometry for the detection of hydrogen.	34
Fig. 2.4	(a) Schematic transmittance measurements. (b) Schematic showing the various reflected and transmitted components.	36
Fig. 2.5	(a) Comparison of indentations made by Knoop and Vickers Indenters.	39



- Fig.2.5 (b) Jonsson and Hogmark model for hardness behavior of thin films The contribution of hardness film to composite hardness is in the region around the edge of indentation  $A_f$  (shadowed area), whereas the inner region of the indentation  $A_s$  transmits the loading force directly to the substrate. 39
- Fig.2.6 Typical Vickers microhardness as a function of applied load for a DLC sample deposited on c-Si substrate. Film hardness  $H_f$  has been calculated from measured composite hardness  $H_c$  and substrate hardness  $H_s$ . 41
- Fig.3.1 Schematic diagram of the dc plasma reactor. 43
- Fig.3.2 (a) Photograph of the dc glow discharge system fabricated for the present work. 43
- Fig.3.2 (b) A nut and screw arrangement for variation of inter electrode gap. 43
- Fig.3.3 Variation of discharge starting voltage ( $V_{st}$ ) as a function of the product of acetylene pressure (p) and inter electrode gap (d) using stainless steel electrodes at a substrate temperature of 250°C. 47
- Fig.3.4 Variation of discharge starting voltage ( $V_{st}$ ) as a function of the product of gas pressure (p) and inter electrode spacing ( $d=2.2\text{cm}$ ) using acetylene diluted in hydrogen ( $\text{C}_2\text{H}_2/\text{C}_2\text{H}_2 + \text{H}_2=0.2$ ). 47
- Fig.3.5 Current versus cathode voltage characteristics for acetylene plasma at (a) 0.27 mbar (b) 0.6 mbar and (c) 1 mbar. 49
- Fig.3.6 (a) Glowing and dark spaces in dc discharges. 49  
(b) Voltage distribution in a dc glow discharge process .
- Fig.3.7 Dependence of deposition rate on the interelectrode spacing for pure  $\text{C}_2\text{H}_2$  glow discharge. 50
- Fig.3.8 Floating voltage ( $V_f$ ) vs p.d. at a fixed cathode voltage of 710V for a  $\text{C}_2\text{H}_2$  plasma at substrate temperature of 250°C. The inset shows variation of  $V_f$  with applied cathode voltage at a fixed value of p.d. 50
- Fig.3.9 Variation of the substrate floating voltage with cathode voltage for dc discharges in  $\text{C}_2\text{H}_2$  ignited at 0.27 mbar, 0.6 mbar and 1 mbar. 51
- Fig.3.10 Mass spectra of pure acetylene discharge at the gas pressures of: (a) 0.55 mbar (region A), and (b) 4 mbar (region B) of Fig.3.3. 52

- Fig. 3.11 Mass spectrum of hydrogen diluted acetylene discharge at a gas pressure of 1.0 mbar. 52
- Fig. 3.12 Mass spectra of hydrogen diluted acetylene discharge at the gas pressures of (a) 1 mbar, (b) 4 mbar, and (c) 10 mbar. 53
- Fig. 4.1 Infrared spectra of a-C:H films deposited at substrate temperature of 250° C and (a)  $p = 0.6$  mbar,  $V_b = -250$  V,  $C_2H_2/C_2H_2 + H_2 = 0.5$ , (Type A); (b) pressure= 0.6 mbar, pure  $C_2H_2$  (Type A); and (c) pressure= 4 mbar, pure  $C_2H_2$  (Type B). 62
- Fig. 4.2 Deconvolution of the infrared stretching band of a-C:H films from the spectra in Fig. 4.1. 64
- Fig. 4.3: Ternary phase diagram for hydrocarbon films. Open circles are published IR data corrected by Jacob and Moller using equation 4.3. Full squares represent the IR data of the present work corrected by the same procedure. Full circles are NMR data and full triangles are EELS data. The data of Grill et al. (241) are shown as full and open stars. Results obtained by EELS on ta-C:H deposited films by MSIB (27) are also shown by open triangles. 67
- Fig. 4.4 1.5 MeV  $He^+$  induced recoil spectra of hydrogen from a DLC film deposited on silicon substrate at  $T_s = 375^\circ$  C using pure acetylene. The surface position of H is indicated by arrow. The spectra were taken for  $He^+$  integrated charge of 5  $\mu$ C and 35  $\mu$ C. They are normalized for an incident charge of 1  $\mu$ C/mSr for the sake of direct comparison. The inset shows the variation of the average bulk hydrogen concentration as a function of integrated  $He^+$  charge. 70
- Fig. 4.5: 1.5 MeV  $He^+$  induced recoil spectra of hydrogen from two representative diamondlike (DLC 51) and polymeric (DLC 18) films corresponding to Fig. 4.1 (a) and (c) respectively. The spectra were taken for the same integrated charge of 5  $\mu$ C. 71
- Fig. 4.6 Hydrogen atomic concentration in DLC films of different microstructures (see Table 4.3) as a function of irradiation dose with 1.5 MeV  $He^+$  ions, as determined by elastic recoil detection analysis. 71
- Fig. 4.7 Thermal gas effusion spectra as a function of heating temperature of typical (a) polymeric ( $p = 10.0$  mbar,  $T_{sub} = 250^\circ$  C,  $V_c = 710$  V, pure  $C_2H_2$ ); and (b) diamond-like carbon ( $p = 0.6$  mbar,  $T_{sub} = 250^\circ$  C,  $V_c = 710$  V,  $V_b = -250$  V, ( $C_2H_2 / C_2H_2 + H_2 = 0.5$ )) films. 75
- Fig. 4.8 Relative concentration of desorbed hydrogen and hydrocarbons as calculated from the thermal effusion spectra in Figure 4.7.

Fig.4.9	Determination of activation energies of hydrogen evolution for polymeric (soft) and diamond like carbon (microhardness~ 2100 kgf/mm <sup>2</sup> ) films of thickness 1.4 $\mu$ m and 1.2 $\mu$ m respectively.	76
Fig. 4.10:	Thermal evolution of methane from a-C:H films of different hardnesses having approximately same thicknesses. DLC18 is soft polymeric sample (see Table 4.1). DLC40 and DLC51 are hard samples (VH ~ 2100 and 2420 kgf/mm <sup>2</sup> , respectively). DLC50 is a thinner sample (d~0.4 $\mu$ m) prepared under conditions of DLC 51. All effusion spectra were recorded at constant heating rate of 20°C/min.	77
Fig. 4.11.	H <sub>2</sub> <sup>+</sup> and CH <sub>3</sub> <sup>+</sup> effusion profile during two consecutive heating cycles of DLC film (DLC49): (a) up to 600° C, followed by heating the same sample up to 1000°C (b).	79
Fig.4.12 :	IR absorption spectra of a-C:H films in the range of stretching modes: (a) as deposited (b) after heating to 600° C as illustrated in Fig.4.11.	82
Fig. 4.13	ERDA spectra measured on the heat treated sample (DLC49).	82
Fig. 4.14	Raman spectra of (a) 600°C and (b) 1000°C heated sample (DLC49).	83
Fig.5.1	Variation in deposition rate as a function of total gas pressure.	83
Fig.5.2	Effect of feed gas pressure on microhardness of the films deposited at 250°C using pure acetylene.	87
Fig.5.3	Hydrogen content vs C <sub>2</sub> H <sub>2</sub> pressure.	88
Fig.5.4	Thermal gas effusion spectra as a function of heating temperature for films deposited at substrate temperature of 250° C and C <sub>2</sub> H <sub>2</sub> gas pressure during deposition as (a) 4 mbar (b) 1 mbar (c) 0.7 mbar.	88
Fig.5.5	(a)Optical absorption coefficients in the near bandgap region for samples prepared at pressures of (1) 0.38, (2) 4.0 and (3) 0.1 mbar.	89
Fig.5.5	(b) Tauc plots corresponding to fig.5.5 (a).	89
Fig 5.6	Variation in the film growth rate as a function of hydrogen dilution of acetylene.	89
Fig.5.7	ERDA spectrum of a sample (DLC40) prepared using 50% hydrogen dilution at T <sub>s</sub> =250°C.	90
		91

- Fig.5.8 Thermal effusion characteristics from a hydrogen diluted sample (DLC40). 91
- Fig.5.9 Dependence of growth rate of a-C:H films on the substrate temperature at a constant acetylene pressure of 0.6 mbar. 92
- Fig.5.10 FTIR transmission spectra of samples prepared under identical conditions ( $p=0.6$  mbar,  $V_c=710$  V, pure  $C_2H_2$ ) but at different substrate temperatures of 125, 375 and 525°C. 92
- Fig.5.11 The deconvoluted intensities of different C-H configurations under stretching modes for samples corresponding to fig.5.10 along with room-temperature-deposited sample. 92
- Fig.5.12 Variation in hydrogen content as a function of substrate temperature. 94
- Fig.5.13 Tauc plot for samples deposited at substrate temperature of 125, 375 and 525°C. 94
- Fig. 5.14 Variation of optical bandgap as a function of deposition temperature on films produced by different growth techniques. Numbers given on the curves represent data from: (1) Ichinose, (2) Anderson, (3) Watanabe, (4) Meyerson, (5) Jones, (6) Munekawa and (7) Lin, from references 287, 66, 84, 49, 62, 288 and 290. Our data is also shown by the solid circles. 94
- Fig.5.15 Effect of substrate bias ( $V_b$ ) on the growth rate of films. 95
- Fig.5.16 Deconvolution of the C-H stretch region of the IR spectrum of DLC films deposited at various substrate potentials of (a)  $V_b=V_f=-85$  V, (b)  $V_b=-250$  V and (c)  $V_b=-350$  V. The acetylene dilution, substrate temperature and total gas pressures were fixed ( $C_2H_2 / C_2H_2 + H_2 = 0.5$ ,  $T_s = 250^\circ$  C and  $p=0.6$  mbar). 95
- Fig.5.17 Effect of substrate bias on optical band gap. 96
- Fig.5.18 Raman spectrum with fitted components for DLC51. 96
- Fig.5.19 A schematic illustration of growing a-C:H film. Reactive species diffuse to the top surface with an energy distribution determined by discharge conditions and ion sheath potential. At the underlying growth zone, thermally activated reactions: cross-linking of C-C atoms in solid networks and dehydrogenation takes place. 103

Fig.5.20	The average coordination number, $m$ , as a function of (a) hydrogen atomic fraction and (b) microhardness of a-C:H films.	108
Fig.5.21	Optical bandgap plotted as a function of hydrogen content for dc glow discharge deposited a-C:H films of different microstructures.	109
Fig.5.22	Sp <sup>3</sup> C-C content on a variety of dc glow discharge deposited a-C:H films in the present work as a function of hydrogen content. The points from plasma beam source (PBS, after ref.29), mass selected ion beam (MSIB, ref. 27), RF chemical vapor deposition (RFCVD, ref. 315, 317(B)) and magnetic field enhanced plasma deposition (MEPD, ref. 152) techniques are also shown for comparison. Solid line represents the predicted sp <sup>3</sup> component for a fully constrained amorphous network (ref 152, 315)	110
Fig 6.1	Schematic diagram of oxy-acetylene flame deposition system.	117
Fig 6.2	Oxy-acetylene flame structure.	118
Fig 6.3	XRD spectra of samples prepared at substrate temperature of (a) 1060°C, (b) 850°C, and (c) 660°C.	120
Fig 6.4	SEM photographs of diamond film grown on untreated Mo for 10 minutes.	121
Fig 6.5	XRD spectrum of a diamond film deposited on Mo for 10 minutes with pretreatment for 1 minute.	122
Fig 6.6	Surface morphology of the film corresponding to fig. 6.5.	123
Fig 6.7	SEM micrograph of a diamond film deposited on Mo for 80 minutes after pretreatment of substrate for 1 minute by outer flame.	123
Fig 6.8	Raman spectrum of a diamond film corresponding to fig. 6.7.	123
Fig 6.9	XRD spectrum from the oxide film on Mo.	124
Fig 6.10	Thermal desorption spectrum of a 2 µm thick diamond film on Mo substrate:	125
Fig 6.11	Scanning electron micrograph of diamond film deposited at substrate temperature of 625° C on stainless steel substrate for (a) 10 minutes and (b) 90 minutes after pretreatment of substrate by outer flame for 3 minutes.	126
Fig 6.12	XRD spectrum of the diamond film on stainless steel substrate corresponding to fig 6.11 (b).	126

Fig 6.13. Raman spectra of diamond films on stainless steel substrate deposited for (a) 10 minutes and (b) 90 minutes, corresponding to figs 6.11 a and b respectively.

126

Fig 6.14 Normalized RBS spectra of steel-oxide -diamond composite.

127

Fig 6.15 (a) SEM photographs showing diamond growth on Ni.

(b) SEM photographs showing diamond growth on W.

128

# CHAPTER I

## INTRODUCTION

Carbon is one of the most versatile and useful element existing in nature. Recent advents in various novel forms of carbon have attracted many researchers for their synthesis and applications. *Diamonds are forever* as they always hold fascination of scientists and laypersons alike due to their unique physical properties. Some of the key properties of diamond are :

- Extreme mechanical hardness.
- Broad optical transparency from the deep UV to the far IR region of the electromagnetic spectrum.
- Good electrical insulation (room temperature resistivity is  $\sim 10^{16} \Omega \text{ cm}$ ).
- Strongest known material with highest bulk modulus ( $1.2 \times 10^{12} \text{ Nm}^{-2}$ ) and lowest compressibility ( $8.3 \times 10^{-13} \text{ m}^2 \text{ N}^{-1}$ ).
- Highest known value of thermal conductivity at room temperature ( $2 \times 10^3 \text{ Wm}^{-1} \text{ K}^{-1}$ ).
- Thermal expansion coefficient at room temperature ( $0.8 \times 10^{-6} \text{ K}^{-1}$ ) is comparable with that of Invar.
- Diamond can be doped to change its resistivity over the range  $10^{-10}$  to  $10^6 \Omega \text{ cm}$ , so possibility of a semiconductor with a wide optical band gap.
- High resistance to chemical erosion.
- High radiation hardness.

Although the impressive superlative properties of diamond were known for centuries, the real breakthrough was achieved when the General Electric Co. of USA declared the synthesis of diamond at high pressure and high temperatures (HPHT) [1,2]. This material is now commonly used in cutting, grinding and polishing. Specialized technique of HPHT and limitations on the potential applications hindered the growth of

synthetic diamonds. Many applications required large areas. Ability to fabricate thin films and coatings of this wonder material has attracted worldwide interest in the physics and technology of chemical vapor deposited diamond and shows the importance and relevance of diamondlike materials. However, tailoring the combination of these properties requires special efforts. The crucial reason for this is the electronic configuration of carbon which allows it to assume a variety of structures. In particular, understanding of the nucleation and growth of thin films of carbon with reproducible and desired properties is still far from complete.

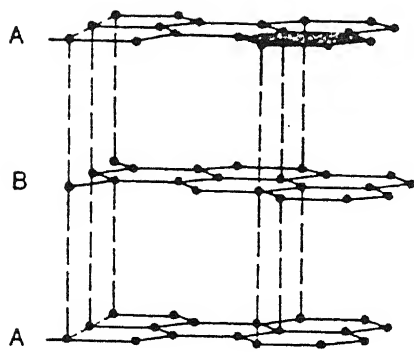
In the following sections, we will describe the structures of carbon and related physical properties. A brief historical perspective on the properties and synthesis of crystalline and amorphous thin films of carbon will be presented. Nature of diamondlike carbon films, their microstructure and properties will then be discussed. Major applications and requirements on the physical properties of diamond and diamondlike carbon films are summarized in section 1.3. Next section gives a comprehensive and critical review of the present status of deposition techniques. This Chapter ends with the statement of objectives for the present work and an outline of this thesis.

## 1.1 FORMS OF CARBON

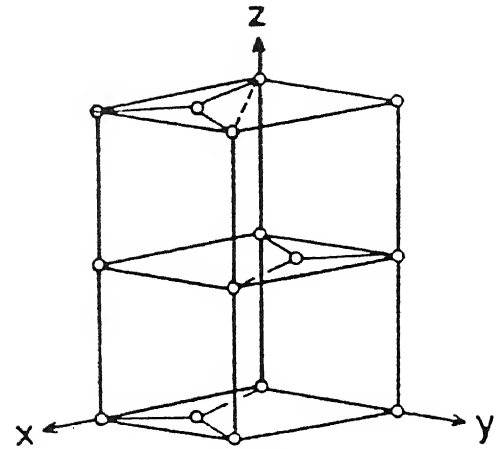
Diamond and graphite are two well known allotropes of carbon. Diamond consists of tetrahedral ( $sp^3$ ) hybridization of valence electrons while graphite has a trigonal bonding with  $sp^2$  hybridization. Consequently, the structure of the two phases is very different as shown in Fig. 1.1. Diamond has a face-centered cubic structure with the highest atomic number density for any material ( $1.76 \times 10^{23}$  atoms/cm<sup>3</sup>). Graphite on the other hand, consists of layers of carbon atoms in a hexagonal closed packed structure. These differences in the structures lead to properties which have extreme values in case of diamond as listed above. Table 1.1 compares some of the properties of diamond and graphite.

Lonsdaleite and carbyne are two other less common allotropes of carbon [3]. Lonsdaleite is close to diamond. Both involve same type of chemical bond ( $sp^3$

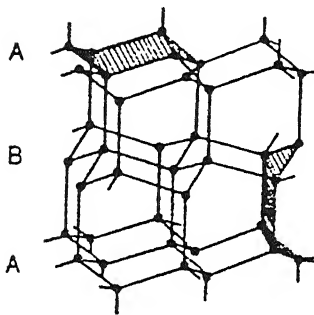




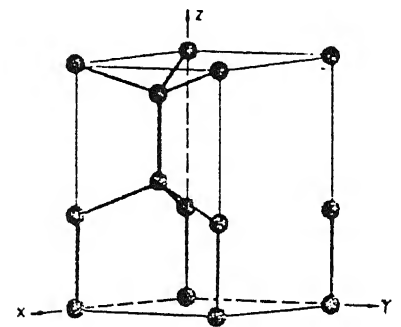
GRAPHITE



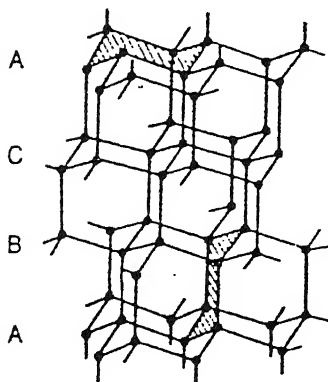
GRAPHITE



LONSDALEITE

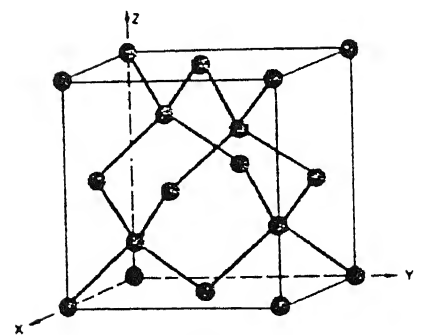


LONSDALEITE



DIAMOND

(a)



DIAMOND

(b)

Fig.1.1(a) The atomic arrangements in graphite, lonsdaleite and cubic diamond (b) Unit cells of graphite, lonsdaleite and diamond.

hybridization) but differ in symmetry. Diamond has cubic symmetry while lonsdaleite is hexagonal [Fig 1.1]. The crystal structure data of lonsdaleite is included in Table 1.1. A diamond polytype structure, 6H hexagonal diamond, has been recently identified by electron diffraction [4]. Natural crystals of diamond also differ from each other in form (octahedron, cubes), in texture and in the nature of impurity centers. Carbyne is another allotrope of carbon with a linear (sp) hybridization of electrons. Three crystalline modifications of graphite are also known: hexagonal, rhombohedral and cubic. In addition, another interesting allotrope of carbon, a molecular crystal of the fullerene molecule  $C_{60}$  has also been recently discovered [5].

**Table 1.1: Properties of cubic diamond, lonsdaleite and graphite (After Ref. 6 and 7).**

Property	Cubic Diamond <sup>6</sup>	Lonsdaleite <sup>7</sup>	Graphite
Symmetry	cubic	hexagonal	hexagonal
Point group	$T_d$	$T_d$	$D_{6h}$
Space group	$O_h^7$ (F d3m)	$D_{6h}^4$ (P6 <sub>3</sub> / mmc)	$D_{6h}^4$ (P6 <sub>3</sub> / mmc)
Atoms per Unit cell	8	4	4
Unit cell constant	$a = 3.57 \text{ \AA}$	$a = 2.52 \text{ \AA}$ $a = 4.12 \text{ \AA}$	$a = 2.46 \text{ \AA}$ $c = 4.12 \text{ \AA}$
C-C bond distance	$1.54 \text{ \AA}$	$1.54 \text{ \AA}$	$1.42 \text{ \AA}$
Bonding	$sp^3$	$sp^3$	$sp^2$
General crystal	Zinc blende type	2H Wurtzite	
Theoretical density (298° K)	$3.515 \text{ g/cm}^3$	$3.52 \text{ g/cm}^3$	$2.3 \text{ g/cm}^3$
Chemical stability	Inert inorganic acids	-	Inert, inorganic acids
Hardness (Vickers, kgf/mm <sup>2</sup> )	7000-10000	-	100
Thermal conductivity (W/cm-K)	20 at 20° C	-	K $\parallel$ 30-40 K $\perp$ 1-2
Thermal Expansion coefficient at 293 K (K <sup>-1</sup> )	$0.8 \times 10^{-6}$	-	-
Transparency	UV-VIS-IR	-	Opaque
Optical gap (eV)	5.5	-	0
Refractive Index at 589 nm	2.42	-	2.15 ( $\parallel$ C) 1.8 ( $\perp$ C)
Resistivity ( $\Omega$ cm)	$>10^{16}$	-	0.4 ( $\parallel$ C) 0.20 ( $\perp$ C)
Dielectric Const.	5.7	-	2.6 ( $\parallel$ C) 3.28 ( $\perp$ C).
Dielectric strength (V/cm)	$>10^{12}$	-	-

## 1.2 THIN FILMS OF DAMOND AND DIAMOND-LIKE CARBON

Material is created *ab initio* in the form of thin films from atomic or molecular constituents [8]. Therefore, thin film technologies provide enormous flexibility to tailor make the material with desired properties. In thin films of carbon, a carbon atom can adopt any or all of the three bonding configurations; tetrahedral diamond-like  $sp^3$ , trigonal graphite-like  $sp^2$  and linear  $sp^1$ . In addition, arrangement of these atomic configurations may lead to crystallites of any sizes from single crystals to nano-crystallites, as well as, amorphous structures.

### 1.2.1 Diamond Films

In contrast to HPHT synthetic diamonds, thin films of chemical vapor deposited (CVD) diamond are produced under non-equilibrium conditions of plasmas at low pressures and relatively lower temperatures. Kinetic factors allow to obtain a metastable phase of diamond in CVD under appropriate conditions. Selective removal of non-diamond forms of carbon occurs mainly when atomic hydrogen and ions/radicals are present in the gas phase in high concentrations. Pioneering work in CVD diamonds includes the successful efforts of Derjaguin [9] and Eversole [10] followed by Angus [11], and Matsumoto [12-15]. The mechanical properties of CVD diamond films are outstanding. Their hardness is comparable to that of single crystal diamond  $\sim 9000 \text{ kgf/mm}^2$ . The second hardest bulk material is cubic boron nitride. In comparison, some of the hard coatings used in industry e.g. carbides and nitrides of titanium and tungsten have hardness of  $\sim 2000 \text{ kgf/mm}^2$ . Several reviews have presented the history of metastable growth of diamond films and their properties [16-19].

Polycrystalline diamond films grown by the CVD require high substrate temperatures (800 to 1000°C) and high hydrogen dilution (>95%) of hydrocarbon source gas. These films contain very low hydrogen content (< 1 at. %). Structurally they may be a composite of crystalline diamond with small amounts of graphite and disordered phases. A working definition of thin film diamond by R. Messier et al [20] demands a crystalline morphology discernible by electron microscopy, crystalline structure identified by x-ray

diffraction which is consistent with the presence of diamond, and characteristic Raman peak at  $\approx 1332 \text{ cm}^{-1}$  typical for natural diamond.

### 1.2.2 Diamond-like Carbon Films

Unlike diamond films, diamondlike carbon films are non-crystalline. The interest in diamond-like carbon (DLC) films was stimulated when Aisenberg and Chabot [21] reported the growth of an *unusually hard* phase of carbon using ion beams in 1971. Next landmark work was reported by Holland and Ojha [22] who used RF discharge technique. Later, Weissmantel et al used dual ion beam to obtain these films [23]. Since then a number of investigators have used a variety of deposition methods to produce hard DLC films.

#### *Nomenclature*

As described above, carbon can assume any crystal structure or bonding configuration in thin film form. Hence, a broad spectrum of properties and a variety of methods for preparation of carbon films have resulted in ambiguous and inconsistent nomenclature [24,25], that often does not reflect the true physical structure of these films. “Diamond-like carbon” (DLC) is a widely used term to describe amorphous carbon films that posses properties (such as hardness, optical transmission, electrical transmission, electrical conductivity, etc.) that are similar or close to those of diamond films. It is expected that the DLC films must have a significant fraction of C-C bonds in diamond-like short range order ( $\text{sp}^3$ , tetrahedral bonds) to attain these properties. In general, amorphous carbon (a-C) refers to an amorphous network of carbon atoms with any possible mixture of  $\text{sp}$ ,  $\text{sp}^2$  or  $\text{sp}^3$  hybridized carbon that has no long range order.

Thin films of DLC are often prepared using hydrocarbon sources (section 1.4) and therefore, may contain variable amount of hydrogen. Hydrogen may bond to carbon in mono-, di-, or trihydride groups in solid networks. Such films may be called by a generic name - hydrogenated amorphous carbon (a-C:H) in analogy with more popular a-Si:H. However, unlike silicon, multiplicity of C-C and C-H bonding structures leads to a large variety of film microstructures and properties. Graphite-like is an adjective used to

describe a-C or a-C:H films having greater proportions of  $sp^2$  carbon bonds. These films are characterized by their low optical bandgap, high refractive index, and low resistivity. On the other hand, a-C:H films having largely  $sp^3$  bonding with a large amount of hydrogen bonded in polyhydride configurations are referred to as polymerlike or polymeric. Other names, such as i-C, i-C:H, dense carbon, hard carbonaceous, are also used to describe DLC films prepared by ion beam techniques.

More recently, the interest has been to produce thin films of “amorphous diamond” ( $sp^3$  short range order with no long range order, no hydrogen) with density approaching that of diamond [26-32]. Such films are called as tetrahedral amorphous carbon (ta-C). Films produced from hydrocarbons may contain small amount of hydrogen and therefore are referred to as hydrogenated tetrahedral amorphous carbon (ta-C:H).

### *Microstructure*

Multiplicity of C-C bonds along with the presence of hydrogen, gives rise to complex microstructure of DLC films which is found to be process dependent. Hydrogen itself can assume various bonding configurations with carbon. In particular, polyhydrides are bond terminators in the solid networks and lead to the formation of voids in thin films of a-C:H.

In an attempt to quantify the diamondlike character, Angus proposed that the films can be grouped according to their gram atom number densities and their atomic composition [33]. The density is a strong function of atomic fraction of hydrogen. Among a-C:H films, dense films fall in the region between diamond and adamantane. Adamantane is a cross-linked unsaturated cyclic hydrocarbon with empirical formula  $C_{10}H_{10}$ , in which the C-C bond is the same as in diamond.

Carbon may contain three bonding configurations,  $sp^3$ ,  $sp^2$  and  $sp^1$  in thin film (Fig. 1.2 a). In the  $sp^3$  configuration, each of the four valence electrons of carbon is assigned to a tetrahedrally directed  $sp^3$  hybrid orbital, which forms a strong  $\sigma$  bond with an adjacent atom. At a carbon  $sp^2$  site, three electrons are assigned to the trigonally directed  $sp^2$  hybrids which form  $\sigma$  bonds; fourth electron lies in  $p\pi$  orbital, forming weaker  $\pi$  bonds with adjacent  $p\pi$  orbitals. At  $sp^1$  sites, only two of the electrons form  $\sigma$  bonds, while the other two lie in  $p_y$  and  $p_z$  orbitals to form  $\pi$  bonds. Typical structure of a DLC

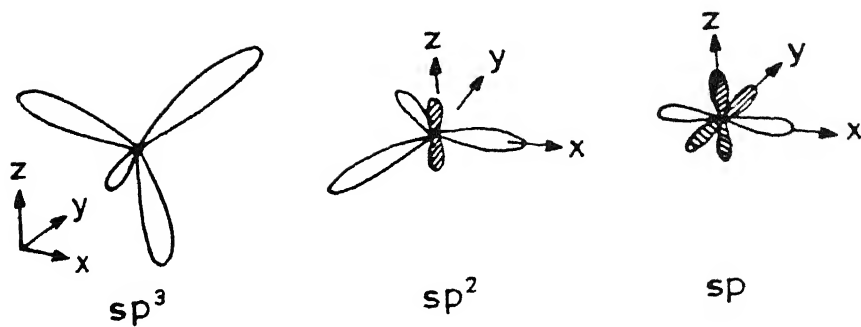


Fig. 1.2 (a) Schematic representation of  $sp^3$ ,  $sp^2$  and  $sp^1$  hybridized atoms.

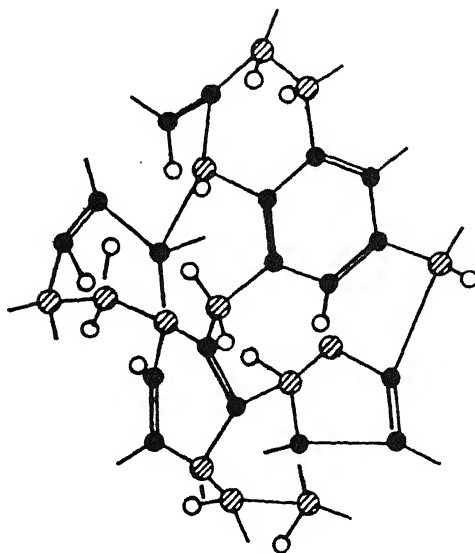


Fig. 1.2(b) A two-dimensional representation of a structure for a diamond-like hydrocarbon (34).  $\textcircled{h}$  =  $sp^3$  carbon atoms,  $\bullet$  =  $sp^2$  carbon atoms,  $\circ$  = hydrogen atoms. Nominal hydrogen fraction is 0.33: nominal fraction of carbon sites with  $sp^3$  coordination is 0.28.

film is shown in Fig 1.2 (b) [34]. DLC films are considered to have bonding composition intermediate between those of diamond ( $sp^3$ ), graphite ( $sp^2$ ) and hydrocarbon polymers. Unhydrogenated amorphous carbon films can be thought of as a three dimensional network of  $sp^3$  and  $sp^2$  bonds. Fink et al [35] concluded from electron energy loss spectroscopy (EELS) and K-edge extended x-ray absorption fine structure (EXAFS) studies that hard DLC films possessing diamond like properties contained 2/3 of carbon atoms in four-fold coordination and 1/3 in three-fold coordination. Smith [36] assumed that a-C:H films consist of four microstructural components: amorphous diamond-like, graphitic, polymeric and voids and used effective medium theory to estimate their volume fractions in a-C:H films. Recently, on the basis of free energy model for bonding, the a-C:H alloys have been proposed to consist of five amorphous components [37]. These are diamondlike, graphitic, polymeric, olefinic, and mixed diamond graphitic (d-g) components. It was predicted that the polymeric and mixed d-g components dominate in typical a-C:H alloy films [37].

In addition, thin films of carbon may contain significant amount of voids leading to film densities much lower than their bulk counterparts. Plasma polymerized hydrocarbon films have lower densities. However, these are still higher than conventional hydrocarbon polymers. The other carbon phases which are based on either trigonal structure or completely unsaturated carbon chains also have low densities.

Due to the loss of long range order, the theoretical description of the a-C:H is extremely difficult. One of the successful models is the constraint counting model of random covalent networks given by Phillips and Thorpe [38]. In amorphous carbon network, depending upon the deposition conditions, the system balances stabilization by hydrogen bonding and destabilization by strain energy. In overconstrained network, changes in hybridization from  $sp^3$  to  $sp^2$  bonding takes place to relieve strain. The  $sp^2$  sites form preferably six fold plane rings which fuse into aromatic clusters of variable size as proposed by Angus and Wang [39]. These clusters embedded in a rigid  $sp^3$  bonded matrix are mainly responsible for the elastic properties. Therefore, hard DLC films are proposed to consist of small graphitic clusters linked in a random network of a high density of tetrahedral carbon [40]. Robertson and O' Reilly [41] have proposed a similar random network model for unhydrogenated a-C, also.

### *Physical Properties*

It is clear that thin films of diamond will exhibit properties which are strongly dependent on the preparation history of the samples. Physical properties may change from graphite-like to diamond-like (Table 1.1) depending upon the microstructural constituents of the films. Hydrogen content and its bonding configurations also govern the properties of films deposited from hydrocarbon sources.

The film structure of hard carbon films are predominantly amorphous with a film density of  $\sim 2 \text{ g/cm}^3$  [42-46]. However, film densities as high as  $\sim 3.3 \text{ g/cm}^3$  have recently been reported [26,47]. In contrast, polymeric films with high hydrogen content, primarily bonded in polyhydride groups, exhibit lower film densities ( $\sim 1.2 \text{ g/cm}^3$ ) [36,46].

Infrared and visible optical absorption [45,46,48-56] and refractive index [45,46,48,52] reflect the opposite contributions from hydrogen content and  $\text{sp}^2$  graphitic clusters. While incorporation of hydrogen increases the optical gap, inclusion of graphitic clusters closes the gap. Typical bandgap energies range from 1 eV to 2 eV. Extreme values of 0.25 eV [57] and 3.1 eV [58] have also been reported. Refractive index values in the nonabsorbing optical region range from  $\sim 1.6$  to  $2.7$  [45,46,48,52,59,60]. Values of reported band gaps should be treated with caution. Higher optical gap [58] does not necessarily indicate a better diamond like character of the films as low density polymeric film also show the large gaps. However, polymeric films are generally characterized by their low refractive indices.

Electrical resistivity [61-64] and interface state density [64,65] of diamondlike carbon films have also been reported. Films usually exhibit a room temperature resistivity of  $\geq 10^9 \text{ ohm-cm}$ . Conductivity of films increases with increasing graphitic content [62,63]. Activated as well as hopping transport mechanisms have been suggested [64,66,67]. Small photoconductivity on DLC films has also been observed [68,69]. In general, better opto-electronic properties have been reported from the highly tetrahedral diamondlike amorphous carbon films [69-71].

Mechanical properties such as film hardness and internal stress [72-75] have been the subject of intense investigations. Film hardness measurements of DLC



coatings can be very subjective due to the small thickness of films on the substrates. DLC films having microhardness up to  $4000 \text{ kgf-mm}^{-2}$  have been reported on Si and metals [72-74].

Thermal stability of films is crucial for applications where working temperature of films is expected to be high. Few studies have focused on the change of film properties as a function of annealing temperature [54, 76-79]. Further, thermal effusion measurements have also been employed to study the evolution of gases on heating the plasma deposited DLC films [80-84]. Hydrogen is found to be evolved from films heated above  $400^\circ\text{C}$ . Hydrocarbons also effuse out of the films in variable amounts depending on the microstructure of films.

It was realized that the extreme properties of *diamond* are not essential for many applications. A trade-off in properties provides sufficient usefulness for a large number of large area requirements. In addition, good quality *amorphous diamondlike carbon* films are smooth and featureless. This makes them attractive for a variety of applications.

### 1.3 APPLICATIONS OF DIAMOND AND DLC FILMS

With its very large band gap, high dielectric strength, high carrier mobilities and saturation velocities, high thermal conductivity, chemical stability and radiation hardness, diamond promises a vast variety of applications. These films are already employed in fabrication of wear resistant protective coatings, abrasives, heat sinks, sensors, windows, and lens materials [17, 85-97]. Among the critical aspects required for the commercial use of diamond films are:

- Small grain size for a smooth surface to minimize stress.
- Small grain size, less grain boundary imperfections and impurities to enhance optical transparency.
- High  $\text{sp}^3$  content to ensure its strength.
- Ability to deposit on a variety of substrates
- Deposition of thin films ( $<1\mu\text{m}$ ) over large area of substrates.

The unusual combination of density, hardness, chemical inertness and optical transparency in DLC films makes them ideal candidates for coating material. DLC films have additional advantage over diamond films that they can be deposited at low substrate temperatures which makes them useful as a coating material on heat sensitive substrates. Moreover, films with nanoscale surface smoothness can be prepared at large areas. Another useful property is that the refractive index can be systematically changed by varying the deposition conditions. The potential applications [98-104] include protective antireflection films for windows, optical components and solar cells. DLC films are being already commercially exploited for electronic packaging applications and as protective coatings in both magnetic and optical discs. Table 1.2 lists the useful and potential applications of diamond and DLC films along with the properties required for each application.

## **1.4 REVIEW OF DEPOSITION TECHNIQUES**

A variety of methods and reactors have been used for the deposition of diamond and DLC films. We have classified the deposition techniques based on the source of carbon and the energy excitation to produce the growth precursor. A summary is presented in Table 1.3. For each technique, the characteristics, major advantages and drawbacks, and the type of films obtained have been outlined in this section. Since a large body of literature exist, the references are by no means exhaustive but show the major trends and recent advances.

**Table 1.2: Applications of diamond and diamondlike carbon films**

Applications	Requirements	Type of film	Ref.
<b>Tribology:</b> - Wear resistant coatings for cutting tools  - Impact resistant coatings for high density computer disks	Hard, corrosion resistant, wear resistant and chemically inert.	DLC, small grain polycrystalline diamond films ,	90,99
	Very thin films (1000nm ) with high hardness, corrosion resistance and chemical inertness.	DLC/diamond composite coatings. Sputtered carbon films	101
<b>Optics:</b> - Protective coatings for optical components: IR window /Laser optics  - Antireflection coatings for Ge infrared devices  - Protective layer for solar cells used in space  - X-ray windows	Transparent in IR-VIS-UV, mechanical properties, low atomic mass	Polycrystalline diamond/ DLC films	92,95
	Hard, corrosion resistant & chemically inert, transparent in region of the EM spectrum and refractive index of ~2.0	DLC coatings	102,103
	Low radiation damage, transparent in visible range of the spectrum.	DLC, polycrystalline diamond, composite DLC/diamond.	99
	Self-standing films with high transmission and low damage threshold for X-rays, smooth surface topography.	Fine grained polycrystalline diamond film.	
<b>Electronic and Optoelectronic</b> - Protective Layer for electronic devices,  - Heat sinks for high frequency & high power devices  - Lasers, UV sensors, LED  - Transistors, photodetectors, high power devices etc.	Hard, chemically inert and corrosion resistant, insulating high break down voltage.	DLC, polycrystalline diamond, or composite of DLC and diamond.	97,99
	Same as above, high thermal conductivity and dielectric strength	Polycrystalline diamond, DLC	96,104
	Same as above, requirements on optical band gap, defects states, surface topography etc.	Large grain polycrystalline/ single crystal diamond, doped diamond.	93,97
	Same as above together with requirements on resistivity. Dielectric const, Coeff. of thermal expansion, mobility, carrier conc. etc.	Single crystal diamond, preferable epitaxial diamond and doped diamond films.	94,97

**Table 1.3:** Comparison of various deposition techniques used for preparation of diamond and diamondlike carbon films.

C-Source	Excitation	Technique	Advantage	Drawbacks	Comments	References
Solid Source of carbon (PVD)		Ion Beam Sputtering	DLC films Easy to control, Low substrate temperature possible	Small area, Diamond film synthesis difficult, low growth rate	Smooth, transparent hard amorphous carbon films	21,105,106
		Laser Ablation	DLC films, High deposition rates possible	Scalability difficult, Optimization required		109-111, 113-114
Gaseous/Vapors Source of Carbon (CVD)	Thermal	Hot Filament	Diamond films, Large area possible, Simple set up	High substrate temperature, Filament stability problematic, Metal contamination, Low deposition rate	Scratching of substrates enhances nucleation	117-121,
		Electron Assisted	Diamond films, Higher deposition rate	Contamination, Scaling-up difficult	Less effect of scratching of substrates	122
	Electrical	DC Discharges	Diamond / DLC / a-C:H films Simple set-up Scalable	Low deposition rate, Stability of discharge difficult		129-136
		DC Arc Discharge and Plasma Jet	Diamond film Extremely high deposition rates (~900 $\mu\text{m/h}$ )	Small deposition area Temperature control problematic Thickness and quality variations	Severe deformation s observed for substrates larger than the plasma beam	159-161

Table 1.3 (Contd.)

		Technique	Advantage	Drawbacks	Comments	References
	Electrical	RF Discharges	Diamond / DLC / a-C:H; hard DLC films. Easy to scale-up Complex substrate shape option	Low deposition rate Poor crystalline quality	Commonly capacitively coupled plasmas used	43,123, 141-144, 148-150
		Microwave Discharges	High quality diamond films Plasma very stable, Uniform deposition rate	Small area High substrate temperatures	Higher plasma density and atomic hydrogen density than RF discharges ECR plasma yields diamond films at lower temperatures and higher rates	153-157
	Hybrid	Remote plasma	-	-	-	158
		Microwave Discharge Jet	-	-	-	162
		Chemical Transport	-	-	-	163,164
		Plasma Source Beam/Mass selected Ion Beam	-	-	-	26-29 166-168
	Combustion	Oxy-acetylene Combustion Flame	Diamond films, High growth rates (20-100 $\mu\text{m}/\text{h}$ ) Simplest and inexpensive set-up	Non-uniform and inhomogeneous deposition, Control of substrate temperature difficult, Contamination	Rates and quality depend up on nozzle size and gas flow rates as well as their ratios.	169-174

### 1.4.1 Physical Vapor Deposition (PVD)

Physical vapor deposition techniques are those which involve a physical process such as thermal evaporation or sputtering for creation of material to be deposited. These techniques use graphite as solid source of carbon. The processes involved can be divided into three steps:

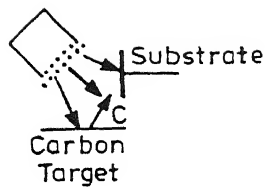
- (i) creation of atomic vapors: necessary energy can be furnished by various ways e.g. thermal, ion beams, lasers, etc;
- (ii) transport of these atoms to the substrate surface,
- (iii) condensation of atoms on the substrate to form a film. This process can be explained by different nucleation and growth models of thin films.

In PVD, all the three deposition steps of creation, transport and deposition of materials can be controlled independently. Schematic diagrams for popular PVD techniques are shown in Fig. 1.3. These techniques have been used to produce amorphous DLC as well as diamond films.

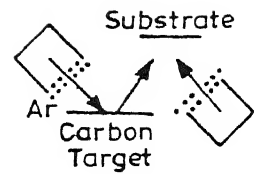
#### ***Sputtering:***

In ion beam sputtering technique, incident ions are generated at the ion source and the target (high purity graphite) is sputtered in a sputtering chamber separated from the ion source (Fig. 1.3 a&b). DLC films are deposited from the beam of carbon ions accelerated in constant electric field. Aisenberg and Chabot [21] in 1971 were the first to report deposition of DLC films by ion beam sputtering. In contrast to other plasma assisted methods, the direct ion beam deposition allows one to deposit the films using selected ions of well defined energy and flux density.

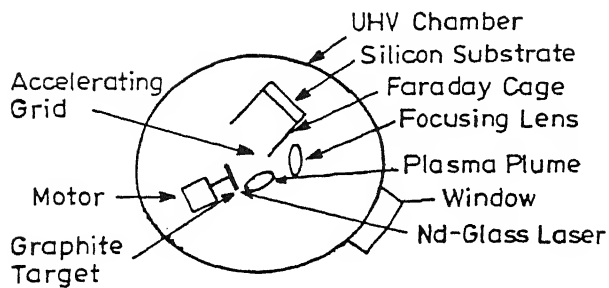
The precise control of ion energy and ion flux is very difficult using single ion source. Therefore, a dual ion beam sputtering method has been employed for synthesis of DLC films [23,105]. In this technique, a primary beam is used to sputter carbon and the growing film is simultaneously bombarded by ions generated from the second ion source. The bombardment of the growing films by an intense flux of ions of energy  $\sim 1\text{KeV}$  affects a transformation from dark amorphous deposit to a hard transparent phase [106]. Although dual ion beam technique provides advantages of independent control of substrate ion bombardment and deposition rate, it suffers from



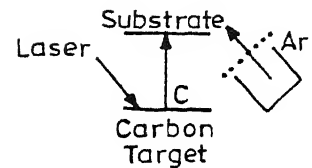
(a) Single Beam Sputtering



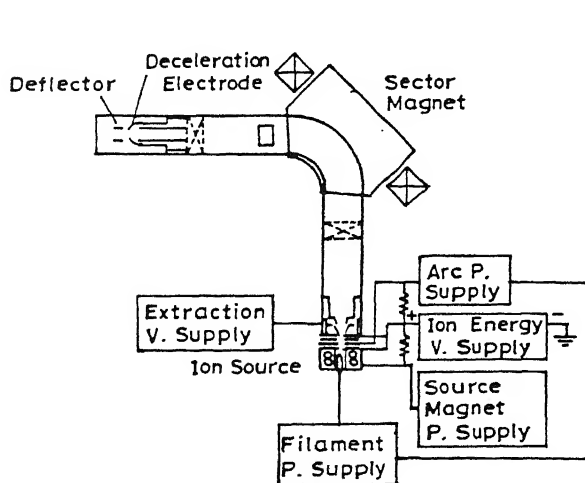
(b) Dual Beam Sputtering



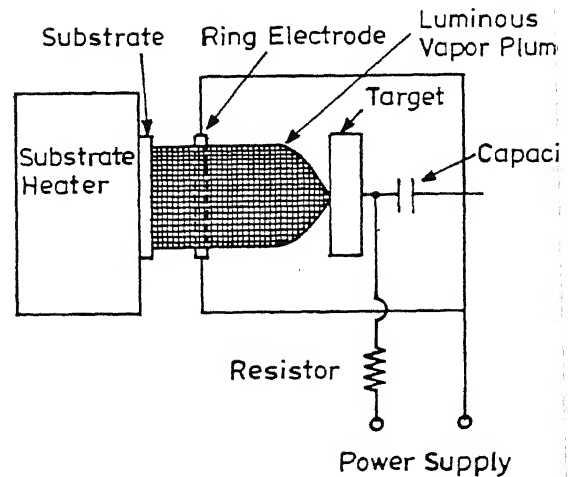
(c) Laser Ablation



(d) Laser Ion Beam



(e) Mass Selected Ion Beam



(f) Laser Plasma Hybrid

Fig.1.3 Schematic diagram of some physical vapor deposition techniques.

the following two major limitations for obtaining diamond and DLC films: (a) Low deposition rates due to the low sputtering yield of carbon, and (b) Limitations for large area deposition due to limitations in the sizes of the ion sources.

Deposition of films having good diamond-like properties using magnetron sputtering and rf sputtering have been only partially successful [107,108]. It is likely that negligible substrate bombardment in the case of magnetron sputtering and substrate overheating in the case of rf sputtering may have restricted the formation of DLC films in the above two techniques.

### ***Laser Ablation***

In this method, laser beam photons are used to eject atoms or molecules out of a solid target (graphite) placed in front of a substrate [109-112]. Good quality DLC as well as amorphous diamond films [109,112] have been grown by this technique. However, in the laser evaporation of graphite powder, the source material tends to evaporate in the form of small clusters with the graphite structure due to peeling off of the weakly bonded interplanar structure. As a result, the films may show properties similar to those of graphite. The bombardment of films with ions during the deposition by laser evaporation can decompose these clusters and excite the atoms to higher energy states resulting in deposition of diamond film at high deposition rate. The properties of carbon films deposited by ablation of a graphite target are found to improve by Ar ion bombardment during deposition [109]. The usefulness of laser ablation method has been anticipated because of the presence of ions in atomic beams generated by pulsed lasers [113].

In laser ion beam technique, laser beam is used to evaporate the material and the growing film is simultaneously bombarded by ions from an ion source. Wagal et al [114] reported high rate of deposition (20  $\mu\text{m/h}$ ) of DLC films using a laser ion source. The advantage of this technique is minimal contamination from the heat source and high deposition rates for materials of high melting points. However, in this method, fragments of source material explode by the laser irradiation and then bombard the



growing films, thus damaging the carbon films. To overcome such problems, a laser plasma hybrid technique [115] has been used to deposit DLC films. The schematic diagram is shown in Fig. 1.3 (f).

### 1.4.2 Chemical Vapor Deposition (CVD)

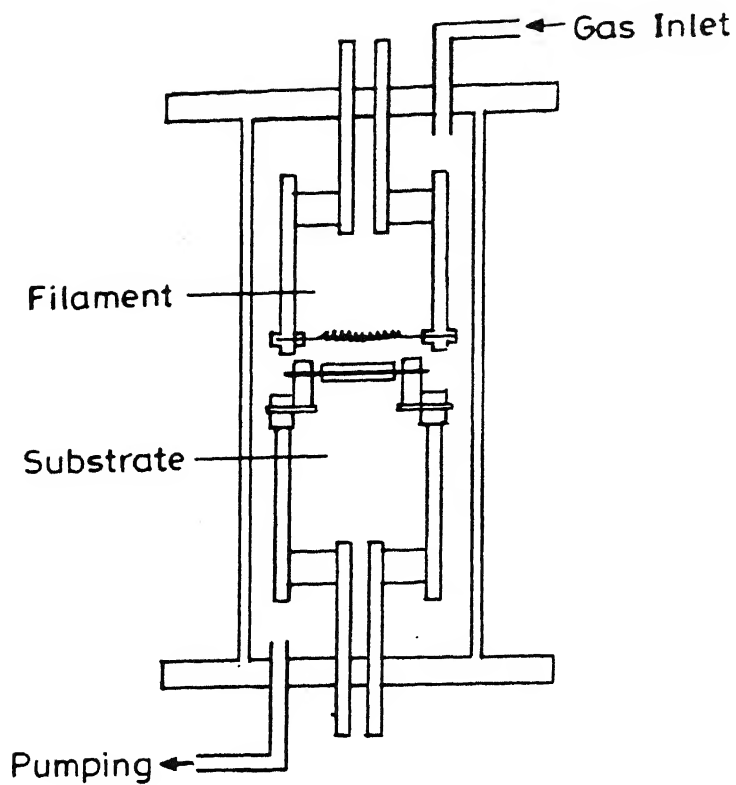
In contrast to a limited choice of solid sources, a considerable variety of gases and liquids containing carbon have been used to produce amorphous and polycrystalline carbon films. Commonly used hydrocarbon gases and liquids are methane, ethane, butane, propane, acetylene, butadiene, ethylene, benzene, acetone, methanol, ethanol, etc. Among the diluents hydrogen, helium, argon, oxygen, nitrogen, etc. have been used. In CVD techniques, major ways of activating gas-phase carbon-containing precursor molecules include thermal, plasma or combustion methods.

#### *Thermal Excitation*

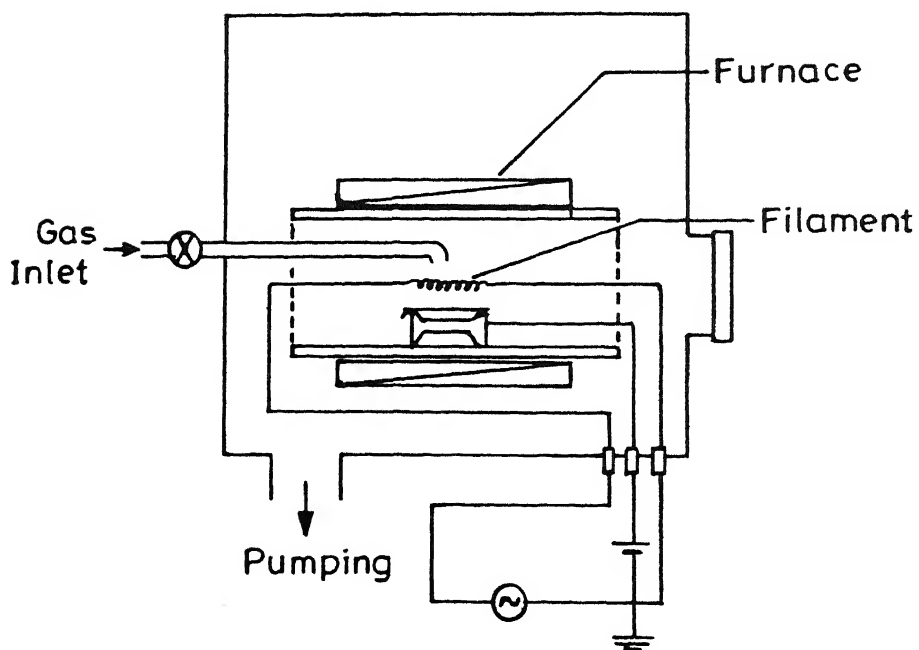
In this method, the energy is supplied in the form of heat to decompose the gas. Fig. 1.4 shows the schematic of thermal CVD reactors. The hot filament thermal CVD is most commonly used for deposition of diamond films.

#### **Hot Filament Thermal CVD (HFCVD)**

This method involves the thermal decomposition of the hydrocarbon gas by a heated filament of tungsten, tantalum or molybdenum [116]. The hot filament [2000-2500 K] placed in the vicinity of the substrate not only dissociates hydrocarbon gas but also heats the substrate, [Fig. 1.4a]. Matsumoto et al [117,118] were first to report the synthesis of diamond microcrystals using this method. The HFCVD technique although inexpensive and easy to operate, is limited by high substrate temperature and low deposition rates. Recently, an advanced hot filament CVD method has been proposed by Kondoh et al [119a], which accurately controls the substrate temperature independently against CVD parameters. This has been employed to obtain homo-epitaxial



(a) HFCVD



(b) EACVD

Fig.1.4 Schematic diagram of thermal CVD techniques.

diamond films [119b]. Good quality diamond and DLC films [120] as well as large area ( $\sim 7 \text{ cm}^2$ ) deposition of diamond was reported by employing convective flow of gases [121] in HFCVD technique.

### **Electron Assisted CVD (EACVD)**

This is a modified version of thermal CVD process involving electron bombardment of the substrate surface during hot filament thermal CVD. The electron bombardment is achieved by biasing the substrate positive with respect to the hot filament. This method was used by Sawabe et al [122] to improve the growth rate of diamond films. The films obtained by this method are found to have rough surface topography and a very low visible-UV optical transmission.

### ***Electrical Excitation***

When a gas is subjected to electrical discharge, the inelastic collisions of electrons with gas molecules result in dissociation or ionization of gas. The most commonly used reactors for producing DLC and diamond films are those which employ plasma excitations [123]. Some common designs are shown schematically in Fig. 1.5. Various reasons can explain the choice of plasma CVD:

- The possibility to realize the deposition at low substrate temperatures. This enables use of a variety of substrates. Control of the temperature is easier which is advantageous from technological point of view.
- Integration of different processes in the same reactor is possible.
- Unlike other techniques, a great variety of a-C:H materials can be obtained by plasma techniques by changing the flux and energy of ion bombardment [40,124-126]. These techniques have been successfully used to produce polycrystalline diamond films also.

Plasma assisted CVD (PACVD) technique used for the synthesis of DLC and diamond films involves decomposition of hydrocarbon gas in a plasma using dc, rf or

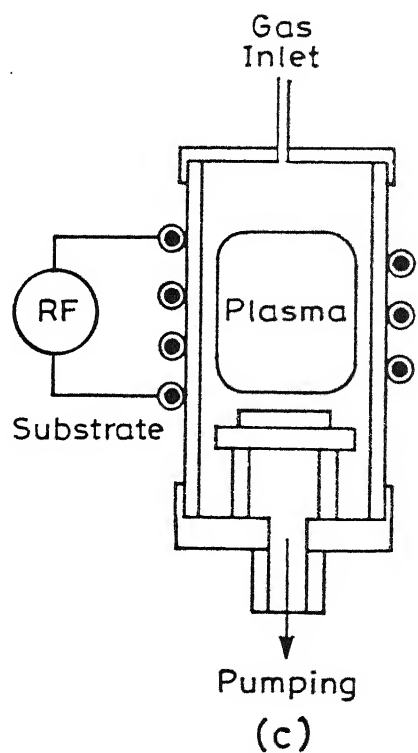
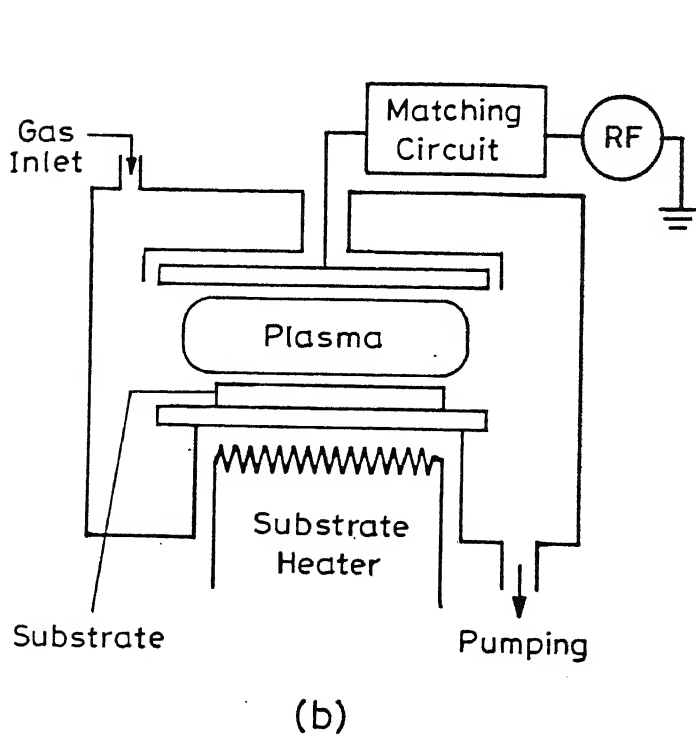
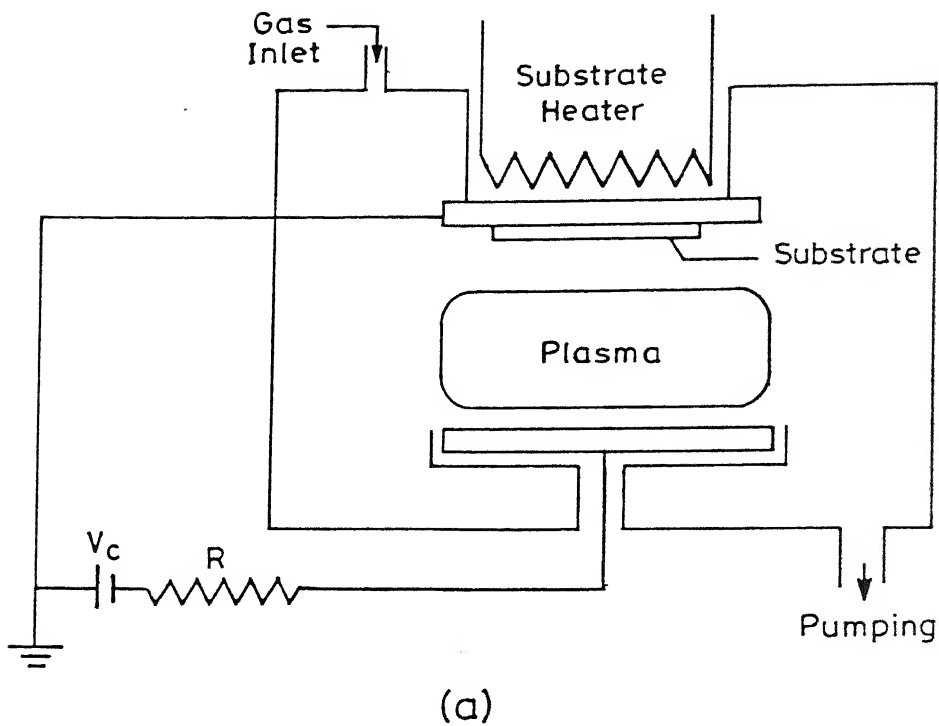


Fig.1.5 Schematic of electric discharges  
 (a) Direct current  
 (b) Radio frequency (capacitive coupling)  
 (c) Radio frequency (inductive coupling)

microwave excitations. Here, various deposition reactors employing these three discharges are described.

### DC Discharge:

A direct current (dc) gas discharge is obtained by applying a potential difference between two plane parallel electrodes (Fig. 1.5a). The substrates when placed on the cathode are subjected to ionic bombardment. In the reverse geometry i.e. substrate placed on anode, a desired bias can be applied to the substrates with respect to the powered electrode in such a way as to directly control the energy of the ions. A dc discharge with confinement of the plasma by a grid has also been adopted. It reduces ionic bombardment on the substrate. Different other configurations of dc discharges have also been used in case of a-C:H films. Two grid geometry has been used to investigate the effect of ion energy on diamondlike carbon film properties [127]. In a dc discharge with multipole confinement used for production of a-Si:H [128], the primary electrons emitted by a hot filament are confined by a magnetic field. This permits to maintain the discharge at very low pressure ( $\leq 0.1$  m torr). In this case the study of the plasma is easier as the secondary reactions (ions and radicals with the molecules) are negligible.

DC glow discharges have been successfully used to produce diamond [129-132] as well as DLC films [127,133-135]. It has been possible to coat large area planar substrates (up to 22 inch size) with uniform DLC coatings using DC plasma CVD method [135]. Boron-doped diamond films have been deposited by dc plasma decomposition of  $\text{CO}_2 + \text{H}_2$  [136].

DC discharge techniques employ simpler experimental equipment as compared to rf and other high frequency discharges [137]. Moreover, because of a simple geometry, modeling of dc discharges is also relatively easier. DC discharges facilitate direct control of the discharge current density and ion energy, allowing greater fine tuning of the film structure. Hence, for understanding the growth processes and the role of ion energies, dc glow discharges are better suited. However, film growth rate is affected by the conductivity of the substrate. Furthermore, discharge formation is generally limited to higher pressures, above 0.1 Torr. This restricts growth rates for high quality DLC films.

The positive attributes of dc and radio frequency discharges are combined in a dc saddle-field discharge. In the saddle-field electrode configuration, electrons are made to oscillate along the axis of the plasma chamber, increasing the effective path length for ionizing collisions. This facilitates efficient activation of reactive gas-phase precursors which are required for film deposition and provides direct control over the energy, direction of motion and density of ions. DLC films using a saddle field source have been grown [138]

### **RF Discharges:**

The discharges using radio frequencies (rf) (25 kHz-100 MHz) may be of two types depending on the type of rf coupling, i.e., capacitive or inductive (Fig. 1.5b&c). Among the two, the capacitive coupling is more widely used. It is characterized by the production of films of uniform thickness and by the possibility of scaling the process to large areas. An external dc or rf bias can also be applied to the substrates to enable the variation of flux and the energy of the ions [123,139, 140].

RF technique was first proposed by Holland [22] to deposit DLC films on a variety of substrates. Over the years, many researchers have investigated this method to prepare DLC films [139-145]. Similar techniques using rf excitation have been used to synthesize diamond films [146,147]. The difference being that very low concentrations of hydrocarbon gas/liquid in the gas hydrogen mixture are used and a very high substrate temperature ( $\sim 900^\circ\text{C}$ ) is maintained. Though it is shown that diamond films can be synthesized by using rf power in an inductively coupled mode [126,148], capacitively coupled rf plasmas have shown poor performance for diamond film synthesis [149,150]. For the synthesis of improved quality diamond and DLC films, the additional bias in the rf plasma CVD systems has been applied [139,]. Magnetically enhanced RF plasma deposition is used by Ehrhardt and coworkers [152] in order to enhance the ionization of rf plasmas and the diamondlike properties of the deposited films.

The rf discharges remain the most common method to deposit insulating material. They have the advantage of not being disturbed by the deposit on the electrodes, as opposed to the dc discharges. Moreover, rf discharges are characterized by the production of films of uniform thickness. However, the method suffers from

two practical limitations. RF system requires asymmetrical surface areas of the discharge electrodes to induce a self biased potential on the cathode. This requirement leads to an unreasonably large vacuum chamber/anode structure if large or many object are to be coated. Also, an impedance mismatch between discharge plasma and rf power supply sometimes becomes non trivial to solve even with an impedance matching network. As compared to microwave discharges, these discharges are less stable. In addition, the rf can electromagnetically couple with any electrically conductive body in the reactor chamber and heat it.

### **Microwave Discharges:**

When the frequency of excitation of the plasma is of the order of GHz (microwaves), the ions are almost immobile and only the effects of collective movement of the electrons under the action of the average field come into play (Fig. 1.6a). A very intensive localized discharge is obtained using microwaves and the plasma generated is stable for long duration. Experiments in the laboratory with discharges of this type have shown the possibility of obtaining good quality diamond films (as compared to rf discharges) with higher growth rates than those obtained by rf [153-155]. This is mainly due to higher plasma density as well as higher atomic hydrogen density in the microwave plasmas. Improved coupling efficiencies obtained with this method over that of conventional rf technique result in plasma densities in the range of  $10^{11}$ - $10^{12}$   $\text{cm}^{-3}$ .

A particular case of microwave discharges is the plasma deposition assisted by the cyclotron resonance of the electrons (ECRPCVD) [156,157] (Fig. 1.6b). In this method, microwave plasma (2.45 GHz) is created in a chamber placed in the interior of a coil, which supplies a magnetic field to induce the cyclotron resonance of the electrons. The species of the plasma are extracted from the chamber towards a zone of deposit. Thus the effects of a too intense ionic bombardment on the films is avoided. This method allows to obtain the increased rates of deposition and good quality material of without heating the substrate. But, there are difficulties in scaling up this method on industrial scale.

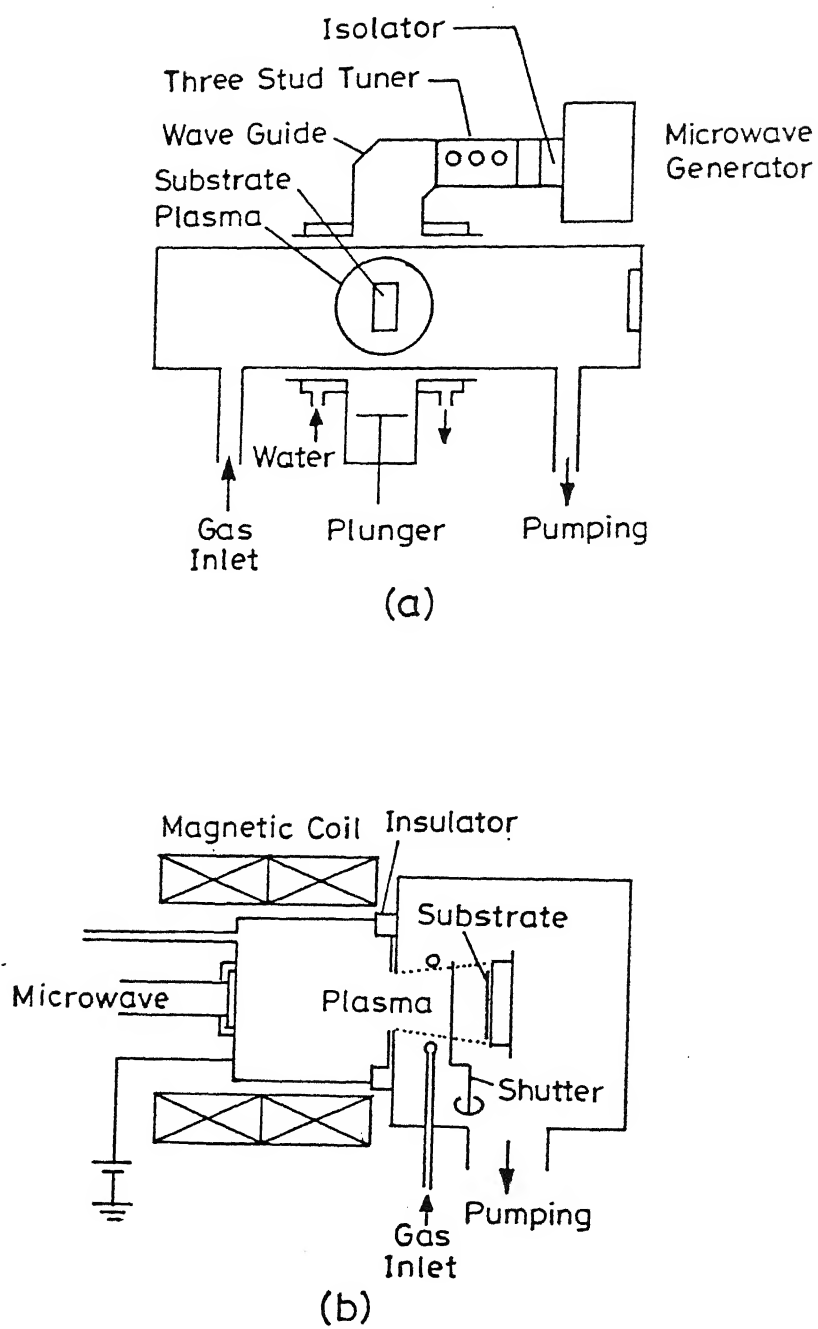


Fig.1.6 Schematic diagram of  
 (a) Microwave plasma and  
 (b) Electron cyclotron resonance (ECR) Plasma CVD techniques.



### 1.4.3 Hybrid Techniques

#### *Remote Plasma:*

This technique, developed by Lucovsky et al [158] involves dissociation of a mixture of reactive and inert gases using rf excitation. The activated species react downstream with the process gas to form complexes in the gas phase which subsequently condense on the substrate. Bombardment by energetic neutrals dissociate the complexes to produce the compound films. Deposition of diamond can be done by using  $\text{CH}_4$  as a process gas and  $\text{H}_2$  or  $\text{H}_2 + \text{He}$  gas mixtures for activation. The deposition rate is low in this technique and limited success has been reported to date.

#### *DC Plasma Jet CVD:*

A high density of activated species (responsible for growth of diamond) is required to form diamond with high growth rates. To obtain this in conventional plasma CVD, the plasma is powered up to dissociate more gas molecules. However, this results in heating up the substrate so much that graphite and amorphous carbon are formed. A high degree of gas dissociation, which generates high density radicals, can occur when using a thermal plasma. However, the temperature of the thermal plasma (over 5,000 K) is too high to be used directly. The most effective method for obtaining high density radicals at low temperature is by quenching the thermal plasma to generate a nonequilibrium composition plasma. It may be formed by spraying the thermal plasma, in the form of a plasma jet, onto a water cooled substrate at high velocity.

The two main methods for generating the plasma jet are through dc or rf excitations. The cooling rate of the plasma jet is higher in the dc plasma method due to 's higher flow rate of the jet. High pressure dc discharges between fixed electrodes at atmospheric pressure have been used to grow good quality CVD diamond from hydrogen-hydrocarbon mixtures at very high rates of  $\sim 200 \mu\text{m}/\text{hour}$  and thickness greater than 1mm [159-161]. Because of technology developments over the years to make plasma torches, these DC discharges are now very stable. One disadvantage of this

process is that the substrate must be continuously cooled with running water to prevent it from melting because large amounts of power per unit of substrate area are used.

### ***Microwave Discharge Jet:***

A high pressure microwave discharge jet has also been used to grow CVD diamond at moderately high rates of  $\sim 30 \mu\text{m}/\text{hour}$  at atmospheric pressure over a square inch of area [162]. The plasma is initially ignited by electric breakdown around the central electrode and then sustained by microwave electromagnetic waves generated between the central electrode and chamber walls. Sustained operation is difficult because of plasma instabilities and the need to vigorously cool the substrate. Unlike low pressure microwave discharges, the jet method uses electrodes, which are immersed in the plasma and therefore can be eroded.

### ***Chemical Transport:***

The chemical transport method involves the transport of some volatile hydrides (of C, Ge, Si etc.) which are formed during the interaction of the hydrogen plasma with the respective element. The transport takes place from the colder zone where the hydrides are formed to the hotter one where they are decomposed. This method was used first by Derjaguin and Coworkers [163] to prepare diamond micro-crystals at low pressures. Subsequently, Angus et al [164] reported deposition of diamond onto natural diamond powder from methane gas at  $1050^\circ\text{C}$  and 0.3 Torr pressure. They have also proposed a qualitative model explaining the kinetics of diamond growth from the vapor phase [46].

### ***Hollow Cathode PACVD:***

Another variant of PACVD process uses hollow cathode to synthesize diamond films [165]. In this process, the gas is passed through the refractory metal hollow cathode and is ionized to a high degree by the hollow cathode discharge. The authors

claim that due to high operating temperatures of the hollow cathode, "efficient dissociation" of the gas occurs via a combination of thermal and plasma mechanisms [165]. Deposition of diamond films and particles onto silicon and Mo substrates placed at some distance in front of hollow cathode nozzle have been reported.

### ***Plasma Source Beam Method:***

The principle of the plasma beam source (PBS) is based on a capacitive magnetically confined rf discharge. The configuration of the electrodes and magnetic field was first reported by Oechsner et al [166]. The ions are extracted through a grid of high transmission by the rf self bias between the plasma and the grid. This technique offers control over the deposition parameters such as particle flux composition, ion kinetic energy and percentage of ionized particles. Recently, this technique has been established to synthesize a new type of carbon films called "highly tetrahedrally bonded carbon films" (high  $sp^3$  content up to 85%) having properties of diamond [167]. An optimum ion energy of 100 eV is reported by Weiler et al [29,168] for growth of tetrahedral carbon films.

### **1.4.4 Combustion Flame Method**

In this technique the requisite energy for activating process gases is achieved by the combustion reaction between acetylene and oxygen. Essentially this process utilizes an oxy-acetylene flame which is caused to impinge onto a temperature controlled substrate. The flame when operated under appropriate gas flow conditions and substrate temperature produces polycrystalline diamond films. The flame is normally operated in a slightly acetylene rich mode. The excess acetylene in the gas mix is the source of carbon for diamond formation. The combustion flame method developed by Hirose and co-workers [169] has unique advantages of economy, easy setup and higher growth rates in comparison to other methods. This deposition process can be conducted in open atmosphere without the need of vacuum systems etc. However, the technique

suffers from inherent drawbacks of non-uniform products and difficulty in precise control of process parameters [170-172]

## 1.5 MOTIVATION AND OBJECTIVES

It is evident from the background presented above that the diamond and diamond like carbon films present enormous potential applications and fundamental challenges. A large number of groups have shown ways to produce thin films of these materials using a variety of deposition techniques at their disposal using mainly empirical approaches. A substantial amount of experimental work has been reported to characterize film growth rates and film properties as a function of deposition conditions. However, an understanding of nucleation and growth processes have started to emerge only recently. In particular, systematic studies are required to understand the growth-properties relationships through the knowledge of film microstructures. We outline a schematic flowchart in Fig. 1.7 to show how various issues are interlinked. Clearly, understanding and control of film microstructure are key links in the process of optimizing the reproducible growth parameters to obtain desirable film properties. Hydrogen participates actively in the growth of carbon films *and* plays a crucial role in determining the film microstructure. Presence of hydrogen in the films affects their properties. Hence, a reliable information on the nature of hydrogen in the films is also essential.

The present work was undertaken to investigate the growth behavior and related microstructural aspects of diamond and diamondlike carbon films. In brief, the objective was:

- to deposit thin films of hydrogenated amorphous carbon under a variety of deposition conditions providing a variation in microstructure leading to films from hard diamond-like to soft polymer-like characteristics;
- to identify the growth parameters which are independent of deposition reactors through the understanding of the discharge characteristics;
- to measure and establish the role of hydrogen in determining the film microstructure using multiple characterization techniques;

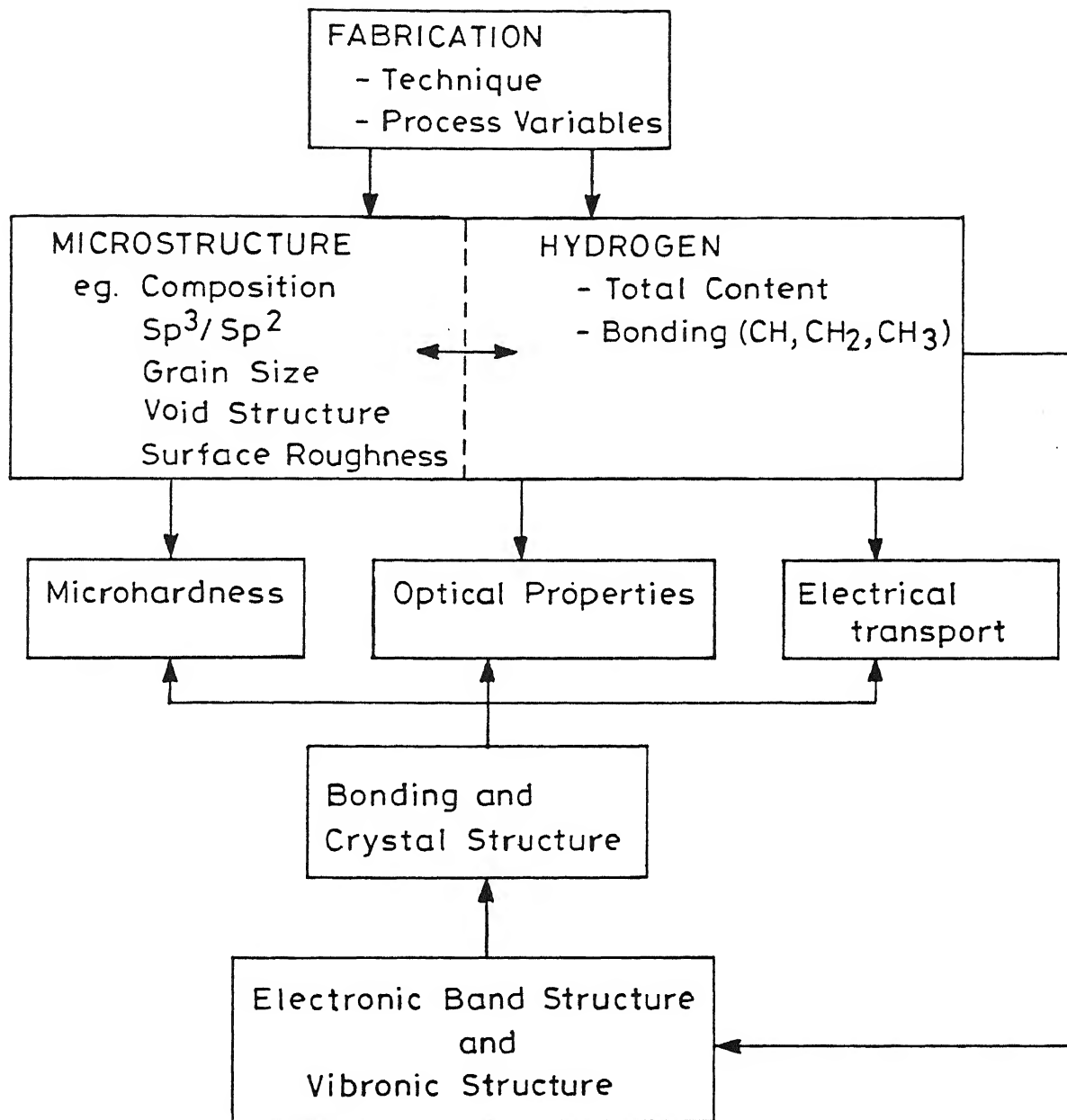


Fig.1.7 Schematic flowchart of growth-property relationship for diamond and DLC films.

- to investigate the role of post deposition treatments like annealing and ion irradiation.
- to correlate hydrogen incorporation, film microstructure, and physical properties with the process variables in a unified picture.
- to explore the possibility of deposition of smooth diamond crystallites on metallic substrates of practical importance using novel approaches.

We have selected two different deposition techniques of dc glow discharge and oxy-acetylene flame CVD for preparation of DLC and diamond films, respectively. DC glow discharge technique offers a simple and effective method to control the ion bombardment which were expected to play a crucial role during film growth. As compared to popular rf discharges, the process parameters can be directly and independently controlled. Oxy-acetylene flame technique on the other hand, is inexpensive and easily installable. The challenges in the growth issues here are to deposit flat and smooth crystals on the metallic substrates. In addition to well known molybdenum, stainless steel was chosen for substrates due to its industrial importance. Knowledge of microstructure of films being central to the understanding of growth-properties relationship, a variety of characterization tools were employed to yield complementary information.

Emphasis of the work is on the dc glow discharge deposited a-C:H films due to the richness of microstructures offered by a-C:H films. Using a single deposition technique, we are able to produce a-C:H films with properties ranging from soft polymeric to hard diamond-like. The ability to control the homogeneous plasma reactions and heterogeneous surface based reactions has been exploited to obtain an overall picture of growth mechanism for a-C:H films. A small part of the work was dedicated to the growth of polycrystalline diamond films on metallic substrates.

## 1.6 THESIS PLAN

After a brief background to the structure, properties and applications of diamond and DLC films, a comprehensive review of various deposition technique has been presented in this chapter. Having established the motivation and objectives, following chapters discuss results of the present endeavor:

Chapter II describes the experimental techniques and methodologies to characterize the amorphous carbon and polycrystalline diamond films. For identifications of physical properties, micro indentation, uv-vis spectrophotometry and Raman spectroscopy were utilized.

Design of our glow discharge reactor and deposition methodology of films is presented in Chapter III. The optimization of reactor parameters and identification of glow discharge characteristics are also dealt with in the same chapter. Results on in situ mass spectroscopy of acetylene plasma are reported.

The characterization of hydrogen and microstructure in a-C:H films is established in Chapter IV using three complementary techniques: infrared spectroscopy (IR), elastic recoil detection analysis (ERDA) and mass spectroscopic thermal effusion (MSTE). Results of thermal annealing on structure and hydrogen profiles of DLC films are also reported in this chapter.

The dependence of film properties on growth parameters is the subject matter of Chapter V. In particular, observation of nanocrystalline diamond phases in films deposited under suitable conditions is reported. Based on these results, a phenomenological model to describe the growth of a-C:H films is also presented.

Chapter VI deals with the growth and structural characterization of oxy-acetylene flame deposited diamond films. Formation of square faceted flat diamond crystallites on molybdenum substrates is reported. Growth of diamond films on stainless steel without the use of external buffer layers will be presented.

Finally, Chapter VII presents the summary and major conclusions drawn from this work. Some suggestions for future work are also highlighted.

## CHAPTER II

# CHARACTERIZATION TECHNIQUES

In this chapter, we describe the techniques and methodologies used for the characterization of diamond and diamondlike carbon (DLC) films. X-ray diffraction (XRD), Scanning electron microscopy (SEM), and Raman Spectroscopy (RS), were used for characterization of diamond films. DLC films were found to be amorphous in nature. These films have been studied by their properties like absorption in visible and infrared, hydrogen content, C-C and C-H bonding, hardness, and thermal stability etc. The technique of thermal desorption spectroscopy was established for the characterization of a-C:H and diamond films. The methods of analyzing experimental data are also briefly discussed.

### 2.1 THICKNESS MEASUREMENT

Thickness is the most significant parameter of thin films and thus constitute an important aspect of thin film characterization [8]. In the present work, the thickness and the deposition rate of a-C:H films on glass substrates was determined by the optical methods and mechanical stylus technique. Thickness measuring instrument Talystep (Rank Taylor Hobson, UK) and surface profiler (Alfastep 200) were used. The instrument measures the height of a step by traversing a diamond stylus on the surface. The vertical movement of the stylus is amplified and recorded as a graphical representation of the difference between the levels of the film and the substrate surfaces. The thicknesses were measured with an accuracy of  $\pm 5\%$ . Thickness of some of the films were estimated from the analysis of the interference fringes obtained in optical transmission data in UV-VIS range (section 2.4). The results of the two techniques agreed within the experimental uncertainties.



## 2 STRUCTURE

Study of the crystallographic structure, composition and surface morphology of diamond films is essential to understand their physical properties. We have used x-ray diffraction, Raman spectroscopy, and scanning and transmission electron microscopies for characterization of films. The elemental analysis was performed using energy dispersive x-ray analysis (EDX), electron probe microanalysis and Rutherford back scattering techniques. An insight into microstructure of a-C:H films was obtained by combining IR measurements with mass spectroscopic thermal effusion analysis, described in section 2.3.

### 2.1 X-ray Diffraction

The crystallographic structure and composition of phases of the deposited diamond films were studied by x-ray diffraction analysis (XRD). The amorphous nature of our DLC films was also confirmed by XRD. XRD experiments were performed by using a x-ray diffractometer (Rich and Seifert ISO Debye Flex 2002). The geometry used is of the conventional Bragg-Brentano ( $\theta$ - $2\theta$ ) geometry. Monochromatic  $\text{CuK}\alpha$  ( $\lambda = 1.5418\text{\AA}$ ) radiation obtained from a copper target was made to fall on the sample at an angle  $\theta$ . Diffracted angle  $2\theta$  was scanned by the detector in the range of  $20^\circ$  to  $145^\circ$  at a scan speed of  $3^\circ/\text{min}$ . This allows to scan the (111), (220), (111) and (400) reflections of diamond. The other recording conditions were (i) counts per minute = 5 K to 20K (ii) accelerating voltage/current = 30 kV/20mA, time constant = 0.1 sec. and (iv) chart speed = 3cm/min. Another target of Fe ( $\lambda = 0.711\text{\AA}$ ) was also employed to access lower Bragg angles.

The interplanar spacing  $d$  was determined from the Bragg relation [173]. Intensity and the inter-planar spacing of the dominant peaks were used for matching with the standard ASTM data card [174] values to ascertain the crystallographic phases in the film. The lattice parameter,  $a$ , for diamond cubic crystal was calculated by indexing the XRD pattern [173].

### 2.2.2 Scanning and Transmission Electron Microscopy

In electron beam techniques incident electrons can be absorbed, emitted, reflected or transmitted. Scanning and transmission electron microscopy (SEM/TEM) are the most widely used techniques for studying surface topography as well as cross-sectional features of DLC and diamond films [175].

In SEM, a finely focused electron beam is scanned over the surface of the specimen. The secondary electrons emanated from about  $10\text{ \AA}$  from the film surface are extracted by a high potential applied to a scintillator-detector system. Secondary electron images are generated by synchronizing the optical output of the detector system with raster of the electron probe across the sample.

Scanning electron microscopy was performed using JEOL 840 JSM scanning electron microscope [176]. The morphologies of the diamond films: the shape, size and density of particles in the samples were determined from SEM micrographs. In some samples, a thin layer of gold was deposited on the sample surface (without altering the surface features) to avoid charging problems. The magnifications up to 100K with a resolution  $\sim 10\text{ \AA}$  were used to study the morphology of diamond and a-C:H films.

The transmission electron microscope (TEM) utilizes transmitted electrons to produce a magnified image of the sample. TEM has essentially two modes of operation, the image mode and the diffraction mode. The transmitted and forward scattered electrons form a diffraction pattern in the back focal plane and the image of the specimen in the image plane of the objective. They are then magnified by a series of intermediate and projector lenses and focused onto the screen. With the help of apertures, a selected area diffraction (SAD) of the specimen can be obtained. Images formed using only the transmitted electrons are bright field images and those formed using a specific diffracted beam are dark field images. TEM used has high resolution  $\sim 1.3\text{ \AA}$ . A JEOL JEM - 2000 FX-II electron microscope was used to study electron diffraction from our diamondlike carbon films. As the sample needs to be sufficiently thin ( $\leq 1000\text{ \AA}$ ) for electrons to be transmitted through it, thin films ( $\sim 500\text{ \AA}$ ) deposited on silicon oxide substrates were floated off the substrate by chemical or acid etching and

ated on copper electron microscopy grids for TEM analysis. Typically the accelerating voltage of 120 kV and camera length of 80 cm were used.

### 2.3 Raman Spectroscopy

The inelastic scattering of light is a sensitive spectroscopic tool to investigate structure and symmetry properties of solids, liquids and gases [177-181]. Raman spectroscopy was used for the characterization and identification of the various phases of carbon.

The Raman scattering measurements were carried out at the Modern Laser Raman Laboratory at IIT Kanpur. The experimental set up used to record the micro-Raman spectrum mainly consists of a Spectra physics 5 and 15 watt 2030 Ar<sup>+</sup> lasers as an excitation source, chilling plants for cooling the laser head and the electronics. The Raman spectra from films were recorded at room temperature with 514.5 nm line of Ar<sup>+</sup> laser in the backscattering geometry with a laser power of ~4 mW on the sample. The scattered light is dispersed by 1200 gr/mm grating. The spectra were recorded with a Spex Triplemate equipped with a liquid nitrogen cooled CCD. The instrumental slit width was 10 cm<sup>-1</sup>. A natural diamond was used for the calibration of the spectra [182]. The spectrum obtained was analyzed for peak positions and half widths. A non-linear curve fitting software described in Section 2.3.1 was used to deconvolute the spectrum. Raman spectroscopy is useful for detecting sp<sup>2</sup> carbon atoms. The scattering efficiency of graphite phonons is much higher than that of diamond. The phases present in the film are identified by carefully comparing the peak positions with the known assignments for various carbon forms [179-181].

### 2.4 Composition Analysis

In the present study, the chemical composition of substrates as well as films was determined by energy dispersive analysis of x-rays (EDX), electron probe microanalysis (EPMA) and Rutherford backscattering (RBS) techniques. EDX and EPMA are part of the scanning electron microscope equipped with appropriate x-ray detectors

[183]. The energy dispersive mode employs a solid state detector connected to a multi channel analyzer. In this mode all elements are analyzed simultaneously and displayed as peaks in the display. The depth of resolution is  $\sim 1 \mu\text{m}$ . EDX model Kevex attached to a JEOL JSM 840A SEM and EPMA model JXA-8600 MX (JEOL, Japan) were used.

For carbon detection, Rutherford backscattering spectrometry (RBS) was employed. RBS is a well established quantitative technique for thin film analysis [184,185]. It has a sensitivity up to 0.1 atomic %. Figure 2.1 shows the schematic diagram of the Rutherford backscattering process. The technique basically involves the scattering of monoenergetic, collimated beam of particles (He) from a target (sample). The particles scattered backwards by angles of more than  $90^\circ$  from the incident directions are detected and energy analyzed by a detector. The energy of the backscattered particle is uniquely related to the mass of the target atoms. The RBS measurements were performed at the Central Nuclear Facility, Department of Physics, IIT Kanpur [186]. RBS simulation program [RUMP] developed by Doolittle [187] was used for the analysis of backscattering data.

## 2.3 HYDROGEN BONDING AND CONTENT

Incorporation of hydrogen in the deposited films, especially in case of DLC, determines their physical properties. Hence, a knowledge of total hydrogen content as well as its bonding to carbon is crucial for understanding film properties and comparison of samples prepared under different deposition conditions. We have used infrared spectroscopy (IR), thermal effusion measurements and elastic recoil detection analysis (ERDA) to characterize hydrogen in our samples.

### 2.3.1 Infrared Spectroscopy

The transmission spectra of samples (thickness  $\geq 1 \mu\text{m}$ ) deposited on polished crystalline silicon were recorded in the range of  $400$  to  $4000 \text{ cm}^{-1}$  using a Nicolet FTIR spectrophotometer (model 510P). The measurements were carried out at BECPRL,

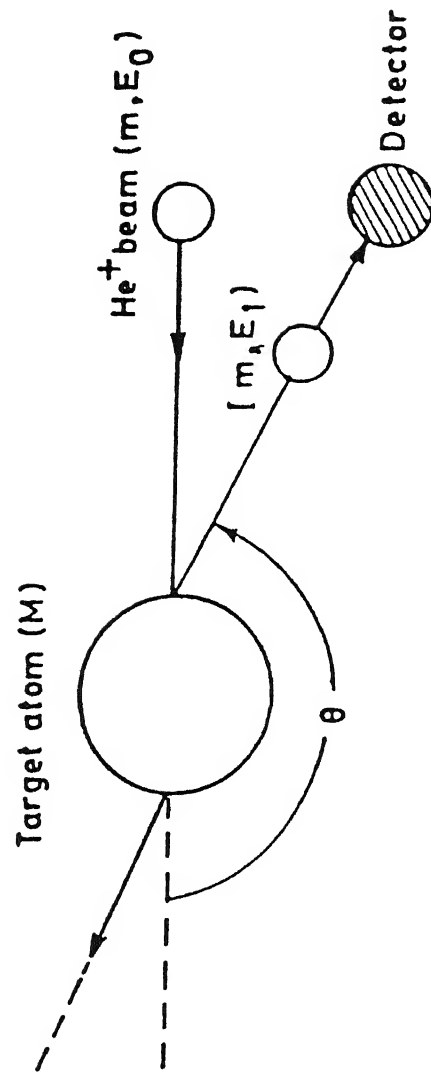


Fig.2.1 Schematic diagram of the back scattering process. Target of mass  $M$  is initially at rest.

National Physical Laboratory, New Delhi. To convert the transmission to absorption coefficient, we approximate the interference free transmission by

$$T = \frac{(1 - R)^2 \exp(-\alpha d)}{(1 - R^2 \exp(-2\alpha d))} \quad (2.1)$$

where  $\alpha$  is the absorption coefficient,  $d$  the film thickness, and  $R$  an empirically determined interface multiple reflection loss. We determined  $R$  by setting  $T = T_0$  (experimentally measured) when  $\alpha = 0$ . Equation (2.1) then becomes [188]

$$T = \frac{4T_0^2 \exp(-\alpha d)}{[(1 + T_0)^2 - (1 - T_0)^2 \exp(-2\alpha d)]} \quad (2.2)$$

which can be solved for  $\alpha$  in terms of the measured  $T$ .

The absorption band around 2800-3100  $\text{cm}^{-1}$  was analyzed more carefully for the individual contributing peaks to the stretching bands. Experimental spectrum was fitted using gaussian peaks after background corrections. Peakfit, from Jandel Scientific [189] utilizing the Lovenberg-Marquardt algorithm to find a global minimum in sum of squares [190] was used. The software first needs a manual approximation. In general, two constraints were imposed on each gaussian peak. Firstly, the peak position had to correspond to a known vibration frequency within  $\pm 10 \text{ cm}^{-1}$ . A component not indicated in the spectra by a hump or a shoulder was introduced only in those cases where the repeated trials failed by large margins and there were other spectral evidence for the existence of such a component. For a sharp band the fitting procedure produces same peak characteristics with a high accuracy even if all the parameters were left free. However in case of very broad convoluted bands the uncertainty in position and width may be as large as  $\pm 5 \text{ cm}^{-1}$ .

The data was analyzed for concentration of various C-H<sub>n</sub> bonding types, total bonded hydrogen and the fraction of sp<sup>3</sup> and sp<sup>2</sup> C-C bonds in the films as discussed in Chapter IV. This has proved to be useful to identify the microstructural variation of the films with the deposition parameters and hence the mechanism of growth.

### 2.3.2 Mass Spectroscopic Thermal Effusion

A thermal effusion experiment involves heating of sample while the rate of out-gassing atoms/molecules is monitored. This technique, also termed temperature programmed desorption spectroscopy (TPD) and thermal desorption spectroscopy (TDS), has been long applied in surface Physics to study the kinetics of surface desorption of atomic or molecular species [191,192].

A computer controlled mass spectroscopic thermal effusion (MSTE) system was designed and fabricated to detect the effusion of gases from thin films. The set-up is shown schematically in Fig. 2.2. The sample is inserted into quartz tube and the system is evacuated by a turbomolecular pump to a base vacuum of better than  $10^{-8}$  Torr. Quartz tube is heated by a tubular furnace, made of alumina baffle and wound with number 22 kanthal heater wire. A chromel alumel thermocouple is placed in contact with the quartz tube to sense the sample temperature. The tube temperature was calibrated with the temperature measured directly on the samples inside the tube in a dummy run. Prior to each experiment, quartz tube is cleaned by baking it to  $600\text{ }^{\circ}\text{C}$  to remove molecules adsorbed at the inner walls of the tube. The samples are normally heated up to  $1000\text{ }^{\circ}\text{C}$  at a linear heating rate ( $\beta$ ) of  $20\text{ }^{\circ}\text{C}/\text{min}$ . Different heating rates are employed for exploring the mechanism of gas effusion from our DLC samples. Quadrupole mass analyzer (Ametek, Dycor Model MA2000) is used for partial pressure detection.

It is important to analyze not only the increase in total pressure due to evolution of gases from the sample but also the species which are evolved. The out-diffusing species are identified by their mass numbers as monitored by the quadrupole gas analyzer. Twelve mass numbers could be simultaneously monitored as a function of temperature. While heating the sample, temperature of sample and partial pressure of evolved gases are continuously recorded through a computer. In addition to hydrogen, the most probable hydrocarbon species were also detected from our a-C:H and diamond films. The gas analyzer can be used to display the data in three different modes and is highly sensitive. Hydrogen effusion from a diamond film containing  $< 1\text{ at. \%}$  hydrogen could be detected using this thermal effusion set-up. Design considerations for higher sensitivity

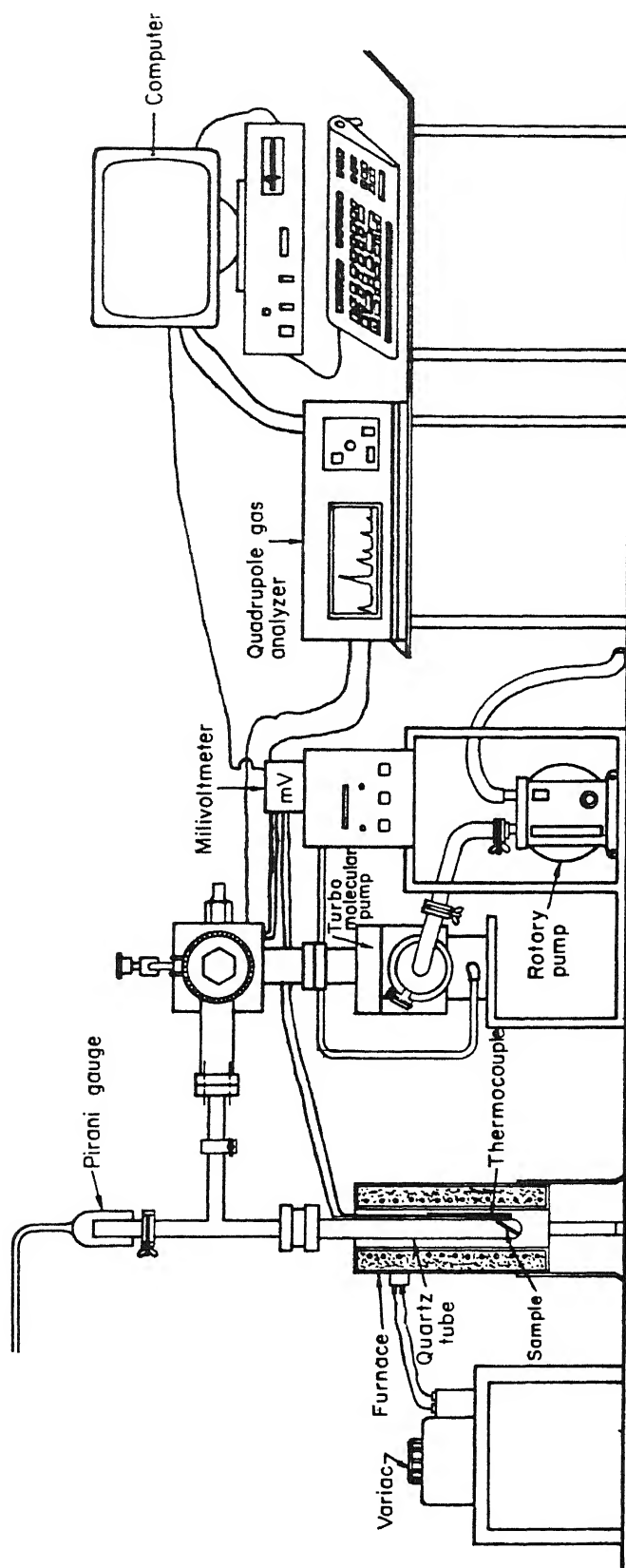


Fig.2.2 Schematic diagram of the thermal gas effusion system.



involves low volume( $\sim 230 \text{ cm}^3$ ) of the sample holder attachment and low leak rate( $< 10^{-4}$  torr.lit/sec). The details of the analysis of thermal effusion data for microstructural characterization of a-C:H films is given in Chapter IV.

### 2.3.3 Elastic Recoil Detection Analysis (ERDA)

The ERDA experiments on our samples were performed at the Central Nuclear Facility, Department of Physics, IIT Kanpur [83,193]. In a typical ERDA experiment, incident  $\text{He}^+$  ions impinge on a target kept at a glancing angle with respect to the incident beam direction as shown in Fig. 2.3. As the collision takes place, hydrogen gets recoiled in the forward direction making an angle  $\theta$  to the incident beam direction [194]. Due to the presence of heavier atoms in the target, primary helium also gets scattered in the same direction. To stop these scattered primaries from reaching the detector, a mylar foil of suitable thickness ( $6.5 \mu\text{m}$ ) is mounted in front of the detector. The recoiled hydrogen atoms enter a semiconductor detector through an aperture and are detected using conventional nuclear electronic set-up. In the present experiment  $\text{He}^+$  ions of 1.5 Mev, making an incident angle  $\alpha$  of  $15^\circ$  with the sample surface, were used. The beam spot was rectangular with an area of  $4 \text{ mm}^2$  on the target. The detector making a solid angle of  $0.865 \text{ mSr}$  was kept at an angle  $\theta$  of  $30^\circ$ .

The quantitative analysis of hydrogen mainly involves three basic concepts: (i) kinematic factor, (ii) the differential recoil cross-sections of the incident and recoiled particles in the target.

The  $\text{He}^+$  ion of incident energy  $E_0$  recoils H from the surface whose energy is given by

$$E_r = kE_0 \quad (2.3)$$

where  $k$  is the kinematic factor given by

$$k = \left[ \frac{4M_p M_r}{(M_p + M_r)^2} \right] \cos^2 \theta_r \quad (2.4)$$

where  $M_p$  and  $M_r$  are masses of the projectile and recoiled atoms respectively. Incident helium ions also get scattered in the forward direction due to the heavier matrix elements.

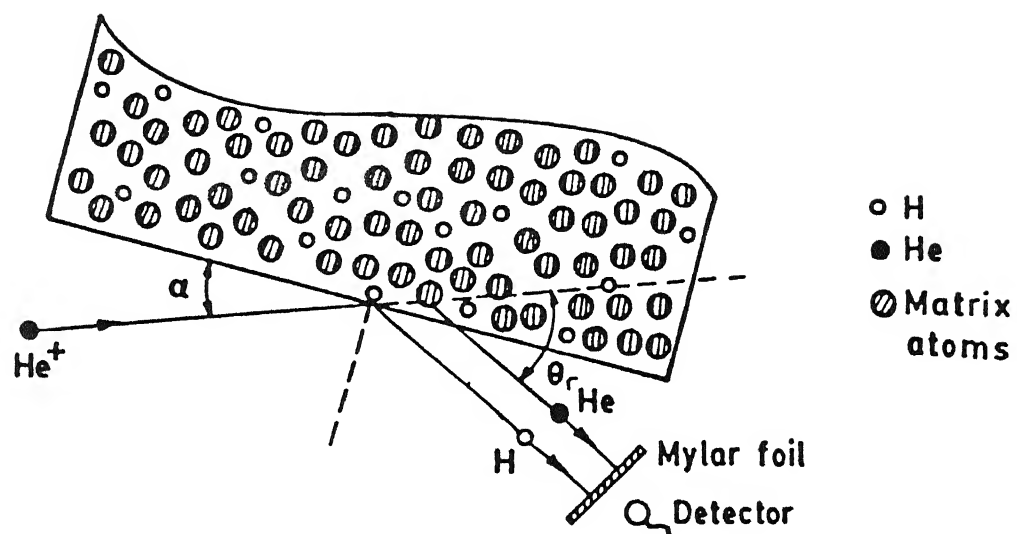


Fig.2.3 A typical ERDA geometry for the detection of hydrogen.

These scattered primary ions are stopped from reaching the detector by the stopper mylar foil. Assuming surface energy approximation [195] the energy of H getting recoiled from a depth within the sample is given by

$$E_d = kE_0 - [S]x - E \quad (2.5)$$

Where  $[S]$  is the energy loss factor given by

$$[S] = \left\{ \frac{k[dE/dx]^{He}}{\cos \theta} \right\} + \left\{ \frac{[dE/dx]^r}{\cos(\theta + \theta_r)} \right\} \quad (2.6)$$

$[dE/dx]^{He}$  is the stopping power for  $He^+$  at its incident energy and  $[dE/dx]^r$  the stopping power for H at the surface recoiled energy  $kE_0$  and  $E$  the energy lost by the recoiled particles in the stopper foil. If the concentration (at./cc) of the recoiling species at a depth  $x$  in the sample be  $N(x)$  then

$$N(x) = \frac{Y}{\left\{ \left( \frac{d\sigma}{d\Omega} \right) \Omega \left( \frac{\delta E}{R} \sin \alpha [S] \right) \right\}} \quad (2.7)$$

Where  $Y$  is the yield of recoils per channel at energy  $E_d$ ,  $Q$  the total number of incident ions on the sample during the data acquisition time,  $SE$  the detected energy window per channel,  $r$  the ratio of the recoiled ion's stopping power in the absorber foil at energy  $E_r$  and  $E_d$ ,  $d\sigma/d\Omega$  the elastic recoil cross-section,  $\Omega$  the solid angle subtended by the detector, and  $\alpha$  the grazing angle which the incident beam makes with the sample surface as shown in fig.2.3. It should be noted that the recoil processes of hydrogen from an incident  $He^+$  ion of energy  $\geq 1$  MeV are not purely coulombic in nature. Therefore, the cross-sections given by Rutherford formula are not valid in this case[196-199]. The RUMP [187] simulation code was used for the analysis of the recoil spectra.

From an experimental recoil spectrum, the depth versus concentration profile of the recoiled hydrogen in the sample was obtained. Considering the uncertainties involved in the measurements of solid angle etc. the set-up was standardized using good quality potassium dihydrogen phosphate (KDP) crystal, a sample of known hydrogen content [200].

## 2.4 OPTICAL PROPERTIES

One of the salient characteristics of amorphous semiconductors is the presence of tunable energy gap. In case of a-C:H films, optical gap is a strong function of film microstructure,  $sp^3/sp^2$  ratio of carbon bonding and hydrogen content in the samples. Thus, determination of optical band gap and optical constants can give useful information on the graphitic, polymeric or diamondlike nature of the films.

Optical properties like dielectric constants and energy gap of thin films may be studied by a large variety of techniques which basically fall into two categories. In the first, photometry, the film is illuminated by unpolarized radiation, and the intensities of reflected and transmitted beams are measured as a function of wavelength. In the second, ellipsometry, polarized radiation is used, and both intensity and phase of reflected beam are determined. Photometric methods are well suited to the determination of optical constants over a wide wavelength range and have traditionally been used for this task. Optical constants of our a-C:H films e.g., absorption coefficient ( $\alpha$ ), refractive index ( $n$ ) and optical band gap ( $E_g$ ) were determined from transmission, reflection and thickness data of the film.

The optical transmission and reflection of dc glow discharge deposited carbon films were recorded in the wavelength range 200 nm to 900 nm, using a double beam spectrophotometer (Hitachi Model 150-20). The transmission measurements were made at normal incidence while those of reflection at an angle of  $4^\circ$ .

### 2.4.1 Spectrophotometry

During transmission measurements light is incident on the sample and the transmitted light is measured as a function of wavelength as illustrated in Fig. 2.4(a). The sample is characterized by reflection coefficients  $R_1$ ,  $R_2$ , absorption coefficient  $\alpha$ , complex refractive index ( $n - ik$ ), and thickness  $d$  as shown in Fig. 2.4(b). Light is reflected back and forth, and each time some of it is reflected to the left and some is transmitted to the right. When all the components are summed, it can be shown that transmittance  $T$  is given by

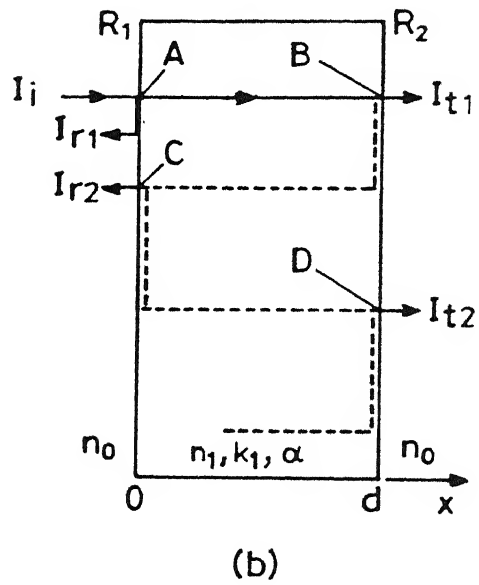
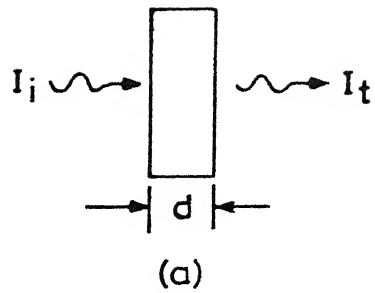


Fig.2.4 (a) Schematic transmittance measurements.  
 (b) Schematic showing the various reflected and transmitted components.

$$T = \frac{I_t}{I_i} = \frac{(1 - R_1)(1 - R_2)\exp(-\alpha d)}{1 + R_1 R_2 \exp(-2\alpha d) - 2\sqrt{R_1 R_2} \exp(-\alpha d) \cos \phi} \quad (2.8)$$

where  $\phi = 4\pi n_1 d / \lambda$ . For symmetrical samples,  $R_1 = R_2 = R$  and

$$T = \frac{(1 - R)^2 \exp(-\alpha d)}{1 + R^2 \exp(-2\alpha d) - 2R \exp(-\alpha d) \cos \phi} \quad (2.9)$$

For a thin film of thickness  $d$  and refractive index  $n_2$  on a substrate of refractive index  $n_3$  under normal incidence and  $k = 0$  conditions, the reflection coefficients are given by [201]

$$R_{23} = \frac{(n_2 - n_3)^2}{(n_2 + n_3)^2} \quad (2.10a)$$

$$R_{12} = \frac{(1 - n_2)^2}{(1 + n_2)^2} \quad (2.10b)$$

Then, expression for transmission is given by

$$T = \frac{Ax}{B - Cx \cos \phi + Dx^2} \quad (2.11)$$

where

$$\begin{aligned} A &= 16n_2^2 n_3 \\ B &= (n_2 + 1)^3 \\ C &= 2(n_2^2 - 1)(n_2^2 - n_3^2) \\ D &= (n_2 - 1)^3 (n_2 - n_3^2) \\ x &= \exp(-\alpha d) \end{aligned} \quad (2.12)$$

For films of uniform thickness, interference effects give rise to maxima and minima in transmission spectrum. The extremes of the interference fringes can be written as [202]:

$$T_M = \frac{Ax}{B - Cx + Dx^2} \quad (2.13a)$$

$$T_m = \frac{Ax}{B + Cx + Dx^2} \quad (2.13b)$$

These fringes are used to calculate the optical constants of the film following the method given by Swanpoel [202].

### 2.4.2 Dielectric Constant and Optical Gap

In the transparent region where  $\alpha \sim 0$ , the refractive index  $n$  is calculated as described by Swanpoel [202]. These values of  $n$  are used to calculate the film thickness  $d$  from the interference patterns appearing in transmission spectrum. From the condition of interference,  $2nd = m\lambda$ , we get

$$d = \frac{\lambda_1 \lambda_2}{2(\lambda_1 n_2 - \lambda_2 n_1)} \quad (2.14)$$

where  $n_1$  and  $n_2$  are the refractive indices at two adjacent maxima (or minima) at  $\lambda_1$  and  $\lambda_2$ . The value of  $d$  was put back into the equation  $2n(\lambda)d = m\lambda$  to get the exact value of  $n(\lambda)$ . The input values of  $d$  as determined above were used to calculate the value of  $2n(\lambda)d / \lambda$ . This was corrected to the nearest integral value if  $\lambda$  corresponded to an interference maximum and to the nearest half integral value if corresponded to an interference minimum. The true value of  $n(\lambda)$  was calculated from the corrected value of  $2n(\lambda)d / \lambda$ . Thus, both  $n(\lambda)$  and  $d$  were determined by iterating so that the product  $2n(\lambda)d / \lambda$  is either an integer or a half integer. In the region of strong absorption,  $n$  is estimated by extrapolating the values calculated in the other regions of the spectrum or is evaluated by using reflection data [203].

The absorption coefficient  $\alpha$  can be determined if the absorbance  $x$  is established from the relation

$$x = \exp(-\alpha d) \quad (2.15)$$

In the region of weak and medium absorption,  $x$  is calculated using methods given by Swanpoel [202].

### *Optical Band Gap*

The optical band gap is usually defined on the basis of a formula for optical transitions between two energy bands, separated by a band gap, which is a linear function of the photon energy. The optical gap is given by the intercept of the linear extrapolation of such a function. Different expression [203-206] are given both for the

imaginary part of the dielectric constant  $\tilde{\epsilon}(\epsilon_1 + i\epsilon_2)$  and the measured optical absorption coefficient  $\alpha$  as a function of the photon energy  $E$  according to different rules and conditions for optical transitions. These function assume different forms according to the structure of the film (amorphous or crystalline).

Optical gap still remains an ill defined quantity in amorphous semiconductors. However, analysis of transmission and reflection curves of DLC film shows that optical transitions follow the Tauc's relation

$$\sqrt{\alpha h\nu} = B_0(h\nu - E_g) \quad (2.16)$$

where  $B_0$  is the constant containing an average matrix element and  $E_g$  is the gap energy.

Plot of the  $(\alpha h\nu)^{1/2}$  versus  $h\nu$  is used to obtain Tauc gap  $E_g$  from the intercept on the abscissa. This gap is the energy difference between the beginning of the exponential tails and is not same as the mobility gap. It has been shown in a-Si:H that Tauc gap may be very different from the mobility gap [207].

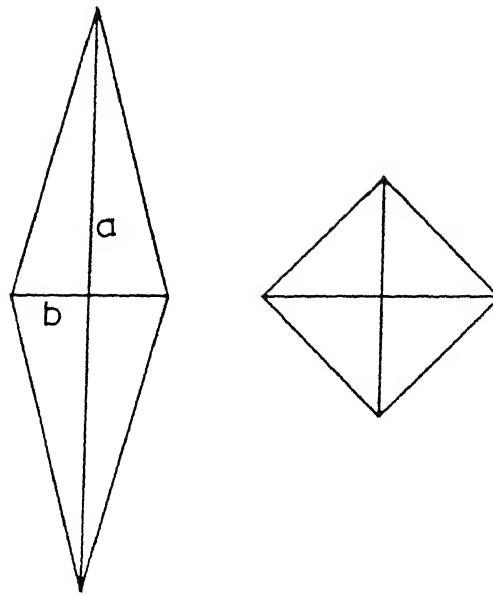
## 2.5 MECHANICAL PROPERTIES

### 2.5.1 Microhardness

The hardness of a material is defined as its resistance to local plastic deformation. Microhardness is normally determined with either one of two diamond pyramid indenters; the Vickers or the Knoop [208] as shown in fig. 2.5a.

The Vickers hardness is a static indentation test where a square based diamond pyramid of face angle  $136^\circ$  is pressed into the specimen surface. The load per unit area of the resulting indentation is taken as a measure of the hardness. With Vickers pyramid geometry, the hardness is expressed by





Knoop Indentation Vickers Indentation

Fig. 2.5(a) Comparison of indentations made by Knoop and Vickers indenters.

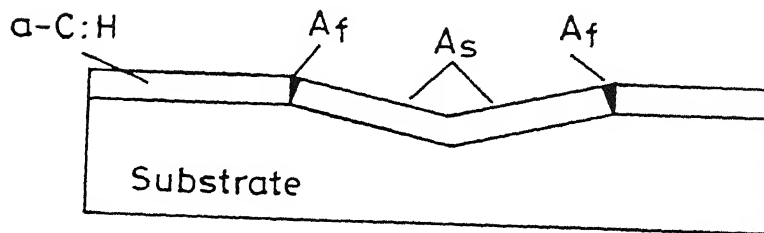


Fig. 2.5 (b) Jonsson and Hogmark model for hardness behavior of thin films. The contribution of hardness (film) to composite hardness is in the region around the edge of indentation  $A_f$  (shaded area), whereas the inner region of the indentation  $A_s$  transmits the loading force directly to the substrate (after Ref. 210)

$$H_V = 2 \sin(\theta / 2) \frac{L}{d^2} (\text{kgf} / \text{mm}^2) \quad (2.17)$$

Where  $L$  is the applied load,  $d$  is the mean diagonal of the indentation and  $\theta$  is the angle between opposite faces of the indenter ( $136^\circ$ ). Equation (2.17) can be rewritten as

$$H_V = 2 \cos(22) \frac{L}{d^2} \quad (2.18)$$

A standard Knoop test makes use of a rhombic base pyramidal indenter. The indentation ratio ( $a/b$ ) between long and short diagonals is approximately 7 to 1. The depth of indentation is about one thirtieth of the length of the long diagonal. The Knoop hardness is expressed in terms of the projected area

$$H_K = \frac{2L}{d^2 \left( \cot \frac{172.5}{2} + \tan \frac{130}{2} \right)} (\text{kgf} / \text{mm}^2) \quad (2.19)$$

where  $d$  is the length of the long diagonal and  $L$  is the applied load.

A comparison of the shape of the indentation made by the Vickers and that by Knoop indenter is presented in Fig. 2.5(a). Knoop test gives more accurate values of microhardnesses of comparatively thinner films because of the longer diagonals. However, Vickers test was successfully applied for accurate determination of hardness values of thin films by analyzing the data as described below. The apparatus used was Leitz mini load 2. Loads between 5 and 100 gf were applied to the sample with a dwell time of 15 seconds. The impression sizes were measured by a micrometer eyepiece mounted on an optical microscope. The hardness at each load is calculated from the average of five measured diagonals in both directions.

The indentation depth in Vickers hardness is close to one seventh of the diagonal of pyramid. The film hardness is influenced by the hardness of substrate if the indentation depth is more than 10% of the film thickness [209]. Hence, for the microhardness measurement of our samples, relatively thicker films ( $\geq 1 \mu\text{m}$ ) were used. Also, the individual contributions from the film and the substrate to the composite (measured) hardness is calculated. A simple model given by Johnsson and Hogmark [210] was employed. The model uses a simple geometric approach, based on the fact that the hardness of a material equals the mean contact pressure developed during the

indentation process. The model for hardness behavior of thin films is shown in Fig 2.5(b). The contribution of hardness of film to composite hardness is in the region around the edge of indentation  $A_f$  (shadowed area), whereas the inner region of indentation  $A_s$  transmits the loading force directly to the substrate. Hence, the composite hardness can be expressed as a weighted mean of the film and substrate hardness

$$H_c = \frac{A_f}{A} H_f + \frac{A_s}{A} H_s \quad (2.20)$$

where  $H_c$  is the measured composite hardness,  $H_f$  is the film hardness,  $H_s$  is the substrate hardness and  $A$  is total area i.e. the sum of  $A_s$  and  $A_f$ . Equation (2.20) with simple geometrical considerations can be rearranged as

$$H_f = H_s + \frac{H_c - H_s}{2c \frac{t}{D} - c^2 \left( \frac{t}{D} \right)^2} \quad (2.21)$$

where  $t$  and  $D$  are film thickness and indentation depth, respectively,  $c$  is a geometrical constant. The value of  $c = 2 (\sin 11) ^2$  for hard film on soft substrate and  $c = 2 (\sin 22) ^2$  for comparable hardness values of film and substrates. This formula is used for separating the film hardness from the measured Vickers composite hardness on our samples. The value of constant  $c = 2 (\sin 11) ^2$  is used for our hard films on soft (silicon) substrates.

Typical hardness curves of a sample composed of a DLC film on a crystalline substrate is shown in Fig. 2.6. The load dependence particularly for small loads is due to the structure of the sample i.e., hard thin film on a soft substrate. The best estimates of the hardness of the film are obtained at the lowest loads.

## 2.5.2 Stress Measurement

The biaxial stress in the diamond films was evaluated from Raman measurements. The shift of diamond peak in the deposited film from the peak position of natural diamond ( $1332 \text{ cm}^{-1}$ ) is used to estimate the stress in the film using the relation [211]:

$$\tau = -1.08 \text{ GPa/cm}^{-1} (\nu_s - \nu_o) \quad (2.22)$$

where  $\nu_o = 1332 \text{ cm}^{-1}$ ,  $\nu_s$  is the wavenumber of peak observed for the film in  $\text{cm}^{-1}$ .

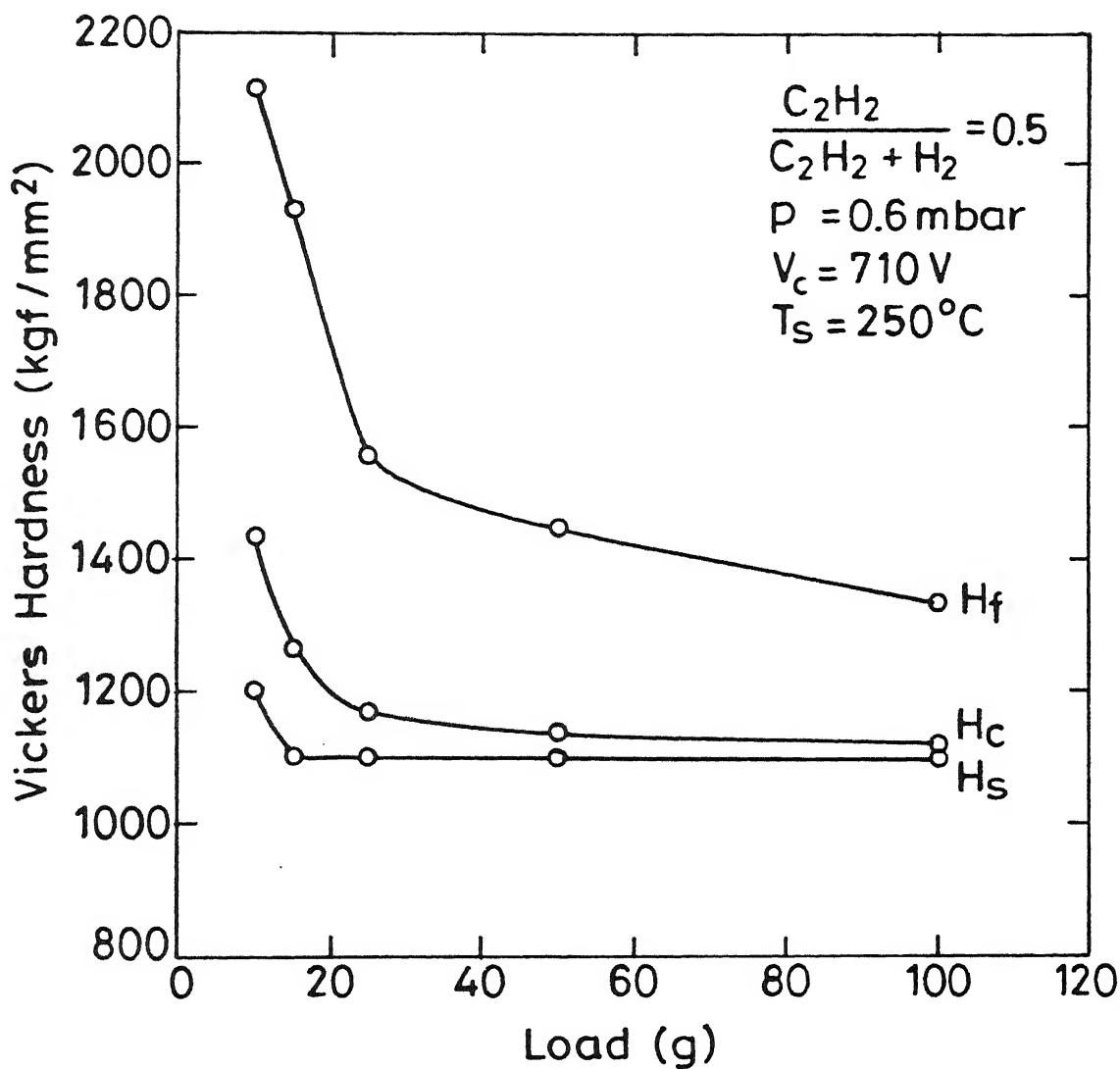


Fig.2.6

Typical Vickers microhardness as a function of applied load for a DLC sample deposited on c-Si substrate. Film hardness  $H_f$  has been calculated from measured composite hardness  $H_c$  and substrate hardness  $H_s$ .

## CHAPTER III

# DC GLOW DISCHARGE DEPOSITION OF DIAMOND-LIKE CARBON FILMS

### 3.1 INTRODUCTION

There are a wide variety of techniques to produce diamond and diamond-like carbon films. Solid carbon, hydrocarbon gases or liquids are used as source material for carbon film deposition (Chapter I). Among the techniques employing hydrocarbon gases, the decomposition of gas is achieved by three major ways e.g. electrical excitation, exposure to high temperatures and combustion in an oxygen flame (Table 1.3). As far as hydrogenated amorphous carbon films are concerned, the films obtained by different deposition methods exhibit a large variation in their properties. Quality of films is a function of deposition parameters and the physico-chemical processes involved in the deposition process. These, in turn, are specific to the deposition technique and the geometry of the reactor employed. It is therefore essential to understand the characteristics of deposition process as well as that of the deposition reactor to correlate the growth parameters with the film properties.

In this Chapter, details of the DC glow discharge plasma reactor fabricated for the present investigations are described. The design considerations crucial for obtaining uniform and reproducible films are incorporated in fabrication of this reactor. Role of system geometry has been identified in controlling the discharge characteristics, homogeneity of deposits, and ionic bombardment of substrates. Plasma species produced during dc glow discharge of acetylene are identified by using in-situ mass spectroscopy. Here focus is on understanding the discharge process itself while the details of films properties - process variable relationships are discussed in Chapter V.

## 3.2 PREPARATION OF DLC FILMS

As described in Chapter I, the plasma deposition techniques are most favored for synthesizing DLC and diamond films. The design of our dc glow discharge plasma CVD reactor, and the methodology employed for film deposition are described in this section.

### 3.2.1 Design and Fabrication of the Reactor

#### *a. Design Considerations:*

The design considerations of the reactor include the suitable provisions for :

- Varying interelectrode spacing
- Applying potential of any polarity to the substrate
- Isolating powered bodies from reactor walls / surfaces
- Uniform pumping for stable discharges
- Using in-situ probes, such as mass spectrometer for characterization of plasma
- Heating of the substrate without contamination
- Deposition of uniform films of dimensions up to 3".

Based on these criteria a deposition system was designed and fabricated. The process chamber is shown schematically in Fig. 3.1. A photograph of the complete dc discharge system is shown in Fig. 3.2(a).

#### *B. Pumping System And Gas Flow*

A diffusion pump (IBP2-N-132) is used for evacuating the process chamber to a base vacuum of about  $5 \times 10^{-6}$  mbar. This pump is connected to the process chamber using 2" diameter stainless steel tubes and a baffle valve. The diffusion pump is backed by a mechanical rotary pump (IBP D2A). During discharge, pumping is carried out directly by the rotary pump through a roughing valve. Gases are delivered to the chamber through stainless steel welded lines and the flows are controlled individually using needle valves and volume flowmeters. For a fixed inflow of gas, the desired pressure for discharge is obtained by throttling the roughing valve.

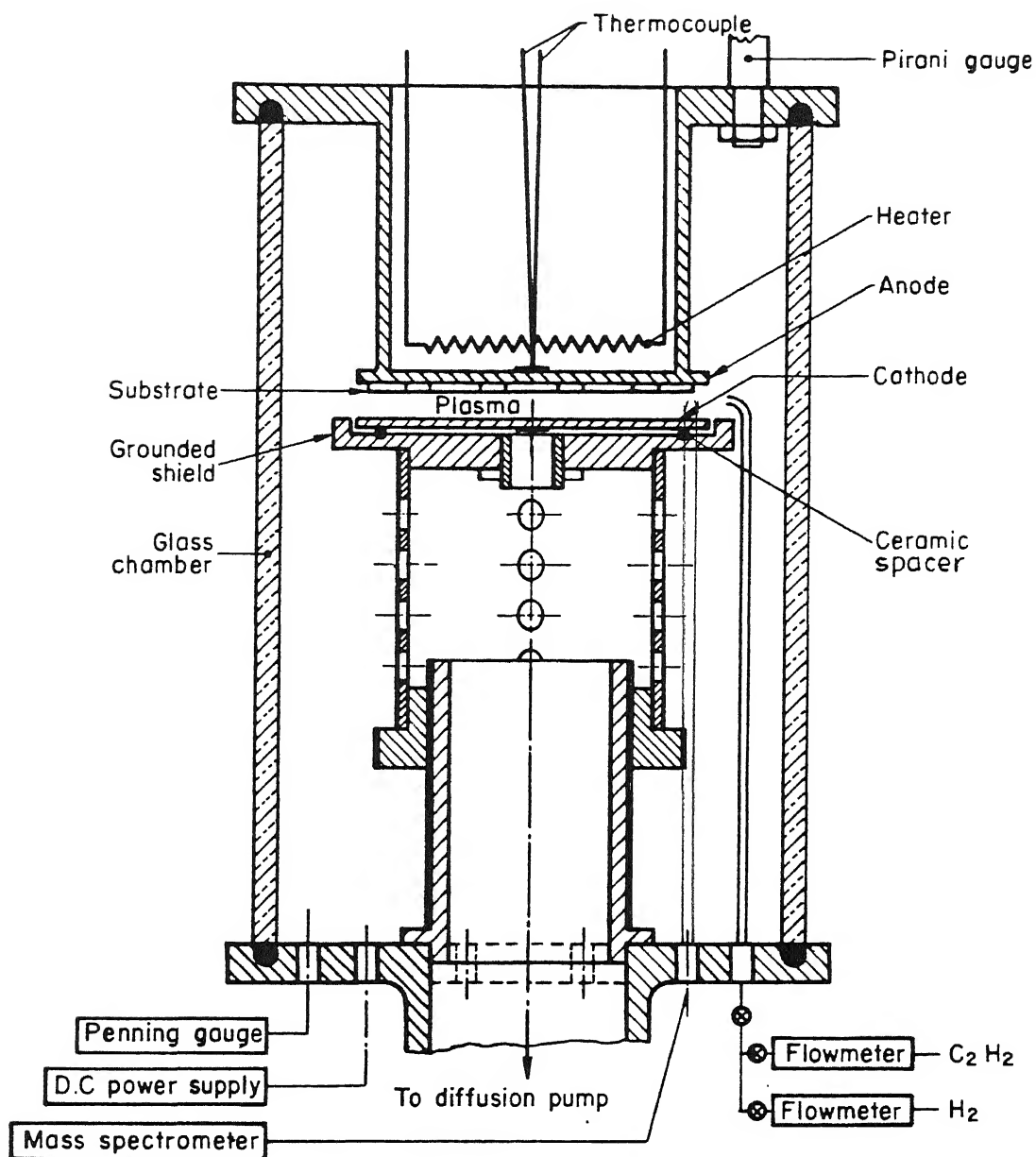


Fig.3.1 Schematic diagram of the dc plasma reactor.

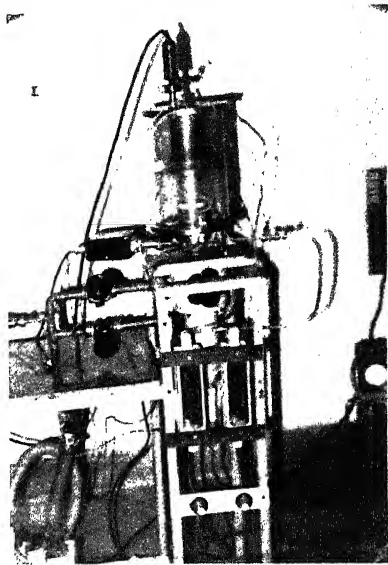


Fig.3.2 (a) Photograph of the dc glow discharge system fabricated for the present work..

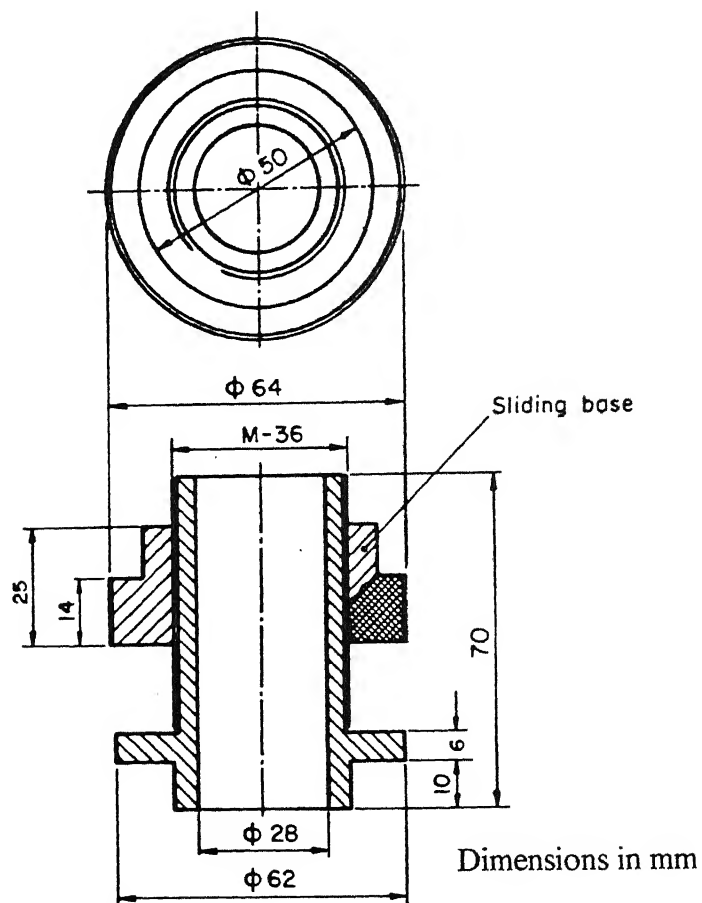


Fig.3.2 (b) A nut and screw arrangement for variation of inter electrode gap.



## 1c. Process Chamber

The process chamber consists of a borosil glass cylinder of 16.2 cm diameter and 25.5 cm height sitting on top of a stainless steel flange having various feedthroughs and vacuum ports (Fig. 3.1).

Horizontal plane parallel electrodes are made of 9 cm diameter stainless steel discs. The lower electrode is powered by a 3 kV/50mA regulated direct current power supply (Aplab 7341P). The cathode is supported by a perforated cylindrical tube resting on a knurled nut. Interelectrode gap can be varied from 4 mm to 70 mm using this nut and screw arrangement as shown in Fig. 3.2(b). The top electrode can be grounded, biased, or left floating. Substrates are normally held at this electrode (anode). Anode is facing downwards to reduce incorporation of macroscopic particulates on the substrates. Particles of powder formed in the plasma fall down thereby facilitating production of pin hole free films on anode. The anode is provided with an external resistive heater (Ni-Fe-Cr wire) to avoid contamination inside the vacuum chamber as shown in Fig. 3.1. Substrate temperature is measured using a chromel alumel thermocouple after stabilization.

The gases, which arrive through a nozzle tube at the level of interelectrode region, are pumped uniformly through a perforated cylindrical tube. Flow patterns of reactant vapors are streamlined to achieve uniform and stable discharges. For our reactor and flow/pumping patterns, a pressure range of 0.2 m bar to 25 m bar could be used without getting any instabilities in the dc discharges.

The plasma was confined to the volume between the two electrodes by a grounded shield surrounding the cathode at a separation of about 1 mm using ceramic spacers (Fig.3.1). This shield avoids any discharge between cathode and other grounded bodies in the chamber and helps in maintaining a localized discharge. Detrimental flickering of the plasma is also suppressed.

### 3.2.2 Deposition Methodology

#### (a) Substrates

Polished crystalline silicon, glass (corning 7059), quartz and steel substrates were used for deposition. Contamination on these substrate surfaces may consist of particulate material, organic or inorganic surface films. Therefore, they need to be properly

cleaned prior to loading in the deposition chamber for good adhesion of films. Particulate removal was accomplished by ultrasonic treatments in cleaning solutions. Organic residues were removed by cleaning in acetone followed by vapor degreasing in propanol or methanol. Crystalline silicon wafers were boiled in trichloro-ethylene and then cleaned in buffered hydrofluoric acid for few seconds. Subsequently they were rinsed in deionized water resulting in droplets beading up indicating an oxide free clean surface. For further in-situ cleaning, glow discharge plasma using pure hydrogen discharge was employed just prior to the deposition of films. This was found to enhance the adhesion of films.

### ***(b) Deposition Procedure***

Though a number of hydrocarbon source gases have been used to produce amorphous carbons films, it is found that growth rate increases with C to H ratio [212] of the gas. Acetylene is shown to produce growth rates about four to seven times higher as compared to methane under the same growth conditions [44]. Amount of energy necessary for complete dissociation and ionization of acetylene is also lower than that for methane. This inhibits further reactions such as polymerization at low pressures. Therefore, we used acetylene for the deposition of a-C:H films.

After evacuating down to  $\sim 10^{-5}$  mbar, the chamber was heated to about 200 °C by putting on the substrate heater and using heat lamps from outside. Other parts of the system were baked using heating tapes. Pure hydrogen gas was introduced through a needle valve and a volume flowmeter. A constant flow was maintained to obtain a pressure of the  $\sim 10$  mbar. Glow discharge was created by applying a suitable high dc voltage between the grounded anode and powered cathode. A stable discharge was obtained. Usual duration of plasma cleaning was  $\sim 15$  min. This plasma cleaning step was found essential for improved adhesion of films to the substrates.

After the hydrogen discharge, all heating was stopped except the substrate heater. The system was evacuated down to  $\sim 10^{-6}$  mbar. The substrate temperature was brought to the desired value by using a variac controlling the substrate heater. Working gases (acetylene or acetylene and hydrogen mixtures) were then introduced in the reaction chamber through separate needle valves. Constant flow of each was maintained.

The desired discharge pressure was obtained by throttling the roughing valve. The system was constantly pumped throughout the operation. A stable discharge was maintained between the electrodes. The deposition parameters scanned for about 70 deposition runs are summarized in Table 3.1. A good reproducibility in the film properties was obtained for samples deposited under similar deposition conditions.

**Table 3.1:** *Parameter space scanned for depositions*

Parameters	Range
Base Pressure (mbar)	$\sim 10^{-6}$
Substrate Temperature ( °C)	30 - 525
Deposition Pressure (mbar)	0.1 - 100
Electrode Separation (cm)	1.0 - 4.0
Gas Flow rates (Sccm)	
C <sub>2</sub> H <sub>2</sub>	10 - 100
H <sub>2</sub>	0 - 100
Hydrogen dilution (C <sub>2</sub> H <sub>2</sub> /C <sub>2</sub> H <sub>2</sub> +H <sub>2</sub> )	0.1 - 1.0
D.C. Cathode Voltage, V <sub>c</sub> (-Volts)	600 - 1200
Discharge current (mA)	2 - 30
Applied Substrate Bias (-Volts)	0 - 425

### 3.3 DISCHARGE CHARACTERISTICS

Understanding of the film growth parameters can be made clear by first examining some of the physical and geometrical properties of the gas discharges. Many effects such as sparking, instabilities or powder formation may be observed during deposition. These are natural results of either the type of discharges or are of the parametric effects such as geometry, temperatures, and surface conditions. In this section, dc discharge characteristics of the plasma produced in our reactor are discussed.

#### 3.3.1 Initiation and Maintenance of the Discharge

In order to parameterize our glow discharge reactor, minimum starting voltage necessary to initiate the discharge ( $V_{st}$ ) was measured as a function of various system parameters.  $V_{st}$  depends on the electrode material, temperature and interelectrode spacing as well as the type and composition of feedgas and its total pressure [213-215]. Fig. 3.3 shows the starting voltages plotted as a function of the product of gas pressure ( $p$ ) and interelectrode spacing ( $d$ ) at a substrate temperature of 250°C using pure acetylene. This is typical of various deposition temperatures used and follows a Paschen-like curve [213]. The two branches of the curve can be easily distinguished. One with lower values of the product  $p.d$ , which we shall refer to as **region A**, and the other with a large  $p.d$ . referred as **region B**. The transition between the two regions takes place for about  $p.d = 1.8 \text{ mbar.cm}$ . Fig. 3.4 shows the  $V_{st}$  as a function of  $p.d$  in case of feedgas being diluted with hydrogen. Significant differences are observed in the behavior of curve as compared to that for pure acetylene (Fig. 3.3). Higher starting voltages are required to initiate the discharge at low pressures due to reduced ionization cross-section of hydrogen molecule. This also leads to the shift in minimum of the Paschen curve to the higher  $p.d$  values.

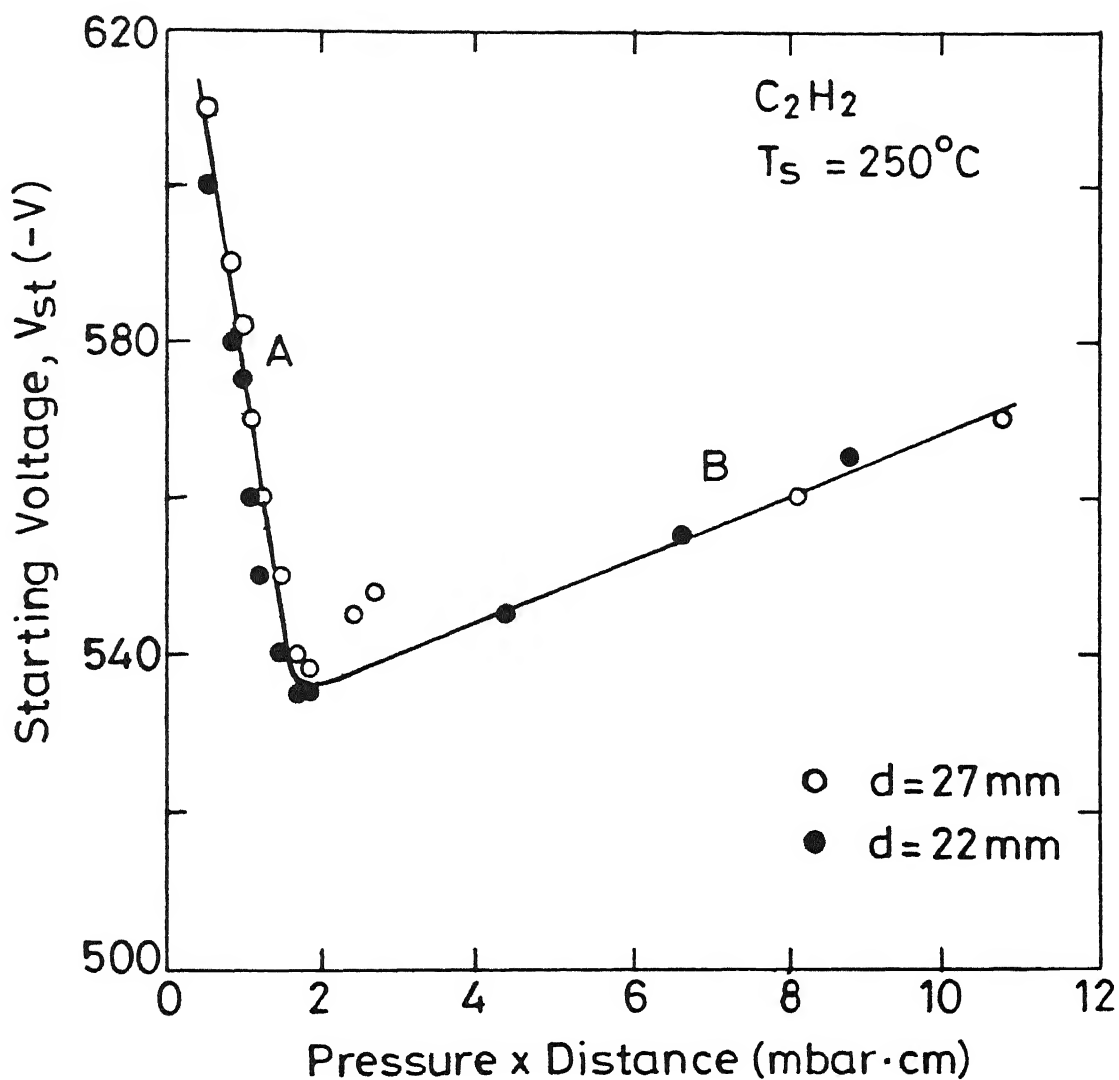


Fig.3.3 Variation of discharge starting voltage ( $V_s$ ) as a function of the product of acetylene pressure ( $p$ ) and inter electrode gap ( $d$ ) using stainless steel electrodes at a substrate temperature of  $250^\circ C$ .

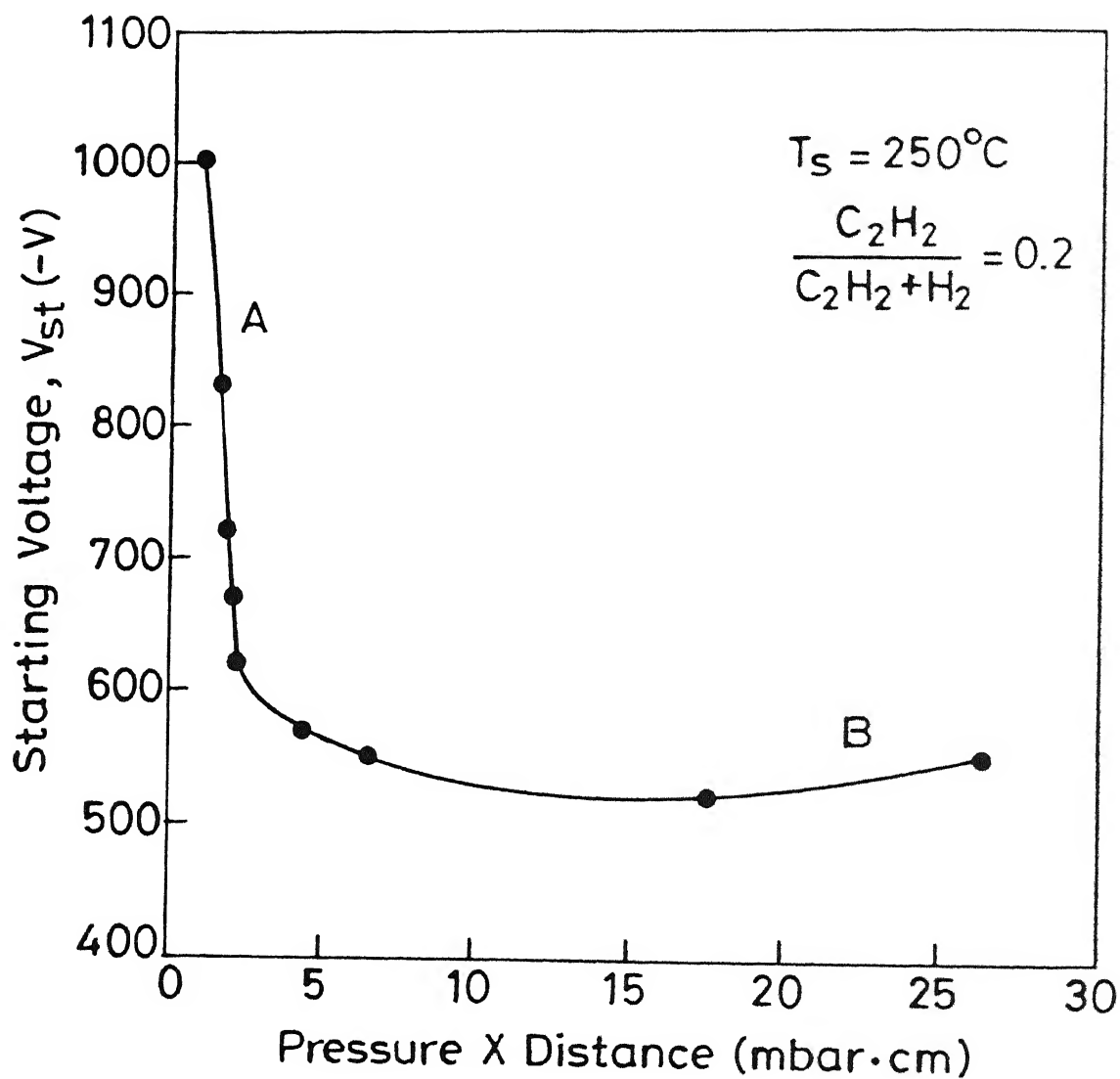


Fig.3.4 Variation of discharge starting voltage ( $V_{st}$ ) as a function of the product of gas pressure ( $p$ ) and inter electrode spacing ( $d=2.2\text{cm}$ ) using acetylene diluted in hydrogen ( $C_2H_2/C_2H_2 + H_2=0.2$ ).

Results shown in Fig. 3.3 and 3.4 can be explained by understanding the physical processes taking place in the glow discharge [213-215]. In region A at low pressures, secondary electrons produced at the cathode surface cannot undergo a sufficient number of ionizing collisions before they strike the anode. Therefore, higher sustaining power is required at lower pressures and smaller interelectrode spacings. In this region, the mean free path of electrons is large. The electrons therefore lose their energy by collision with the electrodes. At the same time, secondary reactions in the plasma are not significant. Hence, the surface based reactions predominate. The discharge is characterized by a low density of reactive species and an increased electronic temperature. At higher pressures (region B), on the contrary, ions generated in the gas are slowed down by inelastic collisions. Ions strike the cathode with insufficient energy and are unable to produce requisite number of secondary electrons. Therefore, a higher input power is required. In this region, electrons as well as radicals have numerous collisions with the gas molecules. Therefore discharge consists of low energy electrons and is richer in chemically active species. Hence, the plasma conditions are more likely to promote ion molecule and ion neutral (or free radical) collisions.

Once the discharge is initiated, its maintenance can be assured by the secondary electrons emitted by the electrodes [215,216]. Two main mechanisms can explain the production of these electrons:

*Ionic bombardment:* As the plasma potential is always positive with respect to the electrodes, ionic bombardment on electrodes (particularly on cathode) results in production of secondary electrons. Secondary electrons are the principal agents of ionization. Secondary electrons produced at the heated substrate electrode (anode) also play an important role. In fact, this process is likely to be significant in case of carbon films. Moreover, nature of electrodes can change the plasma parameters considerably when power is supplied to the discharge via secondary electrons emitted by the electrodes.

*Electronic bombardment:* It takes place on anode when the potential difference through the sheath is small. These electrons therefore have low energy.

Electrons produced in the plasma also help in maintaining the discharge. When mode of functioning of the discharge is in the region of high pressure (region B), the

mean free path of charged species (ambipolar diffusion) is very small. Under these conditions, the transfer of energy takes place by the Joule effect. Energy of electrons is mainly dispersed by collisions with the gas molecules.

### 3.3.2 Plasma Confinement

Discharge is considered to be confined when the plasma is in contact with the electrode surfaces only. The discharge confinement is an efficient way to increase the ionic bombardment as it induces an effect equivalent to a reduction of distance between electrodes [216]. The plasma confinement over the electrode surfaces depends on the discharge mode utilized. It also varies as a function of discharge current. At the discharge current ( $I_d$ ) below  $0.1 \text{ mA/cm}^2$ , Townsend discharge appears [217]. For  $I_d > 0.1 \text{ mA/cm}^2$ , the discharge begins to glow. In the low current region of the discharge, the glow partially covers the cathode area and current density at the cathode surface is nonuniform. This mode is called normal glow discharge. By increasing the current density, glow starts to cover the whole cathode surface. This mode is called abnormal glow discharge and is employed for deposition of films. In this region, the discharge current density is found to increase linearly with the applied cathode voltages as shown in Fig. 3.5. Further, the spreading of plasma outside the volume between electrode surfaces is physically confined by employing a grounded shield surrounding the cathode (Fig. 3.1).

### 3.3.3 Electrode Separation

Various regions of a glow discharge appear as a function of electrode separation  $d$ , as shown in Fig 3.6 (a) [215]. As  $d$  is decreased, the cathode dark space and negative glow are unaffected while the positive column shrinks. This process continues so that only the negative glow and dark spaces adjacent to each electrode are left. This is the condition employed by us for deposition of thin films. In our deposition conditions at low inter-electrode separation, substrate electrode is placed in the negative glow regime. Under the pressures employed, positive column is not observed. At  $d$  less than this, dark space becomes distorted and then the discharge is extinguished. At smaller  $d$  values  $< 10 \text{ mm}$ , the plasma was confined to regions near edges of electrodes. At low values of p.d. used by us,



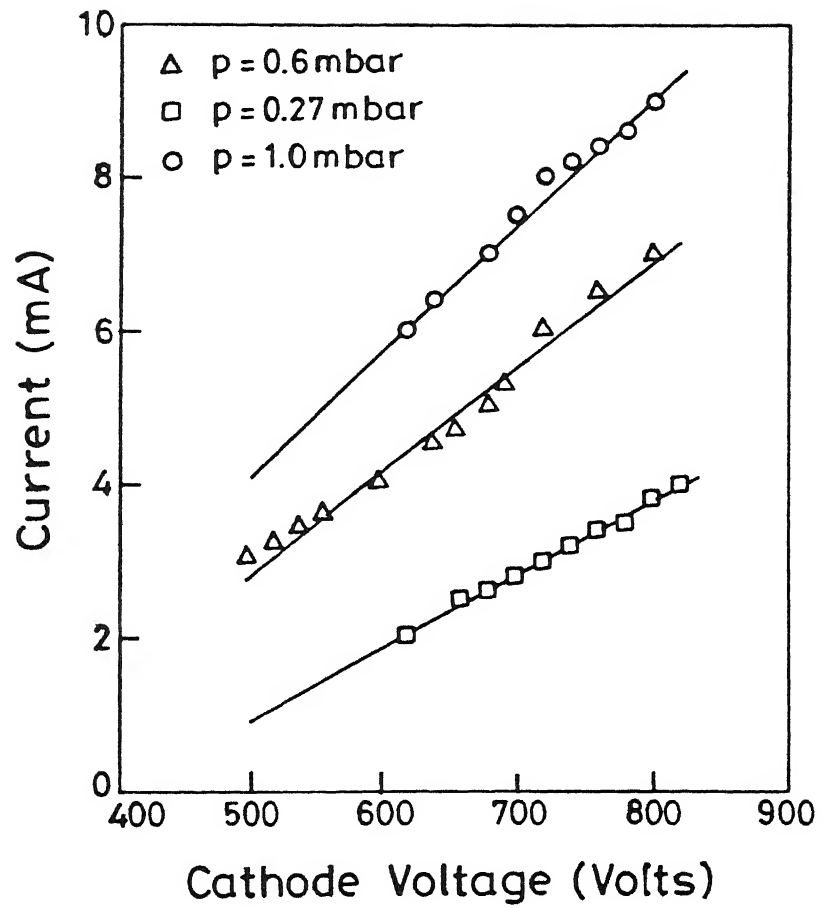


Fig.3.5 Current versus cathode voltage characteristics for acetylene plasma at (a) 0.27 mbar (b) 0.6 mbar and (c) 1 mbar.

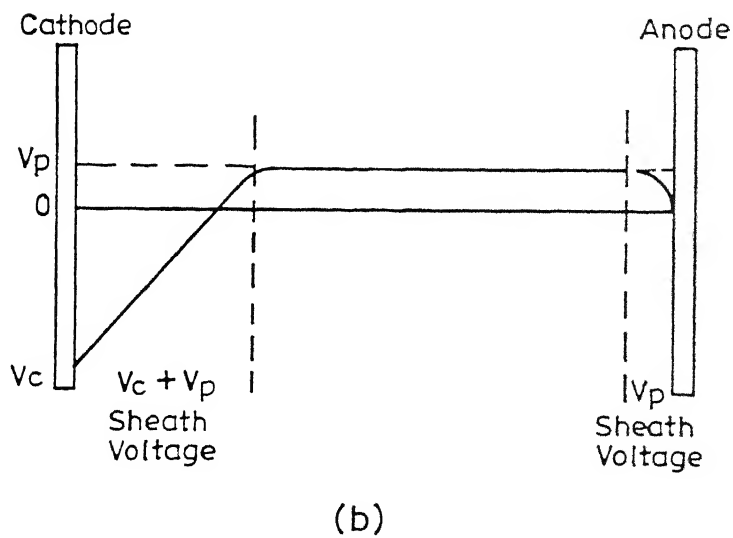
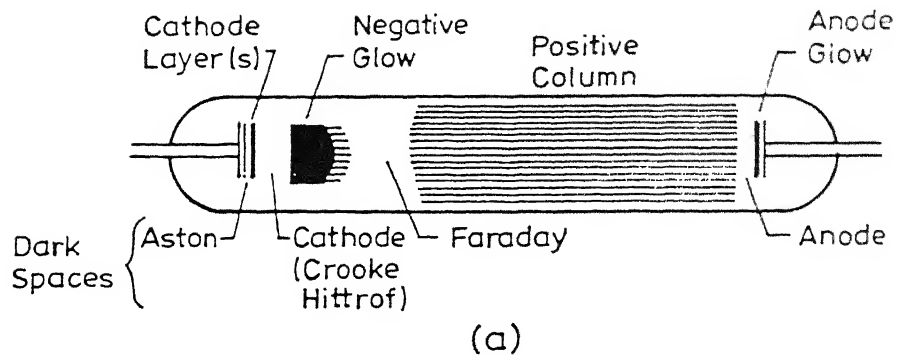


Fig.3.6 (a) Glowing and dark spaces in dc discharges.  
 (b) Voltage distribution in a dc glow discharge process .

the voltage distribution in a dc diode consists of three observed regions shown here in figure 3.6 (b). There is a cathode dark space across which most of the applied voltage is dropped, a low field negative glow that contains approximately equal concentration of electrons and positive ions, and an anode dark sheath.

Effect of interelectrode spacing on the deposition rate is normally much stronger for parallel plate dc diode discharge geometry as compared to the rf glow discharges. The rate and uniformity of deposition is a function of interelectrode gap ( $d$ ) as well as pressure ( $p$ ). In order to confine our studies to a reasonable parameter space, we selected deposition rate for optimization as a function of the interelectrode gap. Fig. 3.7 shows the deposition rate as a function of  $d$  for films deposited on Si at a constant pressure of 0.78 mbar using pure  $C_2H_2$ . Deposition rate first increases with interelectrode gap spacing and then starts decreasing at larger values of  $d$ . This is a typical behavior observed at other deposition conditions also. Similar behavior has been reported in case of a-Si:H [218].

For large  $d$  ( $> 40$  mm), plasma was confined to the region near the center of the electrodes. Plasma polymerization induced by the secondary reactions is found to be significant at large  $d$  values. Heavy hydrocarbon clusters due to their slow diffusion and trapped negative ions in the plasma have long residence times. They encounter other reactive species and may build-up to fairly large sizes. This causes powder formation. Hence a gap of 2.2 cm was used for all subsequent depositions in our reactor.

### 3.3.4 Floating and Bias Potentials

Since the deposited carbon films are highly insulating, the substrate tend to achieve the floating potentials as soon as a thin layer is deposited even if the anode is externally grounded. A knowledge of ion energies is crucial to the understanding of film growth. Therefore, floating potentials,  $V_f$ , at clean anode were measured. Fig. 3.8 shows the values of negative floating potential attained by the substrate electrode as a function of  $p, d$  for  $d = 2.2$  cm. A maximum in  $V_f$  is obtained corresponding to a minimum in  $V_{st}$  on the  $p, d$  curve (see Fig. 3.3).  $V_f$  increases as the number of available electrons increases with pressure. On further increase in pressure, electrons loose their energies due to

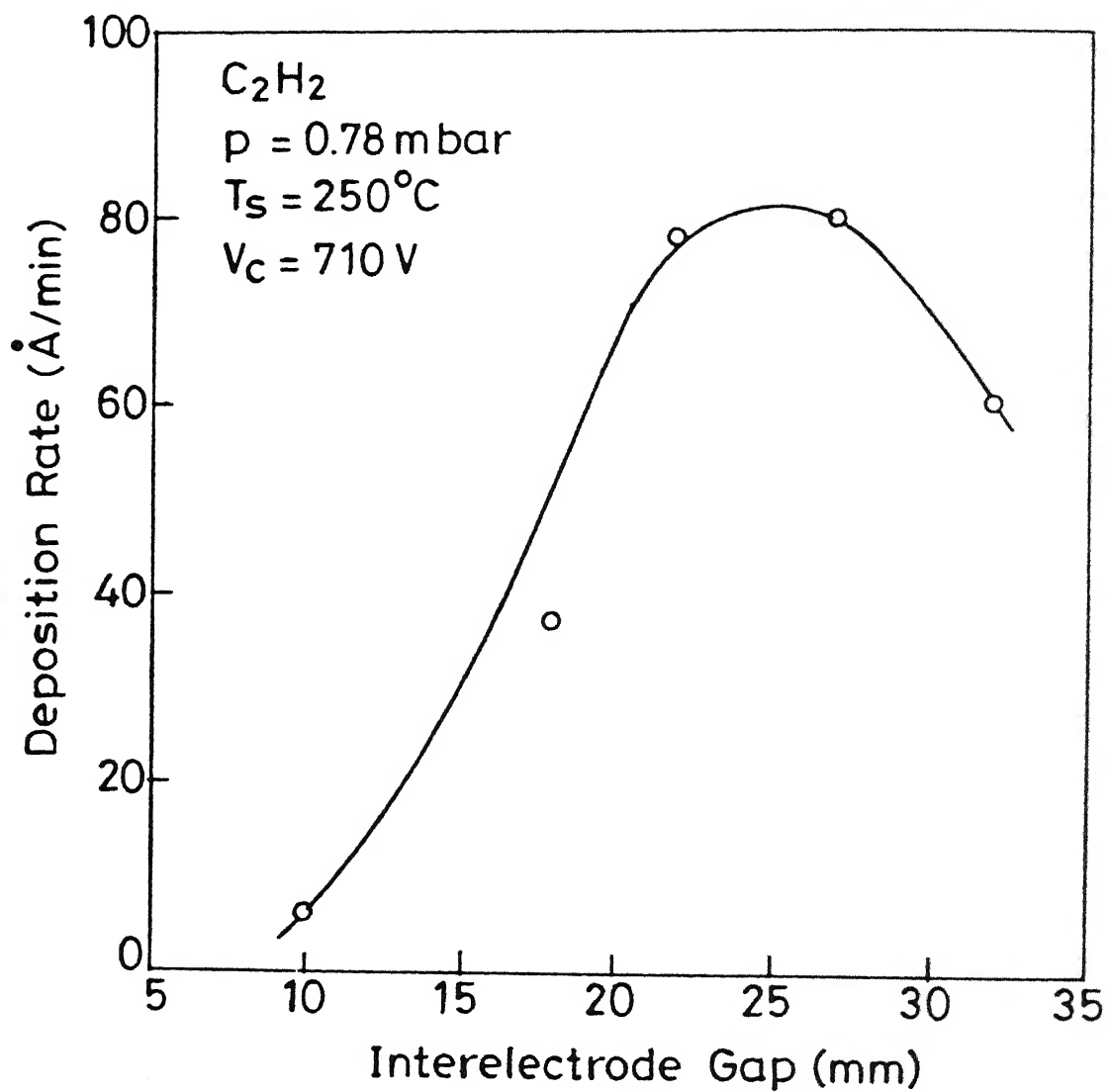


Fig.3.7 Dependence of deposition rate on the interelectrode spacing for pure  $C_2H_2$  glow discharge.

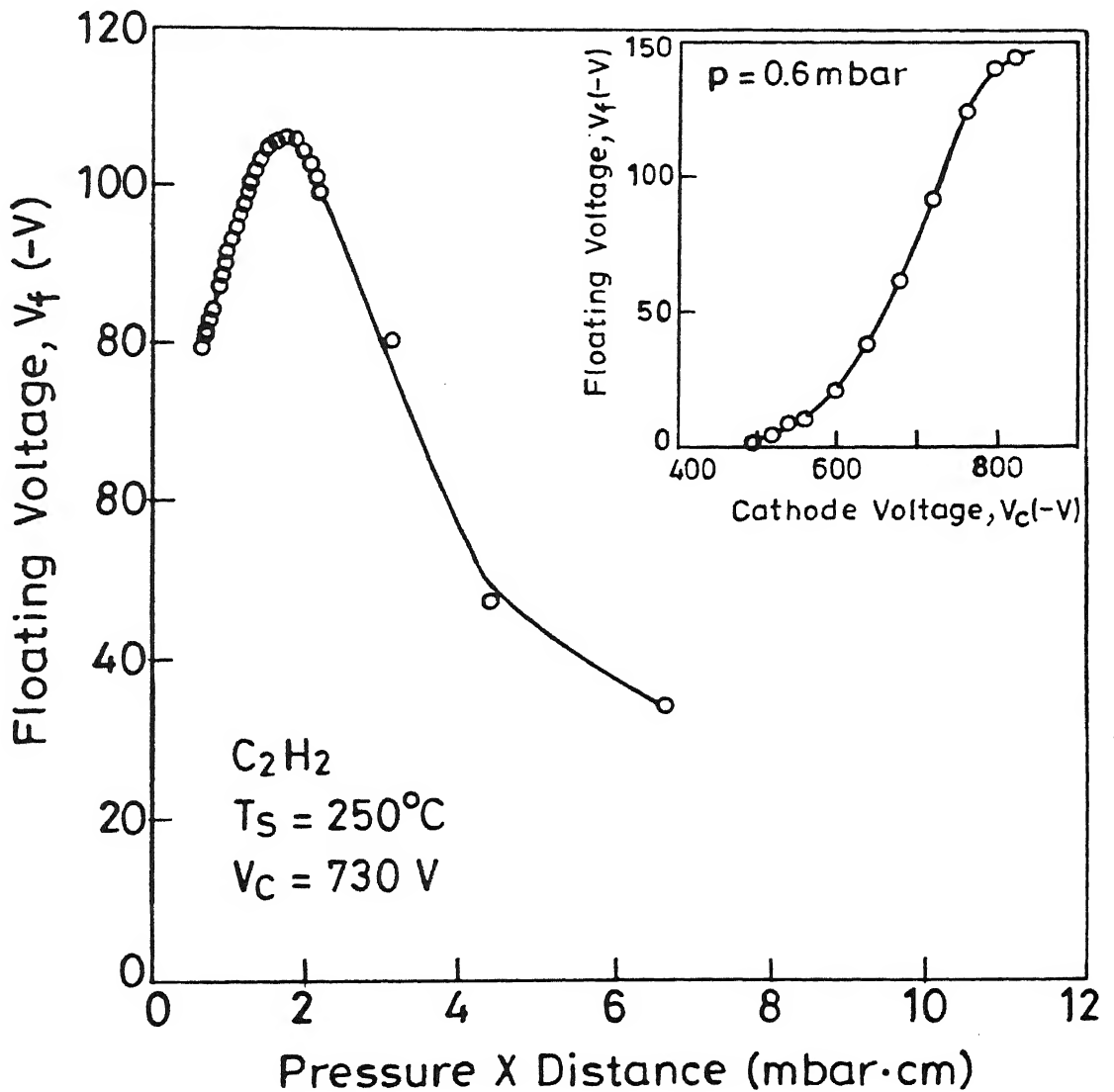


Fig.3.8

Floating voltage ( $V_f$ ) vs p.d. at a fixed cathode voltage of 710V for a  $C_2H_2$  plasma at substrate temperature of  $250^\circ C$ . The inset shows variation of  $V_f$  with applied cathode voltage at a fixed value of p.d.

collisions and are unable to reach the anode. Deposition is normally carried out at cathode voltages ( $V_c$ ) higher than the  $V_{sa}$ . To make a meaningful interpretation of the film properties with ion energies, value of floating potentials are required. Inset in Fig. 3.8 shows the variation in  $V_f$  as a function of applied  $V_c$  at a fixed pressure. Detailed dependence of  $V_f$  on  $V_c$  at various pressures is shown in Fig. 3.9.

An external negative bias on the substrate was applied in order to control the ionic bombardment. It is supposed that the energy of the ions varies in the same way as the applied bias without the perturbations of the plasma induced by the bias. It is to be noted that the correspondence of energy attained by ions to the applied electrode potential is likely to be more in case of dc glow discharge as compared to rf discharge. In rf discharge working at 2.25 Pa, ion energy was found to be  $0.4 eU_B$  where  $U_B$  is the self bias attained by the cathode [123]. We have deposited films on the grounded, floating and negatively biased electrode. The results will be discussed in Chapter V.

Different configurations of electrodes i.e. at top or bottom and their polarities (positive /negative) were employed to study the growth of carbon films in our reactor. The glow discharge plasmas produced may contain ions, radicals and neutral species. No growth on substrates placed on powered electrodes (cathode) was observed. However, occurrence of ion bombardment was found to be necessary for diamondlike properties of the films. It should be mentioned here that in the deposition plasmas, major component is made of neutral stable species (non-reactive molecules) while the fraction of ions and radicals is rather low (about 0.01% and 1% respectively) [229].

### 3.4 MASS SPECTROMETRY OF THE DISCHARGE

There have been some efforts to study the plasma species, primarily using methane to produce DLC and diamond films [219-221]. On the other hand, polymerization from different hydrocarbon monomers has also been studied [222,223]. Radicals like  $C_2H_2$  and  $CH_3$  are proposed to be the main precursors leading to the growth of diamond and DLC films [220, 224-226]. A correlation between  $CH_3$  radical density and carbon film deposition rate was shown using rf discharge of methane [227]. However, not much has been reported on the acetylene plasma species using dc glow discharge.

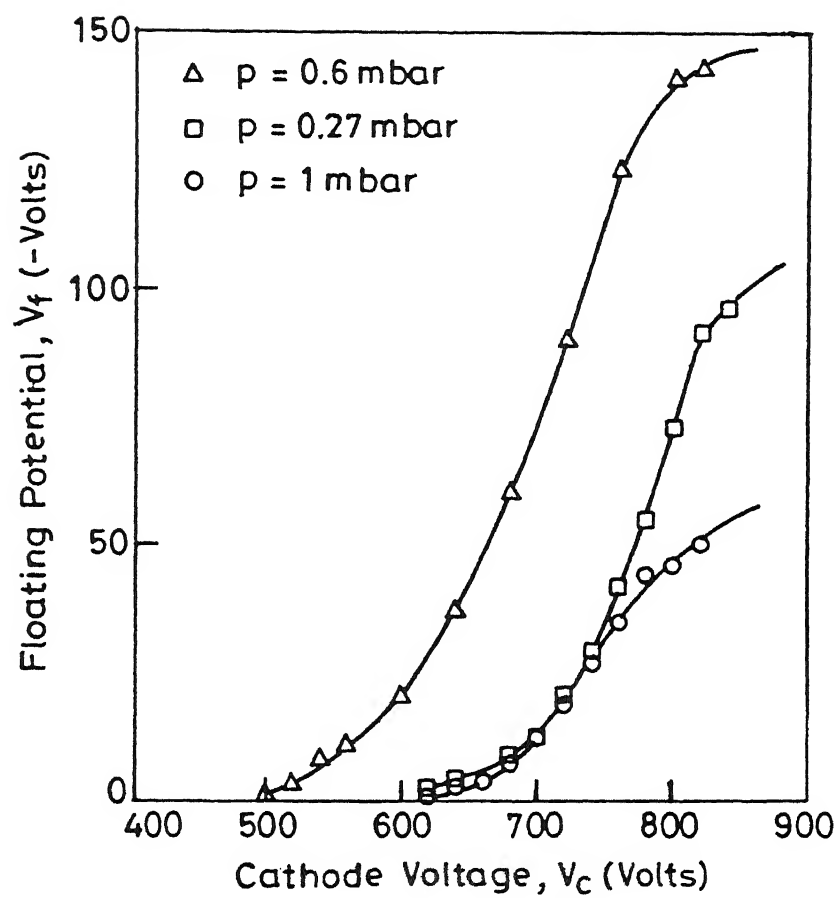


Fig.3.9 Variation of the substrate floating voltage with cathode voltage for dc discharges in  $C_2H_2$  ignited at 0.27 mbar, 0.6 mbar and 1 mbar.

We have used in situ mass spectrometry to analyze the plasma species of dc glow discharge of pure  $C_2H_2$  as well as  $C_2H_2 + H_2$  mixtures. These results will be helpful in understanding film properties to be discussed later. Significant results obtained from this study are presented below:

### ***(a) Effect of Pressure***

The mass spectra recorded during plasma deposition under two different regimes (region A and B of Fig. 3.3) of plasma is shown in Fig. 3.10. Peaks due to atomic and molecular hydrogen are seen indicating hydrogen to be significant byproduct in the plasma decomposition of acetylene.

Relative abundance's of various fragmentation species are observed to be modified by increasing the gas pressure. In particular, ratios of  $H_2/C_2H_2$  and  $C_2H_4/C_2H_2$  are increased by increasing the feedgas pressure in the plasma. Relative abundance of atomic hydrogen ( $H/H_2$ ) is found to be reduced in the region B plasma. It shows that the dissociation of acetylene into higher hydrocarbons and resultant hydrogen is substantially increased in going from region A to region B of plasma conditions. Further, formation of higher mass number species is also evident at higher gas pressure (Fig. 3.10 b). In contrast, at low pressures, the probability of gas phase collisions is low. Thus formation of higher mass number species  $C_xH_y$  ( $x > 2, y > 2$ ) is not favored. The analyses of stable species clearly show the dissociation of the gases at low pressure and increased polymerization at higher pressure.

### ***(b) Effect of Hydrogen Dilution:***

Effect of hydrogen dilution on the fragmentation pattern in the plasma is shown in Fig. 3.11. The relative abundance of higher hydrocarbon species  $C_xH_y$  decreases with hydrogen dilution in acetylene. Thus the effect of hydrogen dilution in the feedgas is to reduce the degree of polymerization in the plasma. Therefore, hydrogen dilution increases the working pressure range without powder formation. In fact, a consistent



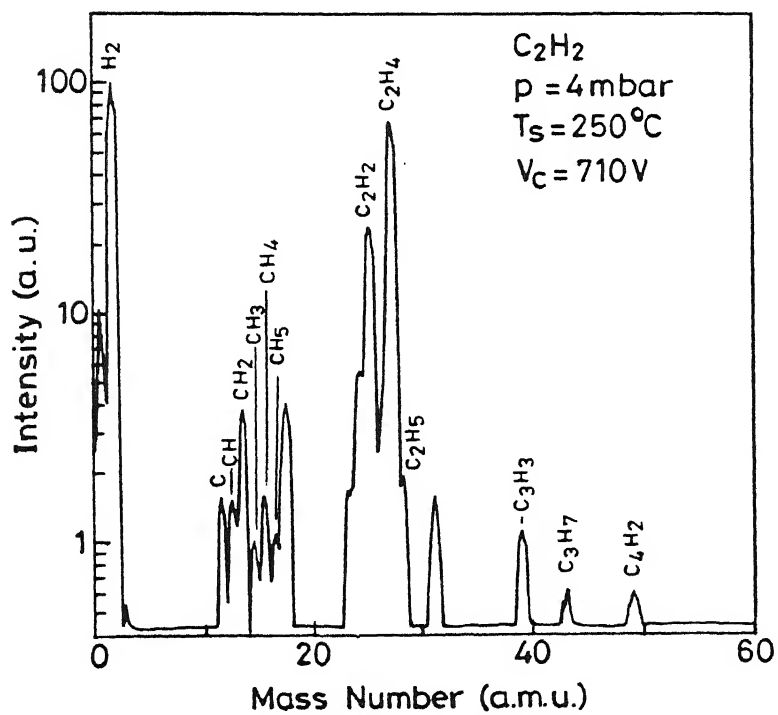
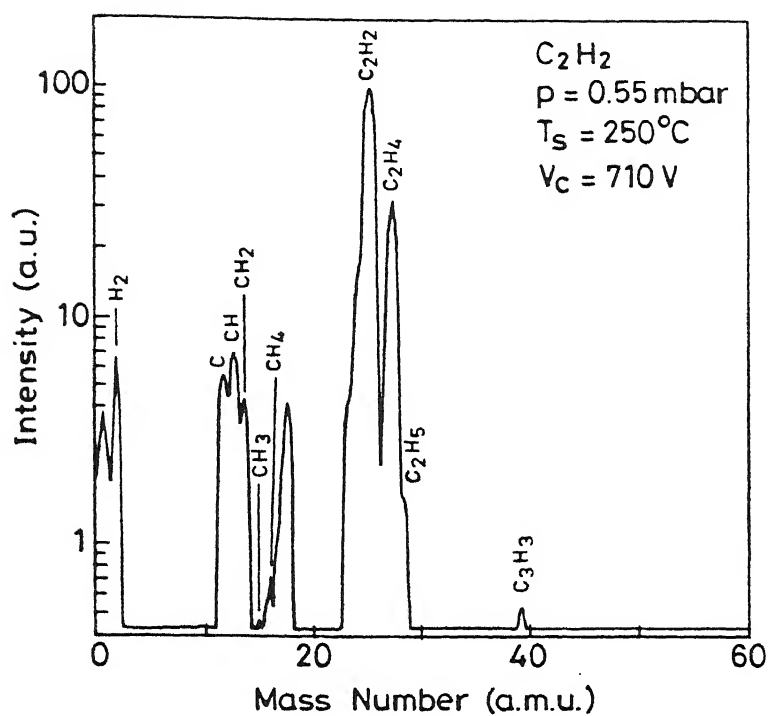


Fig.3.10 Mass spectra of pure acetylene discharge at the gas pressures of: (a) 0.55 mbar (region A), and (b) 4 mbar (region B) of Fig.3.3.

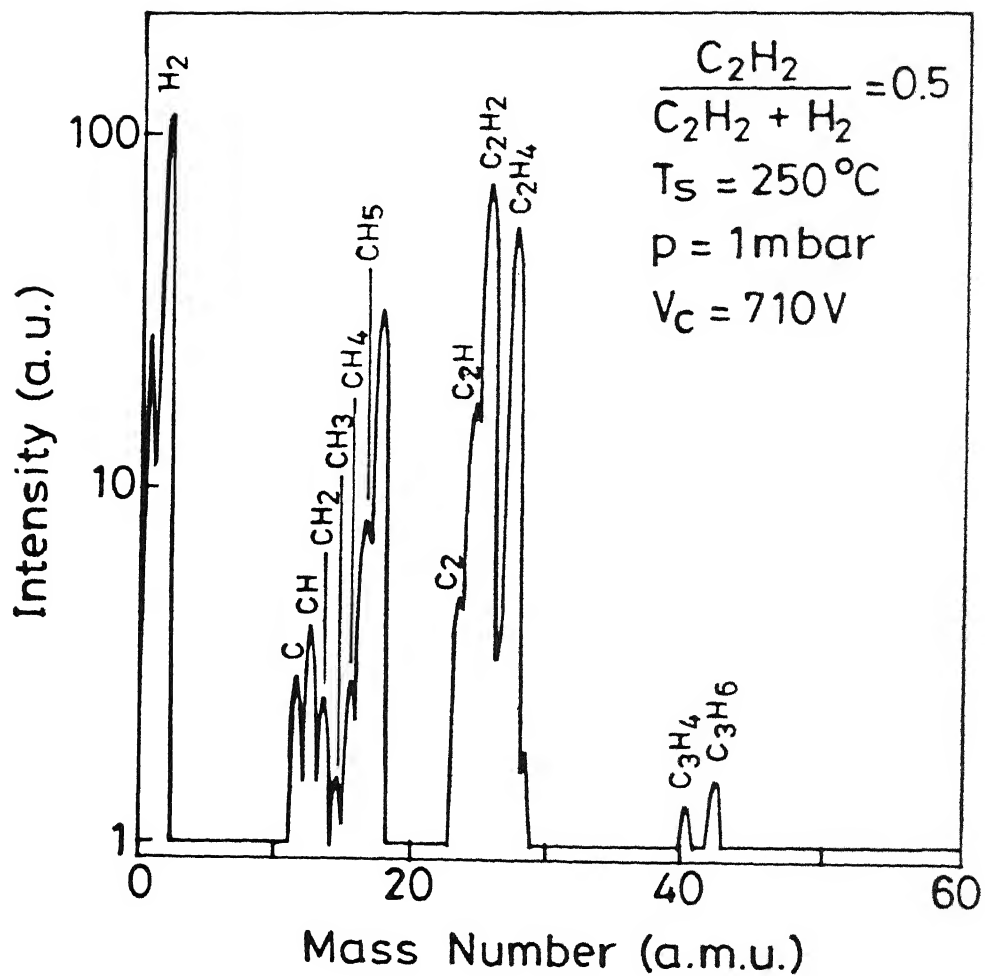


Fig.3.11 Mass spectrum of hydrogen diluted acetylene discharge at a gas pressure of 1.0 mbar.

variation in the byproducts is observed with pressure at a fixed hydrogen dilution. It was observed that the pressure limit at which ratio of  $C_2H_4/C_2H_2$  approaches unity shifts to higher pressures ( $\sim 4$  mbar) with hydrogen dilution (Fig. 3.12) as compared to  $\sim 0.8$  mbar in case of pure acetylene. Clearly, the addition of hydrogen in the feedgas reduces the number of activated gas phase reactions between carbon bearing molecules. It may be pointed out that the molecular hydrogen is seen to be increased in the plasma as a byproduct of polymerization also (Fig. 3.10b), but the effect of hydrogen dilution of the feedgas on the film properties is found to be significantly different (Chapter V). In particular, harder and compact films with low hydrogen content are obtained by increasing the hydrogen dilution.

Further, it should be noted that the effect of hydrogen dilution has an effect on the energy and flux of ions bombarding the substrate (Fig. 3.4). Atomic hydrogen also plays crucial role at the substrate surface during nucleation and growth of films [16].

### *(c) Effect of Applied Cathode Voltage*

Mass spectrometry analysis shows that an increase in dc voltage (from 700 V to 1000V) leads to a decrease in intensity of  $C_2H_2$  signal when the discharge is on as compared to that under discharge off conditions. This indicates an increase in degree of dissociation (dd) of acetylene with the applied voltage. Mass spectrometry analysis shows that the relative partial pressure of  $H_2$  with respect to  $C_2H_2$  in the plasma increases on increasing the applied voltage  $V_c$  (Fig. 3.10). In this way, the increase in  $V_c$  increases dissociation of acetylene molecules. In addition, it changes energy profiles of ions and electrons in the plasma. At higher applied voltage, sparks and spreading of the plasma in regions other than inter-electrode gap were observed and were therefore not applied for depositions.

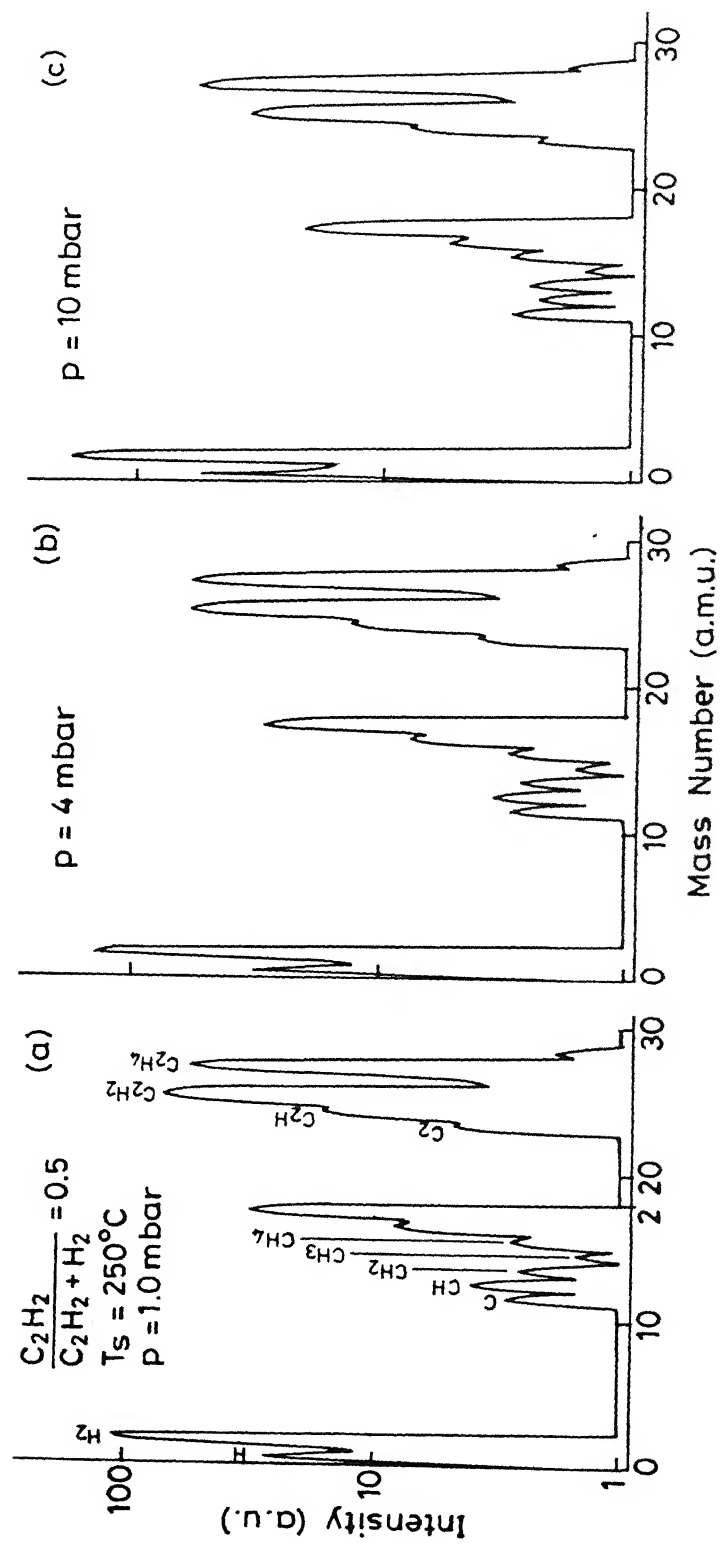


Fig.3.12 Mass spectra of hydrogen diluted acetylene discharge at the gas pressures of (a) 1 mbar, (b) 4 mbar, and (c) 10 mbar.

### 3.5 DISCUSSION AND SUMMARY

Based on the information obtained above and the parameters used in the discharges, we have estimated the plasma and gas parameters relevant for our system. The acetylene discharge reaction and major by-products necessary to understand the growth processes are also summarized.

#### *Density of Discharge Constituents*

$$\text{Gas density: } N = 9.66 \times 10^{18} \left( \frac{P}{T} \right)$$

$$\text{At } p = 1 \text{ Torr, } T = \text{Room Temperature} = 300 \text{ K}$$

$$N = 3.22 \times 10^{16} \text{ cm}^{-3}$$

Electron density: Flux of particles passing to an adjacent wall for a gas of density  $N \text{ (cm}^{-3}\text{)}$  and temperature  $T \text{ (K)}$  is

$$J = \frac{N\bar{v}}{4} = \left( \frac{N}{4} \right) \left( \frac{8kT}{\pi m} \right)^{1/2}$$

For electrons

$$J_e = 1.67 \times 10^7 n_e \sqrt{kT_e \text{ (eV)}} \text{ particles/cm}^2 \cdot \text{sec.}$$

$$= 2.7 \times 10^{-12} n_e \sqrt{kT_e \text{ (eV)}} \text{ mA/cm}^2$$

Consider  $J_e \gg J_i$ ;  $J_i$  is ion current density

$$J_d \cong J_e; J_d \text{ is ion current density}$$

$$\text{For } J_e = 5 \text{ mA/64 cm}^2$$

$$n_e = 9 \times 10^9 \text{ cm}^{-3}$$

$$\text{Ion density: } \approx 10^9 \text{ cm}^{-3} \text{ (order of magnitude)}$$

$$\text{Neutral density: } N - 10^9 = 10^{16} - 10^9 \approx 10^{16} \text{ cm}^{-3} \text{ (order of magnitude)}$$

The Sheath Debye Length ( $\lambda_D$ ):

$$\lambda_D = \epsilon_0 \left( \frac{kT_e}{n_e q^2} \right)^{1/2}$$

$$\text{For } T_e = 10 \text{ eV}$$

$$n_e = 10^9 \text{ cm}^{-3}$$

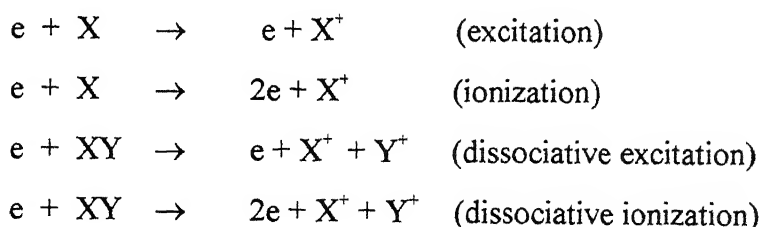
$$\lambda_D = 0.74 \text{ mm}$$

### ***Energy Of Bombarding Ions At Anode:***

This is established by the potential difference between the plasma and the surface on which ions strike. Due to inelastic collisions among ions, they slow down in the sheath region (Fig. 3.6b) near substrate. Therefore ions reach the substrates at all energies from  $e(V_p - V_b)$  to  $eV_p$ . In case of floating potential, the total negative substrate bias is  $-(V_p - V_f)$  and ion energy is  $e(V_p - V_f)$ .

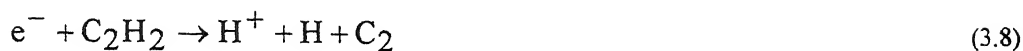
### ***Discharge processes***

At low values of p.d., the voltage distribution in a d.c. diode consists of three regions as shown in Fig. 3.6b: A cathode dark space across which most of the applied voltage is dropped, a low field negative glow that contains approximately equal concentrations of electrons and positive ions, and an anode dark sheath. Within the negative glow, the high energy secondary electrons emitted from cathode interact with the source gas. These electrons transfer their energy to the gas molecules causing their excitation, impact ionization and dissociation of the:



### ***Primary Collision Processes:***

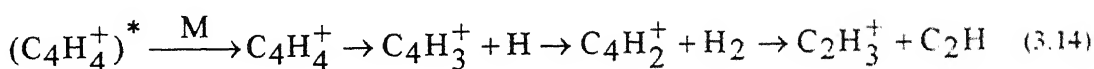
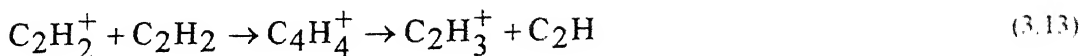
The acetylene molecule is excited to its higher energy states through inelastic collisions with energetic electrons in the plasma. The electron-molecule interaction involves the production of reactive plasma species i.e. radicals, ions, atoms, excited molecules and photons. The main primary collision processes among the electrons and acetylene molecules are as follows [126]:



For lower energy electrons, the neutral dissociation becomes much larger than ionization. As pointed by Turban et al [230], in glow discharges where the active electrons are expected to be in the 8-12 eV range the primary processes should mostly generate radicals. The mass spectra of acetylene discharges show C, CH, CH<sub>2</sub>, CH<sub>3</sub>, CH<sub>4</sub>, C<sub>2</sub>, and C<sub>2</sub>H and C<sub>2</sub>H<sub>2</sub>, as some of the plasma species. The CH<sub>2</sub> concentration is lower because of its lower production rate constant under electron impact. Moreover, the CH<sub>2</sub> radicals are quickly converted to CH through reactions with H atoms. The methyl radical has been proposed to be the growth precursor in our DC glow discharge depositions (see Chapter V). One reasonable reaction pathways for CH<sub>3</sub> production from C<sub>2</sub>H<sub>2</sub> involves the addition of hydrogen to C<sub>2</sub>H<sub>2</sub> through a series of reactions with H and H<sub>2</sub> [231].

### ***Secondary Collision Processes:***

A variety of plasma species are generated by electron impact to C<sub>2</sub>H<sub>2</sub> as described above. The ions and the radicals undergo various secondary reactions mainly with the neutral gas modifying the primary dissociation spectrum. The dominant secondary reactions in an acetylene discharge are following [126,222]:



The mass spectra shows the presence of  $\text{C}_2\text{H}_2$ ,  $\text{C}_2\text{H}_4$ ,  $\text{C}_2\text{H}_5$ ,  $\text{C}_3\text{H}_3$ ,  $\text{C}_3\text{H}_7$  and  $\text{C}_4\text{H}_2$  in high pressure discharges. Since diffusion coefficient is inversely proportional to the density of molecules, lifetime increases as a function of pressure. Hence the probability of secondary reactions is large at high pressures. The secondary reactions lead to the production of higher order hydrocarbons (polymerization) and large size ions and radicals.

As mentioned earlier, we used abnormal glow of discharge in order to obtain uniform processing. In this region, the discharge covers the entire area of electrodes and discharge current density increases with the applied accelerating voltage as shown in Fig. 3.5. We have placed our substrates in negative glow region. Here, substrate picks up a negative potential ( $V_f$ ). Its variation with  $V_c$  and acetylene pressure ( $p$ ) is shown in inset of Fig 3.8. In contrast, high discharge current density ( $\sim \text{A}/\text{cm}^2$ ) dc plasmas have been applied for the deposition of diamond films by a few groups [130,131,232]. As compared to our glow discharge plasma, diamond producing dc plasmas have very different voltage distributions and hence discharge characteristics. Potential in the quasi-neutral region is quite negative with respect to the anode in these high neutral gas density plasmas. They have observed growth of diamond on anode and graphite on cathode. Hydrogenated



amorphous carbon and diamondlike carbon films have been produced using low current dc plasma CVD [36, 134].

In summary, a dc glow discharge system with the flexibility to change and control various deposition parameters has been designed and fabricated. Electrical discharge parameters have been correlated with the reactor geometry to obtain system independent description of the process variables. In-situ mass spectroscopy has been employed to obtain useful information about the decomposition pattern of acetylene source gas. In particular, low pressures and low interelectrode gap spacing are found to be favorable for the growth of hard diamond-like carbon films. Increasing the gas pressure leads to the plasma polymerization which can be reduced by the addition of hydrogen in the feedgas. Interelectrode gap spacing has been optimized to yield maximum deposition rates,

Therefore, a knowledge of total hydrogen content as well as its bonding to carbon is crucial to the understanding of film properties and comparison of samples prepared under a variety of processing conditions in different laboratories. In addition, the information on the release of hydrogen from a-C:H films on heating or irradiation is required for technological applications. Various techniques have been employed to characterize hydrogen in carbon films. However, a quantitative analysis of hydrogen from these techniques still remains controversial [241,242].

In this Chapter, we discuss the characterization of hydrogen in a-C:H films obtained using DC glow discharge decomposition of acetylene. Hydrogen content and bonding in the films were obtained using infrared spectroscopy, ERDA, and mass spectroscopic thermal effusion (MSTE) measurements. These three complementary techniques were employed on the *same* samples to get reliable information on the nature of C-C and C-H bonding. MSTE studies were performed extensively to probe the microstructure of a-C:H films. Exodiffusion kinetics of hydrogen and hydrocarbon molecules from the films were also investigated using MSTE. The activation energies for hydrogen evolution were obtained by the thermal analysis technique and are interpreted in terms of nature of C-C and C-H bonds present in the films. In addition, ERDA depth profiles and annealing experiments were used to investigate the incorporation of hydrogen in the amorphous network and the mechanism of its release. To understand the bonding of H and its effects on the microstructure of films, we present analysis on a few a-C:H films having clearly distinguishable microstructural features. In particular, films prepared under Type A and Type B plasma conditions (referring to figs. 3.3 and 3.4) are chosen. Table 4.1 shows the growth parameters and some physical properties of a-C:H films to be discussed in this chapter. Here, no attempt is made to correlate the deposition conditions with the film properties, which is a subject matter for chapter V.

**Table 4.1** Growth parameters and some of the physical properties of the samples on which hydrogen and microstructural analysis is presented in this chapter.

Sample No. Type	Growth Parameters	Physical Properties	Thickness ( $\mu\text{m}$ )
DLC19 Type A	$p=0.6$ mbar, $T_s=250^\circ\text{C}$ , $V_b=V_f$ , $\text{C}_2\text{H}_2/(\text{C}_2\text{H}_2+\text{H}_2) = 1.0$	$E_g = 2$ eV, $n = 1.9$ , Microhardness = $1600$ kgf/mm <sup>2</sup> $\text{C}_H = 24$ at. %	1.4
DLC18 Type B	$p=4.0$ mbar, $T_s=250^\circ\text{C}$ , $V_b=V_f$ , $\text{C}_2\text{H}_2/(\text{C}_2\text{H}_2+\text{H}_2) = 1.0$	$E_g=2.2$ eV, $n = 1.7$ , Microhardness = $1280$ kgf/mm <sup>2</sup> $\text{C}_H = 33$ at. %	1.6
DLC33/ 49 Type A	$p=0.6$ mbar, $T_s=375^\circ\text{C}$ , $V_b=V_f$ , $\text{C}_2\text{H}_2/(\text{C}_2\text{H}_2+\text{H}_2) = 1.0$	$E_g = 1.8$ eV, $n = 2.2$ , Microhardness = $1780$ kgf/mm <sup>2</sup> $\text{C}_H = 19$ at. %	1.8
DLC51 Type A	$p=0.6$ mbar, $T_s=250^\circ\text{C}$ , $V_b = -250\text{V}$ , $\text{C}_2\text{H}_2/(\text{C}_2\text{H}_2+\text{H}_2) = 0.50$	$E_g = 2.67$ eV , $n = 2.15$ , Microhardness = $2420$ kgf/mm <sup>2</sup> $\text{C}_H = 6$ at. %	1.9
DLC40 Type B	$p=0.6$ mbar, $T_s=250^\circ\text{C}$ , $V_b=V_f$ , $\text{C}_2\text{H}_2/(\text{C}_2\text{H}_2+\text{H}_2) = 0.5$	$E_g = 2.12$ eV, $n=2.1$ , Microhardness = $2100$ kgf/mm <sup>2</sup> $\text{C}_H = 13$ at. %	1.2
DLC53 TYPE B	$p=10.0$ mbar, $T_s=250^\circ\text{C}$ , $V_b=V_f$ , $\text{C}_2\text{H}_2/(\text{C}_2\text{H}_2+\text{H}_2) = 1.0$	$E_g=2.45$ eV, $n = 1.6$ , Microhardness ? (soft) $\text{C}_H = 39$ at. %	1.6

## 4.2 INFRARED SPECTROSCOPY

IR spectra of amorphous networks are determined by the vibrational density of states and optical selection rules. The frequencies of vibrations and charge distribution for a particular bond are mostly affected by the local environment of the bond. The area under the absorption peak is proportional to the number of bonds while width of the peak indicates the environment of a bond. We have used IR absorption spectroscopy to obtain information about the nature of hydrogen bonding in the films. Suitable modifications were incorporated in the analysis to obtain reliable  $\text{sp}^3$  and  $\text{sp}^2$  fraction of C-C bonding. The microstructure and bonding configuration (C-C and C-H bonds) in the films were found to be consistent with the observed changes in microhardness and hydrogen content with deposition parameters.

The complete Fourier transform infrared spectra in the range 4000 to 400  $\text{cm}^{-1}$  on three representative films of comparable thickness ( $\sim 1.5 \mu\text{m}$ ) is shown in Fig. 4.1. Fig. 4.1a represents a DLC sample (DLC51, substrate bias  $V_b = -250 \text{ V}$ , hydrogen diluted acetylene). Fig. 4.1b & c represent plasma conditions of region A (DLC19) and B (DLC18), respectively (Table 4.1). Analysis of the spectra is carried out on the basis of peak assignment available in the literature [54, 243, 244]. Dischler and coworkers [54, 243] have provided the peak assignments corresponding to various bonding configurations in polymeric and hard a-C:H films. Recently, ambiguity in the interpretation of IR spectrum has been further resolved by Bounouh et al [82] by carefully analyzing longer wavelength IR spectra. The analyses of the spectra yield useful information summarized in Table 4.2. The main features to be noted are:

- The H bonding to C gives complex stretching modes in the range 2700-3100  $\text{cm}^{-1}$  corresponding to  $\text{sp}^2$  and  $\text{sp}^3$  bonding in mono-, di- or tri-hydride configurations. In both cases (type A and B films) hydrogen is predominantly bonded in tetrahedral  $\text{sp}^3$  configuration.
- Strong absorption is observed in B type films at  $\sim 3400 \text{ cm}^{-1}$  and  $\sim 1700 \text{ cm}^{-1}$  corresponding to OH and C=O, respectively. These infrared modes are associated with the porous and polymeric nature of films [223, 243]. On the other hand, absence of these bands in the IR spectrum of A type film indicates a compact microstructure.
- The double bonds of  $\text{sp}^2 \text{ C}=\text{C}$  are observed at 1600  $\text{cm}^{-1}$  in B type films only. Curve 4.1c also shows a small absorption around 1280  $\text{cm}^{-1}$  corresponding to olef.  $\text{sp}^2 \text{ CH}$  bonding.
- Absorption around 1380 and 1450  $\text{cm}^{-1}$  is observed in B type sample. 1380  $\text{cm}^{-1}$  peak is ascribed to in-phase and 1450  $\text{cm}^{-1}$  to out-of-phase deformation vibrations of the  $\text{sp}^3 \text{ CH}_3$  groups [82]. Simultaneous presence of the two peaks indicate a relatively higher polymeric content in type B films.

Peak at 1380  $\text{cm}^{-1}$  has been assigned to  $\text{sp}^3 \text{ CH}$  as well as  $\text{sp}^3 \text{ CH}_3$  groups [243,82]. However, sample B also contains substantial fraction of  $\text{CH}_3$  groups observed at 1450  $\text{cm}^{-1}$  ( $\text{sp}^3 \text{ CH}_3$ ) as well as around 2900  $\text{cm}^{-1}$ . Therefore, it is reasonable to assign the 1380  $\text{cm}^{-1}$  band to  $\text{sp}^3 \text{ CH}_3$  bonding in this sample. In type A sample, (Fig. 4.1 (b)), small

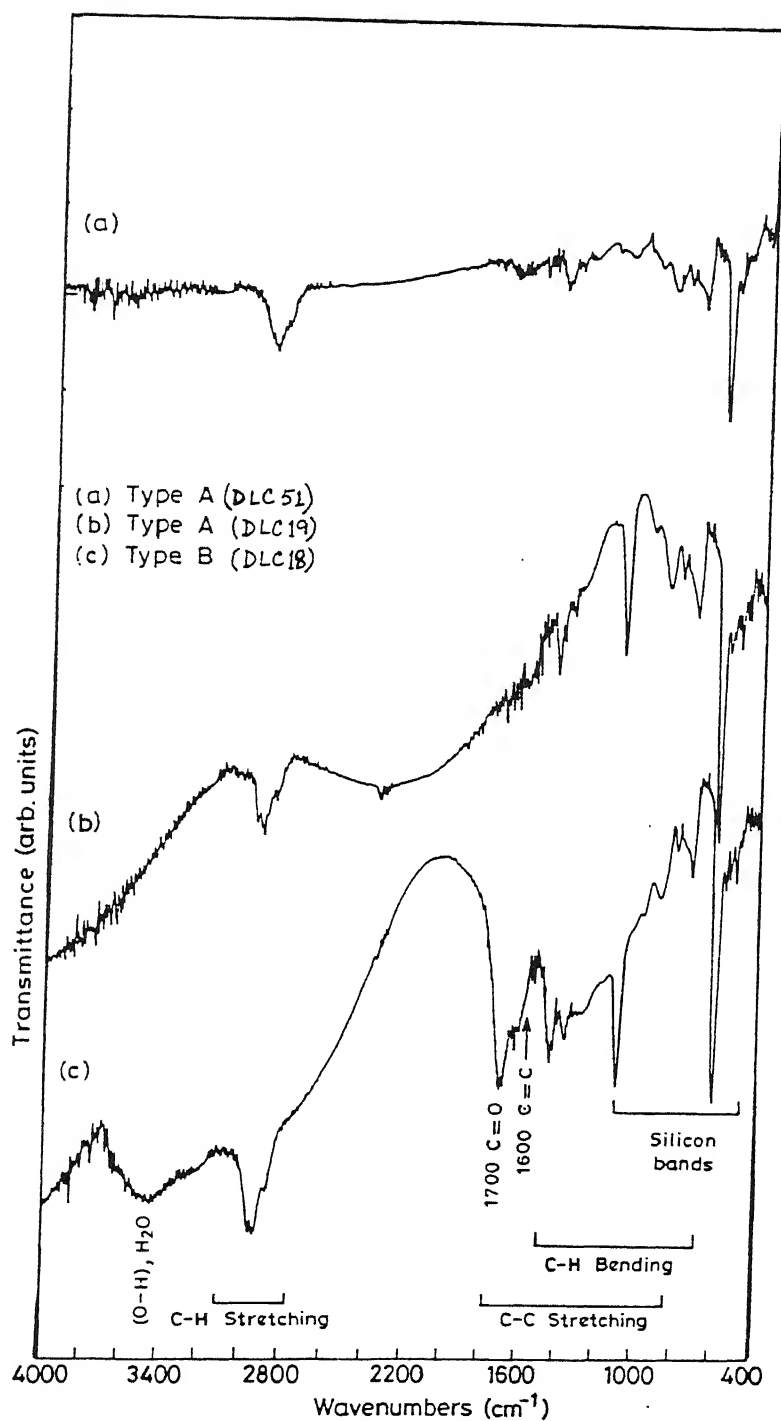


Fig. 4.1 Infrared spectra of a-C:H films deposited at substrate temperature of 250° C and (a)  $p = 0.6$  mbar,  $V_b = 250$  V,  $\text{C}_2\text{H}_2 + \text{H}_2 = 0.5$ ; (Type A); (b) pressure 0.6 mbar, pure  $\text{C}_2\text{H}_2$  (Type A); and (c) pressure 4 mbar, pure  $\text{C}_2\text{H}_2$  (Type B).

**Table 4.2** Peak assignments for various bonding configurations observed in the infrared spectra.

FIG. 4.1 (A) (cm <sup>-1</sup> )	FIG.4.1 (B) (cm <sup>-1</sup> )	FIG. 4.1 (C) (cm <sup>-1</sup> )	ASSIGNMENT (cm <sup>-1</sup> )	BONDING CONFIGURATION
-	-	3400	3300- 3500	O-H-O
-	-	3023	3025	sp <sup>2</sup> CH <sub>2</sub> (olef.)
3003	3000	3004	3000	sp <sup>2</sup> CH (olef.)
2960	2976	2961, 2974	2970	sp <sup>3</sup> CH <sub>3</sub> (asym.)
2936	2946	2951, 2938	2945	sp <sup>2</sup> CH <sub>2</sub> (arom)
-	-	2938	2930	sp <sup>3</sup> CH <sub>3</sub> (asym.)
2924, 2921	2926	2921	2925	sp <sup>3</sup> CH <sub>2</sub> /sp <sup>3</sup> CH (asym.)
2910	-	--	2915	sp <sup>3</sup> CH (asym.)
-	2878	2879	2870	sp <sup>3</sup> CH <sub>3</sub> (sym.)
2851	2854	--	2850	sp <sup>3</sup> CH <sub>2</sub> (sym.)
-	-	1700	1715	C=O
-	-	1600	1600	sp <sup>2</sup> C=C (olef.)
-	-	-	1580	sp <sup>2</sup> C=C (arom.)
	1480	1480	1490	sp <sup>3</sup> CH <sub>3</sub>
	1450	1450	1450	sp <sup>2</sup> CH <sub>2</sub> (olef.)
1445		1440	1440	sp <sup>3</sup> CH <sub>3</sub>
1430			1435	sp <sup>3</sup> CH <sub>2</sub> (olef.)
				sp <sup>2</sup> CH (arom.)
1370	1380	1380	1370	sp <sup>3</sup> CH
			1380	sp <sup>3</sup> CH <sub>3</sub>
	-	1280	1270	mixed sp <sup>2</sup> /sp <sup>3</sup> C-C
			1280	sp <sup>2</sup> CH (olef.)
1110	1100	1100	1110	sp <sup>2</sup> CH <sub>2</sub> (olef.)
			1125-1010	Si-O-Si
970	975	975	970	sp <sup>2</sup> C-C (olef.)
				out of plane C-H bending (olef.)
895	885	885	885	sp <sup>3</sup> C-C (olef.)
-	820	820	800-845	wag Si-H
840			840	sp <sup>2</sup> C=C (arom.)
				sp <sup>3</sup> C-H (olef.)
-	-	-	810	out of plane C-H bending
745	745	745	755	sp <sup>2</sup> C-H (arom.)
620	620	620	630	Si-H (wag)

absorption peak at  $1450\text{ cm}^{-1}$  is observed along with the  $1480\text{ cm}^{-1}$  peak. The  $1450\text{ cm}^{-1}$  peak can be ascribed to the  $\text{sp}^3\text{CH}_3$  vibration mode. The  $1380\text{ cm}^{-1}$  peak could also include some contribution from  $\text{sp}^3\text{CH}$  bending modes [243]. Figure 4.1a shows IR spectrum of another representative Type A sample (DLC 51) characterized as ta-C:H. The intensity of  $\text{sp}^3\text{CH}_3$  further decreases in this sample as is evident from Table 4.2.

In contrast to the low-wavenumber region, where the assignment of different features is difficult due to overlap of various C-H, C-C and silicon bands, the assignment of the high-wavenumber stretching modes are well established. However, some ambiguity exists in identifying the nearby peaks. Care needs to be taken for the assignments of such peaks and for estimating their respective contributions. In case of a slight shift of peak positions, the nearby absorption bands may overlap. For example,  $2950\text{ cm}^{-1}$  ( $\text{sp}^2\text{CH}_2$  Olefinic) and  $2960\text{ cm}^{-1}$  ( $\text{sp}^3\text{CH}_3$ ) bands are often difficult to assign uniquely. In general, the peak at  $2950\text{ cm}^{-1}$  appears as a conjugate of  $3025\text{ cm}^{-1}$  peak in case of polymeric films. The other conjugate pairs are observed at  $2850$  and  $2920\text{ cm}^{-1}$ , as well as  $2960$  and  $2870\text{ cm}^{-1}$ . These may be present in both type of films. Normally, the intensity ratio of  $2850\text{ cm}^{-1}$  to  $2920\text{ cm}^{-1}$  is found to be  $3/5$  [246]. Both of these peaks are assigned to  $\text{sp}^3\text{CH}_2$ . The excess intensity of  $2920\text{ cm}^{-1}$  peak in DLC films then may be ascribed to the  $\text{sp}^3\text{CH}$  (asym.) vibrational modes. Further, it was observed in a large number of samples that the shift in frequency of  $2920\text{ cm}^{-1}$  peak indicates the change in possible C-H configurations. Upward shift to  $2930\text{ cm}^{-1}$  ( $\text{sp}^3\text{CH}_3$ ) is usually associated with the polymeric nature of the films. On the other hand, a downward shift to  $2910\text{ cm}^{-1}$  ( $\text{sp}^3\text{CH}$ ) indicates the diamondlike character. In addition, contribution from the stretching vibrations of  $\text{C-H}_x$  groups gives a clue to the other possible configurations in bending modes. For example, the peak at  $1385\text{ cm}^{-1}$  in A type film may also include some contribution from aromatic  $\text{sp}^3\text{CH}$  bending modes in our case.

In order to obtain quantitative information, infrared transmission data was converted to the absorption coefficient ( $\alpha$ ) using measured film thickness and standard optical analysis as described in Chapter II (section 2.3.1). Figure 4.2 shows the IR absorption coefficient as a function of wavenumber in the range  $2800\text{--}3100\text{ cm}^{-1}$  measured on DLC19 and DLC18 along with that of DLC51. As discussed above, this spectrum range corresponds to the stretching vibrational modes of  $\text{C-H}_x$  complexes. The

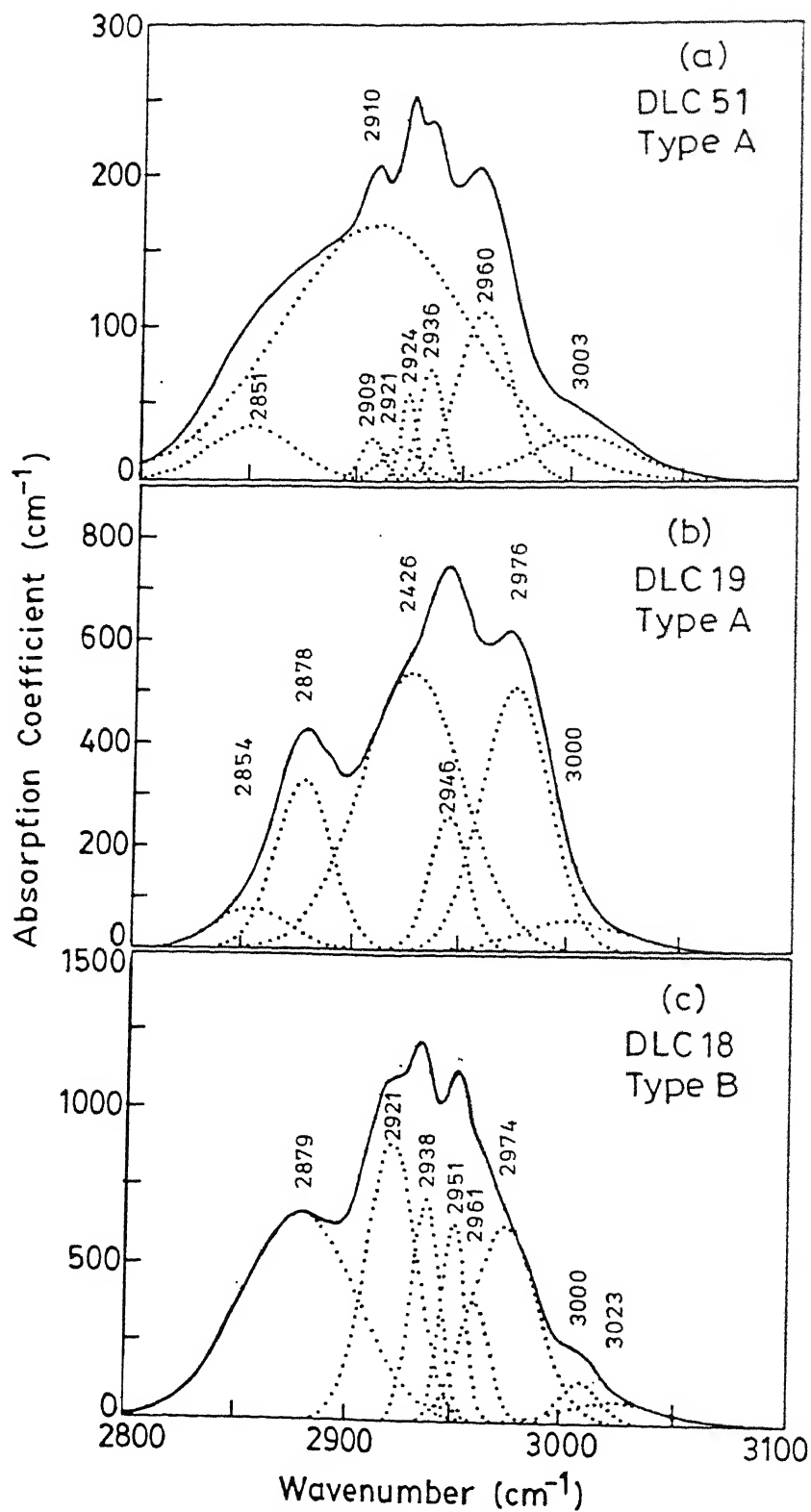


Fig.4.2 Deconvolution of the infrared stretching band of a-C:H films from the spectra in Fig.4.1.



experimental data was fitted using gaussian peaks after background correction [188, 247]. Peak positions correspond to wavenumbers at 2854, 2878, 2926, 2946, 2976, and 3000  $\text{cm}^{-1}$  for DLC19 (Fig. 4.2 b). These are assigned to  $\text{sp}^3 \text{CH}_2$  (sym),  $\text{sp}^3 \text{CH}_3$  (sym),  $\text{sp}^3 \text{CH}_2/\text{CH}_1$  (asym.),  $\text{sp}^2 \text{CH}_2$ ,  $\text{sp}^3 \text{CH}_3$  (asym.), and  $\text{sp}^2 \text{CH}$  (olef) bonding, respectively. There is large contribution from peaks due to  $\text{sp}^3 \text{CH}_2$  and CH type of bonding. The presence of  $\text{sp}^2 \text{CH}$  bonding is also a characteristic of DLC film [45,245,248]. This indicates that the stretching band in this case is dominated by contributions from  $\text{CH}_2$  and CH groups. The sample DLC 51 contains relatively broader peaks around 2850, 2910 and 3000  $\text{cm}^{-1}$  (due to  $\text{CH}_2$  and CH type of bonding) which are characteristic of a hard DLC film.

Relatively sharp absorption peaks are seen in the deconvoluted spectrum of the polymerlike film (Fig. 4.2c) indicating a material with lower internal strain. Vibrational modes at 2870 and 2970  $\text{cm}^{-1}$  correspond to  $\text{sp}^3 \text{CH}_3$ . However, their intensities are higher showing larger concentrations in the films as compared to DLC. Also, there are peaks at wavenumbers 2945 and 3025  $\text{cm}^{-1}$  which are due to  $\text{sp}^2 \text{CH}_2$  bonding, a characteristic of polymeric structure. It is clear that both stretching and bending bands are dominated by  $\text{sp}^3 \text{CH}_3$  and  $\text{sp}^2 \text{CH}_2$  groups in polymeric carbon film.  $\text{CH}_3$  complex is normally a bond terminator and its abundance leads to the enhanced void structure in the films. The  $\text{sp}^2 \text{CH}_2$  bonding should constitute the polymeric chain like component. On the other hand, a higher percentage of C-C cross-linking is indicated by a microstructure having more of  $\text{sp}^3 \text{CH}$  bonding as compared to  $\text{sp}^3 \text{CH}_3$  and  $\text{sp}^3 \text{CH}_2$  in DLC film along with small presence of  $\text{sp}^2 \text{CH}$  bonding. Small contribution from trigonal bonding helps in relieving internal strain associated with the tetrahedral bonding. The non-occurrence of aromatic groups in DLC samples is consistent with the recent theoretical prediction of free energy model of Akkerman[37].

#### 4.2.1 $\text{Sp}^3/\text{Sp}^2$ Ratio

Normally the ratio of integrated intensities under various peaks is taken as the concentrations of particular bonding configurations [54, 245]. This method is

based upon the assumption that the bond strength is same for all vibrating groups. The relationships used to determine  $sp^3/sp^2$  and  $sp^1/sp^3$  ratios are.

$$\frac{sp^3}{sp^2} = \frac{(sp^3CH + sp^3CH_2 + sp^3CH_3)}{(sp^2CH + sp^2CH_2)} \quad (4.1)$$

and

$$\frac{sp^1}{sp^3} = \frac{sp^1CH}{(sp^3CH + sp^3CH_2 + sp^3CH_3)} \quad (4.2)$$

This analysis yields about 90% of total hydrogen bonded in  $sp^3$  configuration in the sample number in DLC51, 87% in DLC19 and 84% in case of DLC18. Often this fraction is directly linked to the  $sp^3/sp^2$  hybridization ratio.

The above estimates of  $sp^3/sp^2$  ratio assumes the hydrogen atoms to have no preferential bonding to any particular C hybridization. In addition, IR detects the hybridization of those carbon atoms only which are attached to at least one H atom. This condition may be met by so called polymeric films having large hydrogen content, but will be far from reality in the case of highly tetrahedrally bonded diamondlike carbon films. Further, a constant transition dipole moment is assumed for vibrational stretching bands. Dipole moments depend on the structural environment and may change with film microstructure. Therefore, doubts have been raised about the validity of such approach to predict  $sp^3/sp^2$  C-C bonding ratios [241]. Grill and Patel used the power of high resolution NMR spectroscopy to provide the carbon coordination and showed the  $sp^3/sp^2$  ratio obtained from IR and NMR to be inconsistent [241]. Hence, the conventional procedure using equation (4.1) yields the ratio of  $sp^3/sp^2$  for C-H bonds only.

Jacob and Moller carried out a comprehensive analysis of IR, NMR, Ion Beam Analysis (IBA) and Electron Energy Loss Spectroscopy (EELS) data from about 20 published reports [242]. By making only single assumption of  $sp^1$  fraction to be negligible, they were able to correlate almost all published data on a ternary phase diagram composed of three phases:  $sp^3$  carbon,  $sp^2$  carbon and hydrogen. This analysis shows that about two thirds of the  $sp^2$  carbon is unhydrogenated and therefore, invisible to IR. However, most of the  $sp^3$  carbon has at least one hydrogen atom attached to it. Recent theoretical modeling has also predicted upto 80% of the  $sp^3$  C atoms to be hydrogenated for an a-

C<sub>0.6</sub> H<sub>0.4</sub> alloy [37]. The corrected  $sp^3$  and  $sp^2$  fractions,  $sp^{3*}$  and  $sp^{2*}$  are calculated using [242]:

$$sp^{2*} = \frac{(sp^2 + sp^3)}{(1 + (sp^3 / 3 sp^2))} \quad (4.3)$$

and

$$sp^{3*} = 1 - H - sp^{2*} \quad (4.4)$$

Here  $sp^2$  and  $sp^3$  are fractions obtained using conventional analysis. H represent the fraction of hydrogen atoms present in the films. We obtained  $sp^{3*}/sp^{2*}$  ratios for our samples with this correction procedure. It may be pointed out that the assumption of negligible  $sp^1$  fraction is valid on all our samples as we did not find IR absorption peak around  $\sim 3300 \text{ cm}^{-1}$  associated with this configuration in none of our samples. Results on samples having diamondlike and polymer-like nature are shown in Table 4.3. Figure 4.3 shows our results on DLC samples plotted on the ternary phase diagram of Jacob and Moller. The  $sp^{3*}$  and  $sp^{2*}$  fractions estimated from this analysis match with the physical properties (hardness, optical and electrical behavior) measured on a large number of samples and hence strongly support this correction procedure. Recent results of  $sp^3$  fractions obtained by EELS on ta-C:H deposited films by MSIB [27] are also shown in Fig. 4.3. Evidently, dc glow discharge deposited samples show lower hydrogen content and high  $sp^3$  C-C fraction as compared to usual glow discharge deposited a-C:H films.

**Table 4.3** *Microstructural and physical properties of a-C:H films.  $Sp^3$  and  $sp^2$  are hybridization fractions calculated from the conventional analysis of IR data.  $Sp^{3*}$  and  $sp^{2*}$  are fractions of C-C bonds bonded in  $sp^3$  and  $sp^2$  hybridization, respectively. Percentages of CH, CH<sub>2</sub> and CH<sub>3</sub> are from the bonded hydrogen content ( $C_H$ ).*

Sample No.	$sp^3$	$sp^2$	$sp^{3*}$	$sp^{2*}$	CH <sub>3</sub> (%)	CH <sub>2</sub> (%)	CH (%)	C <sub>H</sub> (%)	E <sub>g</sub> (eV)	n	μHardness (Kgf/mm <sup>2</sup> )
DLC18	0.89	0.11	0.42	0.25	62	25	13	33	2.2	1.7	1280
DLC19	0.83	0.17	0.55	0.21	47	28	25	24	2.0	1.9	1600
DLC33	0.86	0.14	0.54	0.27	53	13	34	19	1.8	2.2	1780
DLC40	0.88	0.12	0.62	0.25	29	25	46	13	2.12	2.1	2100
DLC51	0.90	0.10	0.71	0.23	13	11	76	6	2.67	2.15	2420
DLC53	0.90	0.10	0.46	0.15	71	24	5	39	2.45	1.6	soft

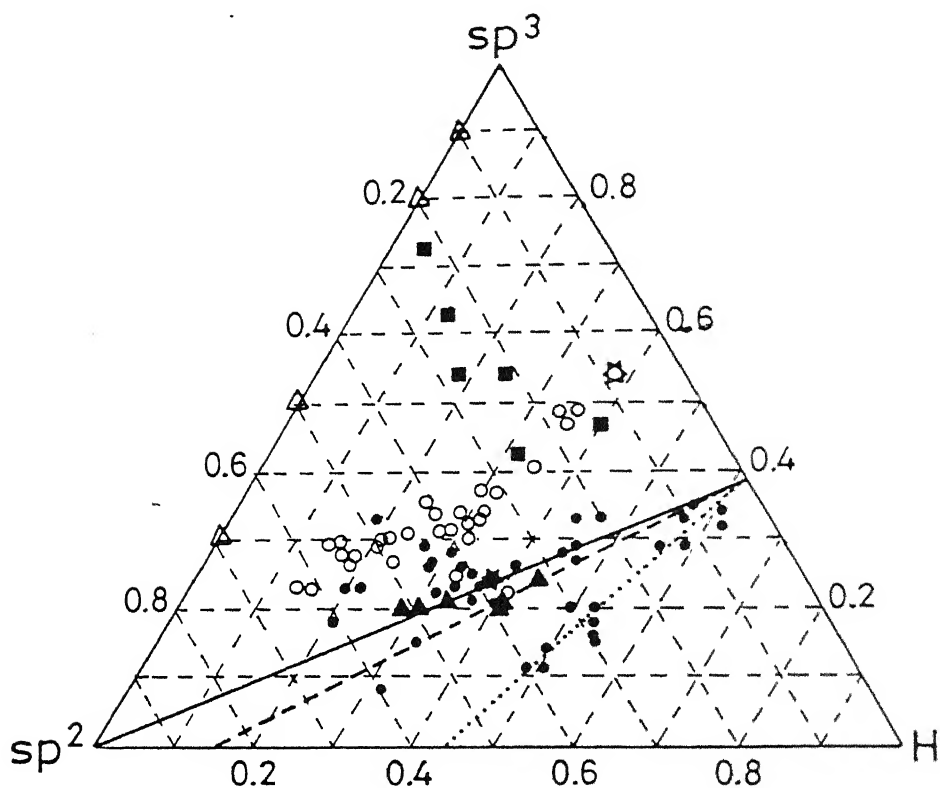


Fig. 4.3: Ternary phase diagram for hydrocarbon films. Open circles are published IR data corrected by Jacob and Moller using equation 4.3. Full squares represent the IR data of the present work corrected by the same procedure. Full circles are NMR data and full triangles are EELS data. The data of Grill et al. (241) are shown as full and open stars. Results obtained by EELS on ta-C:H deposited films by MSIB (27) are also shown by open triangles.

Recently, De Martino et al have suggested further refinement in the above approach [249]. It was pointed out that the assumption of bond strengths to be same for all vibrating groups may not be valid if local surroundings affect bond energy and strength. Hence, knowledge of local bonding environment as well as hydrogen content of the film is needed to estimate the ratio of  $sp^3$  to  $sp^2$  C-C bonds. Then, the amount of  $sp^{3*}$  hybridized hydrogenated carbon atoms is given by:

$$sp^{3*} = \left\{ H - \frac{1 + 2(sp^2CH_2 / sp^2CH)}{sp^3 / sp^2(1 + sp^2CH_2 / sp^2CH)} sp^3 \right\} \quad (4.5)$$

$$\left\{ \frac{1 + sp^3CH / sp^3CH_2 + sp^3CH_3 / sp^3CH_2}{2 + sp^3CH / sp^3CH_2 + 3sp^3CH_3 / sp^3CH_2} \right\}$$

$sp^{3*}$  and  $sp^{2*}$  fraction of  $\sim 0.13$  and  $0.3$  were obtained for the sample DLC18. In this model the basic idea of considering the local environment is justified, but, the methodology to identify the microstructure *a priori* makes the whole procedure unusable.

#### 4.2.2 Hydrogen Content

The C-H stretching absorption band around  $2900 \text{ cm}^{-1}$  in the IR spectrum is used to determine the number of C-H bonds and thus the bonded hydrogen content in a-C:H films. The number of H atoms ( $N_H$ ) contributing to the stretching absorption band is calculated from the integrated absorption under the  $\alpha$  versus wavenumber ( $2700 - 3100 \text{ cm}^{-1}$ ) curve for stretching modes using [188]:

$$N_H = A_s \int \frac{\alpha(\omega)d\omega}{\omega} \quad (4.6)$$

Where  $A_s$  is a constant multiplier which depends on the oscillator strength of C-H bonds in the stretching modes region [243, 250]. Integration is performed over the stretching band region. Atomic percentage of hydrogen can now be calculated as:

$$C_H (\text{at.}\%) = [H] / ([H] + [C]) \quad (4.7)$$

The area under the stretching modes in equation (4.6) can be obtained to a high accuracy. However, problems are encountered in estimating total hydrogen content

using equations (4.6) and (4.7). In particular, errors arise due to two factors: the value of  $A_s$  and the film density ( $[H]+[C]$ ). It is obvious that taking a constant film density is inappropriate for samples produced under a variety of growth conditions and having different microstructures. This problem has been reduced by using measured film densities for individual films or their proper estimates. More serious concern is due to the fixed value of  $A_s$ . Oscillator strengths for C-H bonds in various bonding configurations and solid environments are not known. Many values have been used in the literature. Fujimoto et al give  $A_s = 1 \times 10^{21} \text{ cm}^{-2}$  [250]. Watanabe et al have used a value of  $6 \times 10^{20} \text{ cm}^{-2}$  [84] while Basa and Smith suggested  $1.35 \times 10^{21} \text{ cm}^{-2}$  [251]. Couderc and Catherine used a slightly different approach to evaluate hydrogen content from integrated area under the IR stretching modes [46].

Fujimoto et al have obtained the value of  $A_s$  by empirical comparison of IR integrated area to the hydrogen content measured by nuclear reaction technique for over 25 samples having different microstructures. Ion beam analysis of hydrogen may also lead to erroneous estimates of hydrogen content due to the ion induced out diffusion of hydrogen (to be discussed further in next section). These authors have taken the dose dependence into account and hence the empirical value of the constant multiplier  $A_s$  is more reliable. Consistent with this approach, we have used a value of  $A_s = 1.0 \times 10^{21} \text{ cm}^{-2}$  for hydrogen content determination. Hydrogen content was estimated from  $N_H$  for known film densities. We expect our quantitative results to be accurate to within  $\pm 10\%$ . It may be pointed out that a similar approach in case of a-Si:H has been found to be more acceptable [252] and has been widely used to obtain hydrogen content in those films.

### 4.3 ELASTIC RECOIL DETECTION ANALYSIS

Direct methods to characterize hydrogen include neutron scattering, resonance nuclear reactions, and elastic recoil detection analysis. ERDA has emerged as an important tool to characterize light elements such as hydrogen in heavy atom matrices [194, 253-255]. This technique utilizes high energy ion irradiation to measure hydrogen content. We have used 1.5 MeV  $\text{He}^+$  ions at the Van de Graaff facility in our

department [194]. Details of the measurement and analysis procedure have been described in Chapter II.

ERDA spectra measured on a typical a-C:H film (DLC33, Table 4.1) are presented in fig. 4.4. The two hydrogen recoil spectra shown here are recorded with  $\text{He}^+$  integrated charge of 5  $\mu\text{C}$  and 35  $\mu\text{C}$ , respectively, at a beam current density of 1  $\text{nA}/\text{mm}^2$ . Spot size of irradiation was  $\sim 0.035\text{cm}^2$ . The recoiled hydrogen yield is normalized for an incident charge of 1  $\mu\text{C}/\text{mSr}$  for the sake of direct comparison. Statistical RUMP simulation [187] is used for the determination of hydrogen content. Stopping powers and cross sections under the measurement geometry and conditions have been calibrated on KDP crystals separately [200]. These results have been used in the present analysis. Solid lines in figure 4.4 correspond to the simulated hydrogen depth profiles. Surface position of hydrogen is indicated by an arrow in the figure. Small shift from the surface is indicative of the depth resolution of the system which is estimated to be  $\sim 20\text{nm}$ . A good agreement is obtained with the experimental data by proper simulation of hydrogen depth profiles.

It is interesting to note that an enhanced concentration of hydrogen is required at the surface of the film, as compared to the bulk, to reproduce measured yield. The depth profiles are found to be dependent on the microstructure of the samples and their thermal history. Therefore, it is not an artifact in the simulation but is a reminiscence of the growth of samples. Non-uniform depth profiles have been earlier observed [82]. In addition, it is clear from the figure that the hydrogen content in the film has decreased after continued  $\text{He}^+$  irradiation. Hydrogen depth profile is also modified with further enhancement of the surface hydrogen peak.

In fact, after making the initial measurements of hydrogen recoil yield at low dose,  $\text{He}$  ion irradiation was continued. The effect of cumulative dose on the simulated total bulk hydrogen content is included in the inset of fig. 4.4. Results presented here were reproduced at different spots on the same sample using higher beam current densities upto 6  $\text{nA}/\text{mm}^2$ .

Hydrogen contents in a-C:H films have been widely measured using various ion species ( $\text{He}^+$ ,  $\text{Fe}^+$ ,  $\text{Ar}^+$ ,  $\text{Au}^+$ ,  $\text{N}^+$ ,  $\text{Ni}^+$ ,  $\text{O}^+$  etc.) and ion energies from 15 keV to  $\sim 85$  MeV [82, 256-265]. Concentrations in the range of 10 to 60 at.% have been obtained on a

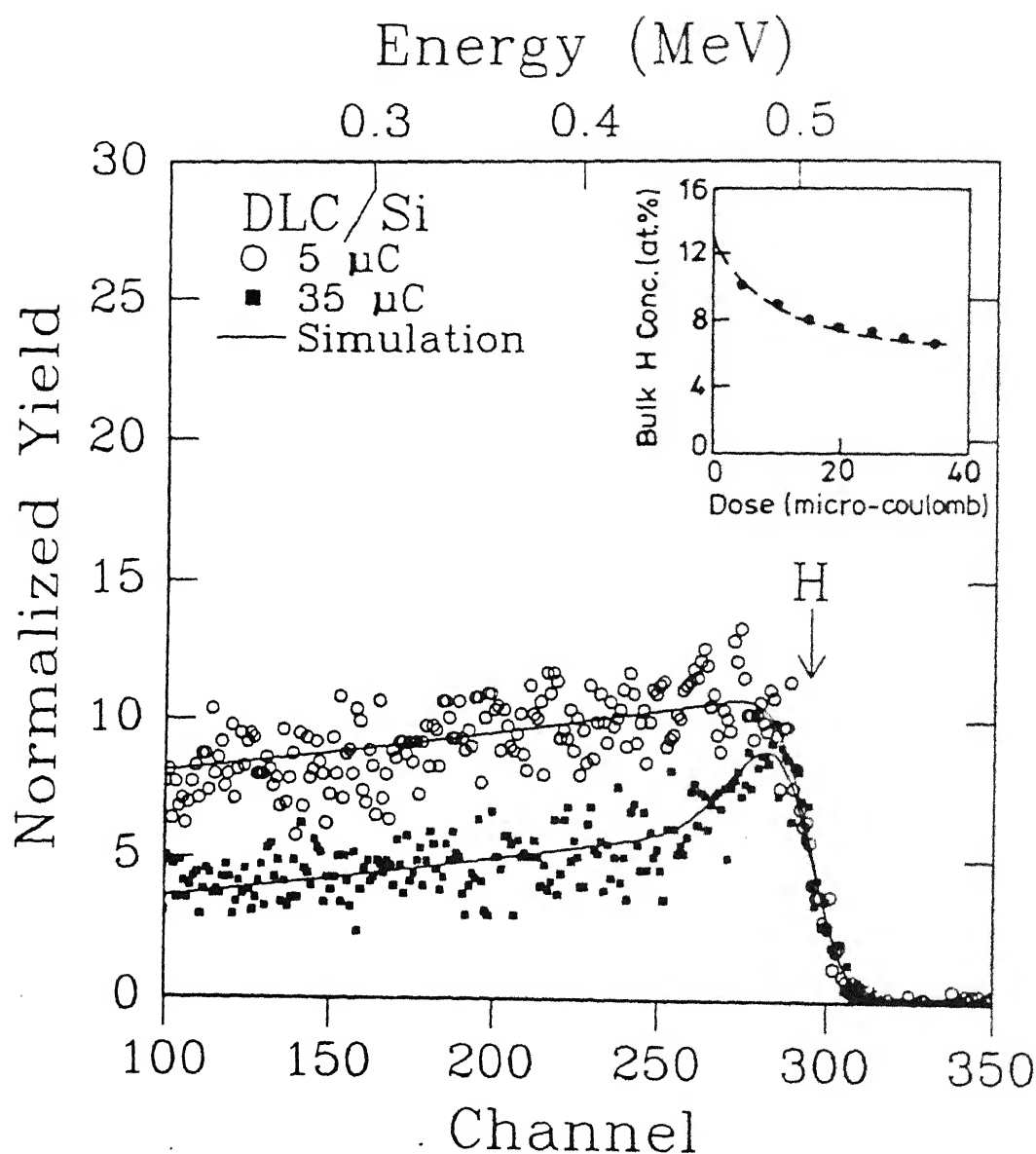


Fig.4.4 1.5 MeV  $\text{He}^+$  induced recoil spectra of hydrogen from a DLC film deposited on silicon substrate at  $T_s=375^\circ\text{C}$  using pure acetylene. The surface position of H is indicated by arrow. The spectra were taken for  $\text{He}^+$  integrated charge of 5  $\mu\text{C}$  and 35  $\mu\text{C}$ . They are normalized for an incident charge of 1  $\mu\text{C}/\text{mSr}$  for the sake of direct comparison. The inset shows the variation of the average bulk hydrogen concentration as a function of integrated  $\text{He}^+$  charge.



variety of a-C:H films prepared by different methods. Release of hydrogen by ion irradiation has been reported by various authors [262a&b, 263]. In contrast, Boutard et al. [234, 264] found no measurable depletion of hydrogen from hard carbonized films under 2.6 MeV He<sup>+</sup> bombardment upto a dose of  $2 \times 10^{16}$  ions/cm<sup>2</sup>. Similar results were reported by Baumann et al [264b]. There are also many reports that do not mention anything about hydrogen loss and show ERDA data at some fixed fluences [43, 82, 245, 255].

Evidently, caution has to be exercised while estimating hydrogen content ( $C_H$ ) of a-C:H films using ion beam techniques. Using the data in fig. 4.4 (inset), an extrapolation of bulk  $C_H$  to zero fluence yields a value of  $\sim 13$  at.% for this sample. Errors on the values of  $C_H$  are estimated to be  $\sim 10\%$  by taking into account various uncertainties such as helium and hydrogen stopping powers in DLC and other parameters used in the simulation [186].

While ion induced migration of hydrogen is detrimental to a quick evaluation of  $C_H$  from ERDA data, it must have a correlation with the microstructure and hydrogen distribution in the films. To probe this dependence, we have carried out ERDA on several samples of known physical properties. Fig. 4.5 shows the ERDA spectra obtained on two samples (DLC51 and DLC18) at the same cumulative ion dose of  $5 \mu\text{C}$ . It may be recalled from IR analysis and optical properties (Table 4.1) that DLC18 can clearly be classified as soft polymeric film while DLC51 is a hard DLC. Normalized yields from the two samples show significant differences in the total hydrogen content as well as hydrogen depth profiles. In particular, yield from DLC51 shows a uniform hydrogen depth profile. This is a typical behavior obtained on compact films having a low hydrogen content. In general, softer films showed a larger hydrogen content towards the surface as compared to the bulk. Influence of ion dose on the recoiled hydrogen yield was measured and data was simulated to yield  $C_H$ . Results are shown in Fig. 4.6. Data for DLC33, a sample having diamondlike properties (same as fig 4.4) is also included for comparison. It shows that large uncertainties can arise on the hydrogen content estimates of soft films due to heavy ion induced migration of hydrogen. In contrast, sample DLC51 shows a uniform hydrogen content. A low hydrogen content of this sample is evident from ERDA ( $\sim 3$  at.%) as well as infrared studies.

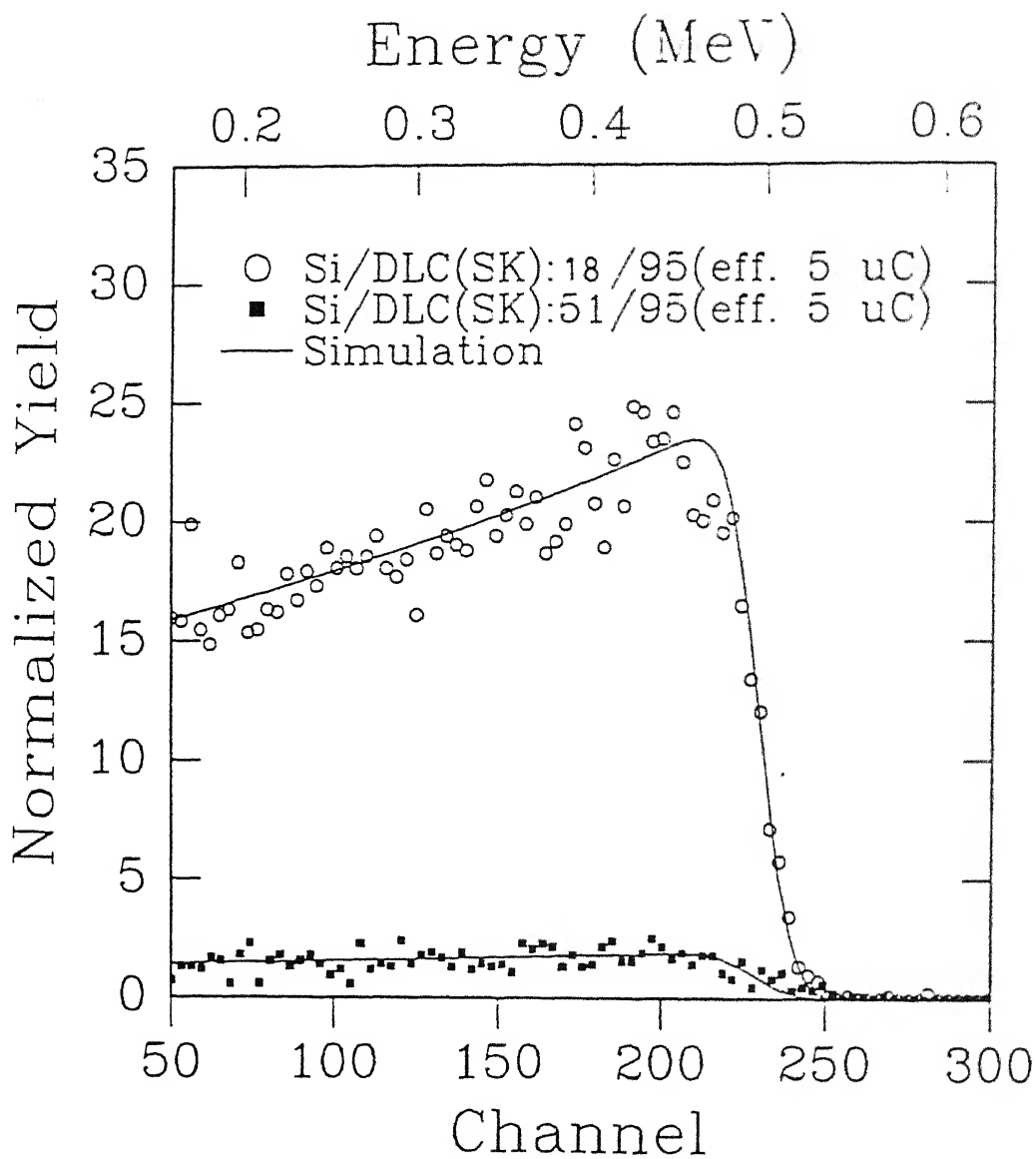


Fig.4.5: 1.5 MeV  $\text{He}^+$  induced recoil spectra of hydrogen from two representative diamondlike (DLC 51) and polymeric (DLC 18) films corresponding to Fig. 4.1 (a) and (c) respectively. The spectra were taken for the same integrated charge of 5  $\mu\text{C}$ .

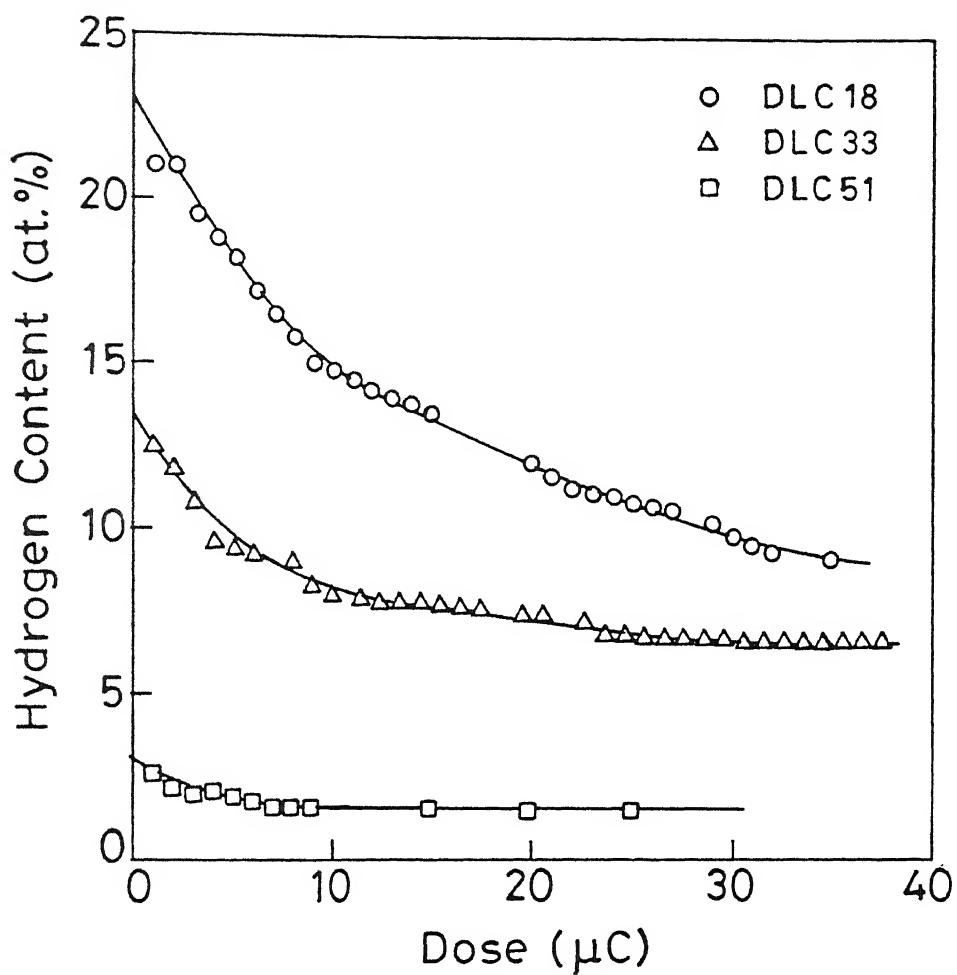


Fig. 4.6 Hydrogen atomic concentration in DLC films of different microstructures (see Table 4.3) as a function of irradiation dose with 1.5 MeV  $\text{He}^+$  ions, as determined by elastic recoil detection analysis.

## 4.4 THERMAL GAS EFFUSION

Thermal gas effusion technique has been widely applied to hydrogenated amorphous silicon (a-Si:H) to study the hydrogen related microstructure [266, 267]. Beyer has presented an excellent review of thermal effusion as applied to a-Si:H [266]. However, unlike a-Si:H, multiplicity of bonding configurations leads to complex effusion spectra in case of a-C:H. The power of this technique has not yet been exploited for microstructural characterization of a-C:H films. Few reports are available on thermal effusion data on a-C:H films primarily deposited using rf plasma technique (80,84,268,269). The role of microvoids in the films was suggested in controlling their effusion characteristics [269]. In this section, we consider the samples having distinctive microstructures belonging to series A and B type.

The experimental setup used for thermal effusion studies has been described in Chapter II. The out diffusing species, up to twelve in number, were recorded as a function of temperature using a quadrupole mass analyzer backed by turbomolecular pumped pressure reduction system. After surveying the complete mass spectrum from 1 to 200 amu range at  $\sim 500^\circ\text{C}$  for a few representative samples, we selected twelve most studies on A variety of hydrocarbons along with hydrogen are known to be evolved when a-C:H films are heated above  $350^\circ\text{C}$  [80, 84, 268,269]. Effusion abundant mass numbers to be recorded during each thermal scan at a fixed heating rate. Pumping speed of turbomolecular pump can be taken as constant over a wide range of pressure. Hence, the partial pressures of effusing species at the pumping port represent a measure of the effusion rate ( $dN/dt$ ). This is applicable under the assumption that adsorption of effused molecules to the walls is negligible and that the gas flow is not inhibited by the finite size of the vacuum lines. Several heating rates (b) from 2 to  $50^\circ\text{C}$  were employed to explore the mechanism of hydrogen effusion from a-C:H films. In addition, samples of different thickness were studied at fixed heating rates.

### 4.4.1 Theory

The kinetics of gas desorption processes follow a rate equation

$$\frac{dN}{dt} = A(1 - N)^n \exp(-E_a/RT) \quad (4.8)$$

where  $N$  is the fraction of gas atoms evolved by overcoming the free energy barrier  $E_a$ ,  $A$  is preexponential factor,  $n$  is the order of reaction and  $R$  is gas constant. If temperature rises at a constant rate  $\beta$ , the evolution rate will first rise to a maximum value and then return to zero when all the available gas for effusion has been exhausted. The temperature of maximum evolution rate ( $T_m$ ) informs about the stability or bonding strength of the evolving atom/molecule to the network. By differentiating equation (4.8), we get,

$$\frac{d}{dt} \left( \frac{dN}{dt} \right) = \frac{dN}{dt} \left[ \frac{E_a \beta}{RT^2} - An(1-N)^{n-1} \exp\left(\frac{-E_a}{RT}\right) \right] \quad (4.9)$$

Maximum evolution rate occurs at a temperature  $T_m$  defined by setting equation (4.9) equal to zero.

$$\frac{E_a \beta}{RT_m^2} = An(1-N)_m^{n-1} \exp\left(-\frac{E_a}{RT_m}\right) \quad (4.10)$$

The amount of hydrogen left in the sample  $(1-N)_m$  is not readily determined from the evolution pattern. However, equation (4.9) can be integrated to obtain a resulting exponential integral. A satisfactory approximation obtained by Murray and White[270] by successive integration by parts gives

$$\frac{1}{n-1} \left\{ \frac{1}{(1-N)^{n-1}} - 1 \right\} = \frac{ART^2}{E_a \beta} \exp\left(-\frac{E_a}{RT}\right) \left(1 - \frac{2RT}{E_a}\right) \quad (4.11)$$

At a temperature  $T_m$ , defined by equation (4.10), the value of  $(1-N)_m$  is given by equation (4.11). Combining equation (4.10) and (4.11), a simplified expression results as

$$n(1-N)_m^{n-1} = 1 + (n-1)2RT_m / E_a \quad (4.12)$$

The product  $n(1-N)_m^{n-1}$  is very nearly equal to unity. Substituting this value in equation(4.10) we get

$$\frac{E_a \beta}{RT_m^2} = A \exp\left(\frac{-E_a}{RT_m}\right) \quad (4.13)$$

For order of reaction and initial concentration of unity, equation(4.13) modifies as

$$v_o \exp\left(\frac{-E_D}{kT_m}\right) = \frac{ED\beta}{kT_m^2} \quad (4.14)$$

Hence, for first order desorption kinetics, the activation energy for desorption ( $E_a$ ) may be determined from  $T_m$  by the relation (4.14), where  $\alpha_s \sim 10^{14} \text{ s}^{-1}$ . Now differentiating equation (4.13) and neglecting small quantities, we get

$$\frac{d\left(\frac{\ln \beta}{T_m^2}\right)}{d\left(\frac{1}{T_m}\right)} = -\frac{E_a}{R} \quad (4.15)$$

regardless of order of reaction. If  $n=0$ , peak occurs when gas atoms in the sample are exhausted. Further, Kissinger's analysis [271] of nonisothermal kinetic curves obtained at constant heating rate gives for the order of the reaction the approximate relation

$$n = 1.26 \left( \frac{b}{a} \right)^{1/2} \quad (4.16)$$

where  $a$  and  $b$  are the absolute values of inverse slope at first and second inflection points of the  $dN/dt$  curve. Equation (4.12) predicts that the number of gas atoms remained in the sample at peak temperature will decrease as exponent  $n$  is decreased. This implies that the evolution peak will become increasingly asymmetric as  $n$  is decreased.

### ***Effect of heating rate***

At low heating rates, more time is available for the evolution process. Therefore, net amount of gas (to be same for two heating rates) will evolve at a lower temperature only. In evolution spectrum, the peak ( $T_m$ ) occurs at lower temperatures with a decrease in heating rate ( $\beta$ ). By measuring the variation of  $T_m$  with  $\beta$ , a graph can be plotted between  $\ln(\beta/T_m^2)$  vs.  $1/T_m$ . The slope of this curve will give the activation energy  $E_a$  using equation (4.15).

### ***Effect of film thickness***

If diffusion of gas atoms in compact material limits the evolution rate, this can be detected by measuring evolution spectra on identical samples of different thicknesses. With the increases in film thickness, the increase in diffusion length results in a shift of the evolution peak to higher temperature. For a diffusion-limited evolution [272], the hydrogen concentration profile  $c(x,t)$  across the film must be compatible with the diffusion equation

$$\frac{\partial^2 c}{\partial t^2} = D(t) \frac{\partial^2 c}{\partial x^2} \quad (4.17)$$

with a time dependent diffusion coefficient  $D[T(t)]$ . Solving the diffusion for out-diffusion from a thin film of thickness  $d$  at a constant heating rate and expressing  $D$  in terms of a diffusion pre-factor  $D_0$  and a diffusion energy  $E_d$  by

$$D = D_0 \exp\left(\frac{-E_d}{kT}\right) \quad (4.18)$$

we get

$$\ln\left(\frac{D}{E_d}\right) = \ln\left(\frac{d^2 \beta}{\pi^2 k T_m^2}\right) = \ln\left(\frac{D_0}{E_d}\right) - \frac{E_d}{k T_m} \quad (4.19)$$

For two different thickness  $d_1$  and  $d_2$  of the identical samples and corresponding peak temperatures  $T_{m1}$  and  $T_{m2}$ , equation (4.19) gives

$$\ln\left(\frac{d_1^2 T_{m2}^2}{d_2^2 T_{m1}^2}\right) = \frac{E_d}{k} \left(\frac{1}{T_{m2}} - \frac{1}{T_{m1}}\right) \quad (4.20)$$

Thus, from measurements of  $T_m$  as a function of the film thickness  $d$  for identical samples, the activation energy for diffusion can be determined.

#### 4.4.2 Hydrogen Effusion

Typical mass spectroscopic thermal effusion spectra are shown in figure 4.7 (a) and 4.7 (b) for samples representing type A and type B, respectively. Thermal effusion spectra of the two samples (DLC51 & 53) recorded at a heating rate of 20°C/min are shown. Difference between the two thermal effusion spectra is striking. In particular, type A sample shows effusion due to molecular hydrogen and  $CH_3$  only. The thermal effusion from soft a-C:H film shows contributions due to hydrocarbons such as  $CH_3$ ,  $C_2H_2$ ,  $C_2H_4$ ,  $C_3H_3$  and  $C_4H_3$  along with  $H_2$ . It may be pointed out that  $CH_3$  desorption is representative of methyl group ( $CH_4$ ) as effusion spectra from all fragments of  $CH_4$  were found to be virtually identical.

The threshold temperature ( $T_0$ ) at which the gas evolution starts indicates the initiation of the rupture of bonds from the matrix or the release of molecular species. Threshold temperature ( $T_0$ ) for evolution of hydrogen is found to be about 400°C which

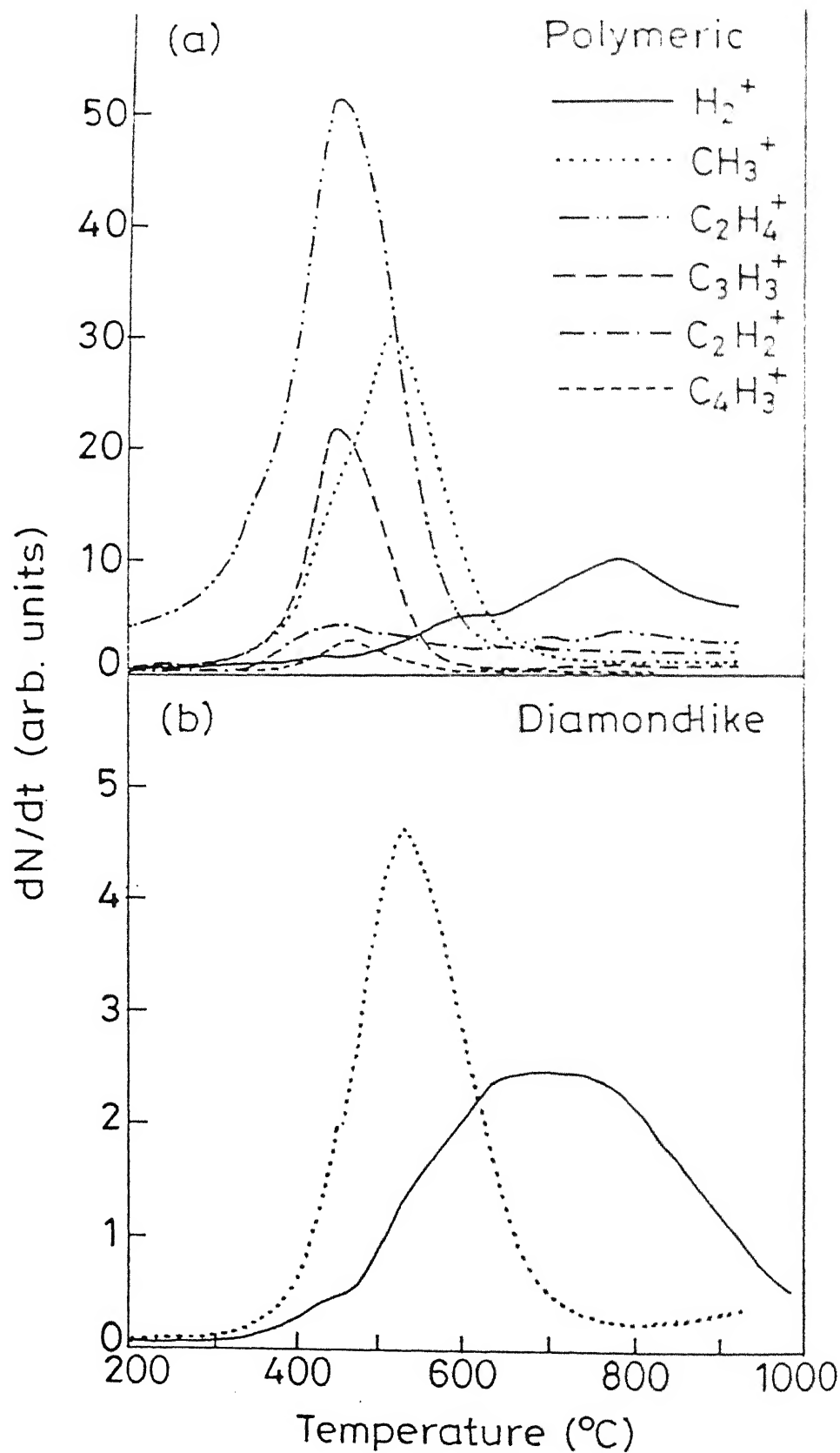


Fig. 4.7 Thermal gas effusion spectra as a function of heating temperature of typical (a) polymeric ( $p=10.0$  mbar,  $T_{\text{sub}}=250^{\circ}\text{C}$ ,  $V_c=710$  V, pure  $\text{C}_2\text{H}_2$ ); and (b) diamond-like carbon ( $p=0.6$  mbar,  $T_{\text{sub}}=250^{\circ}\text{C}$ ,  $V_c=710$  V,  $V_b=-250$  V,  $(\text{C}_2\text{H}_2 / \text{C}_2\text{H}_2 + \text{H}_2=0.5)$ ) films.



increases slightly with increasing hardness. The maximum in evolution temperatures ( $T_m$ ) of the  $C_xH_y$  molecules ranges from  $\sim 450$  to  $550^\circ\text{C}$ .

The type and amount of hydrocarbon effusion are found to be strongly dependent on the film microstructure. Figure 4.8 summarizes the relative concentrations of evolved hydrocarbons and hydrogen molecules for these two typical samples having approximately same volumes. The DLC film having lower total hydrogen content desorbs less amount of hydrocarbons. Hydrocarbons are present exclusively as methyl group. In contrast, from soft polymeric film only 16% of the effusing species are in the form of molecular hydrogen, while rest 84% are hydrocarbon species. Among the hydrocarbons, 41% are  $C_2H_n$  groups. Contribution from  $C_3H_n$  and  $C_4H_n$  is found to be  $\sim 14\%$  and  $2\%$ , respectively. We take this comparison as better homogeneity and density of type A films. Observation of higher hydrocarbons in the MSTE spectra can not be ascribed to the secondary reactions of smaller hydrocarbons effusing out of the films [81]. A clear distinction between the effusion spectra from a large number of samples produced under type A and type B of plasma conditions suggest the role of growth parameters in deciding the microstructure and hence the effusion profiles. In particular, in-situ mass spectroscopic measurements from the plasma (Fig. 3.10 and 3.12) show that the polymeric species are probably incorporated during growth phase itself. A porous and void rich microstructure helps in thermal evolution of such large molecules. This figure also demonstrates that the estimates of total hydrogen content using either hydrogen effusion or total pressures may be highly misleading. However, the sum of evolved hydrogen atoms as calculated from all hydrocarbons when normalized to film volume agrees well with that obtained from IR results.

Similar thermal effusion profiles have been observed by other researchers from a-C:H films [80, 81, 84, 269]. However, a lower  $T_o$  is observed in case of highly polymeric samples deposited by electron gun evaporation of graphite in butane plasma [82]. Lower  $T_o$  was also found in case of samples produced by the rf glow discharge decomposition of benzene [273]. A consistent observation of larger  $T_o$  in case of a large number of our samples deposited by the dc glow discharge of acetylene shows the better thermal stability, and higher density of a-C:H films produced by this technique.

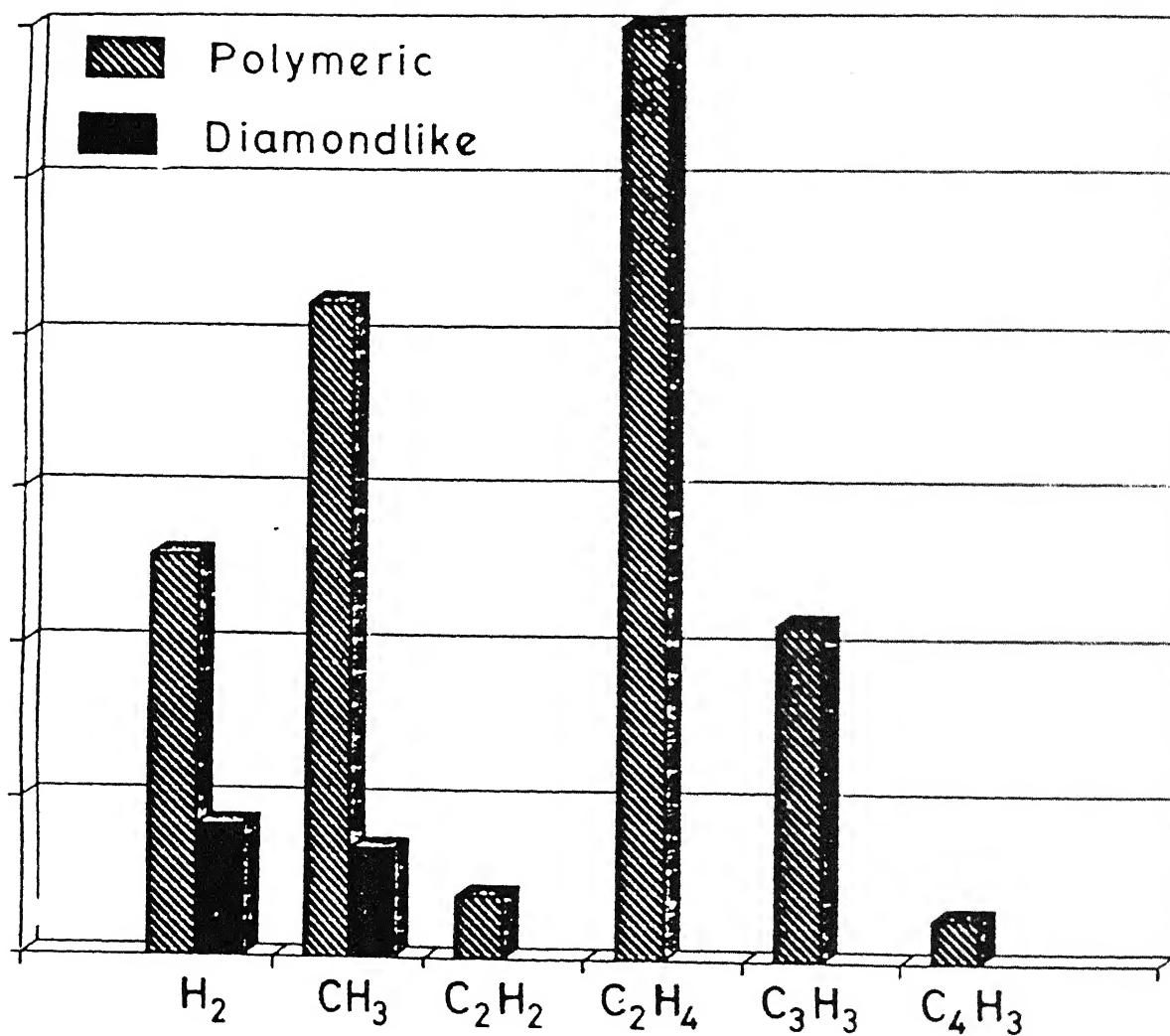


Fig.4.8 Relative concentration of desorbed hydrogen and hydrocarbons as calculated from the thermal effusion spectra in Figure 4.7.

Concentrating on  $H_2$  evolution in figure 4.7, The hydrogen effusion profile shows a characteristic change of decreasing contribution of low temperature evolution with increase in film hardness. This figure shows two major peaks around 600°C and 750°C. In addition, there is a small peak appearing at about 425°C. The hydrogen evolving around 425°C is either unbonded or very weakly bonded hydrogen as its  $T_m$  does not vary with film hardness, film thickness or the heating rate  $\beta$ . This peak disappears in the samples prepared at substrate temperatures higher than 400°C. The two major peaks at 600°C and 750°C may be labeled as low temperature (LT) and high temperature (HT), respectively.

LT peak is attributed, as discussed later, to the release of molecular hydrogen and/or weakly bonded hydrogen through internal surfaces (voids) which may be present in the films during the deposition process [84]. LT peak occurs near hydrocarbon peak temperatures. It shifts to higher temperatures with the increase in hardness of the samples. No variation in peak positions was observed for samples of different thickness deposited under same growth conditions. The thermal analysis of LT as well as HT peaks using equation (4.15) at a number of heating rates  $\beta$  is used to determine the activation energy  $E_a$ . A plot of  $\ln\beta/T_m^2$  versus  $1/T_m$  is shown in Fig. 4.9 for LT and HT peaks obtained using different heating rates for polymeric (DLC53) and diamondlike carbon (DLC40) films. Activation energies of 2.4 eV and 2.7 eV are obtained from the slope of LT curve for soft and hard films, respectively.

The observed activation energies can be understood if the desorption process is assumed to involve the simultaneous rupture of two nearby C-H bonds followed by the recombination of two H atoms to form  $H_2$  as:

$$E_a = 2E(C-H) - E(H-H) \quad (4.21)$$

Literature value for C-H and H-H binding energies,  $E(C-H)$  and  $E(H-H)$  are reported to be 3.68 and 4.5 eV, respectively [269, 274]. The energy for rupture of neighboring C-H bonds is lowered by a H-H binding energy giving an activation energy  $E_a$  of 2.86 eV. This is in close agreement with the experimental value of 2.7 eV obtained by us. LT hydrogen may also be coming from weakened double bond  $-(\overset{H}{\underset{|}{C}}-\dot{C})$  [268]. If hydrogen leaves such a site, C=C bond will be restored. This is indeed observed in Raman spectrum of the samples heated to 600°C (section 4.3).

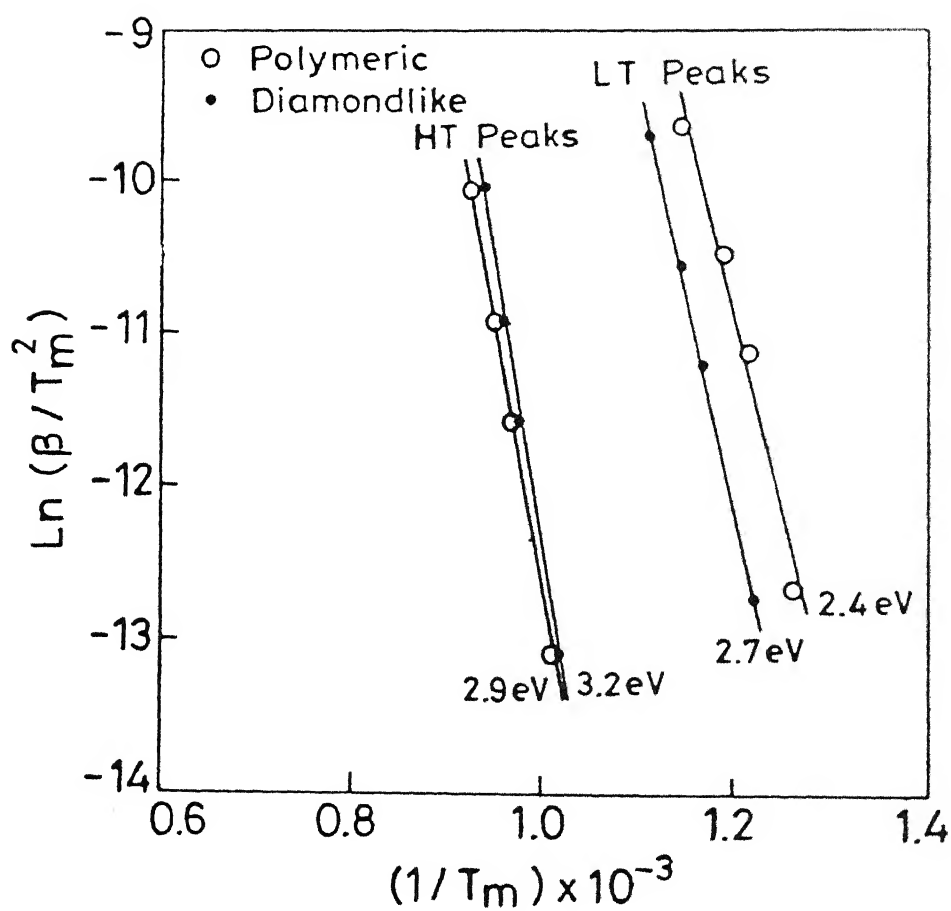


Fig.4.9 Determination of activation energies of hydrogen evolution for polymeric (soft) and diamond like carbon (microhardness~ 2100 kgf/mm<sup>2</sup>) films of thickness 1.6 μm and 1.2 μm respectively.

At temperatures labeled as HT, the effusion rate is maximum. It informs about the stability or bonding strength of the evolving atom/molecule to the network. Apart from structural changes taking place in the sample during the effusion experiment, essentially three processes may influence the effusion rate: the primary rupture of C-H bonds, the diffusion of molecular or atomic hydrogen to the surface, and, in case of diffusion of atomic hydrogen, the surface recombination of atomic hydrogen to form  $H_2$ . In higher hardness DLC film (Fig. 4.7b), most of the hydrogen is evolved at higher temperatures. Interestingly,  $\beta$  dependence of HT can still be fitted using equation (4.15) as seen in Fig. 4.9, indicating desorption to be the rate limiting step. Activation energies obtained are higher for HT peak and these are found to be 2.9 and 3.2 eV for soft and hard films respectively. It is difficult to ascribe a definite mechanism to these energies as structural changes (bond reconstruction to form C = C bonds) are also known to take place at these temperatures. However, it is likely that HT hydrogen is released from uniformly distributed hydrogen in C-H configurations in the solid network. Additional energy and/or time lag may be required for detrapped H atoms to hop to the nearest available H site to form a mobile  $H_2$  molecule [275].

In contrast the rapid fall of  $dN/dt$  in hydrogen effusion profile observed by Jiang et al [269] indicates that hydrogen is exhausted near peak temperature. The gradual decrease of  $dN/dt$  after a constant value over some time in our DLC sample (Fig. 4.7 b) indicates diffusion delay of molecular hydrogen. Wild and Koidl [80] carried out the thermal effusion experiments on bilayers of a-C:H and a-C:D and arrived at the conclusion that hydrogen molecules are formed inside the material after getting detrapped from its hydrocarbon configuration. Our analysis on activation energy also indicate a detrapping limited evolution process of molecular hydrogen. However, it indicates diffusion process to be involved as well.

#### 4.4.4 Hydrocarbon Effusion

Methyl group ( $CH_3$ ) is found to be the common hydrocarbon species evolving from DLC films produced by a variety of deposition techniques using different source gases [80, 82, 84]. While much microstructural information has been derived from  $H_2$  evolution in the literature, sufficient attention has not been paid to the evolution of

methyl radical. It may be pointed out that  $\text{CH}_3$  has been proposed as a growth precursor in formation of diamond/DLC films from plasma of hydrocarbons [219,220,224]. A careful analysis of the evolution pattern may provide important clues about the microstructure of DLC films as well as the growth processes leading to such microstructures.

Fig. 4.10 shows the thermal desorption spectra on samples having distinctly different microstructure as well as on two different thicknesses of a sample. The position of  $\text{CH}_3$  peak ( $T_m$ ) and its shape is almost independent of the type of films.  $T_m$  was found to be  $520 \pm 15^\circ\text{C}$  for all the samples deposited using dc glow discharge of acetylene. Further, peak position for  $\text{CH}_3$  evolution was found to be independent of film thickness. This implies bond breaking or thermal desorption to be the rate-limiting step in case of  $\text{CH}_3$  effusion.  $E_a$  was obtained to be  $\sim 2.3$  eV for  $\beta = 0.33$  K/s. Origin of this activation energy may be explained by simultaneous detrapping of  $\text{CH}_3$  and H followed by the recombination to form  $\text{CH}_4$  [269]. The net energy required for this process is

$$E_a = E(\text{C-H}) + E(\text{C} - \text{CH}_3) - E(\text{H} - \text{CH}_3) \quad (4.22)$$

Taking the values of  $E(\text{C-H})$ ,  $E(\text{C-CH}_3)$  and  $E(\text{H-CH}_3)$  from the literature as 3.68, 3.0 and 4.5 eV, respectively [23], we obtain  $E_a = 2.18$  eV. This is in reasonable agreement with the experimentally obtained value of 2.3 eV. Another possibility is the rupture of two  $\text{C-CH}_3$  bonds from two bonded carbon atoms  $\begin{matrix} \text{CH}_3 \\ | \\ \text{C} - \end{matrix}$   $\begin{matrix} \text{CH}_3 \\ | \\ \text{C} < \end{matrix}$  thereby converting  $\text{C-C}$  to  $\text{C} = \text{C}$ . Energy is gained in this conversion, which is the difference of  $\text{C} = \text{C}$  binding energy (4.33 eV) and that of  $\text{C-C}$  (2.55 eV). Therefore, activation energy for desorption in this process [ $2E_a = 2E(\text{C} - \text{CH}_3) - 1.78$ ] comes out to be 2.1 eV. This process is similar to the one proposed for the LT hydrogen peak. It is not surprising that the LT hydrogen evolution peak is accompanied by the evolution of methyl peak in our data and reported literature [80, 82, 84, 269].

Presence of higher hydrocarbon molecules in the effusion spectra of polymeric films is associated with the porous and void rich microstructure of soft a-C:H films. Wild and Koidl showed that the diffusion of larger hydrocarbon molecules requires a porous microstructure [80]. Results shown in Figs. 4.8 and 5.4 (a) along with high hydrogen content and lower hardness of samples DLC53 and DLC18 are consistent, with a porous microstructure of these samples. In contrast, high microhardness ( $\sim 2420$

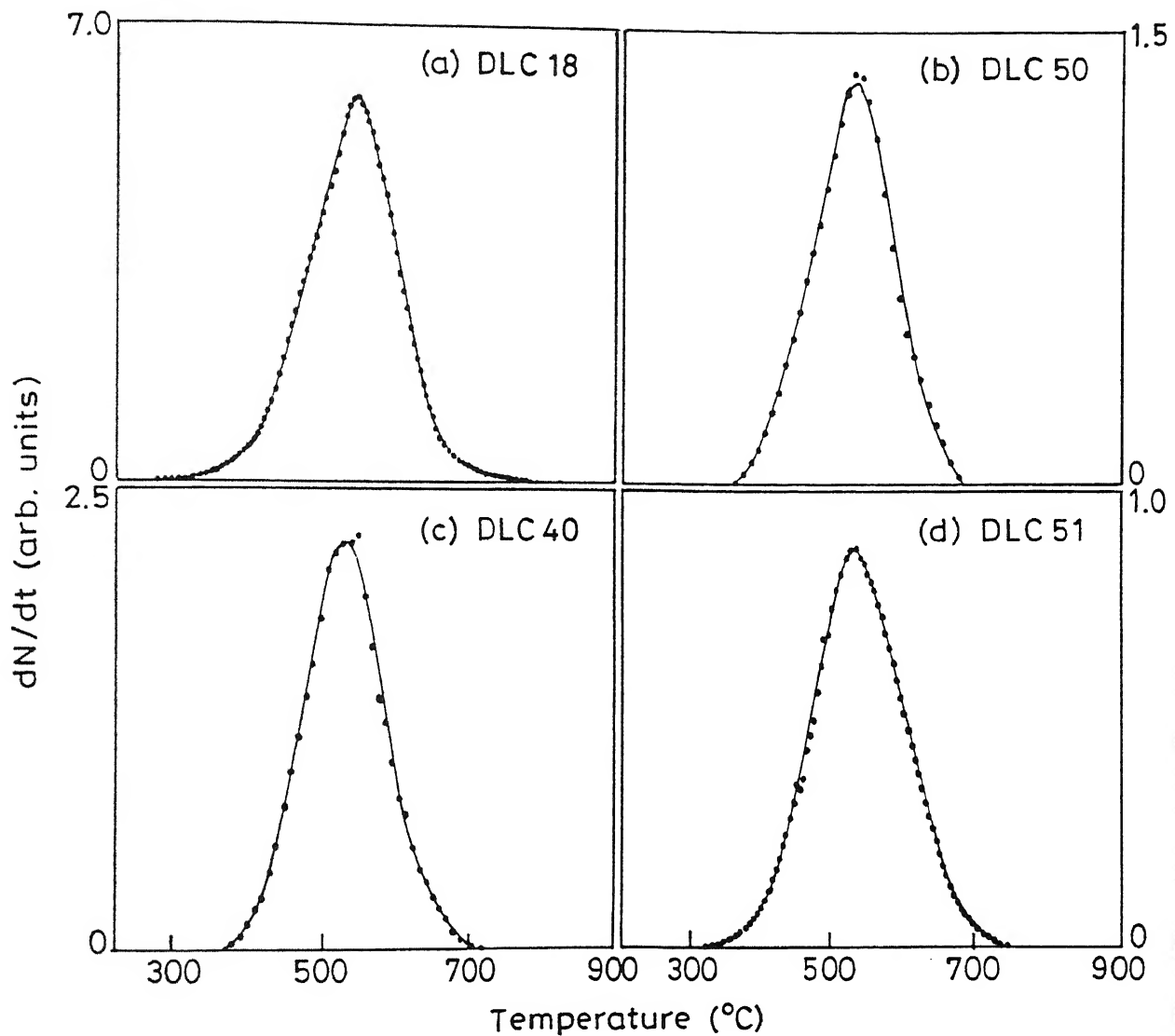


Fig. 4.10: Thermal evolution of  $\text{CH}_3^+$  from a-C:H films of different hardnesses having approximately same thicknesses. DLC18 is soft polymeric sample (see Table 4.1). DLC40 and DLC51 are hard samples (VH  $\sim$  2100 and 2420 kgf/mm<sup>2</sup>, respectively). DLC50 is a thinner sample ( $d \sim 0.4 \mu\text{m}$ ) prepared under conditions of DLC 51. All effusion spectra were recorded at constant heating rate of 20°C/min.

kgf/mm<sup>2</sup>), low hydrogen content and thermal effusion profile (Fig 4.7) of sample DLC51 show its compact microstructure

Combining infrared spectroscopic data with ERDA and thermal effusion, comments can be made on the process of film growth itself. It appears that during the plasma conditions leading to hard and dense films, a thin near surface transitional layer (NSTL) is formed. In this NSTL, film growth precursors arrive and C is incorporated in the film matrix while hydrogen is removed. The growth region below this layer normally stabilizes and results in the uniform distribution of hydrogen. On the contrary, the process of hydrogen removal and carbon incorporation is inefficient in the plasma conditions leading to soft polymeric films. In this case, thickness of NSTL is rather large. Two extreme cases are expected. First is the growth of diamond films, where NSTL should be of the order of a monolayer. This indeed seems to be the case as a high resolution ERDA data shows a sharp hydrogen peak in the microwave plasma deposited diamond films [153]. Other possibility is that of highly polymeric films where practically no stabilized zone occurs and NSTL is of the order of film thickness. ERDA of such films show large non uniformity in the hydrogen depth profiles. Higher hydrogen content, primarily bonded in CH<sub>3</sub> and CH<sub>2</sub> groups (indicated by IR) is responsible for thermal effusion of higher hydrocarbons and high thermal erosion of material. Data shown in Table 4.4 on hard and soft sample show the different thickness of NSTLs in the two samples. Further, consistency in the nature of effusion spectra of CH<sub>3</sub> as shown in Fig. 4.10 along with the proposed effusion mechanism, enforces the view that CH<sub>3</sub> groups are the main constituents of NSTLs. We shall come back to the growth mechanism in the following chapter.

It should be emphasized that the presence of CH<sub>3</sub> in the effusion spectra is a common feature [80, 82-84, 269]. Activation energy estimates and their interpretation suggest that the methyl radical must be present in all these films. Strong support to this argument comes from the estimates of material erosion (amount of hydrocarbon evolved) during the thermal effusion experiments. This data is presented in Table 4.4. Film thickness measured using stylus technique before and after annealing the films is also shown. In general, film thickness is found to reduce after heat treatment. The estimate of thermal erosion loss of material agrees quite well with the actual reduction in film thickness. Slightly lower values in case of effusion data could be due to unaccounted



**Table 4.4** *Values of the thickness for two typical type A and B samples, as deposited and after heating to 600 °C and 1000°C as measured by stylus method and estimated from thermal effusion data.*

Sample No	Thickness (nm)			Thickness Loss (nm)	Thermal Effusion Estimate Thickness Erosion (nm)
	As Deposited	After heating to 600 °C	to After heating to ~1000° C		
DLC51	1500	–	1350	150	20
DLC53	1400	600	500	900	470

hydrocarbon species as well as actual thickness reduction due to structural reorganization of films at elevated temperatures. It is interesting to note that the reduction in film thickness is much lower in hard DLC film as compared to porous and soft polymeric film.

## 4.5 EFFECTS OF ANNEALING

Annealing of a-C:H films leads to the changes in hydrogen distribution and content. This is an excellent way to analyze hydrogen related structural effects in a-C:H films. It is evident from Fig. 4.7 that most of the hydrocarbons are effused out by 600°C anneal at a constant heating rate of 20°C/min. Here we present the results on a well characterized DLC sample (DLC49/33). The sample was first heated to 600°C at a heating rate of 20°C/min and MSTE data was simultaneously recorded. We stopped heating the sample at 600°C and cooled it down to room temperature at a relatively higher cooling rate. The samples were then analyzed using IR, ERDA and Raman spectroscopy. It was again heated to 1000°C at the same heating rate. These thermal stimulated annealing effects are to be distinguished from isothermal annealing at the same temperature (600°C) for extended periods [278].

Many investigators have studied structural changes on annealing using IR and Raman spectroscopy [54, 82, 276, 277, 278]. Effects of thermal annealing on electrical

and optical properties of a-C:H films have also been reported [254]. The results have shown that at temperatures above 350°C the concentration of hydrogen bonded to  $sp^1$  carbon decreases while concentration of  $sp^2$  carbon increases. Dillon et al. have studied the annealing of the ion beam and rf discharge deposited films and found the removal of bond angle disorder and the increasing dominance of crystallites due to annealing [78]. The films prepared by dc magnetron sputtering were annealed to 1000°C to study the low frequency features attributed to disorder induced scattering in the Raman spectra [279]. The changes due to annealing in the rf glow discharge deposited films have been interpreted in terms of dehydrogenation of films followed by the growth of small conducting graphite crystals [280]. In general, a-C:H alloys (polymeric as well as diamondlike) transform to graphite like amorphous carbon on high temperature annealing (~600°C).

Figure 4.11(a) and (b) show the effusion spectra for  $H_2$  and  $CH_3$  measured during the two heating cycles. Absence of  $CH_3$  and  $H_2$  contributions below 600°C during reheating of the sample show that the effusion of these species is site dependent. Once these sites are exhausted and structural transformation completed in the first heating cycle, they do not reappear in the second effusion spectra. These results are strong evidence that the methyl radicals in the effusion spectrum is related to their presence in as deposited samples during growth itself. Effusion spectra above 800°C is dominated by the decomposition of this rather thin sample (~0.4  $\mu m$ ).

Fig. 4.12 shows the IR spectra of samples DLC49 in as deposited and annealed state (600°C). Sample heated to 1000°C did not show any vibrational modes due to hydrogen. Reduction in hydrogen content is clear from the area under the stretching vibration modes. Quantitative analysis using the procedure described above yield hydrogen content of 19 at.% in the as deposited film. Hydrogen content ( $C_H$ ) reduces to 6 at. % in heat treated sample.  $sp^{2*}$  fraction (C-C bonds) increases from 0.27 to 0.66 and  $sp^{3*}$  decrease from 0.54 to 0.28. In addition, analysis shows that the hydride configuration ( $CH:CH_2:CH_3$ ) changes on annealing from (34:13:53) to (33:44:23). Thus most of the methyl group evolution is directly related to the presence of this group in the starting material. There is a relative increase in trigonal  $sp^{2*}$  bonding.

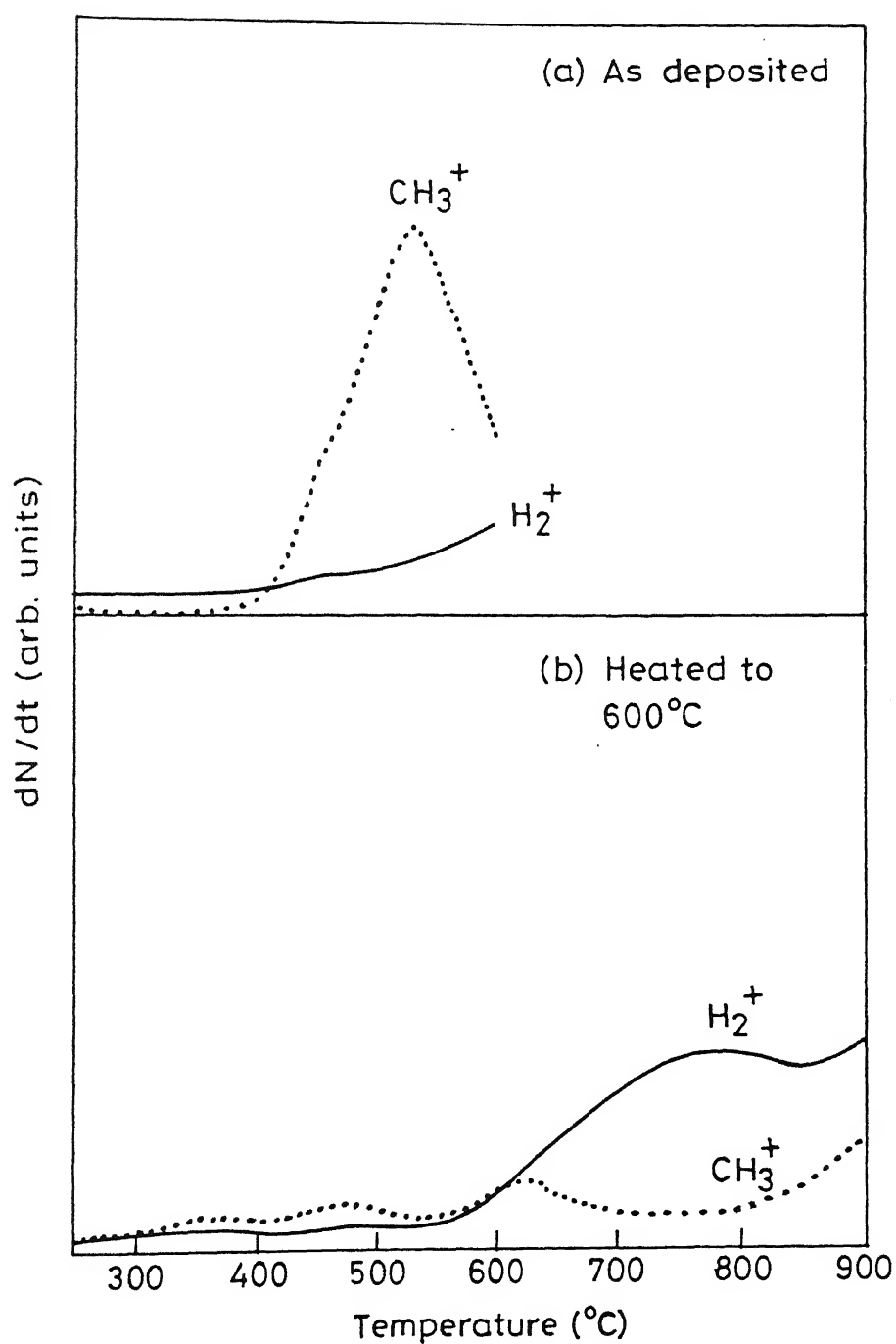


Fig. 4.11.  $H_2^+$  and  $CH_3^+$  effusion profile during two consecutive heating cycles of DLC film (DLC49): (a) up to 600° C , followed by heating the same sample up to 1000° C (b).

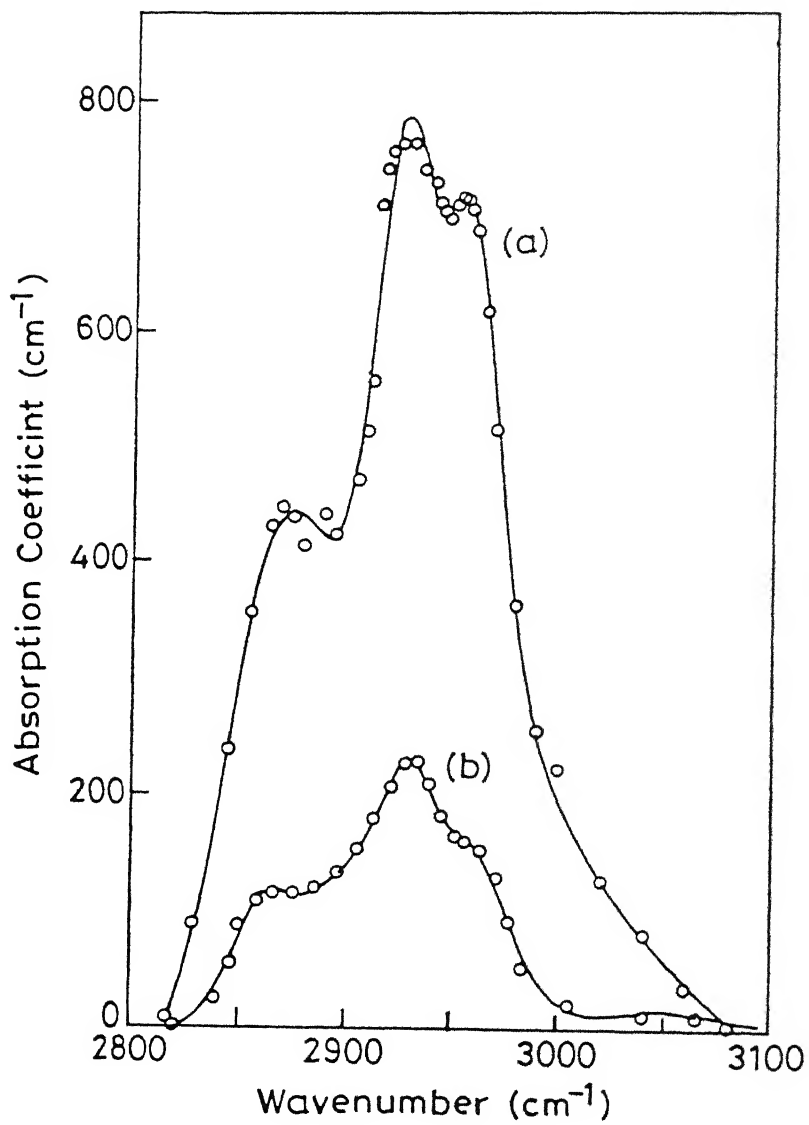


Fig.4.12 : IR absorption spectra of a-C:H films in the range of stretching modes: (a) as deposited (b) after heating to 600° C as illustrated in Fig.4.11.

ERDA spectra of as deposited sample is identical to that of DLC33 and is shown in fig. 4.4. ERDA spectra measured on the heat treated sample is shown in Fig. 4.13. It gives a  $C_{H1}$  value of  $\sim 3$  at % in this sample. ERDA also shows this to be uniformly distributed across the thickness of the sample. No peak at surface in the ERDA spectrum is seen for the step heated sample. It has been mentioned above that the higher hydrogen content at the surface in the as deposited a-C:H film may be the reminiscent of growth. Increasing the total fluence on the as deposited samples resulted in an increase in surface hydrogen concentration (Fig. 4.4). It is interesting to note that the effect of continued  $He^+$  ion bombardment on the hydrogen content and profile is negligible in contrast to the effects observed in as deposited film. These results supports our earlier assertion that the hydrogen effusion corresponding to HT peak is uniformly distributed across the thickness of the sample. Further, formation of  $H_2$  molecules from detrapped H inside the material is an essential step in thermal as well as ion induced migration of hydrogen. Once the separation between two H atoms increases more than a few hopping steps, the hydrogen migration stops unless it is accompanied by a structural transformation also [262, 80, 269]. Therefore, low hydrogen content samples show a better stability under thermal and ion irradiation treatments.

To investigate the structural changes taking place in the samples on heating, Raman spectroscopy was used. Raman spectra recorded on the  $600^\circ C$  and  $1000^\circ C$  heated sample (DLC49) are shown in Fig. 4.14. Two well resolved peaks are observed in the spectra of the films at  $1360$  and  $1580\text{ cm}^{-1}$ . The peak positions and integrated intensity ratio ( $I_D/I_G$ ) after a computer line shape analyses of these spectra are given in Table 4.5. Thus, compared to the literature values of  $1580$  and  $1355\text{ cm}^{-1}$ , the positions of the G and D lines [179], an up shift of the two lines, an increases of the ratio  $I_D/I_G$ , and a narrowing of G line is observed after heating in vacuum. Beeman et al [181] have found that the G band position shifts to lower frequencies on increasing the amount of  $sp^2$  bonded atomic sites in a-C. Dillon et al [78] suggested that the downshifts of the G line in the as deposited films indicates the presence of some  $sp^2$  C-C bonds as well as disorder. According to these arguments, the upshifts of the two lines towards the high frequency side in the films indicates that the crystallites are dominated by  $sp^2$  carbon rather than  $sp^3$  carbon bonds. The decrease in the FWHM of the G line (from  $100\text{ cm}^{-1}$  to  $85\text{ cm}^{-1}$ ) in

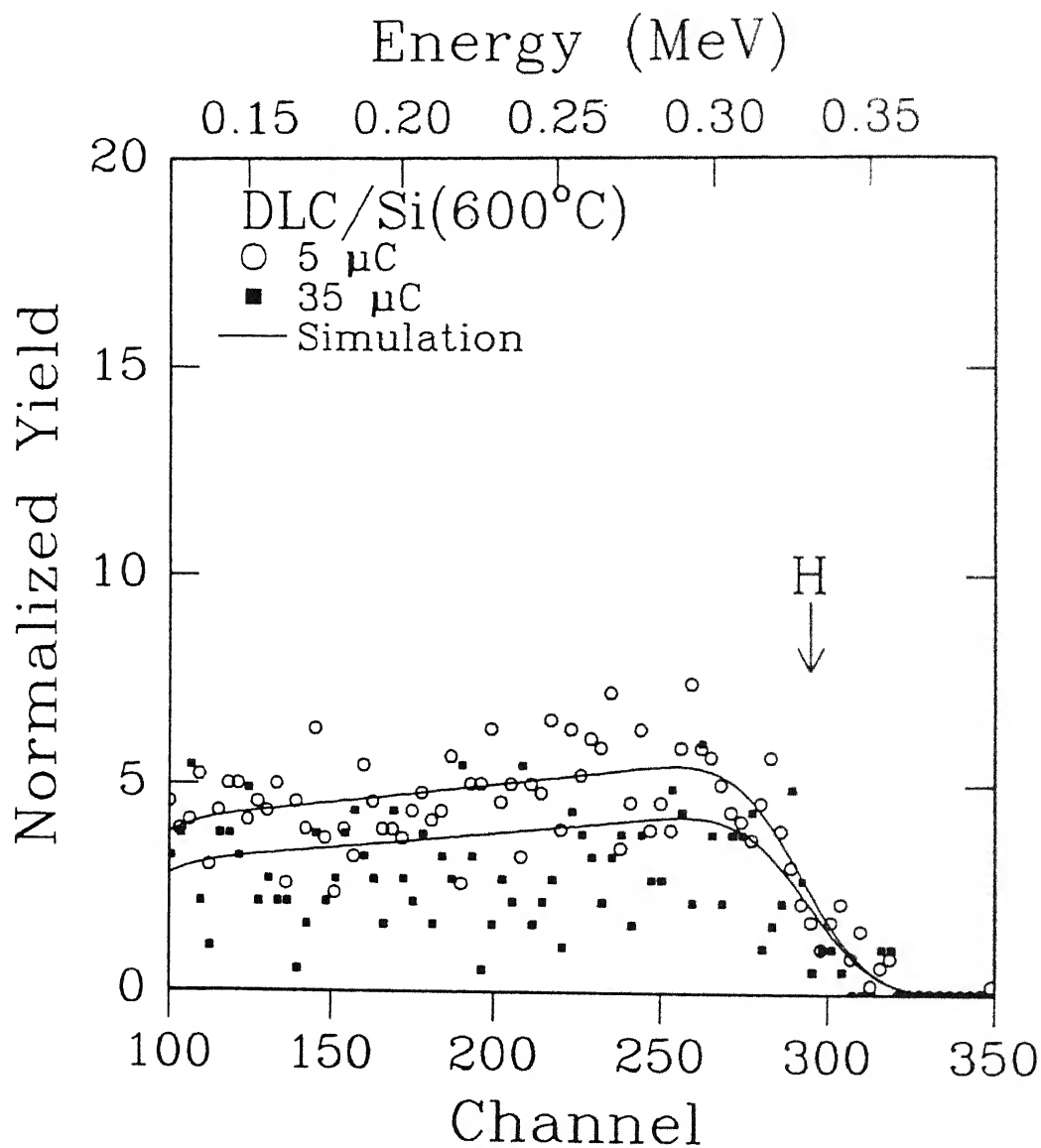


Fig. 4.13 ERDA spectra measured on the heat treated sample (DLC49 ).

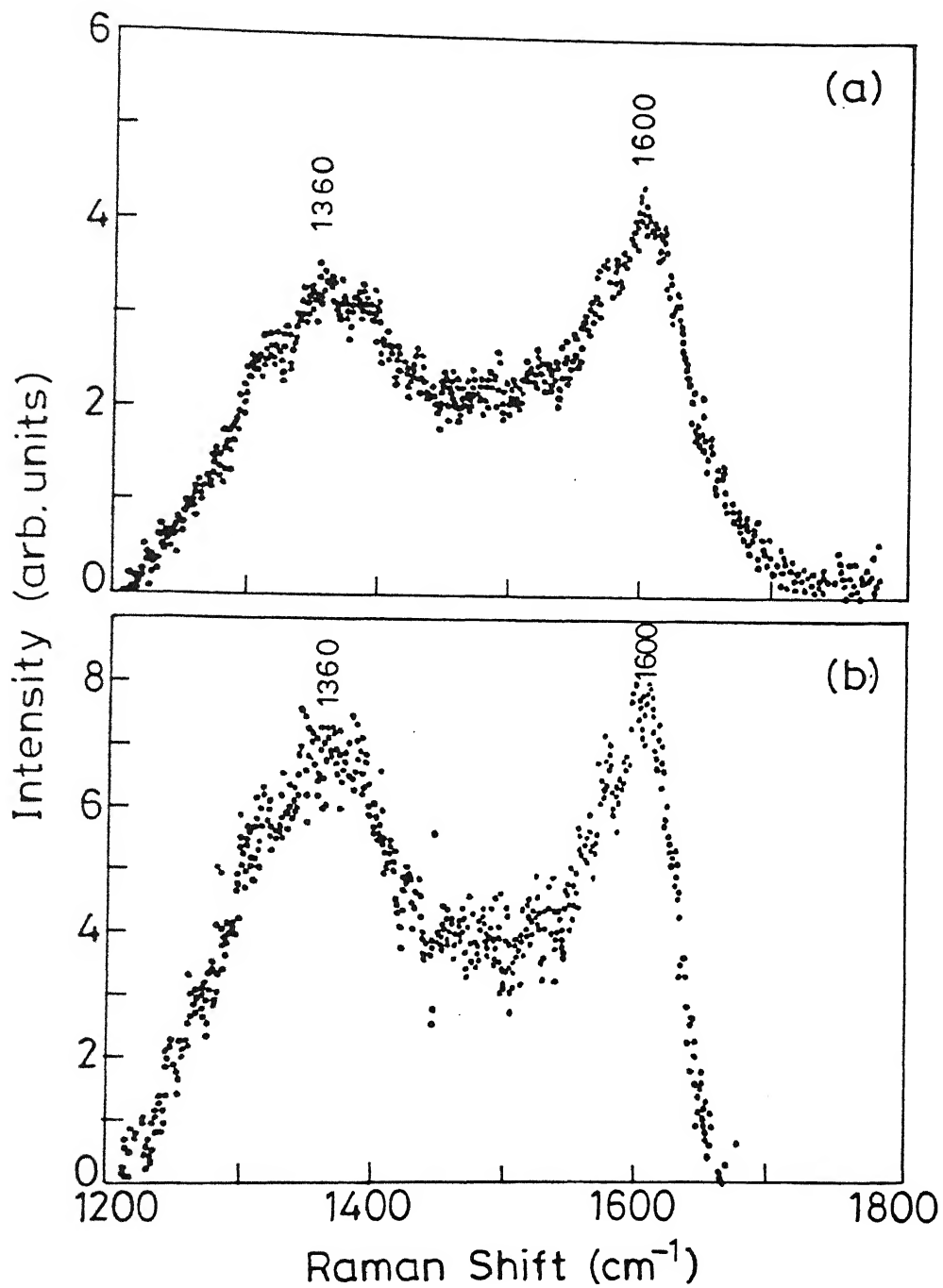


Fig. 4.14 Raman spectra of (a) 600°C and (b) 1000°C heated sample (DLC49).

**Table 4.5** Peak position of D and G bands ( $\text{cm}^{-1}$ ), and integrated intensity ratios of ( $I_D/I_G$ ) obtained after the deconvolution of Raman spectra of the sample (DLC49) after heating up to 600 and 1000°C.

Annealing Temperature T (°C)	$\nu_D$ ( $\text{cm}^{-1}$ )	$\nu_G$ ( $\text{cm}^{-1}$ )	$I_D/I_G$
600	1360	1600	0.71
1000	1360	1600	0.97

the sample heated to 1000°C also shows the removal of bond angle disorder and the increasing dominance of crystallites. This deduction is consistent with our measured IR results which shows a new band at  $3050 \text{ cm}^{-1}$  due to CH stretching vibration of aromatic ring groups consisting of three fold  $\text{sp}^2$  bonded carbon.

## 4.6 SUMMARY AND CONCLUDING REMARKS

We have applied three complementary techniques viz infrared spectroscopy (IR), elastic recoil detection analysis (ERDA), mass spectroscopic thermal effusion (MSTE) to characterize hydrogen in a-C:H films and explored their microstructural features. It is shown that a careful analysis of IR data can yield reliable values of  $\text{sp}^3$  and  $\text{sp}^2$  bonding fractions of C-C bonds in a-C:H films. Further,  $\text{sp}^3/\text{sp}^2$  ratio, as popularly quoted in literature, is not necessarily a good indicator of the film quality. However, we have found that detailed information on hybridization fractions, total hydrogen content  $C_H$  as well as fractions of  $\text{CH}_3$ ,  $\text{CH}_2$  and  $\text{CH}_1$  is required to correlate the measured film properties such as microhardness and optical bandgap etc. ERDA is known to produce total atomic hydrogen concentration (bonded and unbonded) in carbon films. We have shown that the hydrogen content from ERDA should be estimated with caution because of the ion induced migration of hydrogen from the samples. Further, hydrogen depth profiles using ERDA show a non-uniform distribution of hydrogen in soft a-C:H films.



The MSTE technique, though destructive, provided useful microstructural information. Threshold temperature for hydrogen effusion is found to be about 400°C and two major peaks are observed at around 600°C and 750°C in our dc glow discharge a-C:H films. MSTE spectra show the evolution of hydrogen along with a variety of hydrocarbons ( $\text{CH}_3$ ,  $\text{C}_2\text{H}_2$ ,  $\text{C}_2\text{H}_4$ ,  $\text{C}_3\text{H}_3$  and  $\text{C}_4\text{H}_3$  etc.) for soft films. However, the hydrogen evolution at high temperature was found to dominate the spectra in case of hard films with methane being the only hydrocarbon species evolved. The analyses of hydrogen effusion peaks by studying the peak positions as a function of heating rates and sample thicknesses suggest bond breaking or thermal desorption to be the rate limiting step. Study of as-deposited and annealed samples shows that the nature of hydrogen incorporation is different in polymeric and diamondlike films. In DLC, hydrogen is found to be homogeneously distributed as contrast to the case in polymeric films.



## CHAPTER V

# GROWTH AND PROPERTIES OF a-C:H FILMS

### 5.1 INTRODUCTION

In this chapter, results of a detailed variation in suitably chosen growth parameters on the properties of a-C:H films are presented. Parameters influencing homogeneous gas phase plasma reactions such as total working gas pressure, gas composition and electric fields, as well as those influencing the heterogeneous surface based reactions such as substrate temperature and negative bias to the substrates were varied. Physical properties of the films are found to have a complex dependence on the deposition conditions. Considering these results, discharge properties (Chapter III), and in-depth analysis of film microstructure (Chapter IV) a phenomenological model for film growth will be discussed. A unified picture on the role of hydrogen in the plasma and its influence on film properties will be presented. Results will be discussed in the light of fully constrained random covalent network models.

### 5.2 RESULTS

Films were deposited using dc glow discharge of acetylene as described in Chapter III. Having optimized the reactor geometry (Sec. 3.3), four series of samples were prepared. Total pressure of pure acetylene, dilution of acetylene with hydrogen, substrate temperature, and applied bias to the substrate electrode was individually varied keeping the other parameters as constants. Parameter space was chosen based on the following criteria: stability of plasma, uniformity of the deposits, and reasonable growth rates. Table 5.1 shows the deposition parameters employed for sample preparation. Moreover, many samples were prepared at other deposition conditions (usually extreme conditions or cross combinations) to test out various phenomenological models for growth and film properties.

**Table 5.1:** *The deposition parameters used for the preparation of films*

<i>Sample Series</i>	<i>Total pressure (mbar)</i>	<i>Hydrogen dilution <math>C_2H_2</math> (<math>C_2H_2 + H_2</math>)</i>	<i>Substrate temperature (<math>^{\circ}C</math>)</i>	<i>Cathode Voltage <math>V_c</math> (<math>-V</math>)</i>	<i>Substrate bias (<math>-V</math>)</i>
Pressure series	0.1-25.0	100	250	710	Floating voltage
Hydrogen dilution series	0.6	10-100	250	710	same
Substrate temperature series	0.6	100	30-525	710	same
Substrate bias series	0.6	50	250	710	0-425

### 5.2.1 Effect Of Acetylene Pressure

In this series, working pressure of pure acetylene was varied from 0.1 mbar to 25 mbar. Substrate temperature ( $T_s$ ) was maintained at 250°C during deposition. Cathode voltage was kept constant at -710V. No external bias voltage was applied to the substrate electrode. However, insulating substrates could pick up a floating potential ~ 70 V as discussed in Section 3.3.4.

Figure 5.1 shows the variation in growth rate as a function of total gas pressure. Growth rate first increases to about 75 Å/min. at ~1 mbar and then decreases with increasing pressure. We recall the results shown in Fig. 3.3, the two ranges of pressure are labeled as *region A* (lower branch of Paschen curve) and *region B* (higher branch of Paschen curve). The initial increase in growth rate may be attributed to the increased density of growth precursors in the plasma. At higher pressures (Region B), there is a decrease in acetylene decomposition rate because of the reduction of both the concentration of secondary electrons and the reaction rate constants. Thus the concentration of radicals or excited monomers is reduced, thereby reducing the growth rate. As the pressure increases further, the gas phase polymerization dominates and a depletion of acetylene may also occur causing a decrease in the growth rate. In addition,

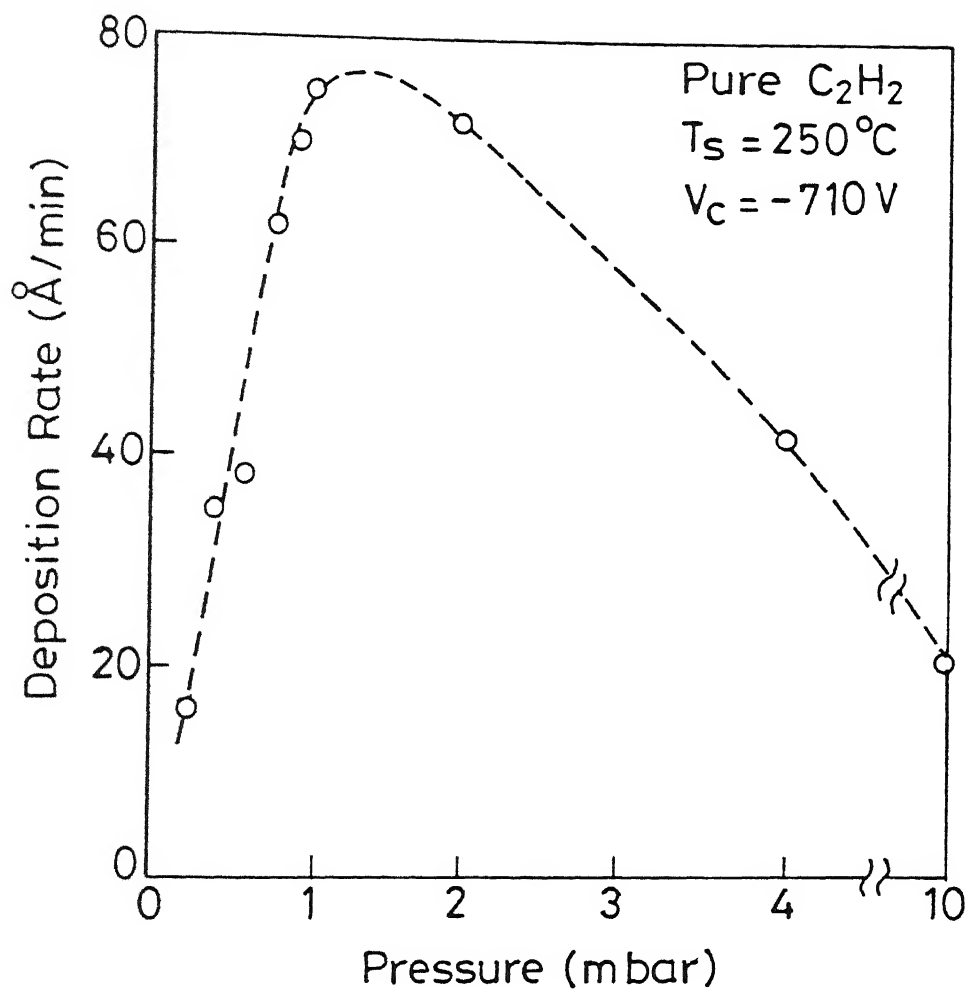


Fig. 5.1 Variation in deposition rate as a function of total gas pressure.

a decrease in ion energy due to an increase in number of gas phase collisions also plays a significant role in the growth process (to be discussed later in Section 5.2.4). Similar deposition rates were reported using plasma enhanced CVD using methane [137,226,282]. However, Zhou et al obtained higher deposition rates using acetylene rf plasma deposition in a significantly different reactor geometry [43,44].

Effect of feed gas pressure on microhardness of the films deposited at 250°C using pure acetylene is shown in Fig. 5.2. At low growth pressures, a good hardness of films is observed. Films become softer when deposited at higher gas pressures. In particular, microhardness decreases exponentially with pressure and a significant change is observed in the microhardness of the films deposited under plasma conditions A and B (Fig. 3.3).

The observed changes in microhardness with gas pressure indicate the modification of film microstructure and bonding configuration (C-C and C-H bonds) in the films. Information on film microstructure can be obtained from FTIR and thermal effusion measurements as discussed in Chapter IV. The complete infrared spectra in the range 4000 to 400  $\text{cm}^{-1}$  on the films produced at two pressures in region A and B has been shown in Fig. 4.1. The absorption coefficient in the stretching mode region along with the deconvolution spectra for the same samples was shown in Fig. 4.2. From the analysis it was shown that the film prepared at low pressure is compact and diamondlike while other prepared at high pressure conditions shows porous and polymeric characteristics [243,223]. Using this procedure (Sec. 4.2) a detailed analysis of hydrogen content and bonding type was carried out for this series of samples and the results are given in Table 5.2. It is seen that the films deposited at lower pressure contain a larger fraction of  $\text{sp}^3$  C-C bonds (represented by  $\text{sp}^{3*}$ ). The high pressure deposited films contain relatively higher concentration of hydrogen and  $\text{sp}^3$   $\text{CH}_3$  bonding. Whereas, the increase in intensity of  $\text{sp}^3\text{CH}_2$  and  $\text{sp}^3\text{CH}$  type bonding is seen in samples deposited at lower pressures (Table 5.2). In addition, hydrogen content in the films is found to increase with increasing total pressure (Fig.5.3). It may be recalled that  $\text{CH}_3$  is a bond terminator, and its abundance in the samples is an indication of films with void structure having lower densities. Though it may be noted that the numbers given in the Tables are in percentages from the total hydrogen content  $\text{C}_\text{H}$ .

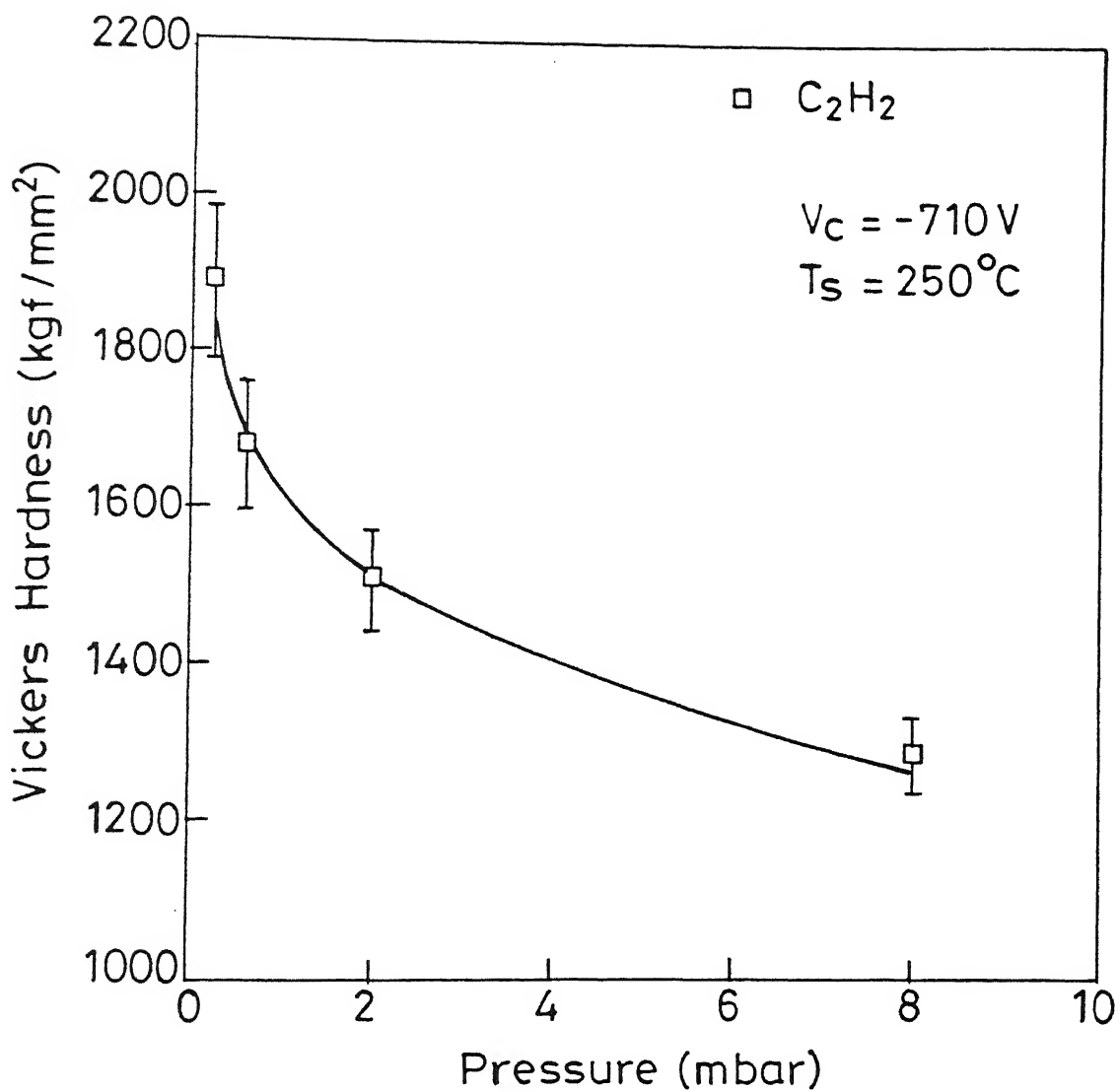


Fig.5.2 Effect of feed gas pressure on microhardness of the films deposited at  $250^\circ C$  using pure acetylene.

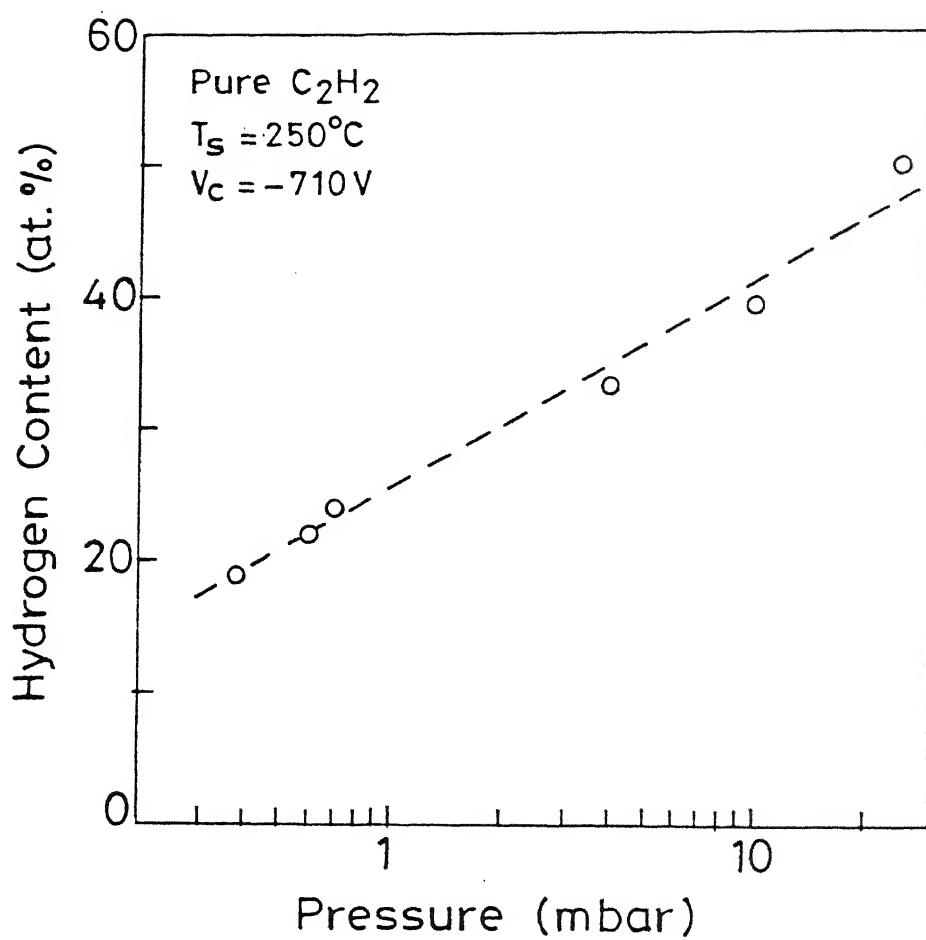


Fig.5.3 Hydrogen content vs  $C_2H_2$  pressure.



**Table 5.2** *Effect of gas pressure on the properties of a-C:H films.  $sp^{3*}$  and  $sp^{2*}$  are the percentages of C-C bonds bonded in  $sp^3$  and  $sp^2$  hybridization, respectively. Percentages of CH,  $CH_2$  and  $CH_3$  are from the bonded hydrogen content ( $C_H$ ).*

Sample No.	Pressure (mbar)	$C_H$ (at.%)	$sp^{3*}$ (%)	$sp^{2*}$ (%)	$CH_3$ (%)	$CH_2$ (%)	CH (%)	Hardness (VHN)	$E_g$ (eV)	Ref. Index
DLC22	0.10	-						2350	3.1	2.3
DLC42	0.38	18.9	65	16	30	44	26	1890	1.92	1.9
DLC19	0.6	24	55	21	47	28	25	1600	2.0	1.9
DLC18	4.0	33.2	42	25	62	25	13	1280	2.2	1.7
DLC53	10.0	39.3	46	15	71	24	5	-soft	2.45	1.6
DLC61	25.0	49.8	25	25	58	38	4	-soft	2.5	1.6

Vital clues about the nature of hydrogen bonding and resultant microstructure of these films are provided by thermal desorption spectroscopy. Fig. 5.4 shows the evolution of hydrogen and other hydrocarbons as a function of heating temperature on three samples, grown under Type A and B growth conditions. The effusion measurements were carried out at a heating rate of  $\sim 20^\circ\text{C}/\text{min}$ . Sample deposited at lower pressure shows the evolution of molecular hydrogen along with  $CH_3$  and traces of  $C_3H_3$  (Fig 5.4 c). Increase in gas pressure during growth increases the relative concentration of evolved hydrocarbons ( $CH_3$ ,  $CH_2$ ,  $C_2H_4$  and  $C_3H_3$ ) to that of hydrogen. From the discussion presented in Chapter IV, thermal effusion results confirm the porous nature of films deposited under higher growth pressure. These results also show that the threshold temperature for gas effusion and hence thermal stability of samples decreases with increasing feed gas pressure during deposition.

Optical absorption coefficients in the near bandgap region are shown for selected samples in Fig. 5.5 (a). Samples prepared at pressures of 0.38 and 4.0 mbar show typical behavior observed in hydrogenated amorphous carbon films. However, DLC22 (0.10 mbar pressure) shows the energy dependence of absorption coefficient indicating a two phase system. Two slopes in absorption spectrum imply a phase segregation. In a-C:H films having a multiplicity of structures such a behavior is not surprising. Inset in Fig. 5.5

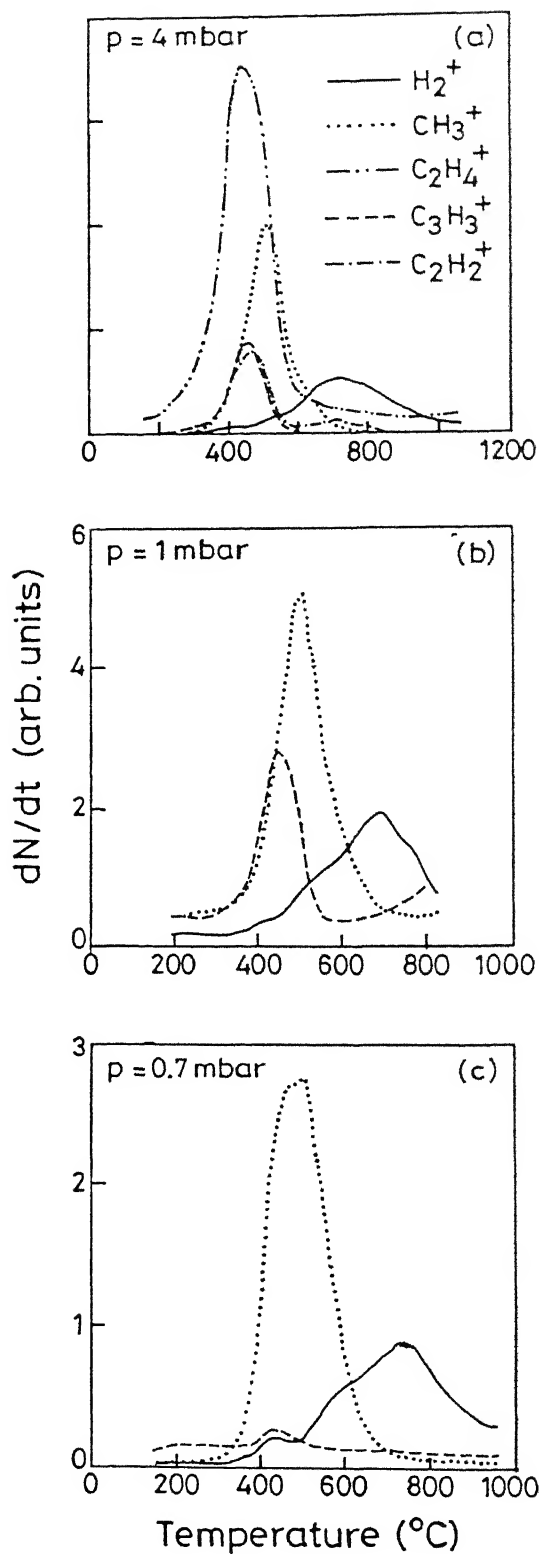


Fig. 5.4 Thermal gas effusion spectra as a function of heating temperature for films deposited at substrate temperature of 250°C and C<sub>2</sub>H<sub>2</sub> gas pressure during deposition as (a) 4 mbar (b) 1 mbar (c) 0.7 mbar.

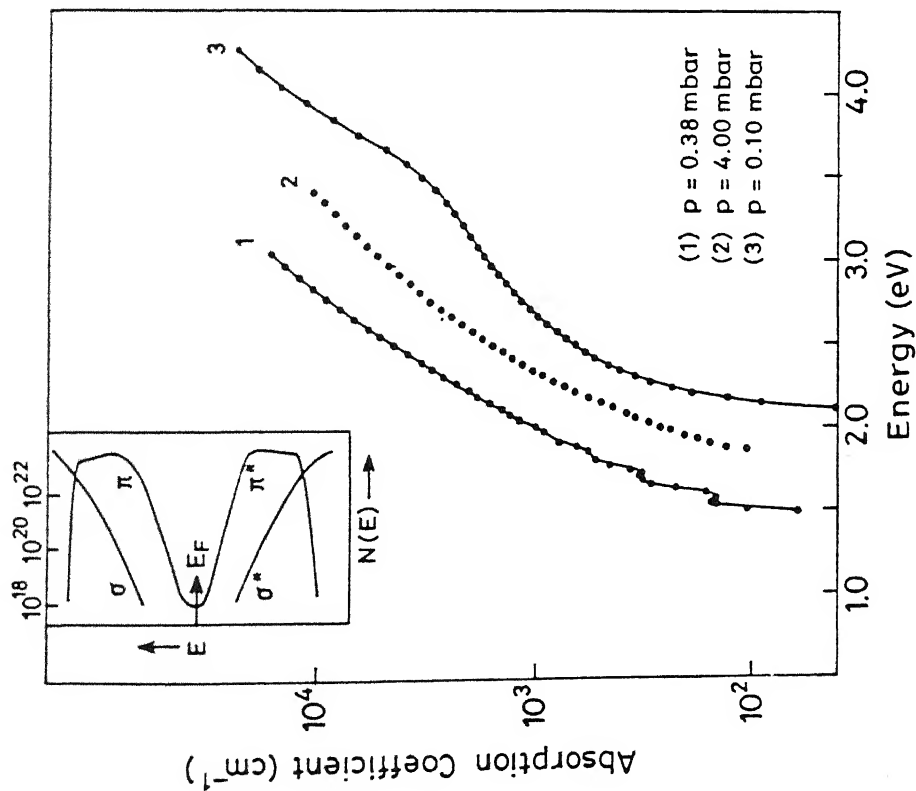


Fig.5.5 (a) Optical absorption coefficients in the near bandgap region for samples prepared at pressures of (1) 0.38, (2) 4.0 and (3) 0.1 mbar.

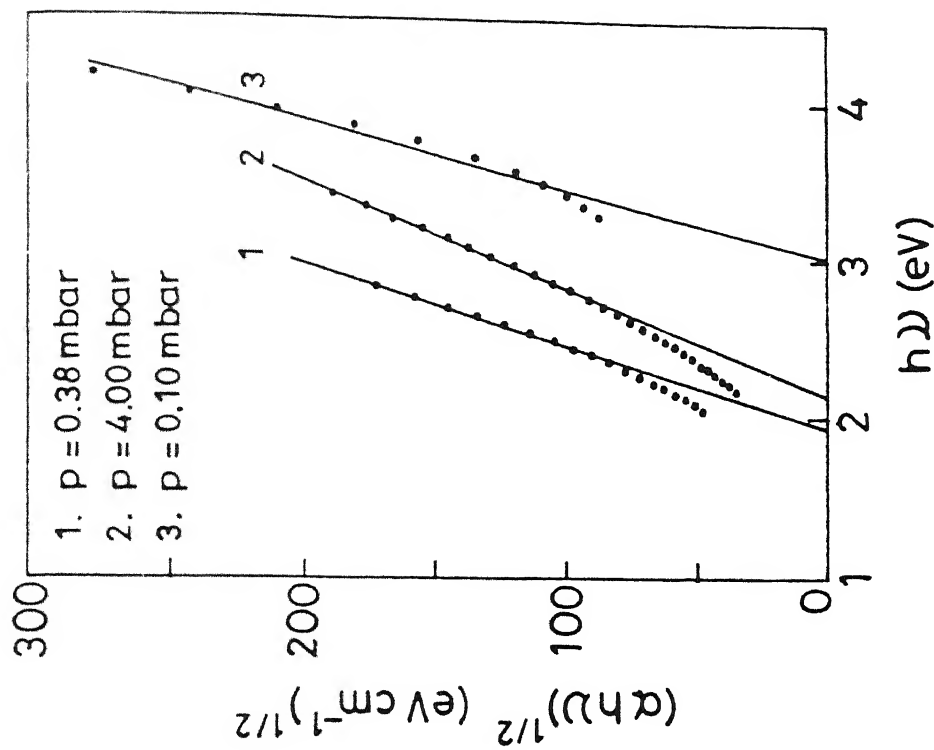


Fig.5.5 (b) Tauc plots corresponding to fig.5.5 (a).

films having a multiplicity of structures such a behavior is not surprising. Inset in Fig. 5.5 (a) shows a schematic energy band diagram for DLC films as suggested by Robertson and O'Reilly [41]. The absorption in lower photon energy range of 0.5-3.5 eV is controlled by the transitions in  $\pi-\pi^*$  states. On the other hand, transitions in  $\sigma-\sigma^*$  mainly affect the absorption in the energy range above 3.5 eV. Tauc plots (see Sec 2.4.2) corresponding to these samples are shown in Fig. 5.5 (b). Optical gap is found to increase in samples produced with increasing acetylene pressure (Table 5.2). Determination of a unique optical gap in DLC22 is difficult. A value of 3.1 eV is obtained for the phase with higher absorption coefficients. A careful look at Table 5.2 shows that samples produced at increasing acetylene pressures exhibit higher optical gaps accompanied by lower refractive indices. This is consistent with their polymeric nature deduced from the microstructural information using IR, MSTE and ERDA measurements.

Double absorption edges are also seen in highly tetrahedrally bonded amorphous carbon films deposited by the plasma beam source technique [283]. It may also be pointed out here that our low pressure deposited film (DLC22) had high stresses and film peeled off after storing for few days.

### 5.2.2 Effect Of Hydrogen Dilution

Composition of feed gas is expected to have strong effects on the constituents of plasma as well as the properties of the films. In particular, hydrogen affects the gas phase reactions as well as reactions occurring at the substrate surface. To recall from the results obtained in Chapter III, dilution of acetylene with hydrogen shifts the minimum in Paschen curve to higher working pressures (Fig. 3.4). In addition, constituent species in the plasma as observed using in-situ mass spectroscopy are also found to be modified (Fig. 3.11, 3.12).

Figure 5.6 shows the variation in the film growth rate as a function of hydrogen dilution of acetylene. In general, deposition rate is found to decrease with increasing dilution of acetylene at all deposition conditions. The variation of growth rate with dilution is consistent with earlier reported data [284,285]. Detailed film characterization were carried out on the thick samples only.

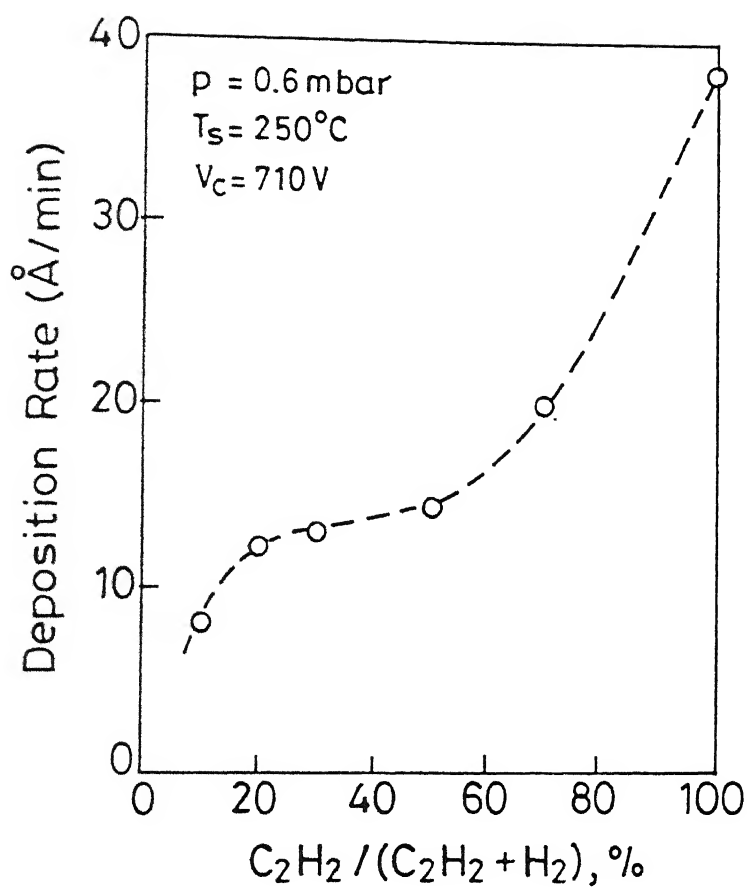


Fig 5.6 Variation in the film growth rate as a function of hydrogen dilution of acetylene.

Increase in the hydrogen concentration in the feed gas is found to influence the hydrogen content, bonding configuration and microstructure of the deposited films. At a fixed set of deposition conditions, hydrogen content in the samples is found to be less for films deposited with hydrogen diluted acetylene. Fig.5.7 shows an ERDA spectrum of a sample (DLC40) prepared using 50% hydrogen dilution at  $T_s=250^\circ\text{C}$ . ERDA yields a hydrogen content of 12 at.% in this sample. This value is half of the  $C_H$  obtained for a corresponding sample (DLC19) grown with no hydrogen dilution. In addition to a decrease in the hydrogen content, microhardness of the sample (DLC40) is found to increase to  $\sim 2100 \text{ kgf/mm}^2$ . In contrast, microhardness of the pure acetylene grown sample (DLC19) was measured to be  $\sim 1600 \text{ kgf/mm}^2$ .

Further, the increased hardness and compactness of the sample is demonstrated by the thermal effusion characteristics from hydrogen diluted sample (Fig. 5.8). Hydrogen is evolved at relatively higher temperatures along with  $\text{CH}_3$  as the only hydrocarbon species. Analysis of FTIR data also suggest hydrogen to be bonded in trihydride, dihydride and monohydrides with increasing relative fractions of 0.29, 0.25 and 0.46, respectively (Table 5.3).  $\text{sp}^3/\text{sp}^2$  ratio is found to be 2.48.

Analysis of optical data on DLC40 provided an optical bandgap of 2.05 eV and refractive index of 2.1 (to be discussed further in Section 5.2.4). Combining the above results, it is clear that the films become denser and harder when produced with the feedgas ( $\text{C}_2\text{H}_2$ ) diluted with hydrogen. In other words, one obtains a better *diamondlike* character for the sample produced with the hydrogen dilution of acetylene.

**Table 5.3** *Effect of hydrogen dilution on the properties of a-C:H films*

SAMPLE NO.	PRESSURE (mbar)	HYDROGEN DILUTION $\text{C}_2\text{H}_2/(\text{C}_2\text{H}_2+\text{H}_2)$	$C_H$ (at. %)	HARDNESS (VHN)	$\text{SP}^3$ (%)	$\text{SP}^2$ (%)	$\text{CH}_3$ (%)	$\text{CH}_2$ (%)	$\text{CH}$ (%)	$E_g$ (eV)	REF. INDEX
19	0.6	100	22	1600	55	21	47	28	25	2.0	1.9
40	0.6	50	13	2100	62	25	29	25	46	2.12	2.1
54	0.6	20	9	2250	62	29	28	22	49	-	-

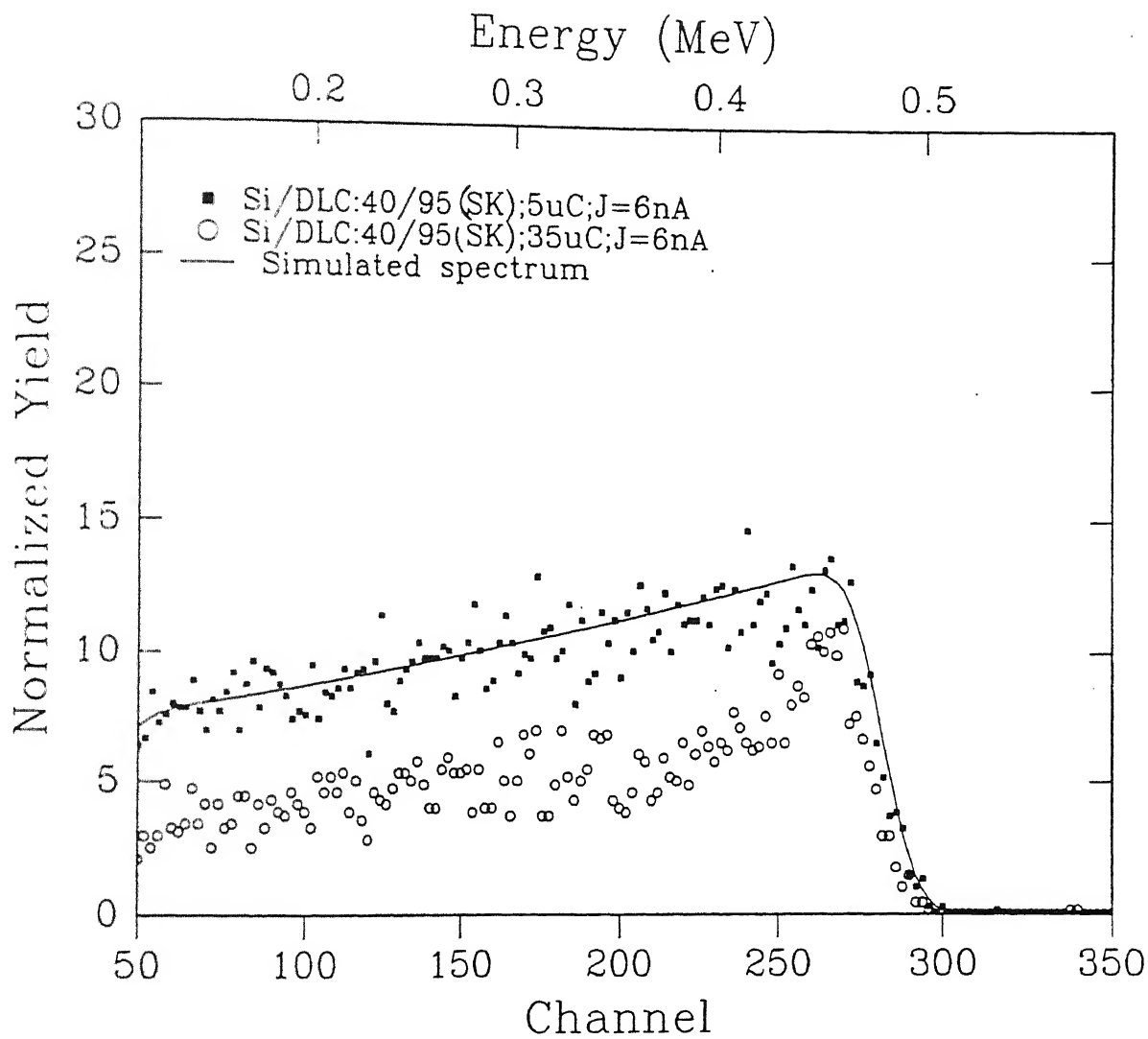


Fig.5.7 ERDA spectrum of a sample (DLC40) prepared using 50% hydrogen dilution at  $T_s=250^{\circ}\text{C}$ .

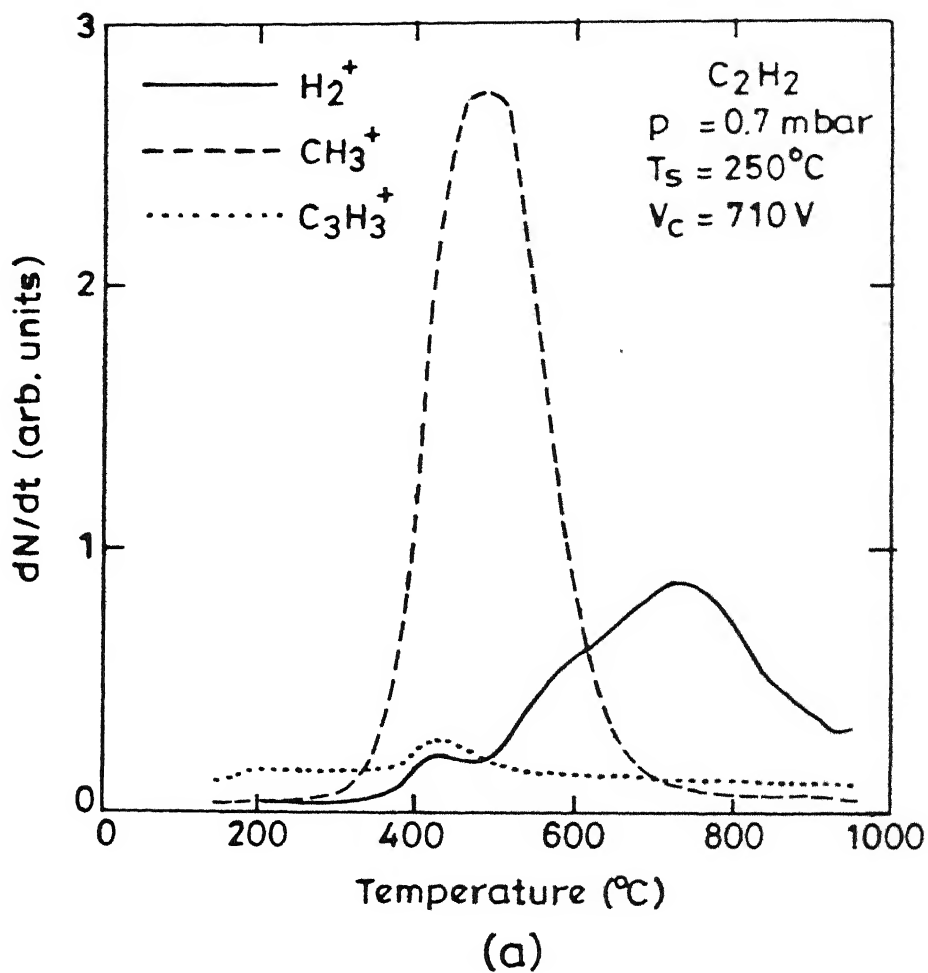


Fig.5.8 Thermal effusion characteristics from a hydrogen diluted sample (DLC40).



### 5.2.3 Effect Of Substrate Temperature

The substrate temperature has an explicit effect on the structure and properties of plasma deposited a-C:H films. Primary role of the substrate temperature is to govern the adatom mobility and surface based reactions. Any thermal activated processes will be strongly influenced by the substrate temperature. In addition, substrate temperature may also affect the emission of secondary electrons from the substrate or growing films, thus controlling the plasma properties in the vicinity of the substrate electrode. Therefore, controlling the substrate temperature constitutes the most determining step in the structure of the amorphous network. It is not surprising that a significant number of reports are available on the substrate temperature dependence of a-C:H film properties grown by a variety of deposition techniques using different carbon source material [49,62,66,286-288].

For thin film growth processes, the residence time  $\tau_i$  of the adsorbate depends on the surface temperature  $T_s$  in accordance with the Frankel equation

$$\tau_i = \tau_{i0} \exp \left( \frac{E_i^{\text{des}}}{kT_s} \right)$$

where  $\tau_{i0}$  is pre-exponential factor and  $E_i^{\text{des}}$  is desorption energy. The surface diffusion and surface reactivity is also influenced by the substrate temperature [8].

Fig. 5.9 shows the dependence of growth rate of a-C:H films on the substrate temperature ( $T_s$ ) at a constant acetylene pressure of 0.6 mbar. These results indicate that the growth kinetics is controlled by mass transport for the low-temperature region and by the surface reaction for the higher temperature region [289]. Further, a negative temperature slope at higher temperatures indicates that the incorporation of particles in the film may be intermediated by an adsorbed layer [229].

Fig. 5.10 shows the FTIR transmission spectra of three samples prepared under identical conditions but at different substrate temperatures of 125, 375 and 525°C. The deconvoluted intensities of different C-H configurations under stretching modes for these samples along with room temperature sample are plotted in Fig. 5.11. Results of the

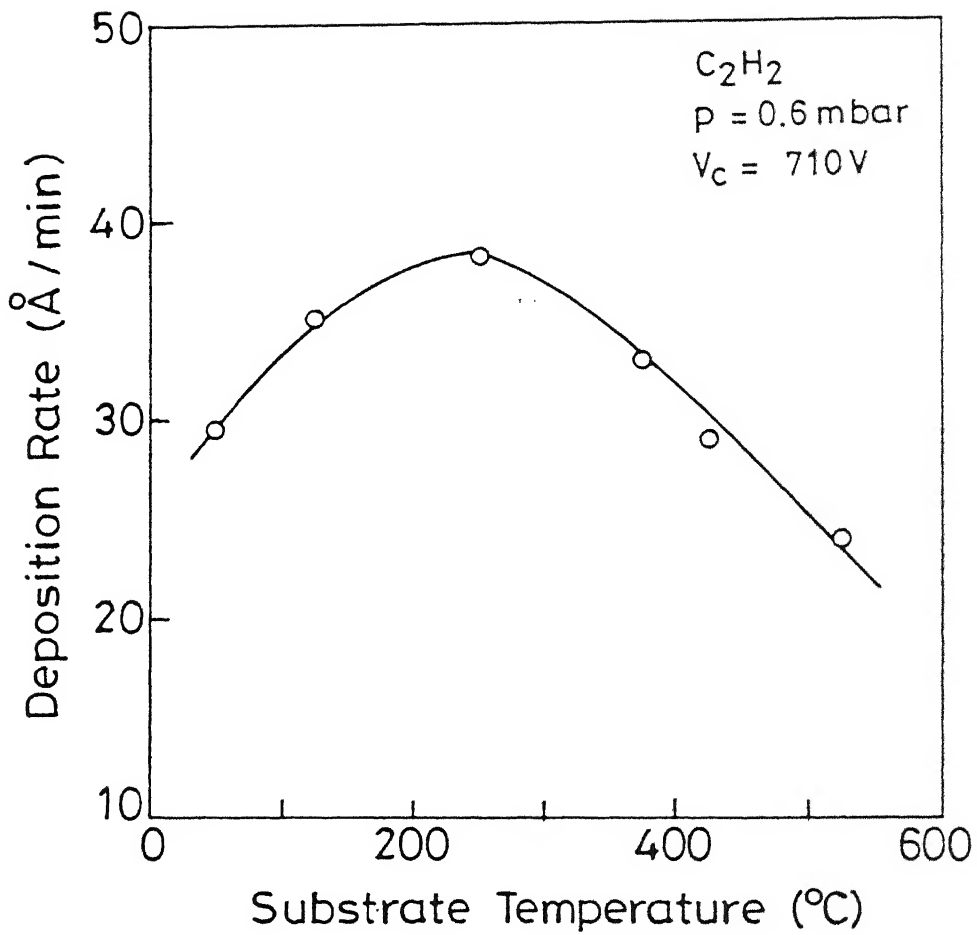


Fig.5.9 Dependence of growth rate of  $\text{a-C:H}$  films on the substrate temperature at a constant acetylene pressure of 0.6 mbar.

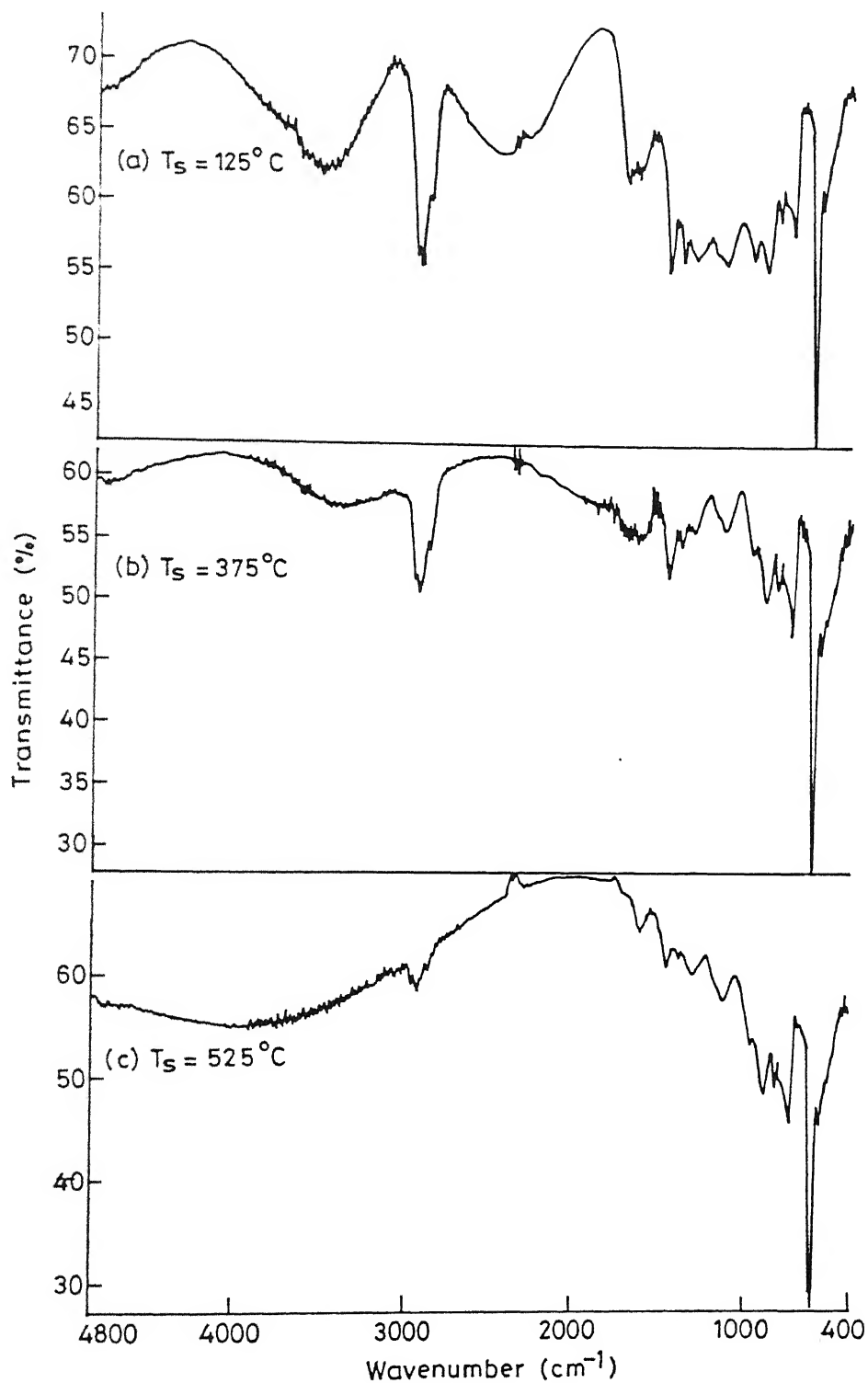


Fig.5.10 FTIR transmission spectra of samples prepared under identical conditions ( $p=0.6$  mbar,  $V_C=710$  V, pure  $\text{C}_2\text{H}_2$ ) but at different substrate temperatures of 125, 375 and  $525^\circ\text{C}$ .

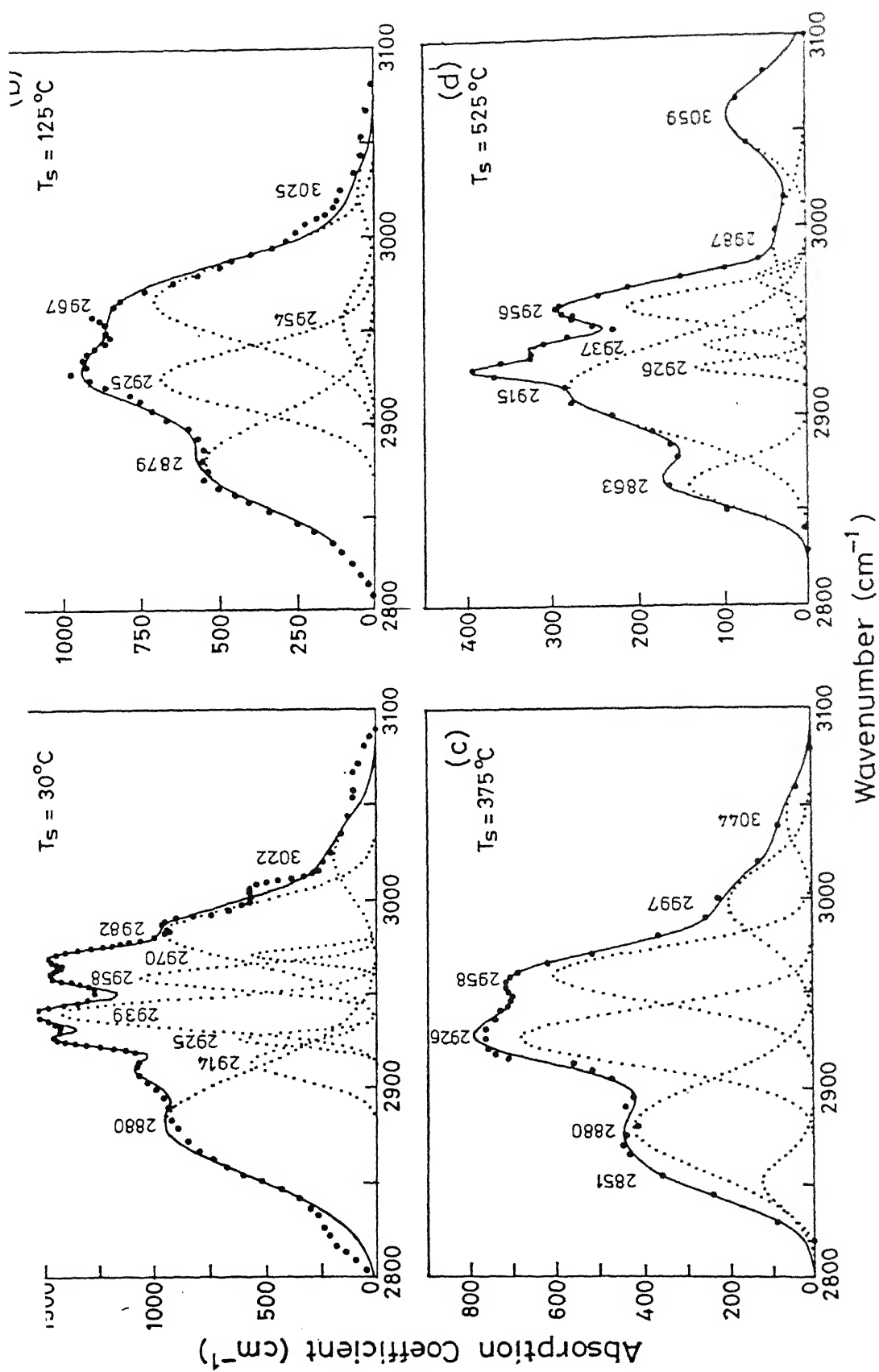


Fig. 5.11 The deconvoluted intensities of different C-H configurations under stretching modes for samples corresponding to fig. 5.10 along with room-temperature-deposited sample.

IR analysis are summarized in Table 5.4 along with other physical properties of the films. The significant features to be noted are:

- i. Room temperature deposited film shows the IR spectrum with many sharp peaks (Fig. 5.11 a). In this series, this sample contains the highest percentage of hydrogen bonded in  $\text{CH}_3$  polyhydride configuration.  $\text{sp}^3 \text{CH}_3$  and  $\text{sp}^2 \text{CH}_2$  decreases with increasing substrate temperature and the bonding in  $\text{sp}^3 \text{CH}_2$  and  $\text{CH}_1$  type is favored.
- ii. With increase in  $T_s$  above  $400^\circ\text{C}$ , the graphitic regions in the film appear to grow at the expense of the tetrahedral regions as indicated by the appearance of  $\text{sp}^2$  (arom. CH) absorption peak at  $3060 \text{ cm}^{-1}$  (Fig. 5.11d).
- iii. At the highest substrate temperature of  $525^\circ\text{C}$  in this series, C-H complexes consist a significant contribution from 3-fold coordinated regions. The major absorption peaks are observed at wavenumbers  $2863$  ( $\text{sp}^3 \text{CH}_3$ ),  $2915$  ( $\text{sp}^3 \text{CH}$ ),  $2956$  ( $\text{sp}^2 \text{CH}_2$ ), and  $3059$  ( $\text{sp}^2$  arom. CH).
- iv. Peak intensity at  $1370 \text{ cm}^{-1}$  decreases on increasing  $T_s$  and it becomes very weak for sample deposited at  $525^\circ\text{C}$ . The contribution from  $\text{CH}_3$  asymmetric bending mode ( $1450 \text{ cm}^{-1}$ ) also reduces (Fig. 5.10).
- v. Sharp peaks around  $1590 \text{ cm}^{-1}$  and  $3050 \text{ cm}^{-1}$  indicate that more C=C (double bonds) are being formed at higher substrate temperatures.
- v. Low  $T_s$  film contains broad band around  $1700$  and  $3500 \text{ cm}^{-1}$  (OH & C = O) while it reduces in  $375^\circ\text{C}$  sample and disappears in high  $T_s$  ( $525^\circ\text{C}$ ) deposited sample.

**Table 5.4** Effect of substrate temperature on the properties of a-C:H films. DLC 33A is the sample #DLC33 after heating to  $500^\circ\text{C}$  at  $20^\circ\text{C/min}$ . heating rate.

Sample No.	Substrate temperature $^\circ\text{C}$	$\text{C}_\text{H}$ (at.%)	Hardness (VHN)	$\text{sp}^3$ * (%)	$\text{sp}^2$ * (%)	$\text{CH}_3$ (%)	$\text{CH}_2$ (%)	CH (%)	$E_g$ (eV)	Ref. Index
DLC39	30	38.6	soft	34	28	67	25	7	2.2	1.65
DLC32	125	28.5	1420	60	11	67	20	13	2.0	1.85
DLC33	375	19.0	1780	54	27	53	13	34	1.8	2.2
DLC34	525	9.0	soft	38	53	20	18	62	1	2.5
DLC33A	600	5.5	soft	28	66	23	44	33	-	-
DLC19	250	24.0	1600	55	21	47	28	25	2.0	1.9

The variation in hydrogen content as a function of substrate temperature is shown in Fig. 5.12. An increase in ( $T_s$ ) from room temperature to 525°C results in the reduction of hydrogen content from about 39 to 9 at.%. The thermal energy supplied to the film by heated substrate releases hydrogen by bond breaking. Two adjacent C-H bonds on the film surface may break with the subsequent release of molecular hydrogen. It is accompanied by the association of two carbon atoms resulting in the densification of film and lowering of total hydrogen content.

As the nature and content of hydrogen varies significantly, the optical properties of these samples should show the accompanied changes. Tauc plot for the three samples deposited at 125, 375 and 525°C are shown in Fig. 5.13. Values of optical bandgap and the refractive index are shown in Table 5.4. Room temperature deposited films are characterized by high optical gap and low refractive index. High temperature deposited films at 525°C were found to be visually dark and opaque ( $\sim 1.2 \mu\text{m}$  thickness). These show a low bandgap ( $\sim 1\text{eV}$ ) and high refractive index. When seen in the light of our IR results, it is easy to understand the dependence of  $E_g$  on  $T_s$ . Decrease in hydrogen content with increasing  $T_s$  results in the lowering of the optical gap. In addition, above 400°C, the proportion of  $\text{sp}^2$  to  $\text{sp}^3$  coordinated carbon atoms increases resulting in a gap of about 1eV at  $T_s = 525^\circ\text{C}$ . Further, the films deposited at 525°C were electrically conducting. The graphitic bonding in this sample was also confirmed by Raman measurements (results not shown).

Angus et al have summarized the optical band gap observed by many research groups using different deposition techniques [33]. We have plotted the substrate temperature dependence of  $E_g$  obtained by various researchers along with our own data in Fig. 5.14. The observed temperature dependence of  $E_g$  of our dc plasma deposited films is comparable with that obtained by other deposition techniques [49,62, 66, 286-288,290]. A similar lowering of  $E_g$  occurs as a result of post deposition annealing also [35,36,54]. Annealing temperature of 600°C has been reported at which most of the hydrogen from a-C:H is evolved and  $\text{sp}^3/\text{sp}^2$  ratio falls down to zero [35,36,43,49,54]. A hydrogen content of 9 at.% and  $\text{sp}^3/\text{sp}^2$  ratio of 0.72 is observed for the sample deposited at 525°C in our case.

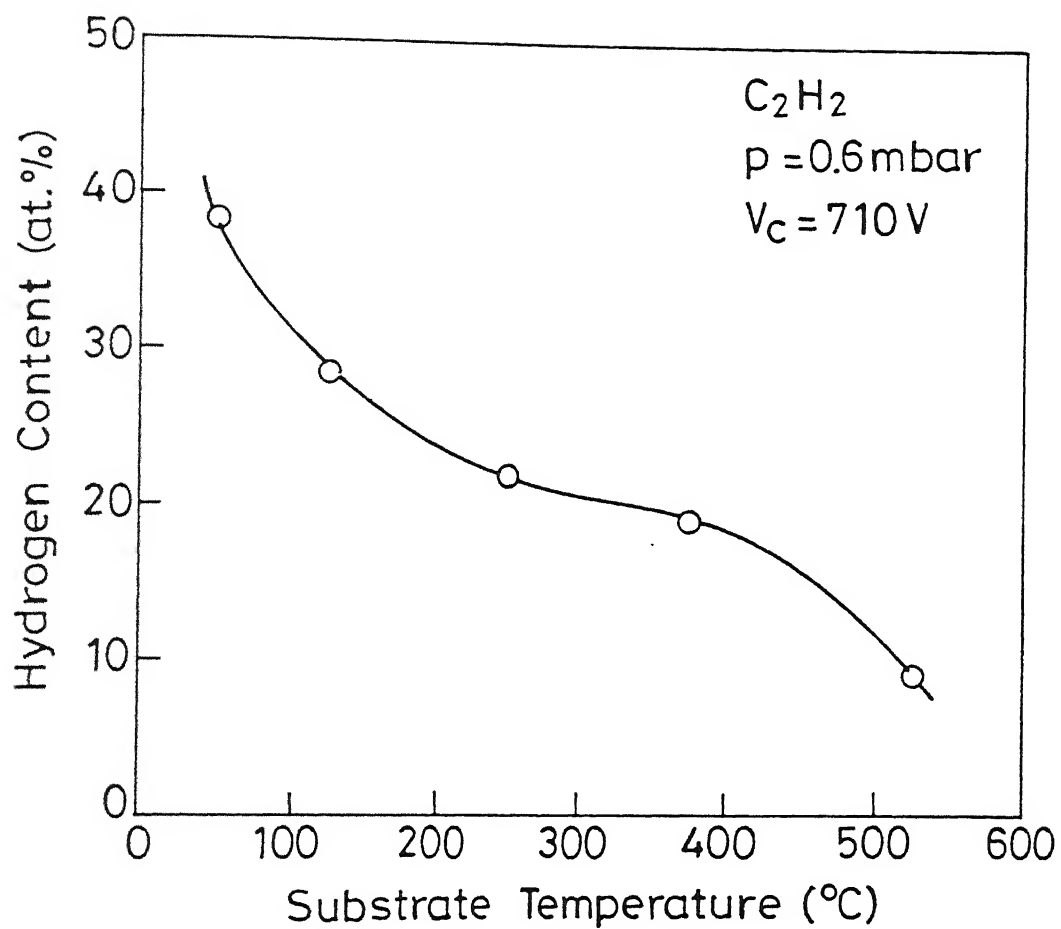


Fig.5.12 Variation in hydrogen content as a function of substrate temperature.

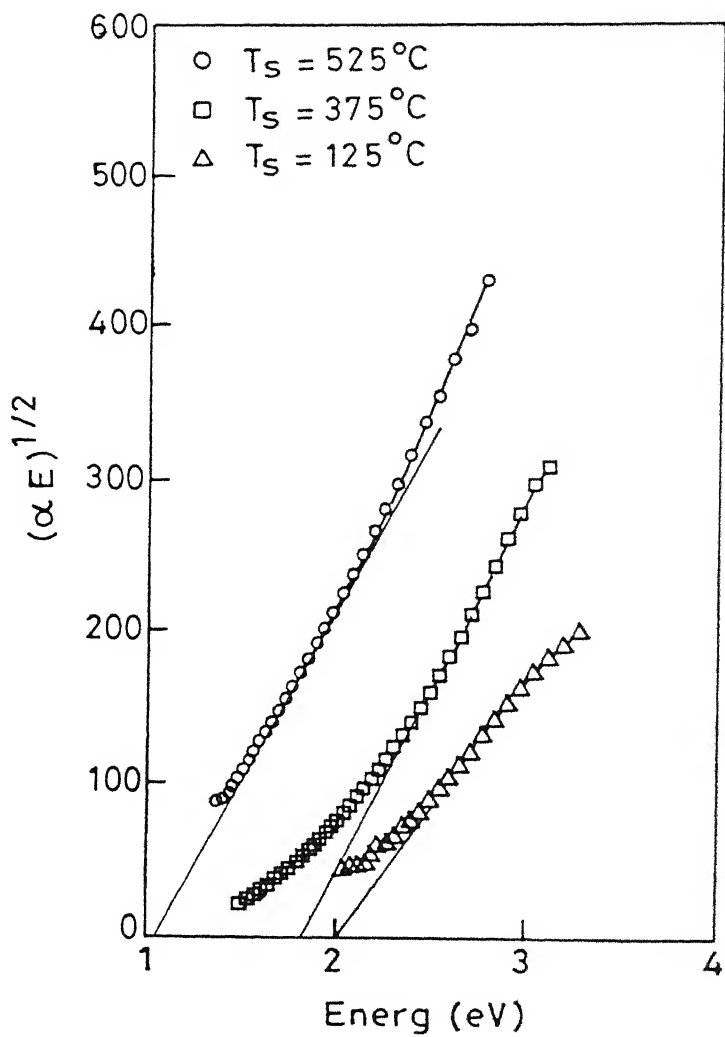


Fig.5.13 Tauc plot for samples deposited at substrate temperature of 125, 375 and 525°C.



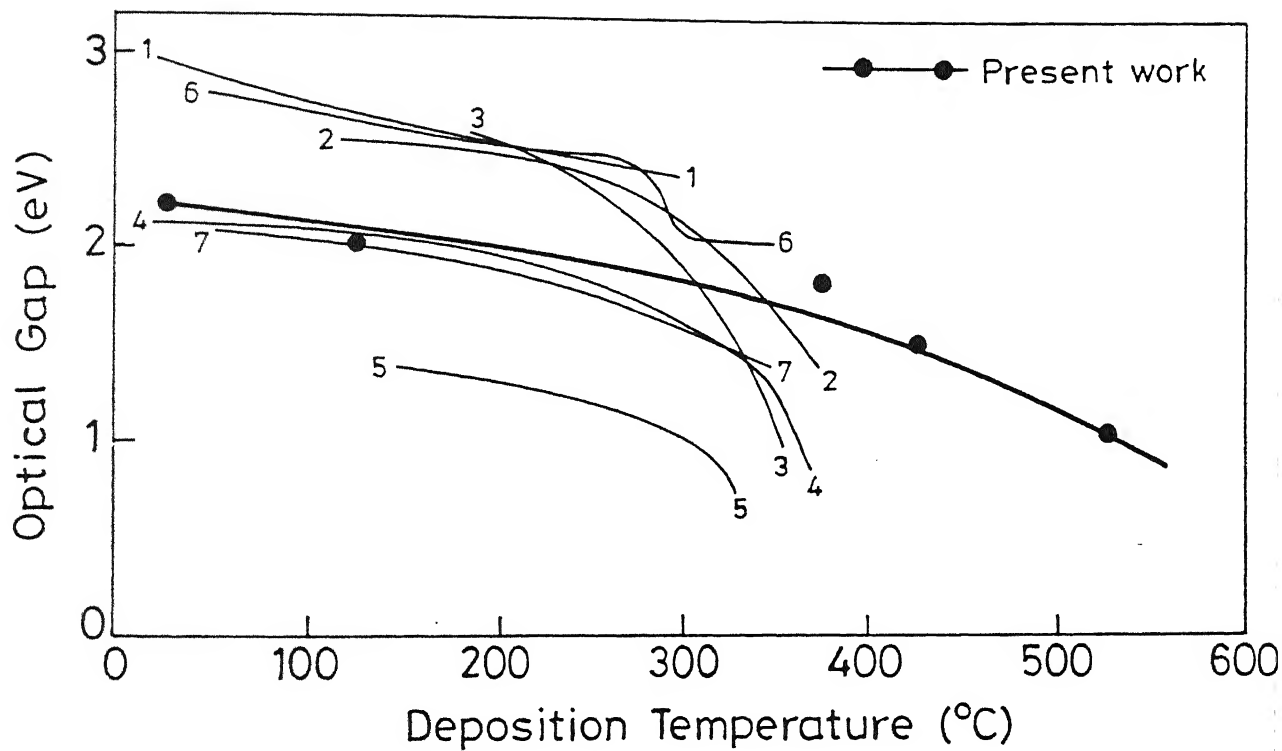


Fig. 5.14 Variation of optical bandgap as a function of deposition temperature on films produced by different growth techniques. Numbers given on the curves represent data from: (1) Ichinose, (2) Anderson, (3) Watanabe, (4) Meyerson, (5) Jones, (6) Munekawa and (7) Lin, from references 287, 66, 84, 49, 62, 288 and 290. Our data is also shown by the solid circles.

## 5.2.4 Effect Of Substrate Bias

Other than the substrate temperature, energy of the incoming species impinging on the growing film is expected to play a critical role in controlling the surface based reactions.

We have varied the substrate potential from grounded to  $-425\text{V}$ . The plasma was found to be unstable when higher ( $>350\text{V}$ ) negative potentials were applied to the anode. A negative potential is attained by the floating substrate electrode as discussed in Chapter III. Having established the results of total feed gas pressure, hydrogen dilution, and substrate temperature, these parameters were fixed at 0.6 mbar, 50% and  $250^\circ\text{C}$ , respectively.

Effect of substrate bias ( $V_b$ ) on the growth rate of films is shown in Figure 5.15. An increase in the growth rate is observed up to  $V_b$  of  $-250\text{ V}$ . Increasing the substrate bias further, growth rate is found to decrease.

Figure 5.16 shows the deconvolution of the C-H stretch region of the IR spectra for three different samples produced at  $V_f = -85\text{V}$ ,  $V_b = -250\text{V}$ , and  $V_b = -350\text{V}$ . Film deposited at floating voltage of  $-85\text{V}$  with 50% hydrogen dilution (DLC40) shows the IR spectrum typical of diamondlike carbon films. On the other hand sharp features are observed in the IR spectrum of film prepared at a bias voltage of  $-250\text{ V}$  (DLC51). The spectrum exhibits broad absorption peaks at  $2850\text{ cm}^{-1}$  ( $\text{sp}^3\text{ CH}_2$ ),  $2910\text{ cm}^{-1}$  ( $\text{sp}^3\text{ CH}$ ) and  $3000\text{ (sp}^2\text{ CH) cm}^{-1}$ , characteristic of a hard DLC film as shown in Fig. 5.16b. In addition, vibration mode at  $1140\text{ cm}^{-1}$  is seen in the lower wavenumber range which is assigned to  $\text{sp}^3\text{ C-C}$  stretching vibrational modes. Table 5.5 shows the results of hydrogen and bonding

**Table 5.5:** *Effect of substrate bias on the properties of a-C:H films*

Sample No.	Substrate bias (–V)	C <sub>H</sub> (at.%)	Hardness (VHN)	sp <sup>3</sup> * (%)	sp <sup>2</sup> * (%)	CH <sub>3</sub> (%)	CH <sub>2</sub> (%)	CH (%)	E <sub>g</sub> (eV)	Ref. Index
40	85	13	2100	62	25	29	25	46	2.12	2.1
51	250	6	2420	71	23	13	11	76	2.67	2.15
58	350	23	-	44	33	23	26	51	1.88	1.85

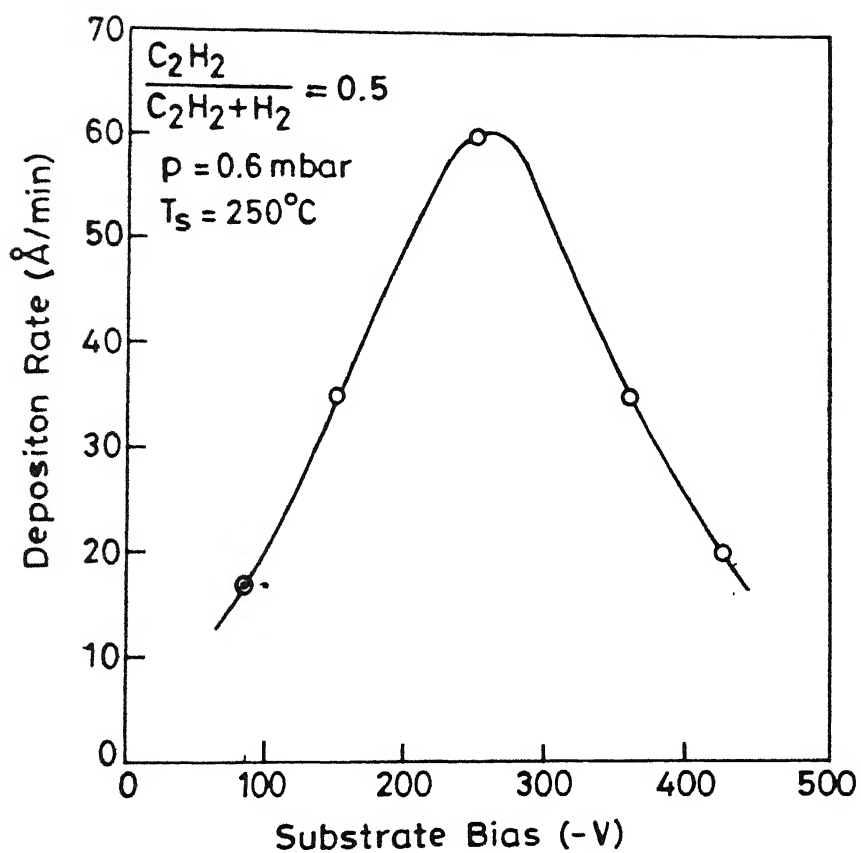
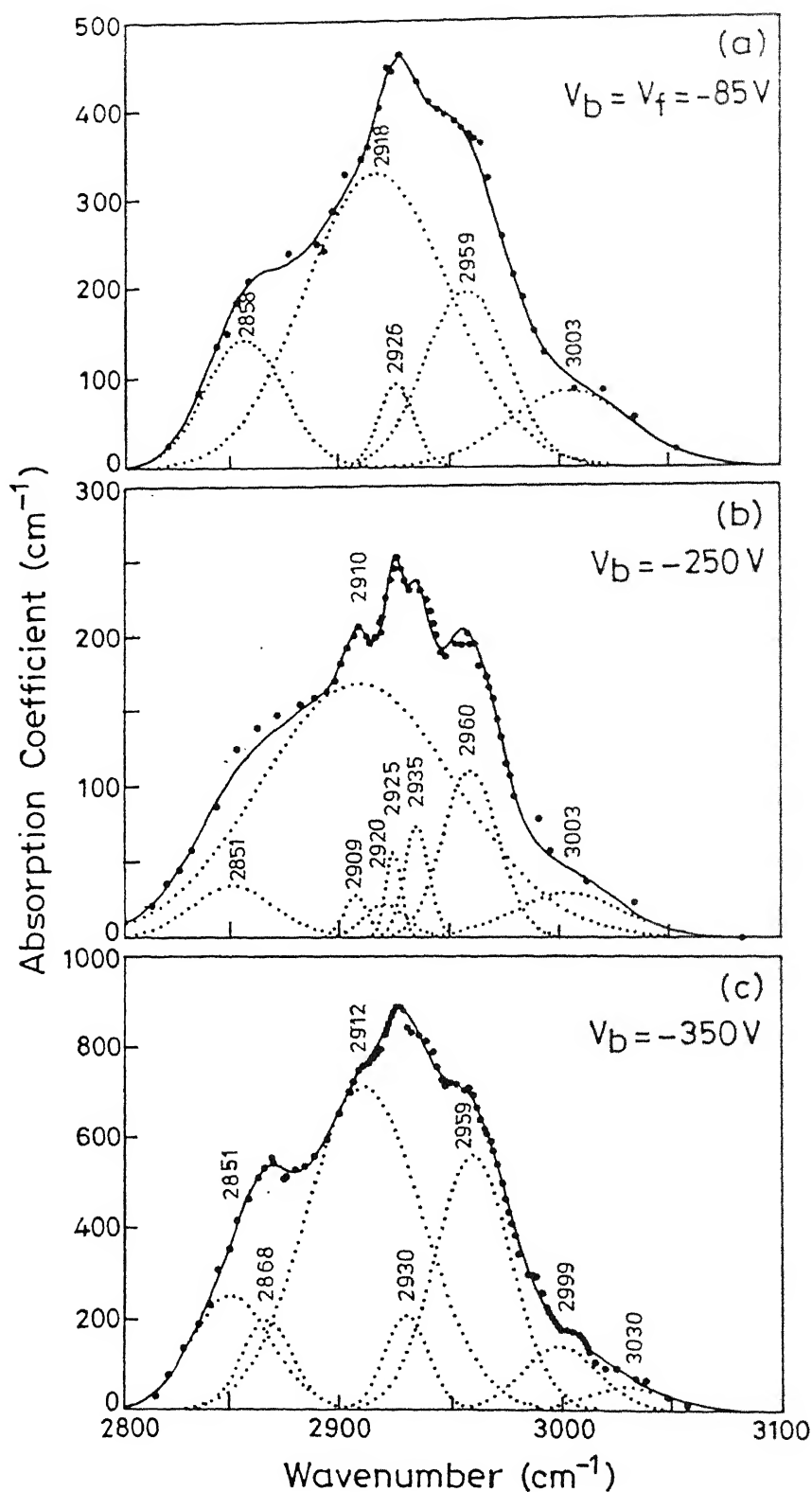


Fig.5.15 Effect of substrate bias ( $V_b$ ) on the growth rate of films.



**Fig. 5.16** Deconvolution of the C-H stretch region of the IR spectrum of DLC films deposited at various substrate potentials of (a)  $V_b = V_f = -85 \text{ V}$ , (b)  $V_b = -250 \text{ V}$  and (c)  $V_b = -350 \text{ V}$ . The acetylene dilution, substrate temperature and total gas pressures were fixed ( $\text{C}_2\text{H}_2 / \text{C}_2\text{H}_2 + \text{H}_2 = 0.5$ ,  $T_s = 250^\circ \text{ C}$  and  $p = 0.6 \text{ mbar}$ ).

analyses along with the physical properties. It is interesting to note that the total contributions from  $sp^3$  C-C bonding ( $sp^{3*}$ ) is about 71%, which is one of the highest in the samples under study. In addition, DLC51 contains lowest amount of hydrogen ( $C_H \sim 5.6\%$ ), most of it ( $\sim 76\%$ ) bonded in monohydride configuration. Similar infrared spectra has been reported by Steif et al [81] on hydrogenated tetrahedral amorphous carbon (ta-C:H) films of Ehrhardt et al [29]. We shall come back to the unique physical properties of this sample later.

The hydrogen concentration is found to decrease from 13 at.% to 5.7 at.% when negative bias voltage is increased from 85 to 250V. At higher bias of  $-350V$ , hydrogen content increases to  $\sim 23$  at.%, and ratio of  $sp^{3*}/sp^{2*}$  decreases (Table 5.5). These results on bias dependence are qualitatively similar to those observed using rf plasmas [123,139,140]. However, the effect of applied external bias are much stronger in case of our dc discharge deposited films. Exact nature of bias effects depends on the actual energy per carbon ion reaching the growth surface [291]. This, in turn, is a function of the reactor geometry, process parameters, and the composition of hydrocarbon source gases.

Thermal Effusion measurements on these samples also support the compact and void free microstructure containing low hydrogen concentrations (Fig 4.7 and 5.8).

A higher percentage of  $sp^3$  C-C bonding in the samples is indicated by increased microhardness as well as a microstructure having more of  $sp^3CH$  bonding in IR data (Table 5.5). As a consequence, optical properties of the samples deposited under bias and hydrogen dilution are significantly affected. An increase in relative amount of  $sp^3$  C-C (tetrahedral diamond,  $E_g \sim 5eV$ ) to  $sp^2$  C-C (trigonal graphite,  $E_g \sim 0eV$ ) bonding has an important effect on the optical bandgap energy. Figure 5.17 shows the effect of substrate bias on the Tauc plot. The optical gap of a DLC film deposited at  $V_b$  of  $-250V$ , is estimated to be 2.67 eV. High optical gap combined with high refractive index ( $\sim 2.15$ ) again indicates a strong diamond-like component in these films.

In order to probe the microstructural features in samples produced under bias, the power of Raman spectroscopy was employed. Striking features are observed in the micro-Raman spectra recorded on samples produced under  $-250V$  bias. Fig 5.18 shows Raman spectrum in the range  $1100-1800\text{ cm}^{-1}$  with fitted components for DLC51. The spectrum consists of a broad Raman band. A careful peakfit analysis produces sharp features

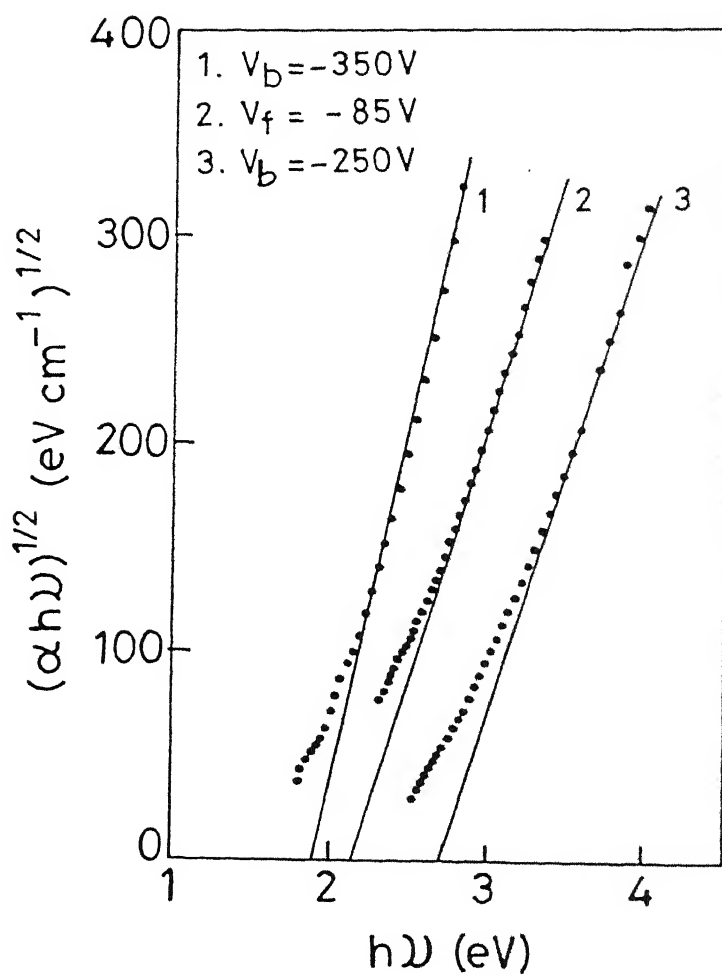


Fig.5.17 Effect of substrate bias on optical band gap.

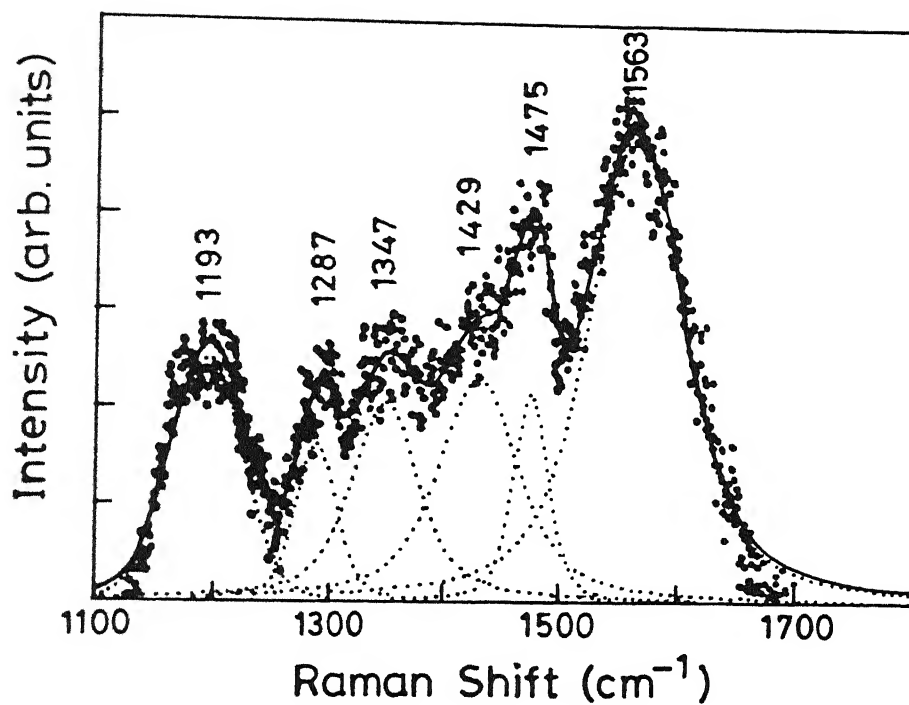


Fig. 5.10 Raman spectrum with fitted components for DLC51.

providing the signatures of hexagonal 6H diamond polytypes in this film at 1193 and 1287  $\text{cm}^{-1}$  [4,292]. The figure also shows additional features including characteristic Raman peaks of DLC centered at 1428 and 1563  $\text{cm}^{-1}$ . The observed band positions, their full width at half maximum (FWHM) and relative contributions along with the assignments are given in Table 5.6.

It may be recalled here that carbon exhibits a number of polymorphs i.e hexagonal diamond, cubic diamond, graphitic and recently identified 6H polytype [4, 292]. The presence of low wavenumber Raman peak below 1300  $\text{cm}^{-1}$  is predicted by many groups to the presence of nanocrystalline hexagonal diamond in tetrahedral amorphous carbon (ta-C:H). The vibrational modes and band positions ( $\text{cm}^{-1}$ ) for Raman active modes in 6H diamond polytype are theoretically predicted at  $A_{1g}E_{1g}$  (1332),  $2E_{2g}$  (1298),  $2A_{1g}$  (1270),  $E_{2g}$  (1210) and  $2E_{1g}$  (1208) [293]. Another theoretical prediction of broad Raman band around 1200  $\text{cm}^{-1}$  was made by Beeman et al in 1984 from the calculation of density of states [281]. This Raman mode was associated with a form of nanocrystalline diamond by Nemanich et al [294].

**Table 5.6** *Peak positions ( $\text{cm}^{-1}$ ), and their assignments of a sample (DL.C51) deposited with acetylene-hydrogen mixture (50%) at 250°C substrate temperature with a bias of -250V, observed in the Raman spectrum*

$\text{cm}^{-1}$	FWHM ( $\text{cm}^{-1}$ )	Relative Contribution (%)	ASSIGNMENT
1193	72	14	Hexagonal diamond
1287	41	6	Hexagonal diamond
1347	71	13	Cubic diamond, doublet
1429	85	18	Diamondlike carbon
1475	36	7	Amorphous carbon
1563	97	42	Diamondlike carbon



In their study, they scaled the hexagonal SiC Raman modes and postulated that hexagonal diamond should give its strongest vibrational frequencies at  $1175\text{ cm}^{-1}$ . Maruyama et al reported a Raman response at  $\sim 1150\text{ cm}^{-1}$  on hexagonal diamond [295].

Similar broad Raman band was reported earlier in *diamond films* by Yarbrough and Messier for HFCVD samples [296], Wagner et al for HFCVD samples [297], and Silva et al for rf PECVD samples [298]. Amaratunga and coworkers observed both graphite and nanocrystalline diamond peaks at  $1580$ ,  $1350$  and  $1170\text{ cm}^{-1}$  ta-C:H films. The Raman peak at  $1170\text{ cm}^{-1}$  was attributed to microcrystalline hexagonal diamond. Further, it is well known that the scattering cross-section amplitude is  $\sim 50$  times greater than that of diamond. Therefore, the absence of standard graphite peaks at  $1350\text{ cm}^{-1}$  and  $1580\text{ cm}^{-1}$  is significant. This implies that the relief in the structure of our sample is not provided by clustering of  $\text{sp}^2$  bonded phases as generally observed [40], but by the formation of nanocrystallites of diamond.

Nanocrystallites were recently reported in ta-C:H films produced by filtered cathodic arc deposited carbon films. It appears that the presence of ion beam irradiation during growth is a necessity for producing such mixed phase systems. Clearly, Micro-Raman analysis shows the presence of nanocrystallites of hexagonal diamond polytypes in these dc glow discharge plasma deposited CVD samples produced under appropriate bias conditions. The observed features in the microstructure and dependence of  $\text{C}_\text{H}$  on substrate potential may be explained by an effect of ion bombardment of the films during growth as discussed in next sections.

### 5.3 PROCESSES IN GROWTH OF a-C:H FILMS

Growth of thin films from plasma decomposition of gases depends on the homogeneous processes occurring in the plasma and heterogeneous processes taking place at the substrate surface [228]. In this section, we discuss the dominant plasma and surface processes in a-C:H deposition from dc glow discharge decomposition of acetylene. These processes are controlled by varying the deposition parameters discussed above.

The primary processes of electron- $\text{C}_2\text{H}_2$  molecule interaction produce reactive plasma species i.e. radicals, ions, atoms, excited molecules and photons (as shown in

Chapter III). The main collision processes among these reactive plasma species in a glow discharge include electron impact ionization, dissociation, excitation, relaxation, recombination and  $e^-$  attachment [215]. The ions and radicals undergo various secondary reactions with  $C_2H_2$  molecules (Chapter III, section 3.5). The chemical species created in the plasma volume are transported towards the substrate by a diffusion mechanism. The deposition process involves condensation of hydrocarbon species into the amorphous carbon matrix and liberation of some excess hydrogen. The surface processes include the reactions of the radicals and the secondary electron emission. The flux of high kinetic energy electrons, ions and neutral atoms along with metastable atoms, free radicals and UV radiation on substrate may cause etching, sputtering and deposition [229].

### 5.3.1 Homogeneous Processes

Due to lower energy electrons (8-12 eV) in the glow discharges [230], primary processes of electron-impact dissociation of acetylene generate mostly radicals. In the CVD plasmas, major constituents are neutral stable gases while the fraction of ions and radicals is found to be rather low [299]. These ions and radicals may undergo various secondary reactions, mainly with the neutral gas molecules, producing higher hydrocarbons. The probability of secondary reactions is large at high pressures due to the large life time of radicals [216]. Mass spectroscopic analysis of the stable species clearly show the dissociation of gases at low pressures and increased polymerization at higher pressures (Fig. 3.10). At low pressures, the probability of plasma phase collisions is low. Thus, formation of higher mass number species  $C_xH_y$  ( $x > 2$ ,  $y > 2$ ) is not favored. Addition of hydrogen in the feed gas further reduces the number of activated plasma phase reactions between carbon bearing molecules and/or leads to cracking of already formed polymers. The physical properties of the films are consistent with the observed behavior of the discharge. In particular, hardness of the films decreases exponentially with increasing pressure while hydrogen content increases. Similar behavior in microhardness has been observed by Zou et al using rf discharge of acetylene over a larger pressure range [43,44].

Infrared spectra (Fig. 4.1) and thermal effusion measurements (Fig. 5.4) support the role of homogenous reactions in the plasma in determining the properties of films. A high concentration of additional hydrocarbons like  $C_2H_2$ ,  $C_2H_4$ ,  $C_3H_3$  and  $C_4H_3$  is

observed in the effusion spectra of B type films (Fig. 5.4). These species are available in abundance in the plasma (Fig. 3.10) and are possibly trapped in the films during growth [223]. While films deposited under region A are hard, compact and diamondlike, those deposited under deposition conditions of regions B are soft, porous (void rich) and polymeric in nature.

Addition of hydrogen to the hydrocarbon gas has major impact on the discharge characteristics (Figs. 3.4 and 3.11). In particular, a shift in minimum of the Paschen curve to the higher p.d values is observed (Fig. 3.4). Therefore, hydrogen dilution also increases the working pressure range without polymerization. Although molecular hydrogen is seen to increase in the plasma as a by-product of polymerization also (Fig. 3.10), the effect of additional hydrogen dilution on the film properties is significant. Presence of additional hydrogen suppress the forward reactions leading to higher hydrocarbons (polymerization). Therefore, harder and compact films with low hydrogen content are obtained at the same deposition temperature.

### 5.3.2 Heterogeneous Processes

Keeping the discharge conditions in region A of the Paschen curve, film properties could be further tailored by tuning the surface based reactions. Temperature of the substrates and negative bias applied to the substrates were found to affect the surface reactions significantly.

Using pure acetylene, a decrease in absolute hydrogen content and an increase in hardness is observed with increase in substrate temperature. The role of heterogeneous reaction is thermal activation of the surface mobility of the adsorbed radical species and the thermal desorption of hydrogen. The dehydrogenation of  $\alpha\text{-C:H}$  may take place by the reaction  $\equiv\text{C-H} + \text{H-C}\equiv \rightarrow \equiv\text{C-C}\equiv$ . This leads to an increase in carbon-carbon cross-linking and reduction of voids in the films. Thermal effusion characteristics show evolution of methane as the only hydrocarbon species from a DLC film deposited at  $\sim 375^\circ\text{C}$  and support this view. Result presented on the high temperature deposited samples are consistent with their expected compact network.

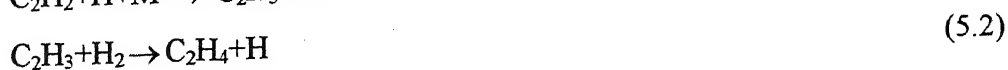
We have observed a deterioration of diamond like properties at and above substrate temperature of about  $425^\circ\text{C}$ , consistent with earlier observations. The high

## 5.4 GROWTH MODEL

Based on the results presented in previous sections on dc glow discharge decomposition of acetylene, and understanding of the growth processes, it is possible to present a growth model to qualitatively explain the growth of a-C:H films.

Substantial work has been reported by Turban and Coworkers [124, 221, 231] on the growth of carbon films from CH<sub>4</sub> using rf glow discharge plasma. Mutsukura et al have also proposed a growth model for hard carbon films in a CH<sub>4</sub> rf plasma [226]. In general, methane dissociation mechanisms have been proposed similar to the well studied growth of a-Si:H using silane [299,300]. In other cases, specially to describe the growth of diamond films, modeling of the gas phase reactions has been centered around hot filament systems due to their simplicity [301-303]. Proposed growth mechanisms have identified the methyl radical (CH<sub>3</sub>) [304] and the acetylene molecule (C<sub>2</sub>H<sub>2</sub>) [305] as the growth precursors to deliver carbon from the hydrocarbon gas to the growing solid network. As mentioned earlier, there are few reports of growth from acetylene and still fewer using dc glow discharge of acetylene.

To describe the growth mechanism, the first task is to identify the growth precursor. Based on our in-situ mass spectroscopic data from the dc plasma (Chapter III), evidences from thermal effusion data (Chapter IV), and parametric dependence of film properties on the process variables (section 5.2), we propose methyl radical (CH<sub>3</sub>) to be a primary candidate for the growth of hard carbon (DLC) films. While methyl radical production from CH<sub>4</sub> is fairly well known, conversion of C<sub>2</sub>H<sub>2</sub> to CH<sub>3</sub> is not well understood. One reasonable reaction pathway for CH<sub>3</sub> production from C<sub>2</sub>H<sub>2</sub> involves the addition of hydrogen to C<sub>2</sub>H<sub>2</sub> through a series of reactions with H and H<sub>2</sub> until C<sub>2</sub>H<sub>5</sub> is formed [226,305]. This radical can now react with atomic hydrogen to form a pair of methyl radicals using the reactions:



It is important to note that if atomic hydrogen is not present then key reactions can not proceed to form  $\text{CH}_3$  from the acetylene in gas phase. Fig. 3.10 - Fig. 3.12 show significant presence of acetylene dissociation products in the mass range 12 to 17 corresponding to  $\text{CH}_n$  ( $n=0$  to 5). In addition,  $\text{C}_2\text{H}_4$  and atomic hydrogen is also formed in abundance in the dc plasma of  $\text{C}_2\text{H}_2$ .

Another possible  $\text{CH}_3$  production mechanism for initiating the conversion of  $\text{C}_2\text{H}_2$  into  $\text{CH}_3$  involves breaking of C-C bond in  $\text{C}_2\text{H}_2$  at the cathode surface, rather than by gas phase reactions with hydrogen atoms.  $\text{C}_2\text{H}_2^+$  is easily produced in the acetylene plasma [222] as observed in Fig. 3.10. These ions are accelerated towards the negative cathode and may fragment at the surface. Hydrogen adds onto the fragments to form  $\text{CH}_3$ .

Indirect evidence of presence of  $\text{CH}_3$  as a growth precursor is obtained from the mass spectroscopic thermal effusion (MSTE) measurements on a large number of samples produced under a variety of growth conditions (section 4.10 and 5.2). Activation energies obtained from MSTE data suggest the  $\text{CH}_3$  to be available as a unit in the film and not a product of gas phase reactions. Further, estimates of mass erosion from the films on heating using MSTE data also indicate the extent of the  $\text{CH}_3$  available in the film (sections 4.4&4.5).

Isotopic labeling experiments have been performed using  $\text{C}_2\text{H}_2$ , and the results were found to be consistent with the  $\text{CH}_3$  acting as a gas phase precursor for diamond growth [307]. Ultraviolet absorption spectroscopy of the  $\text{CH}_3$  radical density and  $\text{C}_2\text{H}_2$  molecule fractions in a hot filament diamond growth process using  $\text{C}_2\text{H}_2$  and  $\text{H}_2$  gas mixtures[231] also support the formation of  $\text{CH}_3$ . However, it should be mentioned as suggested earlier [283] that a variety of hydrocarbons could act as growth precursors and no single species is *always the* growth species.

Once the carbon carrying species are formed in the plasma, they arrive at the substrate surface through drift or diffusion along with atomic and molecular hydrogen. Energy of the ions impinging on the substrate is governed by the sheath potential at the substrate electrode surface (Fig. 3.6). A solid network of carbon film is formed through a complex set of processes. We can discuss some of these steps qualitatively in analogy with the well known growth of a-Si:H [299,300]. A schematic illustration of growing a-C:H film is shown in Fig. 5.19 [226]. Reactive species arrive at the top surface with an energy

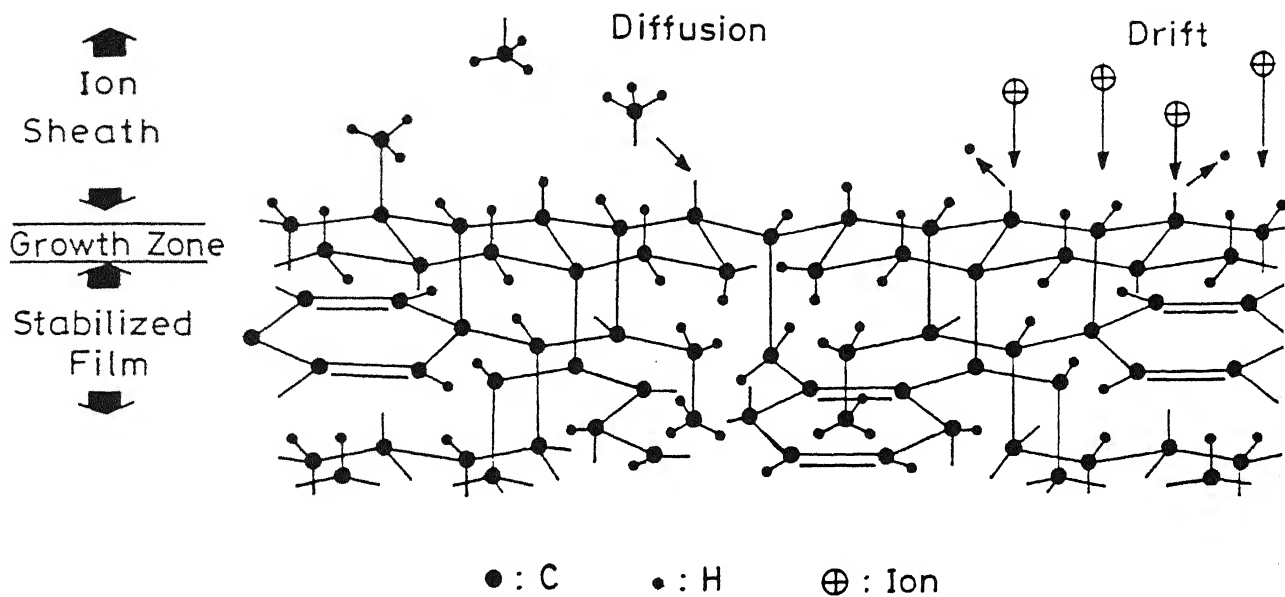


Fig.5.19 A schematic illustration of growing a-C:H film. Reactive species diffuse to the top surface with an energy distribution determined by discharge conditions and ion sheath potential. At the underlying growth zone, thermally activated reactions: cross-linking of C-C atoms in solid networks and dehydrogenation takes place.

distribution determined by the discharge conditions. At the underlying *growth zone*, thermally activated reactions: cross linking of C-C atoms in solid networks and dehydrogenation takes place. These processes would depend on the substrate temperature and the subplantation range of ions [308]. Thus, thickness of the *growth zone* will be a function of externally controllable parameters such as  $T_s$ ,  $V_b$  and gas pressure. As the deposition time is increased (i.e., film thickness), a stabilized a-C:H solid network would be formed below the growth zone. Microstructure of this stabilized layer would no more be dependent on plasma parameters. However, at high substrate temperatures, hydrogen migration and structural reorganizations may take place in the stabilized layer due to long term thermal annealing effects. In our case, only at substrate temperatures above 400°C, thermal annealing effects may contribute to the observed microstructure and film properties (Chapter IV).

At the usual deposition temperatures (~250°C), the growth surface of film is saturated with hydrogen through  $\equiv\text{C-H}$  bonds. In addition, some dangling bonds  $\equiv\text{C}^\cdot$  may also be present. The atomic hydrogen may form a chemical bond with  $\equiv\text{C}^\cdot$  or recombine with a hydrogen atom to produce molecular hydrogen. The radicals C, CH and  $\text{CH}_2$  can transport carbon atom by constructing chemical bonds on  $\equiv\text{C}^\cdot$  as well as on  $\equiv\text{C-H}$ . The radical  $\text{CH}_3$  on the other hand, can form a chemical bond only on one site  $\equiv\text{C}^\cdot$ , but it can be physisorbed on  $\equiv\text{C-H}$ . The weak energy of the bond allows it to diffuse till it finds a site  $\equiv\text{C}^\cdot$ . During this diffusion,  $\text{CH}_3$  can undergo desorption, take out a hydrogen atom from the surface to form  $\text{CH}_4$  or can recombine with another  $\text{CH}_3$  to produce  $\text{C}_2\text{H}_6$ . In growth zone, thermally activated cross-linking of neighboring C-H bonds and hydrogen desorption takes place.

The probability of incorporation of different radicals in the growing film depends largely on their sticking coefficient [124, 309]. The most dominant radical  $\text{CH}_3$  possesses a low sticking coefficient (0.02 to 0.03) [220] which is significantly influenced by ion flux as suggested by Moller [310]. The deposition rate, therefore, may be expressed as [226]

$$R_d = (mS/\rho) \phi(\text{CH}_3) \quad (5.5)$$

where  $m$  and  $\rho$  are mass and density of carbon film,  $\phi(\text{CH}_3)$  is incident flux density and  $S$  the effective sticking probability of  $\text{CH}_3$  radicals on the surface.  $S$  depends almost linearly on the number density of dangling bonds on the growth surface [311]. The

dangling bonds may be formed due to hydrogen abstraction through molecule formation by atomic hydrogen or  $\text{CH}_3$  as described above. However, the main source of dangling bonds on the growth surface is considered to be the sputtering of hydrogen on the surface due to ion bombardment [220, 312]. The generation rate of dangling bonds and hence the concentration of reactive carbon incorporation sites in the growth zone is proportional to the number density and kinetic energy of the ions. This process explains the observed increase in growth rate and a decrease in hydrogen content in our samples on increasing the ion bombardment on growing film surface. The effect of ions on growth may be in terms of influencing the mobility of surface radicals, the surface chemistry and the ionic implantation.

Further, the availability of atomic hydrogen also plays a crucial role in top surface reactions. In our case of low substrate temperature and light hydrogen dilution, atomic hydrogen is expected to mainly attack the weak C-H bonds that are found on the surface of the growing film and recombine with a hydrogen atom to form molecular hydrogen. This leads to a lower hydrogen concentration in the film in case of hydrogen dilution of the feedgas in the plasma as compared to pure acetylene (see Fig. 5.7). Atomic hydrogen is believed to ensure high surface mobilities for the depositing species by maintaining a hydrogen - terminated surface. This along with the etching process as proposed by many workers suppresses the growth of non-diamondlike carbon [16].

Under the discharges, where homogeneous reactions may dominate leading to polymerization (region B, plasma conditions), the carbon may be transported to the growth zone by a variety of precursors. Moreover, larger hydrocarbon molecules may get trapped in the films yielding films with high hydrogen concentration with polymeric nature and large void networks. Indeed, our thermal effusion data on the films, combined with in-situ mass spectroscopic analysis of the plasma support this view.

In light of the above growth model, let us now look at some reactor and process dependent effects in their ability to yield films diamond-like carbon films. At the gas density and electrode separation used for a-C:H deposition, the positive column is not observed (Fig. 3.6a). In the negative glow, the electrons dominate due to their much larger drift velocity relative to ions. Substrates are kept just inside the negative glow at the anode which is grounded, biased or left floating. At this electrode, electron density is large



but energy is low such that electrons cannot ionize acetylene. Hence, dissociation dominates near anode. In contrast, ionization dominates near cathode. The high density of activated species leads to high degree of polymerization near cathode. This results in formation of powder and a *yellowish* layer as seen by other researchers also [135]. Further, the high field at cathode accelerates ions into the cathode surface leading to graphite formation on cathode. Hence, polymeric and graphitic deposits may result on cathode.

Good quality DLC films are deposited on anode under appropriate plasma conditions. Dissociation of molecular hydrogen near anode surface provides abundant atomic hydrogen on the growth surface. The growth on anode takes place predominantly by neutral radicals with diamond  $sp^3$  bonding due to the presence of atomic hydrogen. A continuous arrival of activated hydrocarbon molecules and atomic hydrogen on the surface of substrate provides enough energy to convert the  $sp^2$  bonded carbon atoms into a relatively stable network of the  $sp^3$  bonded carbon. In addition, the etching of unstable phases ( $sp^1$  &  $sp^2$ ) compete with the growth of stable phases. The atomic hydrogen plays a crucial role in promoting this reaction and stabilizing the phase. It is apparent from the effect of substrate temperature and anode bias on the film growth rate Fig. 5.9 & 5.14 that film deposition results from interactions between the films bulk and a physisorbed layer. The physisorbed layer (growth zone) is transformed into a growing film by the assistance of ion bombardment. The growth rate is therefore proportional to the particle flux forming physisorbed layer as well as the ion flux. The energy of bombarding ions is also crucial for growth as it increases sticking probability of growth species on the growing film.

All of our results can be understood in the light of the ion assisted growth model presented here. IR spectroscopy and thermal effusion data clearly indicate that the process of hydrogen removal decreases the hydrogen content and increases the C-C cross-linking probability. Less hydrogen content and denser features with higher percentage of C-C cross-linking gives rise to a higher optical bandgap and index of refraction of the DLC films (Tables 5.2-5.5). Of particular interest is the evidence of a growth zone thickness (near surface transitional layers, NSTL) estimated by us from the combination of IR, ERDA and MSTe data (Section 4.4.4). In addition, the nonuniform hydrogen distribution in the samples (hydrogen rich at the surface or NSTLs) as observed

in ERDA depth profiles for films prepared under certain growth conditions can be easily understood in terms of the above growth model.

## 5.5 DISCUSSION

In the results presented above, we have seen the dependence of film microstructure and physical properties on the process parameters. In this section, we look at a unified picture of the properties and microstructure relationship of a-C:H films deposited by acetylene dc glow discharge irrespective of the growth condition.

### 5.5.1 Average Coordination Number

The multiplicity in C-C and C-H bonding in a-C:H networks can perhaps be unified by a single parameter, known as average coordination number. In amorphous semiconductors, the average nearest-neighbor bonding environment can be described in terms of the theories of random covalent networks of Phillips and Thorpe [313]. According to Phillips, a random covalent network is completely constrained when the number of constraints per atom is just equal to the number of mechanical degrees of freedom per atom. The number of degrees of freedom of a single atom is three, the dimensionality. The number of constraints per atom can be calculated from its coordination number, i.e., the number of directed valence bonds to nearest neighbors. Increasing the number of bonds contributes to stabilization of the solid. However, in a random covalent network, increasing number of directed bonds will also cause strain energy because of bond stretching and bond angle distortion. Phillips has suggested that an average coordination number of  $m = \sqrt{6} = 2.45$  of the amorphous material represents the best compromise between mechanical stability (related to cross-linking) and stress minimization (due to minimal bond length and bond-angle disorder). The average coordination number,  $m$ , in a-C:H can be defined as [314]:

$$m = \frac{4C_{sp^3} + 3C_{sp^2} + C_H}{C_{sp^3} + C_{sp^2} + C_H} \quad (5.6)$$

We have determined the average coordination number,  $m$ , from calculated values of  $C_{sp^3}$  (i.e.  $sp^3$  fraction) and  $C_{sp^2}$  ( $sp^2$  fraction) and  $C_H$ . The results are plotted as a function of hydrogen content and film hardness in Fig 5.20 (a) and (b), respectively. As expected, average coordination number decreases with increasing hydrogen content in the films. However, for hydrogen content <40%, the average coordination number is substantially greater than the optimal predicted value of 2.4 for monoatomic random covalent networks. Angus and Jansen [315] also showed high  $m$  on good quality DLC films deposited by other techniques. Wang et al [314] reported a decrease in  $m$  from 2.6 to 2.3 with increase in  $C_H$  from 28% to 44% and  $sp^3/sp^2$  ratio from 0.29 to 0.75. Zou et al have reported values of  $m > 3$ , on plasma deposited films [43,44].

Possible presence of divalent atoms (such as oxygen) or  $sp^1$  bonded carbon could help in explaining the results. However, these sites will be required in large quantities to account for the higher estimates of  $m$ . Our RBS analysis on limited number of samples rules out the possibility of high oxygen content in the films. Presence of unaccounted voids or dangling bonds can also rationalize the discrepancy. Again, our thermal effusion analysis, optical gap and refractive index measurements suggest a relatively compact microstructure of films with lower hydrogen content and rule out this possibility. Assuming the structure to be 'over constrained' and  $m$  as the true representation of the a-C:H networks, a linear fit to the data yields:

$$m = 3.68 - 0.027 C_H$$

Taking this empirical relationship,  $m = 3.7$  is obtained for  $C_H = 0$ . Therefore, if a tetrahedral amorphous carbon (ta-C) without hydrogen content is to be formed, this model predicts an upper limit on the  $sp^3$  hybridization of  $\sim 70\%$ , rest being trigonal  $sp^2$  phase. Indeed, within experimental uncertainties the results of recent ta-C are consistent [27]. More data is required for better estimates of the upper limits on  $m$  of amorphous carbon system, but the concept has significant ramifications. A higher  $sp^3$  hybridization can be obtained only by reducing the average coordination number through the introduction of dangling bonds or voids. Robertson's theoretical prediction of  $sp^2$  clustering does provide a mode of strain relief in the network by introducing some medium range ordering [40,41]. However, this

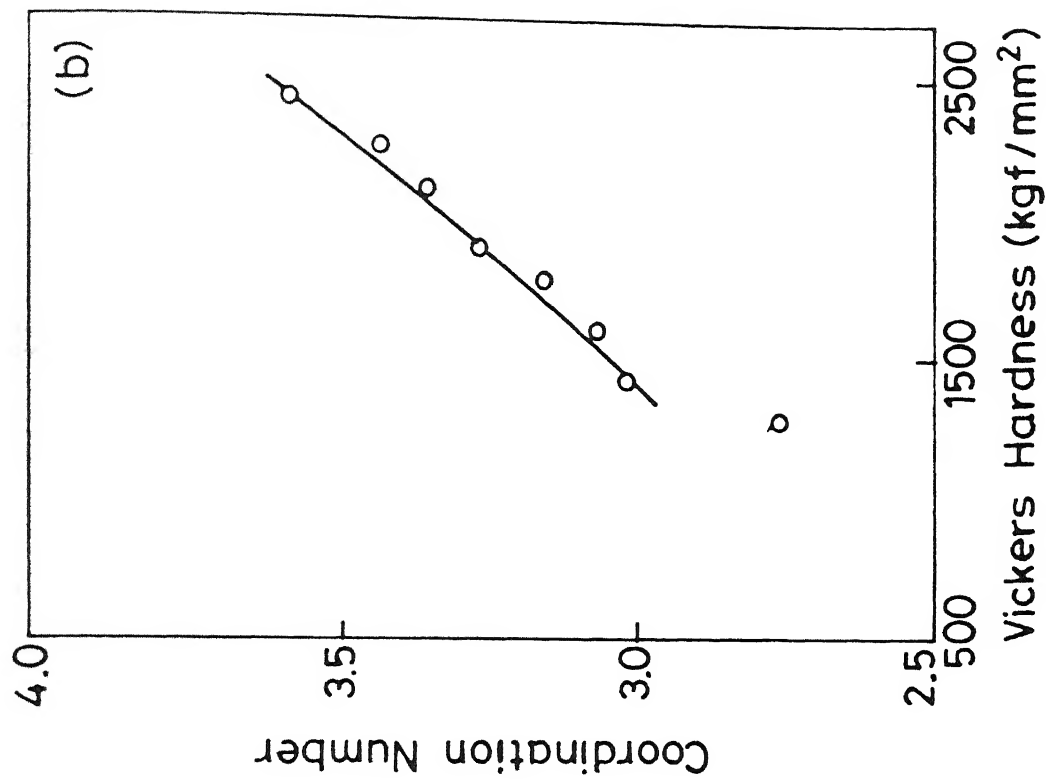
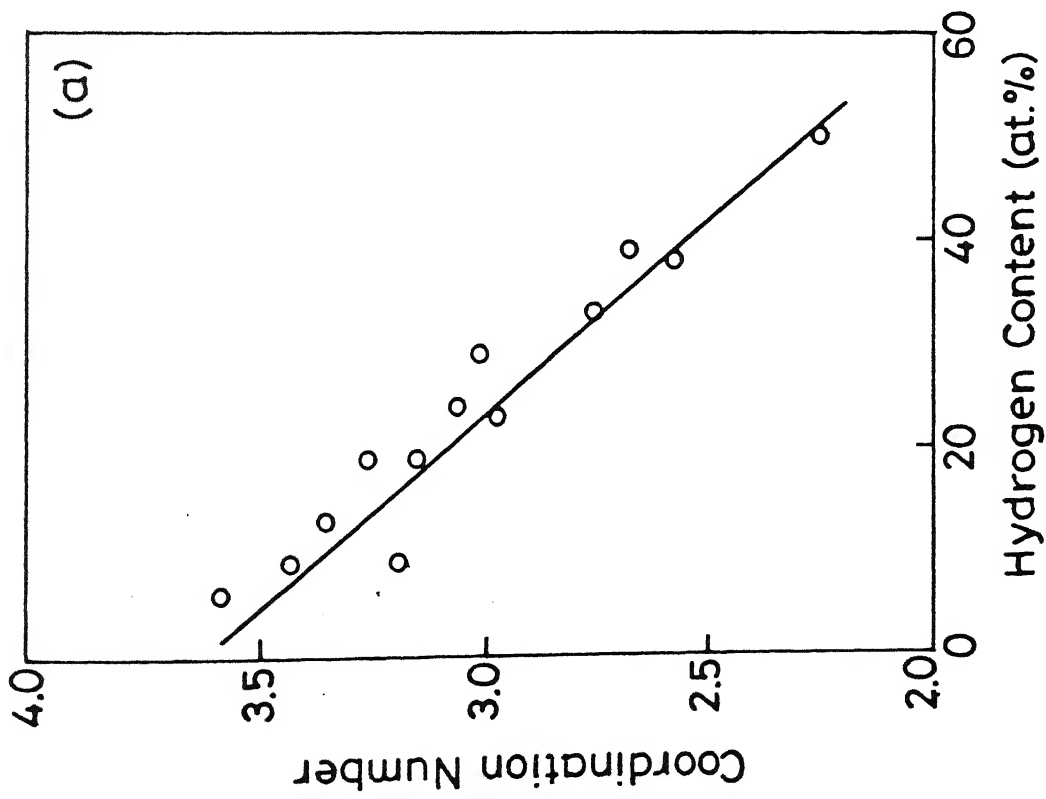


Fig.5.20 The average coordination number,  $m$ , as a function of (a) hydrogen

will be reflected by a decrease in optical band gap. This is not the case in our low hydrogen content high optical gap samples (e.g. DLC51). On the contrary, the bandgap values are estimated to be quite high (Table 5.5). Another possibility is that the higher constraint in the network will lead to crystallite formation. This indeed seems to be the case in our sample containing 71%  $sp^3$  C-C bonding.

The hardness and rigidity of the films arise from the structure of the matrix that makes up the bulk of the film. The variation in film hardness with average coordination number (Fig. 5.19b) is consistent with the above discussion.

### 5.5.2 Effects of Hydrogen On Film Properties

Hydrogen plays a crucial role during growth of DLC films from hydrocarbons as has been discussed above. Once incorporated in the films, hydrogen govern the properties of the films. In general, hydrogen interacts with  $\sigma$  and  $\pi$  states and should remove the states from the gap. However as we have seen above, hydrogen participates in determining the film structure. Therefore, effect on film properties is found to be more complex.

One of the direct consequence of hydrogen incorporation in amorphous carbon network is to influence their optical properties. We summarize the values of optical band gaps as a function of hydrogen content in the films (section 5.2) as shown in Fig. 5.21. At first instance there appears to be no correlation between  $E_g$  and  $C_H$ . However, a careful look at the figure yields vital information on the role of hydrogen in influencing the film properties. Fig. 5.21 can be divided in three parts, dashed lines providing a guide to the eye without attaching much significance to their slopes. Low hydrogen content and high optical gap are represented by a film (DLC51) deposited under bias and hydrogen dilution that shows a high  $sp^3$  C-C content (Table 5.5). On the other extreme, high optical gap and high hydrogen content are representing the films that are polymeric in nature. These films show lower refractive index ( $\sim 1.6$ - $1.8$ ) and most of the hydrogen bonded in  $CH_3$  configuration. Such films are obtained at high pressures and low substrate temperatures. In addition, there is a film showing low hydrogen content ( $\sim 9$ at.%) and  $E_g=1.0$ eV. This sample has a high  $sp^2$  content of more than 50% and may be termed graphitic. Most of the

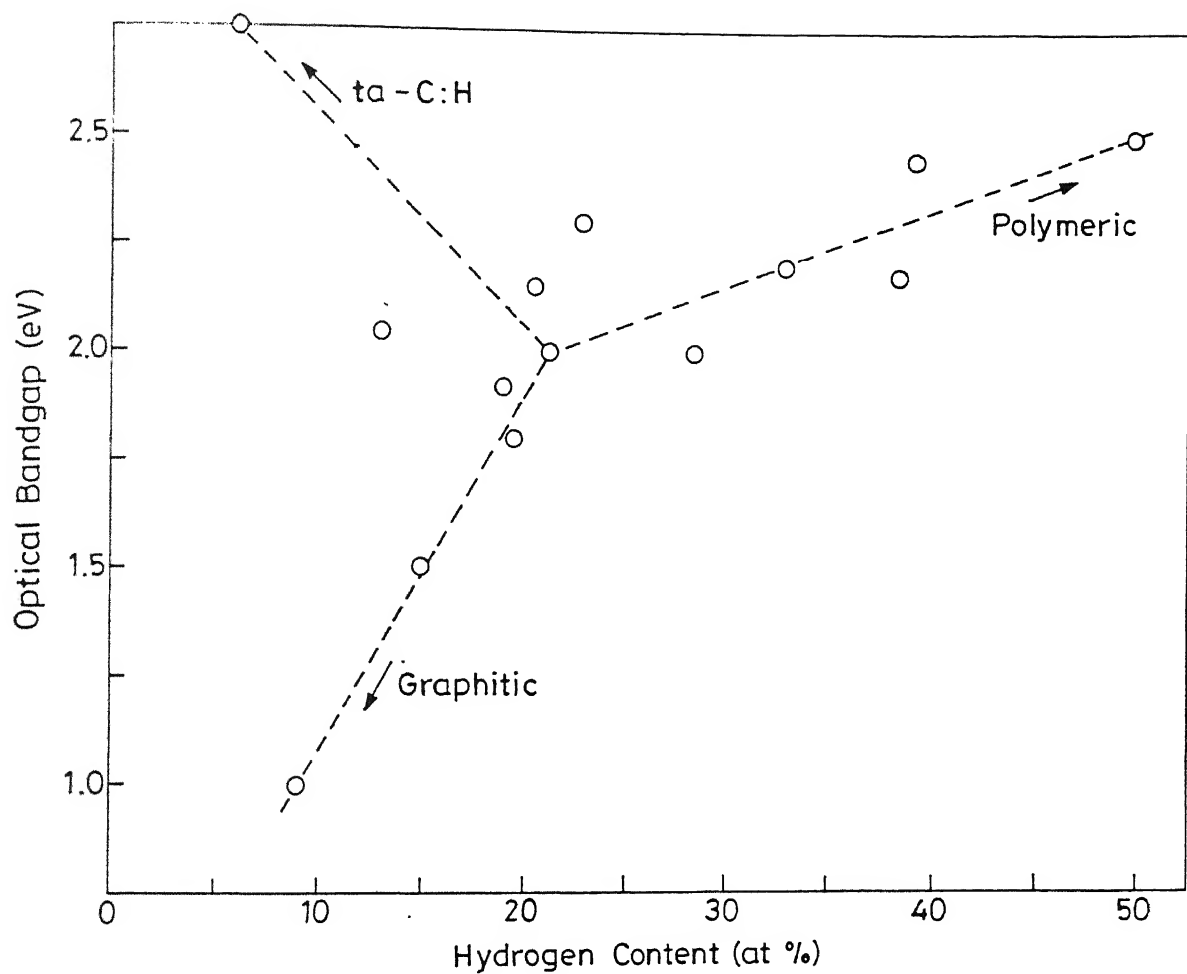


Fig 5.21 Optical bandgap plotted as a function of hydrogen content for dc glow discharge deposited a-C:H films of different microstructures.

samples are found having 15-35 at.% hydrogen with bandgaps in the range of 1.8-2.2 eV. These samples contain  $sp^{3*}$  C-C bonding between 40 to 65% and may be called as typical DLCs.

Usually, it is reported that the optical energy gap increases with increasing hydrogen content in a-C:H films [33,54]. Clearly, a linear direct relationship between  $C_H$  and  $E_g$  cannot be subscribed in our case except in the limited range (p-line). Hydrogen is expected to remove the gap states and increase the band gap as is a case in a-Si:H. However unlike a-Si:H, multiplicity in carbon bonding configuration leads to the complex dependence of  $E_g$  on  $C_H$  as observed in Fig. 5.21. We should emphasize that by using a single deposition technique, we are able to obtain all the manifestations of the amorphous carbon microstructures by choosing the deposition parameters carefully.

In order to establish the role of microstructures further, Fig. 5.21 provides a summary of  $sp^3$  content in a variety of a-C:H films as a function of hydrogen content [152] along with our results. Solid curve represents hydrogenated amorphous carbon structures which can be described by fully constraint network (FCN) model given by Angus and Jansen [315]. The FCN model indicates that amorphous carbon (ta-C) and hydrogenated amorphous carbon films with a high fraction of  $sp^3$  C-C bonding are highly overconstrained. These materials are formed under metastable conditions and are stabilized by compressive stresses. As discussed in the preceding section, these stresses can often be reduced by the formation of medium-range order and microcrystallinity (two phase structures). Indeed, the Raman spectra on our lowest hydrogen content (~5.7at%) and highest  $sp^{3*}$  fraction (~71%) show the signatures of nanocrystallinity (Fig. 5.17).

Concentrating on our results in Fig. 5.22, most samples show an overconstrained network. Only the films deposited at room temperature and high pressure conditions with  $C_H$  of ~50at% show an underconstrained behavior. A soft and “floppy” structure of such films was suggested by other characterization techniques also. These results are supported by our estimates of average coordination numbers as shown in Fig 5.20. If we leave the results of high substrate temperature (525°C) film with 9at%  $C_H$ , all other data show a linear decrease in  $sp^3$  C-C content with increasing hydrogen concentration (dotted line, Fig. 5.22).

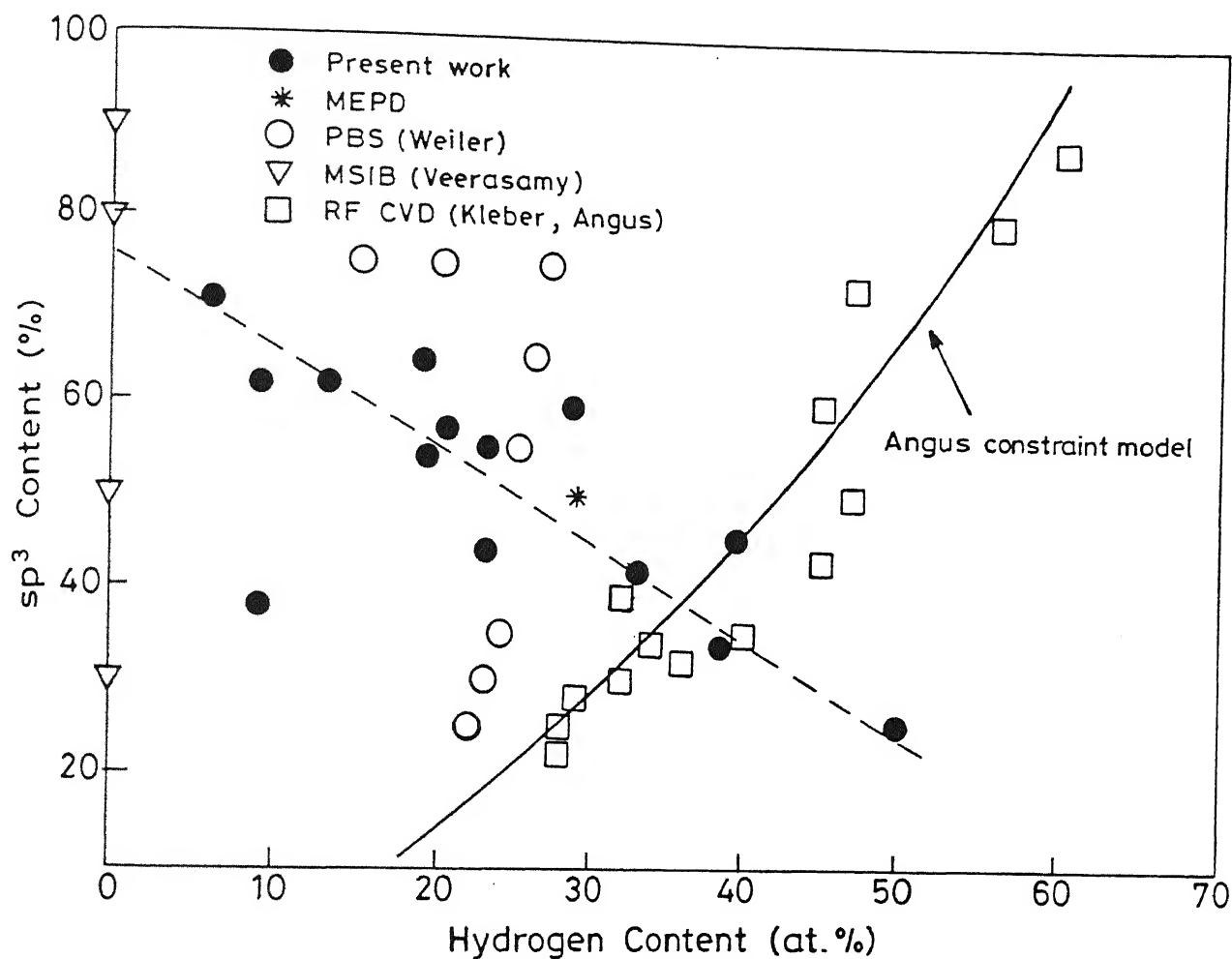


Fig. 5.22  $sp^3$  C-C content on a variety of dc glow discharge deposited a-C:H films in the present work as a function of hydrogen content. The points from plasma beam source (PBS, after ref.29), mass selected ion beam (MSIB, ref. 27), RF chemical vapor deposition (RFCVD, ref. 315, 317(B)) and magnetic field enhanced plasma deposition (MEPD, ref. 152) techniques are also shown for comparison. Solid line represents the predicted  $sp^3$  component for a fully constrained amorphous network (ref 152, 315)



Films deposited by dc glow discharge compare favorably with highly tetrahedral diamond-like amorphous carbon films (ta-C:H) prepared by Weiler et al [29] using more exotic technique of plasma beam ion source. Common in the two techniques is the source of carbon - acetylene. Ion beams of well defined energies were extracted in plasma beam ion source [29].

### 5.5.3 Role of Ion Energies

It is now becoming evident that the energy of the ions impinging the growth surface play the most crucial role in determining the structure of a-C:H films. Ion energy distribution can be modified directly by using bias to the substrates (Section 5.2.4) or by changing the operating conditions of the plasmas such as pressure, interelectrode gap and geometry of the system (Chapter III, and Sec. 5.2.1).

We first summarize the role of ions energies in the growth model presented above. The effect of  $V_b$  on growth process seems to be two-fold. In addition to the modification in ion energies, it influences ion flux as well as atomic hydrogen. The ion flux at the substrate surface enhances the mobility of physisorbed atoms and the diffusion coefficients can increase by up to five orders of magnitude [229]. The deposit on anode is built up by two mechanisms. (i) by neutral hydrocarbon gas molecules at the surface of the substrate dissociating because of electron impact and ion impact (ii) by positive hydrocarbon fragments created in the plasma region just outside the cathode dark space. Since, the plasma potential is positive relative to the grounded anode, positive hydrocarbon fragments are accelerated towards grounded anode. In addition, when a negative potential is applied to anode, the ion molecule interactions near anode surface become dominant. The dissociation of hydrogen molecule near substrate surface results in production of atomic hydrogen. The increase of atomic hydrogen and bombardment by positive hydrocarbons on the growing film surface are essentially responsible for the above discussed structural modifications of DLC films.

Several careful experiments have been performed by using mass selected ion beams and filtered cathodic vacuum arc techniques. Robertson [316] showed that penetration of ions is only probable if the energy of the ions exceeds a penetration threshold. If the

energies of the ions are too high thermal annealing leads to a decrease in density and  $sp^3$  content. The stress and density enhancement are a result of subplantation of ions as suggested by Lifshitz [291,308]. All neutrals and a fraction of ions are incorporated on the surface of an a-C:H films. Still the ion bombardment creates interstitials in the subsurface thus leads to an increase in compressive stress [168]. The interstitials leads to an increase in local density which combined with higher stress promotes  $sp^3$  bonding.

The  $sp^3$  and hydrogen content of the films depend mainly on the  $\phi_i/\phi_o$  ratio, the ion energy and the type of ions. The  $\phi_i/\phi_o$  denotes the ratio of the deposition rate by ions  $\phi_i$  and deposition rate by the film forming species. DLC films which usually possess low hydrogen content and high  $sp^3$  content are normally deposited at ion energies over 250 eV and  $\phi_i/\phi_o$  ratio higher than 20% [126,317a&b]. Polymerlike a-C:H films are mainly deposited at high pressures with  $\phi_i/\phi_o$  ratios lower than 5% and lower ion energies.

It is now possible to compare our dc glow discharge performance with other deposition techniques. The negative bias effects in rf plasma CVD systems have been studied by a self-bias method [318-322]. Influence of ion energy and flux on properties of plasma deposited a-C and a-C:H films has been studied for other deposition systems such as magnetron sputtering and plasma beam deposition [29]. In rf plasma deposition process, the average ion energy  $E_i$  is typically found to be 0.3 to 0.4 times the bias voltage [323]. However, in case of rf plasmas, the individual ionic species have large ion energy distributions (IED) when arriving at the surface.  $\Delta E/E$  ranging between 0.5 -1. In case of dc glow discharges operating at low pressure and small interelectrode gap separation such as ours, IED's are expected to be much sharper with maximum ion energies approaching that of sheath potentials at the anode [324,325]. Therefore, energy per carbon atom in our optimum  $V_b$  conditions (-250V) using  $C_2H_2$  are in agreement with ~90V/ion of optimum ion energies found in case of plasma beam source [29] and filtered cathodic vacuum arc techniques [32].

## 5.6 CONCLUDING REMARKS

In summary, we have produced diamond-like carbon films using acetylene dc glow discharge, having properties comparable to those produced by other more complex deposition techniques. In general, films produced by this method contain lower hydrogen concentration and a more compact film structure. A detailed variation in the process parameters and their correlation with multiple properties of the deposited films has led us to the understanding of the growth of a-C:H films. Micro-Raman data shows the evidence of nanocrystallites of hexagonal diamond phase in DLC films. So far such structures have been observed only in mass selected ion beam techniques. Results have been explained in terms of a fully constrained network model.

# CHAPTER VI

## DIAMOND SYNTHESIS BY COMBUSTION FLAME CVD

### INTRODUCTION

As described in Chapter I, thin films of diamond can be grown by various low pressure chemical vapor deposition (CVD) methods e.g. plasma or thermal CVD [16,296]. As compared to low pressure CVD processes, higher growth rates are obtained by activating the hydrocarbon gases at atmospheric pressures by the use of combustion flame CVD. This method was first proposed by Hirose and Kondo in 1988 who used oxy-acetylene combustion flame for synthesis of diamond films [323]. Later, this technique has been widely used by various researchers [170-172, 324-335] for synthesis of high crystal quality diamonds. An advantage of flame CVD over other CVD techniques is its inexpensive and simple deposition set-up without any requirement of vacuum reactors and power generators. Therefore, there has been a growing interest in diamond films using oxy-acetylene flame. Using the combustion flame synthesis, Snail et al [336] have demonstrated high rate ( $>150\mu\text{m/h}$ ) homoepitaxial growth of diamond on  $\{100\}$  and  $\{110\}$  oriented natural diamond crystals. High quality flame-deposited diamond films of high resistivity ( $\sim 10^{14} \Omega\text{-cm}$ ) and good optical transparency have been reported by Tzeng and Phillips [337]. A thin film Schottky diode was also demonstrated from flame grown diamond by Snail et al [338]. In addition, scanning and multi-nozzle flame geometry's have been used to deposit large area diamond films for industrial applications [327,339,340].

Substrates like Si, Cu, Mo, Ti, Ta, Nb, TiC TiN and BN etc have been used [170-172, 324-326, 329]. In general, the choice of substrates for diamond deposition is made from two types of materials [341]. First are those having thermal expansion coefficients or lattice constants close to that of diamond, e.g., Si, Ni (See Table 6.1) The other type of preferred substrate materials are those which form carbides having high surface free-energies relatively close to the surface free energy of diamond, e.g., Mo, Ta and W. Molybdenum substrates are particularly well suited for the study of the diamond growth mechanisms using oxy-acetylene flame. This is because of their ability to withstand large thermal gradients inherent to flame deposition [172, 324-327]

**Table 6.1:** *Lattice parameters, crystal structures, and solid surface energies (ergs cm<sup>2</sup>) of various materials [341].*

	Lattice parameter (Å)	Thermal-expansion coefficient (x10 <sup>-6</sup> )/K (at 1200 K)	Crystal structure	Surface free energy (ergs/cm <sup>2</sup> )
Diamond	3.567	5	Diamond	3387
Mo	3.147	6	BCC	2463
W	3.165	5.3	BCC	3111
Ni	3.524	12.7	FCC	2072
Si	5.43	4.6	Diamond	1457
Steel (γ-iron)	3.65	14	FCC	-

Steel being the most widely used commercial alloy in the engineering industry attaches a special significance to its applications. Attempts have been made in the past to grow diamond films directly on steel with undesirable results [342-344]. Problems arise due to high solubility of carbon in steel at the processing temperatures which hinder nucleation and growth of diamond. Additionally, the growth is complicated by the formation of layers of graphitic soot due to catalytic reactions of the growth precursors [342,345]. However, formation of intermediate barrier layers prior to diamond deposition has been suggested to improve nucleation and adhesion of diamond on steel. A variety of

barrier layers, like amorphous Si and C, TiN, WC, cubic BN, Mo, and Mo/Ni bilayers, has been attempted [342-348]. Recently, 10  $\mu\text{m}$  thick nitridized chromium films have been used as intermediate layers [349]. Moreover, Kohzaki et al. developed a brazing technique that allows a free-standing diamond film, grown on another substrate, to be 'glued' to a stainless steel plate [350]. It is evident that the introduction of these layers at the interface pose their own set of problems regarding deposition, adhesion and stresses. Different types of deposition techniques are often required to obtain various interlayers and diamond films. This increases the number of process steps and parameters to be controlled. Nevertheless, motivation to make diamond films on steel substrates in a simple deposition process has kept the interest of researchers high in the area [342-351].

Hot filament and microwave CVD techniques employing a mixture of methane and hydrogen have generally been used for the growth of diamond films on steel substrates. DC arc plasma reactor is also used to grow diamond films on steel with CVD grown tungsten as an intermediate layer [351]. Substrates temperature ranges from about 600  $^{\circ}\text{C}$  to  $\sim 1050^{\circ}\text{C}$  [347-349]. So far there were no reports of successful deposition of diamond on steel using oxy-acetylene flame.

We have studied oxy-acetylene flame deposition of diamond films on Mo and steel substrates [353]. The deposition methodology has been investigated for the growth of good quality diamond films. Films are characterized structurally by SEM, XRD, Micro-Raman spectroscopy, EPMA, and RBS. The deposition parameters have been varied for the growth of diamond films on W and Ni substrates also. In particular, we have investigated the role of an in-situ pretreatment of Mo and steel substrates in determining the growth and quality of films. This pretreatment was carried out for a short duration by exposing the substrates to the outer zone of diamond producing flame itself at lower substrate temperatures. As mentioned earlier, the attempts to increase the area of deposition using oxy-acetylene flames include the use of multinozzle torches [327, 339] or scanning flame geometry [340]. Unless one intentionally screens out the outer flame [329], substrates will be exposed to it. Therefore, its effect on subsequent diamond growth needs careful studies.

Finally, we have presented an evidence for the growth of adherent polycrystalline diamond films on stainless steel substrates at low substrate temperatures, without external barrier layers, using oxy-acetylene flame [352]

## **6.2 PREPARATION OF DIAMOND FILMS**

### **6.2.1 Experimental**

An oxy-acetylene flame deposition system was fabricated for the present investigations. The schematic diagram of the set-up is shown in Fig. 6.1. It mainly consists of a copper substrate holder with water cooling arrangement. A standard oxy-acetylene brazing torch fitted with 1 mm nozzle tip is mounted on a stand for vertical positioning of the flame on the substrate. Commercial grade oxygen and acetylene of purity about 99.5% were used for these experiments. The volume flow meters and torch handle needle valves were used to control the flow rates of gases. Ultrasonically cleaned Mo, W, Ni, and steel sheets (size ~1.5 cm x 1 cm) were used as substrates. Substrate was self heated by heat transfer from the flame and its temperature was controlled by adjusting the flow rate of water to the substrate holder. The substrate temperature was measured by a chromel-alumel thermocouple embedded in a small copper block and touching the block surface just below the substrate. Actual temperatures may be somewhat higher than the measured ones. In order to obtain better thermal contact, substrates were fixed by silver paste on the copper block. Substrate surfaces pretreatment is carried out using specific zone (outer flame as shown in fig. 6.2) of the flame. Scratching the substrate with diamond powder was not employed unless otherwise stated. For deposition experiments, flame structures were varied by varying the flow rates of gases and their flow ratios. Substrate pretreatment time and temperature were also varied to study the growth of diamond on Mo and steel substrates.

### **6.2.2 Oxy-Acetylene Flame: Structure and Compositions**

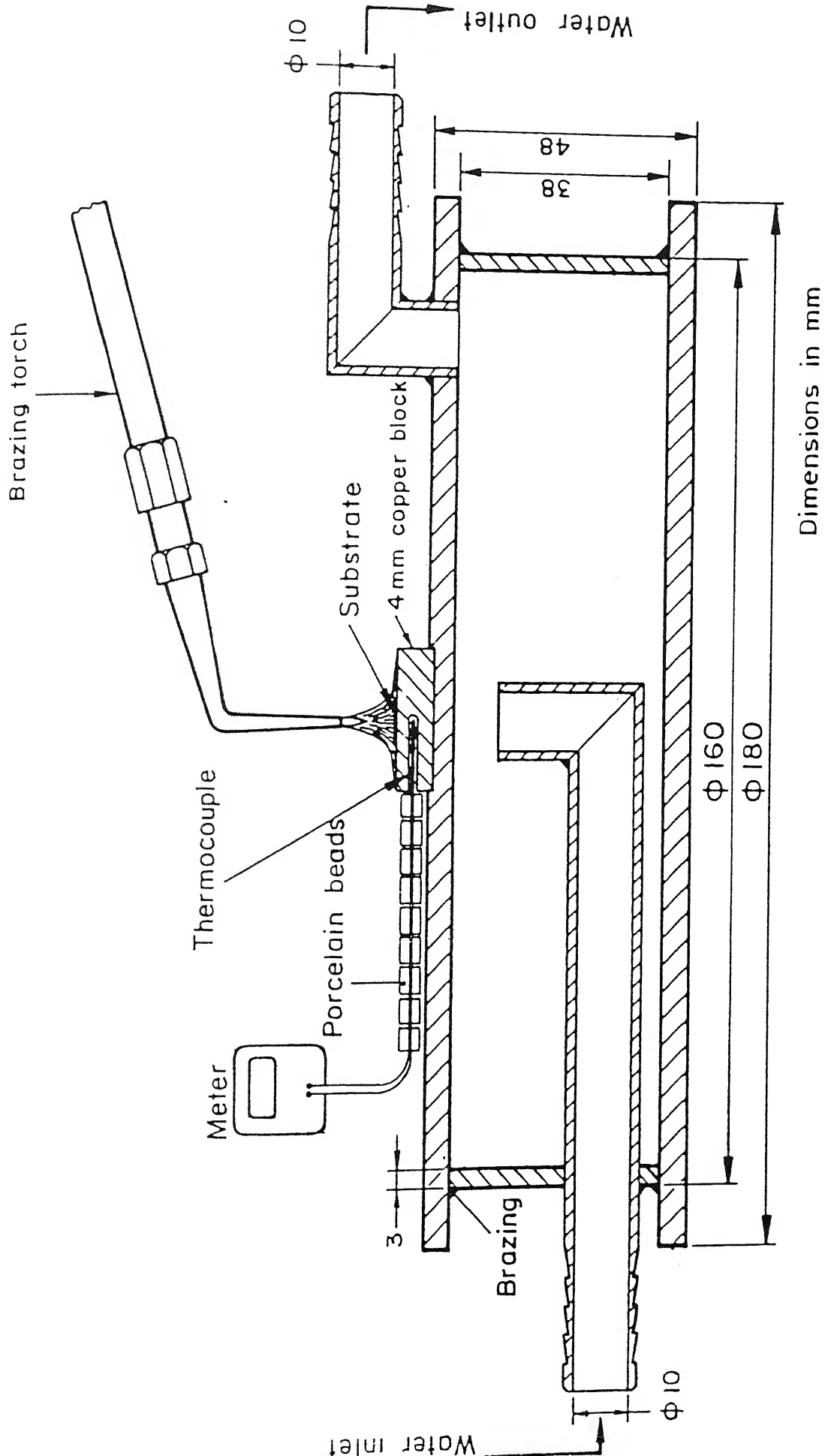


Fig 6.1 Schematic diagram of oxy-acetylene flame deposition system



Acetylene rich oxy-acetylene flame consists of three identifiable zones viz inner cone, acetylene feather (middle zone) and outer flame. The structure of a typical oxy-acetylene flame is shown in Fig. 6.2. The flame structure and relative sizes of three zones are dependent on flow rates and flow ratios of oxygen and acetylene gases. Investigations of flame by optical emission and planar laser-induced photo dissociation fluorescence [353,354] suggest that the flame composition varies along the portions of the flame

The inner cone, close to the nozzle tip, is bright yellow and transparent. It is sharply conical for the laminar flames extending up to ~5mm from the torch tip depending on the flow rates and nozzle size.

The acetylene feather is a region of incomplete combustion. It is a blue-green colored (due to  $C_2$  band radiation) reducing flame, where excess acetylene burns with oxygen. The estimated temperature is  $\sim 3000^\circ C$ . It appears only for acetylene rich flames. The size of the feather is a function of the gas flow ratios. The species  $C$ ,  $C_2$ ,  $CH$  and  $H$  are present in abundance in this region of flame [354] and have been proposed to be the growth pressures for diamond [354,355]. The flame composition in its middle zone include  $CO$ ,  $H_2O$ ,  $H_2$ ,  $CO_2$ ,  $C_2H_2$ ,  $CH_4$ ,  $C_4H_2$ ,  $C_3H_2$ ,  $CH_3$ ,  $C_3H_3$ ,  $C_2H_4$ ,  $HCCO$  and  $OH$  species [353].

In combustion process, the premixed gas emerging from the nozzle is heated to high temperature to ignite and burn. The combustion produces carbon monoxide and hydrogen according to the following reaction [356]



The reaction takes place at  $3400^\circ C$ . Hydrogen atoms are created during the burning of hydrocarbons. High temperature ( $2800-3400^\circ C$ ) of the flame causes a plasma to form, creating various atomic and excited species. The atomic hydrogen attacks molecular oxygen to form  $OH$  and  $O$  radicals as  $O_2 + H \rightarrow OH + O$ . These radicals produce  $CH$ ,  $CO$  and  $HCCO$  species via the reactions



Similar active species such as  $CO$ ,  $O$ ,  $OH$  and  $H_2O$ , although through somewhat different reactions, are present in other C-H-O systems.

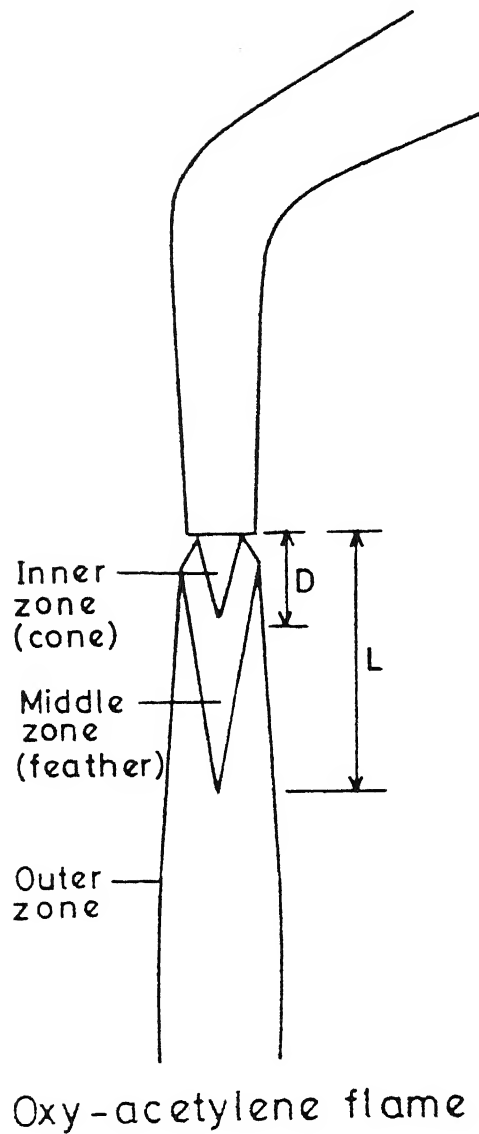
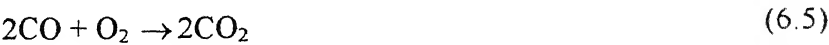


Fig 6.2 Oxy-acetylene flame structure.

The outer flame constitutes the largest volume of the flame. It is a blue-violet (due to C-H band radiation) oxidizing flame where the products from the inner cone burn with atmospheric oxygen according to the reaction



At low C/O ratio in this region, there is almost no carbon deposition due to its complete oxidation.

Combustion flames of fuel other than acetylene like ethylene and oxygen-ethane have been used to deposit diamond [357-359] at lower growth rates than those for oxygen and acetylene flames. However, from the chemistry of combustion, acetylene is the most desirable fuel in combustion diamond CVD applications [360]. This is because it has a relatively high flame temperature and therefore high burning velocity (2600 K and 150 m/s, respectively; maximum values in air at atmospheric pressure) [361]. The high flame temperature results in a large fraction of radicals such as hydrogen atoms (H) and methyl radicals (CH<sub>3</sub>) in the postflame gases, and leads to high burning velocities due to the exponential dependence of reaction rates on temperature. The high burning velocity permits the use of high inlet cold gas flow velocities which subsequently results in a shorter residence time for reactive intermediates as they are transported from the flame to the substrate. The short residence times prevent the conversion of methyl radicals into carbon monoxide (CO) and C<sub>2</sub> species and thereby maximize the delivery of radicals such as CH<sub>3</sub> and H to the substrate.

### 2.3. Optimization of flame:

Diamond films could be grown only from acetylene rich flames using middle cone of the flame (Fig. 6.2). Quality of the deposit was found to be a function of gas ratio which is directly related to the feather length (L) and the placement position of substrates in the feather (D) (Fig. 6.2). D and L were measured using a millimeter scale made of quartz plate. The optimized values of gas flow rates were found to be about 1 lpm for our nozzle geometry. Flow ratio of O<sub>2</sub>/C<sub>2</sub>H<sub>2</sub> for optimum diamond growth was

found to be 0.94 which corresponds to a L of about  $30 \pm 3$  mm. Lesser gas flow ratios yielded deposits which were x-ray non-diamond and their surface morphology did not show any observable features. Higher gas flow rates lead to the production of noisy turbulent flames which were not applied to grow diamonds in the present work. These results suggest that the growth of diamond from oxy-acetylene flame is limited to a narrow region of gas phase C/O ratio. Torch tip to substrate distance (D) was found to be optimum at  $\sim 12$  mm. At smaller D, distortion in flame structure and deposition of accumulated ball like structure consisting of non-diamond carbon phases (soot) was obtained. A decrease in particle density was observed at larger D values. This variation in density and quality of deposit with L and D identifies a specific region of flame which is appropriate for diamond growth. This is due to the nature and type of combustion products in contact with the substrate [353,362] as well as surface based reactions controlled by the temperature of the growth surfaces. These parameters, in turn, are functions of the interaction region of flame with the substrates. Therefore, it is significant that reproducible results could be obtained by adjusting only three parameters namely, L, D and the substrate temperature.

## 6.3 RESULTS AND DISCUSSION

### 6.3.1 Diamond Growth on Mo

The deposition experiments on Mo substrates were performed for varying flame structures, substrate temperatures and deposition times and substrate pretreatment.

#### *Effect of substrate temperature:*

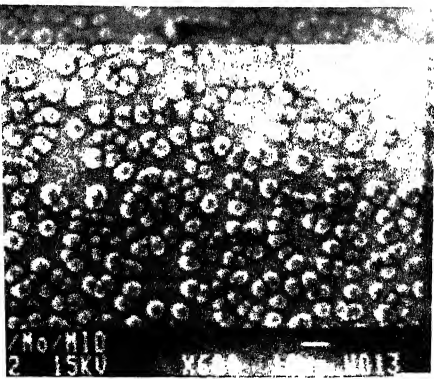
Figure 6.3 shows the x-ray diffraction spectra measured on films deposited using  $O_2/C_2H_2$  flow ratio of 0.94 at three representative substrate temperatures (660, 850 and  $1060^\circ\text{C}$ ). The optimum substrate temperature for diamond film deposition on Mo under these flame conditions was found to be  $850 \pm 50^\circ\text{C}$  (Fig. 6.3b). Figure 6.3b clearly shows four crystalline planes of diamond viz. (111), (220), (311) and (400). The



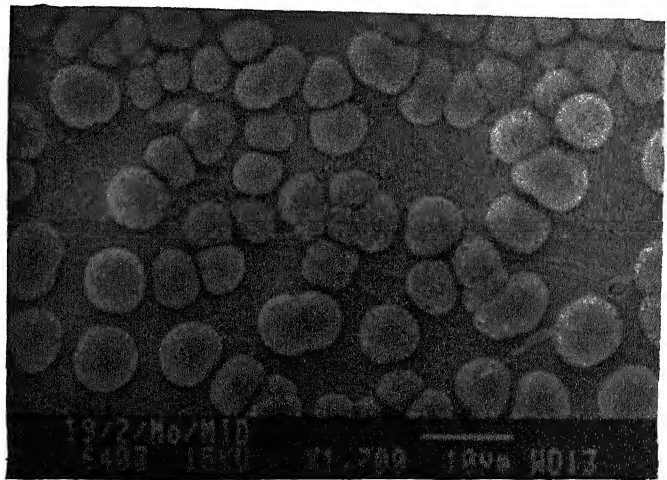
interplanar spacing ( $d$ ) obtained from the XRD pattern are consistent with those of cubic diamond crystal (ASTM card 6-0676). Other peaks related to carbides and oxides of Mo are also seen. Increasing the substrate temperature leads to the formation of graphite (Fig. 6.3a). XRD spectrum of a sample prepared at 1060 °C (Fig. 6.3a) indicates that the film is basically composed of the graphite phase of carbon with no diamond peaks present.

These observations are in general agreement with the results of Hanssen et al [363], but are in contrast to those of Marks et al [325] who reported the diamond growth on Mo at a temperature of 1250 °C using a turbulent flame. It has been mentioned that the presence of chemical species in the flame is a function of position. Preferential growth of graphite at high substrate temperatures may be attributed to atomic hydrogen which plays a paramount role in diamond vs. graphite deposition in CVD processes [364]. At high substrate temperatures (above 950 °C), hydrogen desorption from the diamond surface takes place (to be discussed later) [365]. As the short residence time of hydrogen on the surface is not enough to stabilize the surface hybridization, reconstruction of  $sp^3$  hybridized carbon sites into  $sp^2$  graphitic phase takes place. Moreover, Spitsyn et al. [366] have indicated that the etching rate of diamond by atomic hydrogen increases with temperature, while the etching rate of graphite exhibit only a weak temperature dependence. This etching behavior may contribute to the increasing amount of graphite in diamond films at higher temperatures. On the other hand, if the temperature is too low, the reduced mobility of carbonaceous species on substrate surface prevents crystallization which explains the absence of graphite or diamond peaks in the XRD spectrum of a sample prepared at 660 °C (Fig. 6.3c). In addition, oxidation and thermal decomposition of deposits may also play a crucial role in determining the formation of various polytypes of carbon and their growth rates [292,367].

SEM micrographs of the sample corresponding to Fig. 6.3b are shown in Fig. 6.4. It shows the formation of individual particles distributed uniformly over the surface with a particle density  $N$  of the order of  $10^5$  particles/cm<sup>2</sup> (Fig. 6.4a). The morphology of the deposits is seen to consist of round shaped grains (Fig. 6.4b) having linear dimensions of about 10  $\mu$ m and consisting of a number of crystallites which tend to grow as faceted particles. The variation in the particle size as well as density was observed across the



(a)



(b)

6.4 SEM photographs of diamond film grown on untreated Mo for 10 minutes.

radial distance from the center of the combustion flame. The non-uniformity in deposit is caused by the variation in the substrate temperature as well as the flame constituents and is one of the inherent drawbacks of this deposition technique [363,368].

### *Surface Pretreatments:*

In order to get uniform films on various substrates, a novel surface pretreatment method using the outer zone of oxy-acetylene flame was attempted. The substrate surface was exposed to the outer flame for different time-spans, immediately before the diamond synthesis using the middle oxidizing flame. For this purpose, the same flame (fixed L) was utilized. However, larger D values ( $D > L$ , typically  $D \sim 50\text{--}60\text{ mm}$ ) and lower substrate temperatures ( $300\text{--}350^\circ\text{C}$ ) were employed. Deposition of diamond films was immediately followed by lowering the oxy-acetylene torch to adjust the D value to  $\sim 12\text{ mm}$ . and controlling the substrate temperature to  $\sim 850^\circ\text{C}$ . The XRD pattern of a sample deposited for 10 min. after a 1 min. pretreatment is shown in Fig. 6.5. It clearly shows the formation of diamond peaks marked D (peaks 1,8,12 and 18). In addition, peaks due to graphite (21 and 22), Mo (3,6 and 14) and compounds of Mo namely molybdenum-carbides (2,5,7,9,10,13,15,19,22), oxides (2,9,13,20) and oxy-carbides (4,11,16) are also seen. Evidently, the diamond (400) peaks is enhanced relative to other diamond peaks in the presence of interfacial layer.

The lattice parameter obtained on indexing the pattern was  $3.564\text{ \AA}$ , which is quite close to that of natural diamond ( $3.567\text{ \AA}$ ). A decrease in lattice parameter indicates the synthesized polycrystalline diamond film in a state of compressive stress. The thermal stress is caused by the difference in thermal expansion of diamond and the substrate. As the film and substrate cool from the growth temperature ( $\sim 850^\circ\text{C}$ ), the Mo substrate which has a large thermal expansion coefficient (see Table 6.1) contracts somewhat more than the diamond film, producing compressive stresses in the film.



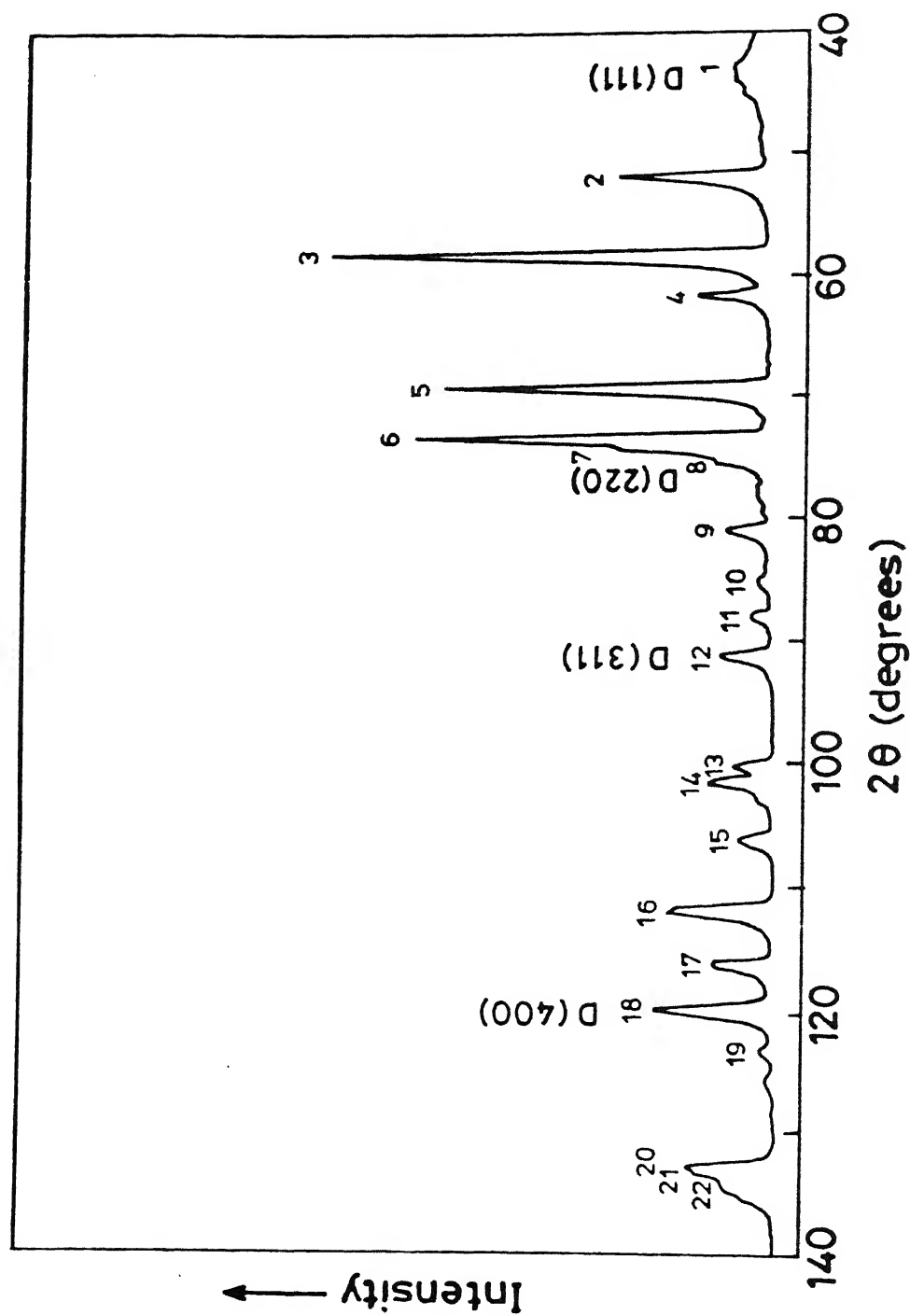


Fig 6.5 XRD spectrum of a diamond film deposited on Mo for 10 minutes with pretreatment for 1 minute.

The enhancement of diamond (400) peak in XRD spectrum indicates the growth of (100) square faceted flat diamond crystallites. This flattening of crystallites is seen clearly in the SEM pictures (see Fig. 6.6) in which a number of diamond crystallites are connected with each other forming clusters of size ranging from 20 to 25  $\mu\text{m}$ . This indicates that the interfacial layer formed during pretreatment facilitates in the coalescence of nearby grains across the surface and thus helps in the formation of bigger clusters of faceted particles.

To demonstrate the role of surface pretreatment by scratching Mo substrate with diamond powder of the substrate, another deposition run was performed under identical growth conditions as were used for sample corresponding to fig. 6.6 for a duration of 80 minutes. In this case, as is evident from the SEM micrograph (Fig. 6.7), continuous square faceting was clearly demonstrated.

The diamond growth was confirmed using laser-Raman scattering measurements. Figure 6.8 shows the presence of diamond peak at  $1337\text{ cm}^{-1}$  corresponding to fig. 6.7. Knight has reported a range from  $1327$  to  $1345\text{ cm}^{-1}$  for diamond Raman line subjected to substrate hardness and preparation history of CVD diamonds [86,179-181]. In addition, the presence of Raman signals other than diamond at around  $1355$  and  $1585\text{ cm}^{-1}$  suggests that graphitic and amorphous carbon phases are also present. The Raman mode at  $1355$  is the well known D band of graphite [179,181]. The Raman signal in the range of  $1500$ - $1600\text{ cm}^{-1}$  is also an indication of presence of carbon atoms in  $\text{sp}^2$  (graphitic) sites. The intensities for diamond and graphite peaks in Fig. 6.3a is not a direct measure of their concentrations in the sample. The width of Raman peak for diamond phase is found to be  $\sim 15\text{ cm}^{-1}$  which is consistent with earlier reports [78,179,181].

The positive shift in diamond line observed in our sample is consistent with the XRD data and indicates the film in compressive stress by both these measurements. The film stress of  $4.86\text{ GPa}$  is obtained from the shift of Raman line using analysis described in section 2.4.2. The compressive stress in these films can be attributed to presence of the non diamond carbon.

Pretreatment time by outer flame was varied from 30 sec to 3 minutes keeping the subsequent diamond deposition time fixed at 10 min. Formation of this interfacial layer for 1 min. gave the maximum surface coverage with a particle density of  $>10^4/\text{cm}^2$  [368]. At

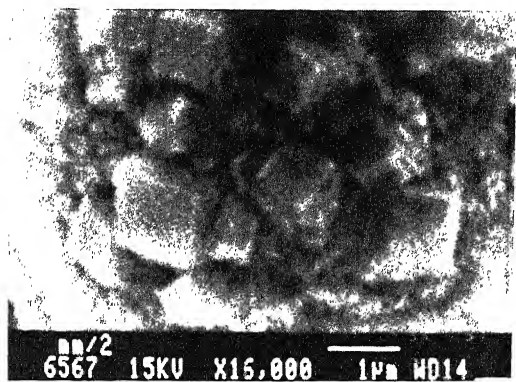


Fig 6.6 Surface morphology of the film corresponding to fig. 6.5.

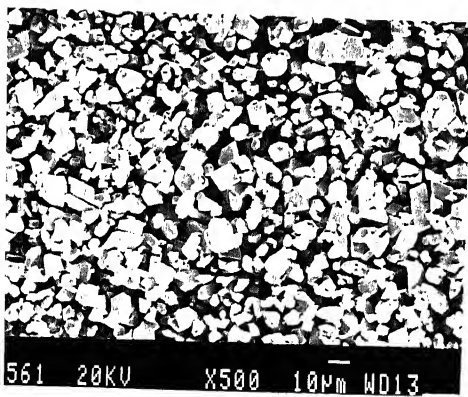


Fig 6.7 SEM micrograph of a diamond film deposited on Mo for 80 minutes after pretreatment of substrate for 1 minute by outer flame.

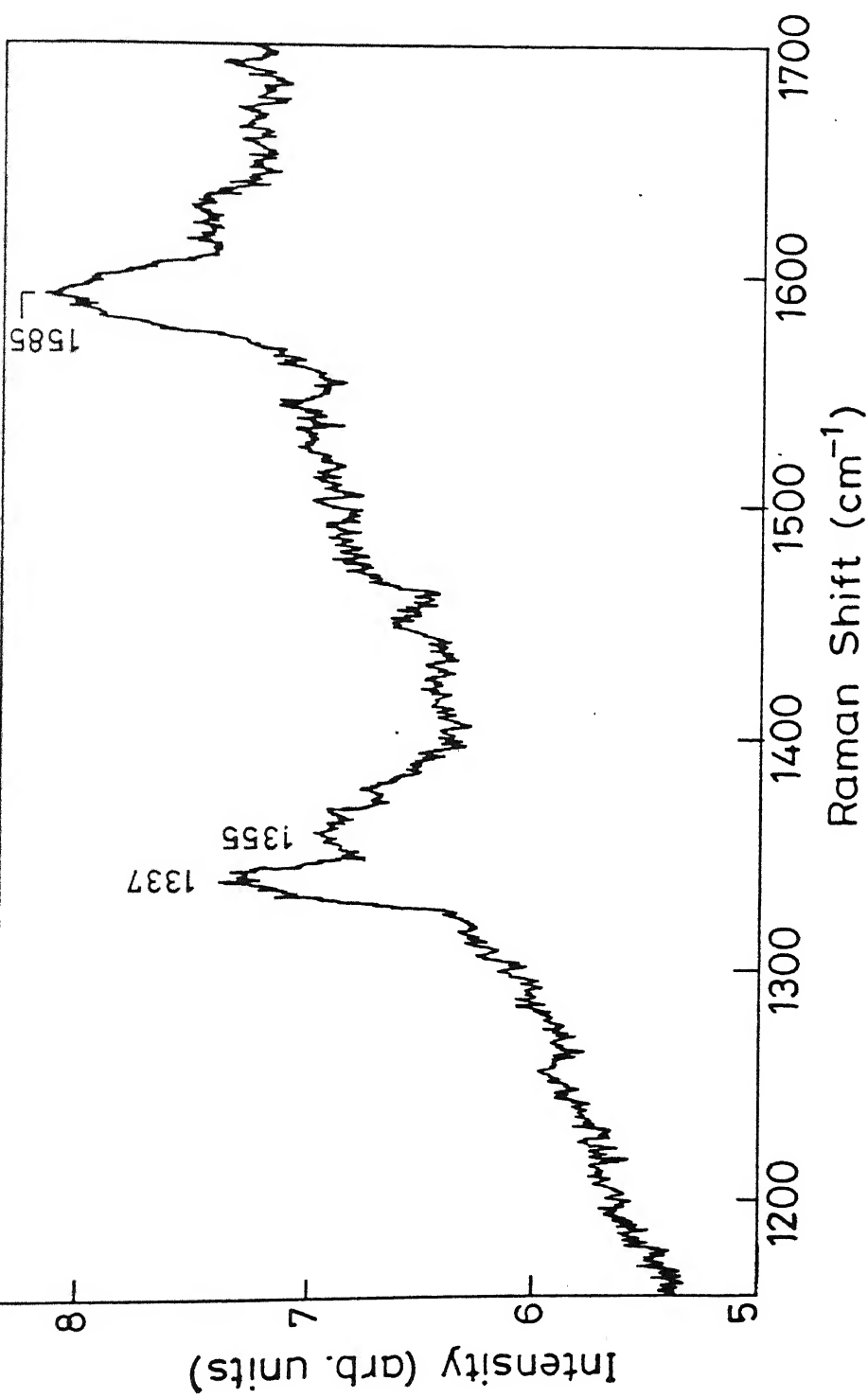


Fig 6.8 Raman spectrum of a diamond film corresponding to fig. 6.7.

lower pretreatment time no change was observed in the diamond growth as compared to no pretreatment conditions. This may be due to the fact that the self heating of the substrates takes some time to reach the desired temperature of about 350 °C. Increasing the pretreatment time to 3 minutes leads to a decrease in particle density to by approximately an order of magnitude.

Based on the above results on diamond films deposited on untreated and pretreated Mo substrates, a comparison of growth processes can be made. During the growth, initially the substrate is covered with isolated and stable islands of the deposited materials. There are two routes by which atoms can reach an island and thereby cause it to grow. These are, by direct addition from the gas specie above the substrate and by migration across the substrate surface. Later is the dominant initial process when there is an interfacial layer as evident by larger particles of diamond with lesser density in case of pretreated Mo (Fig. 6.6). While in case of direct deposition, a very high rate of incoming species combined with a large value of surface diffusion energy causes the island to grow more rapidly in height than in area. This is evident by smaller particles of diamond seen in SEM micrographs in case of untreated substrates.

Lateral growth of diamond on Mo by sideways propagation of ledges formed on {100} diamond surfaces by oxidation has been observed by Ravi and Joshi [331] at higher substrate temperatures. Our results compare favorably with those of Abe et al [329] who obtained a particle density of  $3 \times 10^4 / \text{cm}^2$  after a preoxidation of the substrates at much higher temperature of 1050 °C for longer duration ~20 minutes. The faceting of diamond crystallites on Mo oxides may be due to the suppression of graphite [329] and lateral growth of diamond [331].

In order to probe the nature of interfacial layer formed during pretreatment, we exposed the cleaned Mo substrate to outer flame only, for a duration of 90 minutes under the identical pretreatment conditions. XRD spectrum (Fig. 6.9) shows the peaks corresponding to oxides of molybdenum as identified from ASTM 5-441, 13-142, 21-569, 32-671 tables. No traces of graphite or DLC are observed. These results are in contrast to observation of Abe et al [329] on the interfacial layer formed on Mo at 1050 °C using outer zone of the flame. In this study [329], the interfacial layer was found to contain large amount of molybdenum carbides along with oxides.

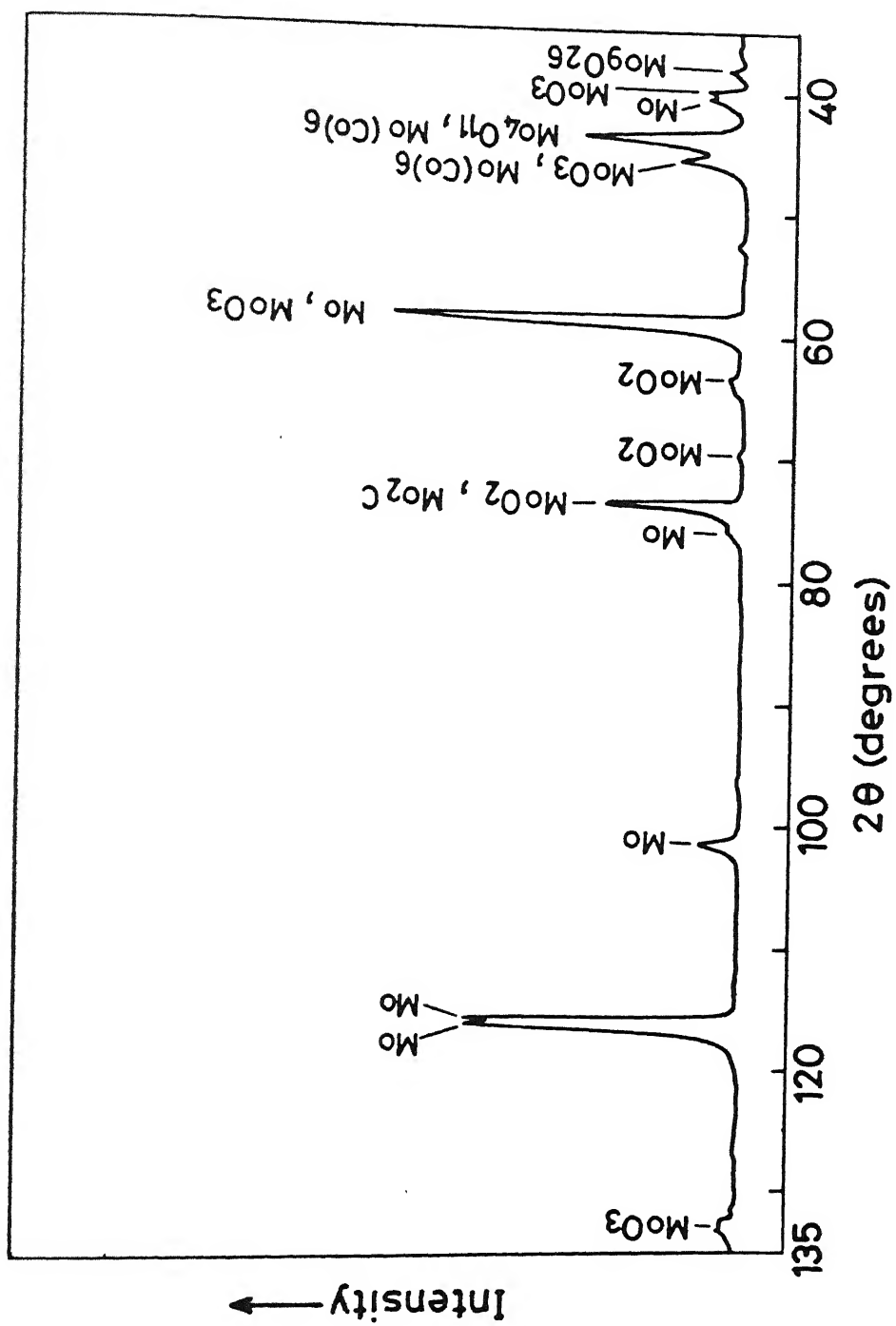


Fig 6.9 XRD spectrum from the oxide film on Mo.

Formation of carbides ( $\text{MoOC}$  and  $\text{Mo}_2\text{C}$ ) have been speculated to be the nucleation sites for diamond growth and oxide layer to be the suppresser of graphite formation [329]. Though absence of any graphite in our case does support that the interfacial oxide layer inhibits graphite formation, it may be mentioned that the short duration (1 to 3 minutes) pretreatment used by us leaves the Mo surfaces shiny without any traces of visible carbon. Change in surface composition could be detected by X-rays also. The EPMA data shows presence of oxygen on the surface (not shown).

In order to find the nature of oxides which are helpful in diamond growth, we examined the XRD spectra of other kinds of molybdenum oxides also. These were the oxides formed by heating Mo in air and molybdenum native oxides. We found that heating Mo in air at the pretreatment temperatures or leaving the native oxides at the substrate surfaces prior to diamond deposition using standard middle zone conditions did not yield the faceting effects as observed with pretreatment. This may be due to different compositions and structures of the oxides formed in these cases.

In analogy with DLC films, which may be considered as alloys of polymeric, tetrahedral and trigonally bonded carbon, polycrystalline diamond films may also consist of these components, though in different concentrations, along with diamond. The evidence comes from Raman studies which show the presence of non-diamond phases of carbon even in good quality diamond films. It is observed that these non-diamond components reduce on heating the samples up to  $600^\circ\text{C}$ . This may be associated with the evolution of hydrogen. The thermal desorption spectra from our flame deposited diamond film on Mo shows a sharp peak due to  $\text{H}_2$  evolution around  $600^\circ\text{C}$  as seen in Figure 6.10. This hydrogen may be ascribed to the desorption of chemisorbed hydrogen at the surfaces as discussed earlier (Chapter IV). The increase in hydrogen QMS above  $800^\circ\text{C}$  indicates the temperature of maximum evolution rate ( $T_m$ ) to be higher than  $900^\circ\text{C}$ . This hydrogen may be originating from the structural regions in which hydrogen is uniformly distributed and bonded almost completely to  $\text{C}(\text{sp}^3)$  atoms. The  $T_m$  for hydrogen desorption from CVD diamond films was found to be around  $900^\circ\text{C}$  [369]. Thermal Effusion data clearly shows a better thermal stability of diamond films as compared to DLC films.

### 6.3.2 Diamond Growth On Steel

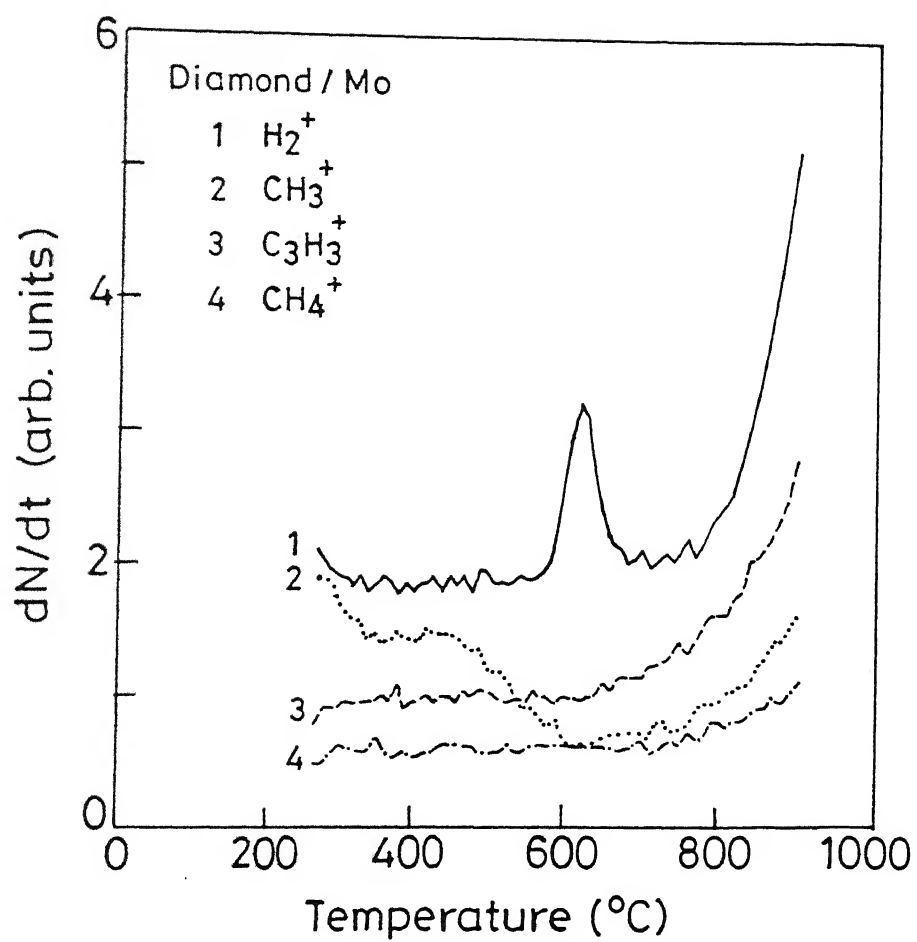


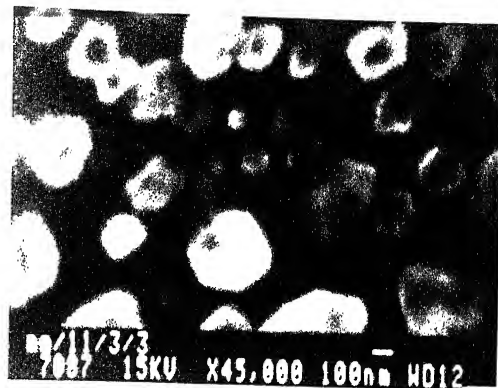
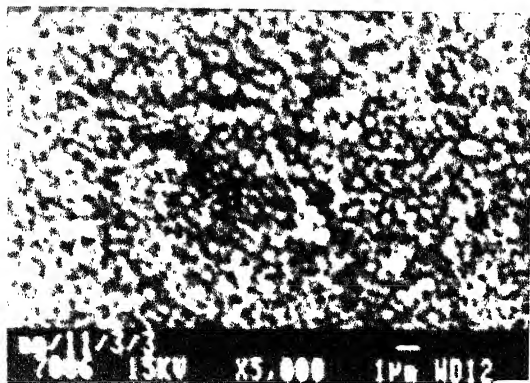
Fig 6.10 Thermal desorption spectrum of a 2  $\mu\text{m}$  thick diamond film on Mo substrate.



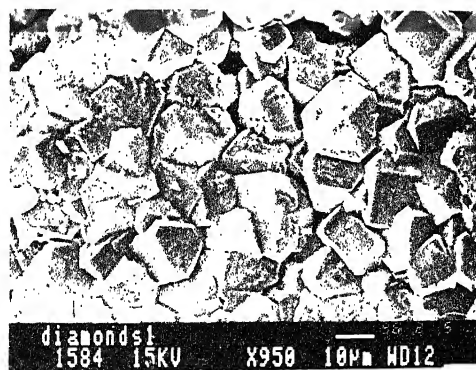
Diamond deposition experiments were carried out on commercial AISI 304 stainless steel substrates. Energy Dispersive X-ray Analysis (EDX) showed the composition to be 20.2 at % Cr, 8.7 at % Ni, 1.2 at % Mn, and balance Fe. Carbon is usually present in this steel having atomic concentration of <1%. The substrate surface preparation includes cleaning and polishing using 1-2  $\mu\text{m}$  size diamond paste. For depositions, same procedure was applied as in case of Mo, but lower feather length L of about 25 mm and substrate temperatures ( $\sim 650^\circ\text{C}$ ) were found to be optimum. Pretreatment was carried out for 3 minutes duration at a substrate temperature of about  $300^\circ\text{C}$ . Films deposited without this pretreatment had poor adherence to the substrate and no faceted diamond particles were seen in their SEM micrographs.

Figure 11(a) shows the scanning electron micrograph of the diamond films obtained after 10 min. deposition on steel. It shows the faceted diamond particles. There is no evidence of soot formation in the early stages of growth (fig. 11a). Large grain size well faceted diamond films were obtained by increasing the deposition time. SEM micrograph of a sample deposited for 90 min. is shown in Fig. 11 (b). X-ray diffraction pattern of the film corresponding to Fig. 11b is shown in Fig. 12. Presence of diamond is clearly seen by the peaks corresponding to (111), (220), (311), and (400) planes of diamond marked in this figure. It must be pointed out that the X-ray diffraction peaks due to austenitic steel [370] substrates are very close to that of the polycrystalline diamond and the interpretation of X-ray diffraction peaks assigned to diamond can be misleading. However, increase in x-ray intensity of diamond related peaks on films deposited for longer duration confirms the x-ray assignment. In addition, lower planes of diamond were also observed in XRD spectrum of the film using lower wavelength x-ray target of iron ( $\lambda=0.71 \text{ \AA}$ ) (not shown). Figure 12 also shows the presence of oxides of iron (mainly  $\text{Fe}_2\text{O}_3$ ) at peaks marked 2,3,6,10-12 and 16-18, and the oxides of Cr at peaks 1-3. There is no clear evidence of carbide formation due to the overlap in interplanar spacing (d) values of iron carbides with that of oxides of iron. Peak numbers 5,14 and 18 also correspond to 'd' values of graphite.

Fig. 13(a) shows the Raman microprobe spectra of the diamond films corresponding to fig. 11(a). The deconvolution of spectrum in fig. 13(a) shows that there



(a)



(b)

Fig 6.11 Scanning electron micrograph of diamond film deposited at substrate temperature of  $625^{\circ}\text{C}$  on stainless steel substrate for (a) 10 minutes and (b) 90 minutes after pretreatment of substrate by outer flame for 3 minutes.

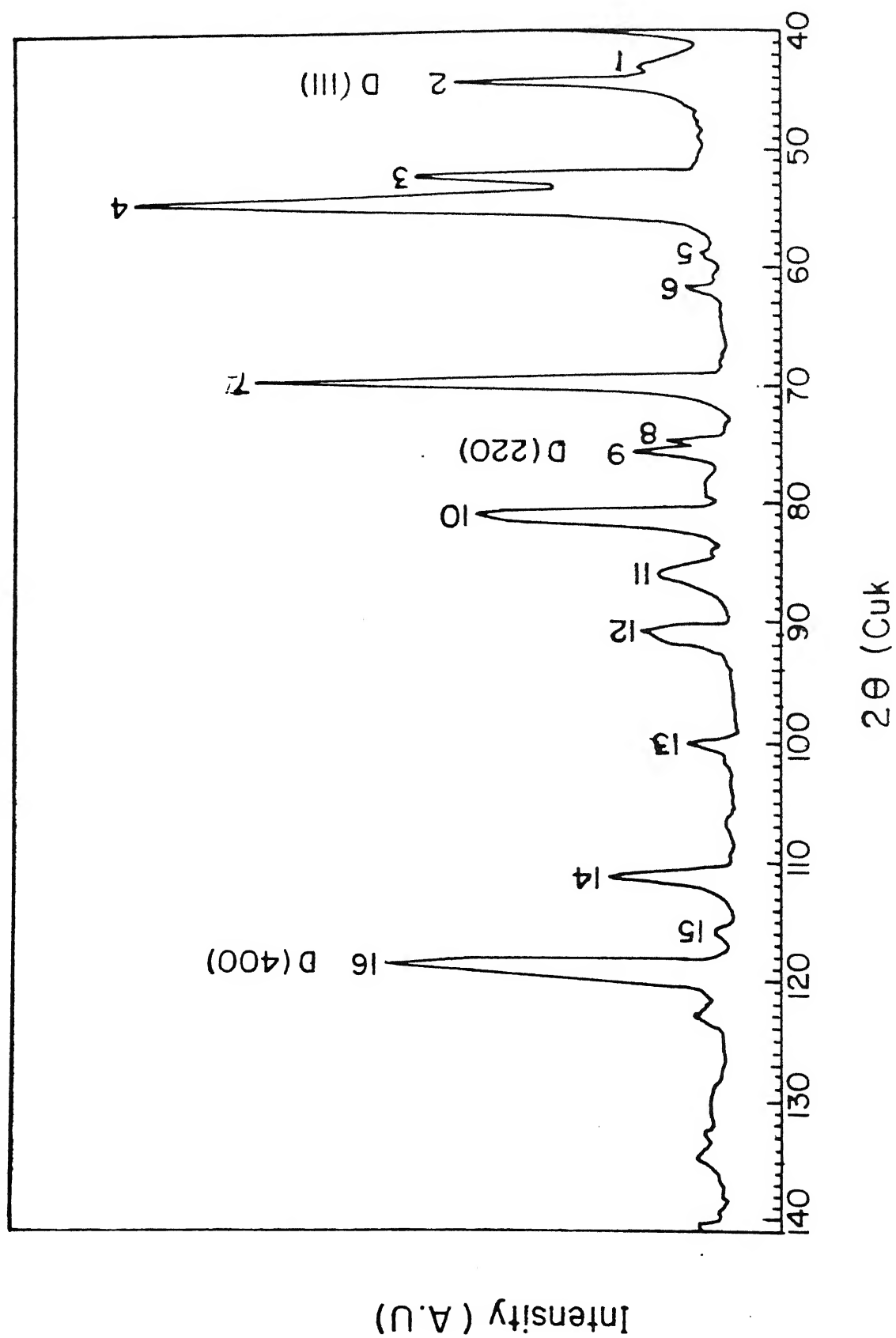


Fig 6.12 XRD spectrum of the diamond film on stainless steel substrate corresponding to fig 6.11 (b).

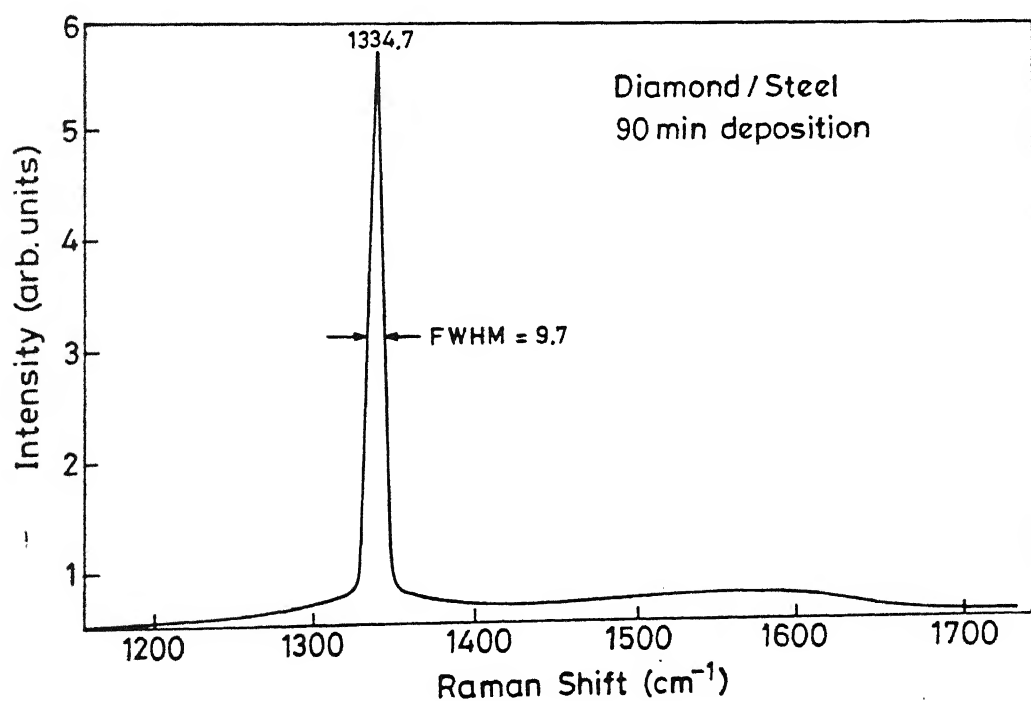
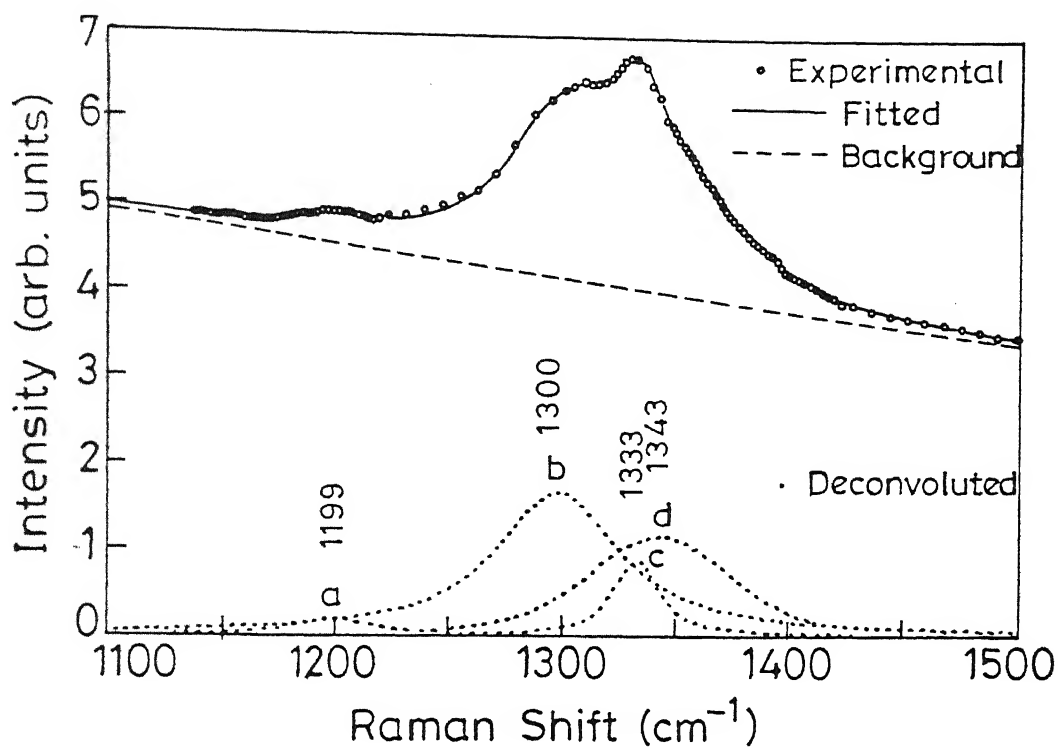


Fig 6.13. Raman spectra of diamond films on stainless steel substrate deposited for (a) 10 minutes and (b) 90 minutes, corresponding to figs 6.11 a and b respectively.

are four Raman modes present in the sample. The 1333 peak is obtained from diamond crystallites. The lower peak at 1300 and 1199  $\text{cm}^{-1}$  are due to  $\text{sp}^3$  C-C vibration modes which do not have perfect cubic symmetry. A broad band at 1343  $\text{cm}^{-1}$  could be ascribed to the disorder induced vibrational modes of graphite [371]. This band has been observed earlier in diamond deposited at hard substrates where the mismatch of thermal expansion between the substrate and the diamond particle is large [179].

Fig. 13(b) shows a Raman spectrum measured on the thicker sample corresponding to fig. 11(b). A sharp peak at 1334.7  $\text{cm}^{-1}$  is observed which is characteristic of cubic diamond. FWHM of 9.7  $\text{cm}^{-1}$  is obtained without instrument correction and is indicative of the high quality of diamond films. A broad and weak Raman band at  $\sim 1580 \text{ cm}^{-1}$  can also be seen in the background of Raman spectrum. This is a signature of graphitic phase having  $\text{sp}^2$  bonding configuration. This component is negligible in the sample area under observation. A slight upward shift in the Raman band from the standard values can be attributed to the stresses in the films. Stress value of  $\sim 1.5 \text{ GPa}$  is estimated from the Raman shift.

In order to elucidate the role of pretreatment by outer zone of the flame, a variety of experiments were carried out. Films deposited without the pretreatment were graphitic as detected by Raman data having non-faceted particles. Long duration ( $\sim 45 \text{ min.}$ ) exposure of the substrates to the outer flame alone did not result into any carbon deposit. Surfaces were visibly smooth and no deposition was observed. EPMA analysis showed the presence of oxygen. X-ray analysis showed the presence of oxides of iron and chromium only.

It is interesting to note that there is no evidence of soot formation at early stages of growth (Fig. 11a). This is in contrast to the earlier reports on the growth of diamond films on steel using plasma CVD methods employing high substrate temperatures [345]. It is proposed that the pretreatment of the substrates using oxidizing flames converts the top surface layers of steel to form an interfacial layer of iron and chromium oxides. Further evidence for this comes from the composition analysis by Rutherford backscattering (RBS) measurements. The RBS spectrum of the diamond film is shown in Fig. 6.14. Besides C from the diamond film and Cr/Fe from the substrate, oxygen was observed. The RBS depth profile confirms the presence of oxide layer at the interface. In addition to the

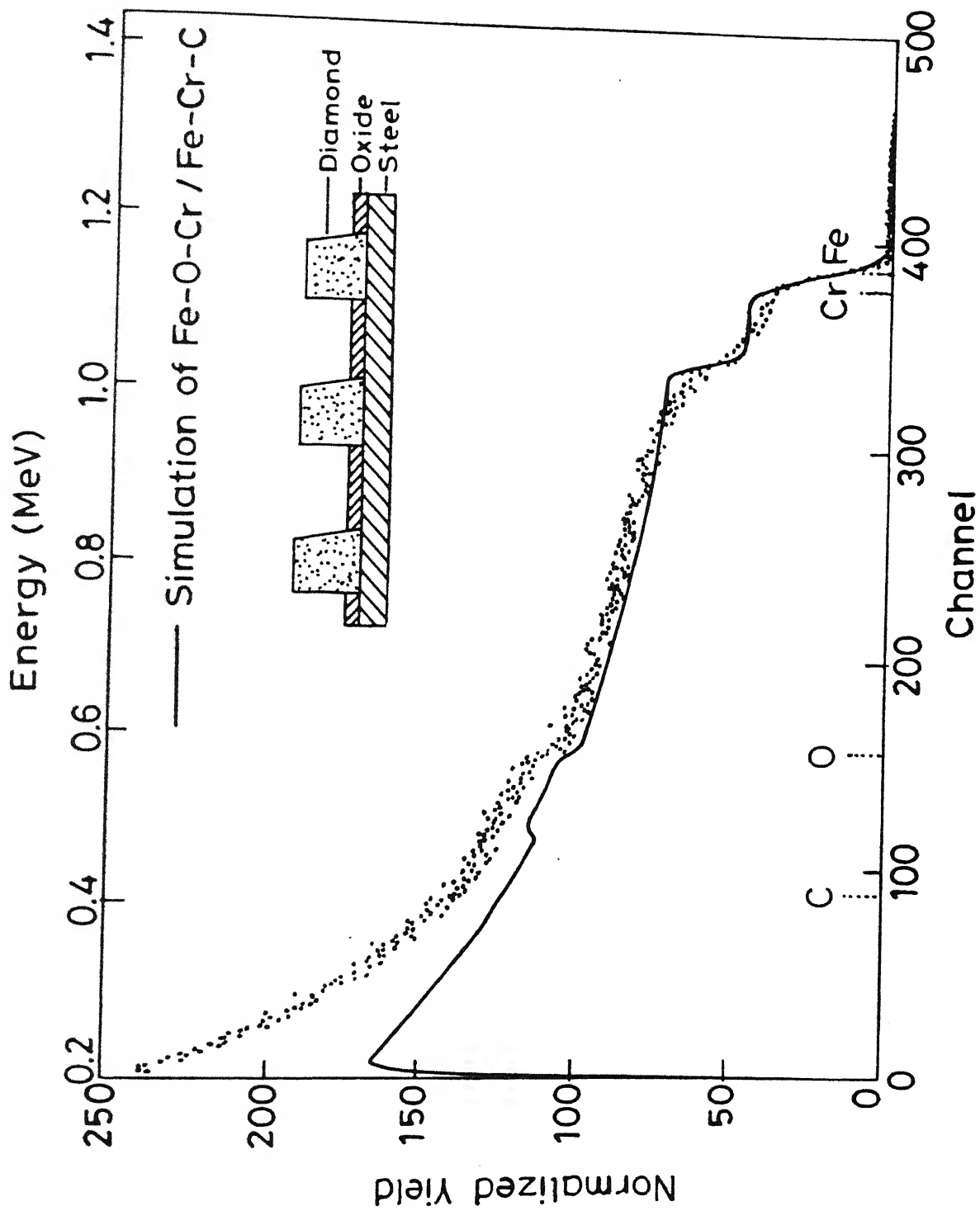
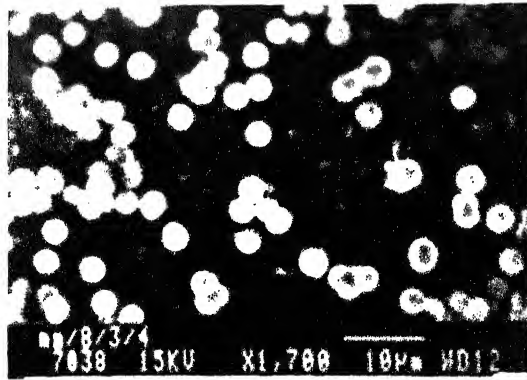
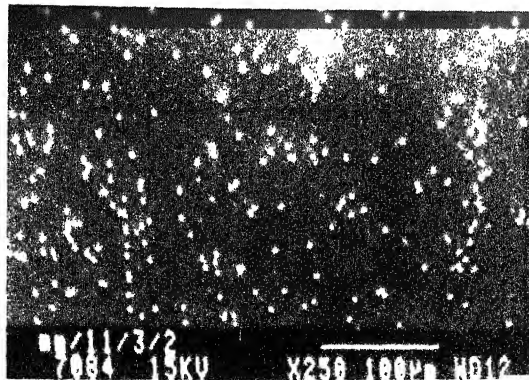


Fig 6.14 Normalized RBS spectra of steel-oxide -diamond composite



(a)



(b)

g 6.15 (a) SEM photographs showing diamond growth on Ni.  
 (b) SEM photographs showing diamond growth on W.

presence of oxide layer, the lower substrate temperatures in our process are expected to help in minimizing the diffusion of carbon in steel.

### 6.3.3 Diamond Growth on W and Ni

Nickel being lattice matched to diamond (see Table 6.1) attracts special attention as a substrate material [362]. However, an intermediate graphitic layer is usually present while depositing diamond on Ni. Godbole et al [372] have overcome this problem by using AlN interfacial layer. A seeding and multistep deposition process is also reported [373] which shows the formation of certain types of nickel-carbon-hydrogen intermediate states. However, no reports of diamond deposition on Ni substrates by oxy-acetylene flame method are available. We have attempted to grow diamond films on Ni using this method[368].

SEM micrograph of a sample (Fig. 6.15a) prepared on nickel substrate using feather length of  $L \cong 15$  mm and substrate temperature of  $650^\circ\text{C}$ , shows the growth of 4-5  $\mu\text{m}$  size diamond crystallites with a density of  $\cong 3 \times 10^6 / \text{cm}^2$  in a deposition run of 20 minutes. Further optimization of flame parameters and substrate temperature etc. is required to obtain good quality diamond films.

A SEM picture of a sample prepared on tungsten using acetylene feather length  $L$  of  $\sim 25$  mm and substrate temperature of  $800^\circ\text{C}$  without any pretreatment is shown in Fig 6.15 (b). The SEM micrograph shows the particles of  $\sim 4$   $\mu\text{m}$  size with a density of  $\cong 10^5 / \text{cm}^2$  in deposition run of 20 minutes. It has been observed by many workers that the formation of carbides is an important step in nucleation of diamond on W substrates. Similar results were obtained by Akatsuka and Shimura [374] and Williams et al [375] using other deposition techniques. Perry and Somorjai [376] studied the interfacial layer formed during growth of CVD diamond films on metal substrates including Ti, W, Mo and Cu. Their results show the presence of carbides and oxides of the native metals at the interface under diamond deposition conditions. The presence of interfacial layers favours the rapid formation of critical nuclei of carbon atoms before they re-evaporate during deposition.



## 5.4 CONCLUSIONS

Nucleation and growth of diamond crystals and films grown by oxy-acetylene flame method are found to be strongly dependent on nature of flame as well as that of substrate surface.

Diamond films with predominantly  $\{100\}$  facets are deposited on Mo substrates in a stationary, single nozzle oxy-acetylene flame using an in-situ surface pretreatment method. Deposition runs using different parts of the flame as well as using different gas ratios to obtain different flame structures were carried out. The results suggest that diamond is deposited via the transport of hydrocarbon species produced in the acetylene feather of the flame for the gas flow ratios close to unity. Formation of an interfacial layer on molybdenum by outer zone of the flame suggests that this layer improves quality and adherence of the films via growth of  $\{100\}$  faceted crystals of diamond.

Our results on Mo, W, Ni and steel substrates and nature of intermediate compounds formed suggest that the formation of a carbide layer is not necessary for diamond growth in all cases. The diamond nucleation on various metal substrates is favored under the conditions producing a diffusion barrier layer. This layer prevents carbon diffusion into the substrate bulk, either by carbide formation or by surface carbon saturation.

A short duration exposure to the outer flame at low substrate temperatures, is found to improve the quality and adherence of diamond films on stainless steel substrates.

## CHAPTER VII

### SUMMARY, CONCLUSIONS AND SCOPE OF FURTHER WORK

Ability to synthesize thin films of diamond and diamond-like carbon phases using low pressure low temperature techniques has heralded an era of immense activity full of potentials and challenges. In noncrystalline thin films, especially in the presence of hydrogen, carbon can assume a variety of structures. We have employed dc glow discharge technique to systematically study the growth of hydrogenated amorphous carbon (a-C:H) films to understand the inter-relationships between growth parameters, film microstructures and resultant properties. A parallel plate research plasma system was designed and fabricated for this purpose. Electrical discharge parameters were correlated with reactor geometry to obtain system independent description of the process parameters. In-situ mass spectroscopy of the plasma provided useful insight into the decomposition pattern of acetylene source gas. In particular, role of hydrogen, which influences both growth conditions and properties of the deposited films, was investigated.

A large number of films were prepared under carefully chosen deposition conditions and a variety of characterization techniques were utilized to explore their microstructure and properties. In particular, three complementary techniques viz infrared spectroscopy, elastic recoil detection analysis, and mass spectroscopic thermal effusion techniques (MSTE) were applied to characterize hydrogen in a-C:H films and related microstructure. MSTe was established for the characterization of films having different microstructures. Vickers microindentation method was used for microhardness evaluation of films. Spectrophotometry measurements in the visible and ultraviolet range provided the information on absorption coefficient, optical bandgap and refractive index.

Based on the results obtained from the effects of deposition conditions on the plasma and film properties, a correlation between hydrogen incorporation, microstructure

films, and their physical properties was established. A phenomenological model for film growth was presented. Physical properties of films were explained in terms of a fully constrained network model.

In addition, a simple and inexpensive oxy-acetylene flame technique was employed to explore the possibility of the deposition of smooth crystallites of diamond on metallic substrates of practical importance.

Some major conclusions drawn from the present study are summarized as follows:

We have found that the gas phase plasma processes in a DC glow discharge acetylene plasma are mainly influenced by the reactor geometry, applied electric fields, and composition and pressure of the feedgas. All these parameters are unified in the Paschen curve for the deposition system.

Good quality diamondlike carbon films are obtained at low pressures and small interelectrode spacing. Increasing the gas pressure results in gas phase polymerization as well as degradation in film properties.

Substrate temperature and the energies of ions impinging on growing film surface are found to have a strong influence on the microstructure of deposited a-C:H films. Films deposited at room temperature are found to result in void-rich and density deficit material. A structural transformation to a mixed phase material containing DLC, amorphous and graphitic carbon is found to take place in the films deposited above  $\sim 400^\circ\text{C}$ .

An ion assisted growth from methyl radical as the growth precursor is found to explain the dependence of growth rate on various external parameters controlling plasma and surface based reactions such as gas pressure, hydrogen dilution, substrate temperature, and negative bias. This model qualitatively explains the microstructure and film properties.

In general, we have found that the films produced by dc glow discharge of acetylene, under appropriate ion bombardment at surface and atomic hydrogen concentration in the plasma, contain low hydrogen concentration and a compact film structure.

Threshold temperature for hydrogen effusion is found to be  $\sim 400^\circ\text{C}$  and two major peaks are observed at around  $600^\circ\text{C}$  and  $750^\circ\text{C}$  in the dc discharge deposited DLC

films. A variety of hydrocarbons such as  $\text{CH}_3$ ,  $\text{C}_2\text{H}_2$ ,  $\text{C}_2\text{H}_4$ ,  $\text{C}_3\text{H}_3$ , and  $\text{C}_4\text{H}_3$  etc. are evolved from soft films on heating above  $400^\circ\text{C}$ . In contrast, evolution spectra of hard films are dominated by molecular hydrogen along with small amounts of methyl groups only.

7. Analysis of thermal effusion suggests thermal desorption or bond breaking to be the rate limiting step for effusion of hydrocarbons and low temperature hydrogen evolution. Thermal annealing experiments, along with the infrared and elastic recoil detection analysis, have revealed that the hydrogen is uniformly distributed in samples containing low hydrogen contents and it evolves at higher temperatures ( $\sim 750^\circ\text{C}$ ).
8. It is shown that a careful analysis of infrared data can yield reliable values of  $\text{sp}^3$  and  $\text{sp}^2$  C-C fractions. Methodology to obtain  $\text{sp}^3$  and  $\text{sp}^2$  fractions of C-C bonds using infrared spectroscopy is found to be satisfactory by comparing film properties with the expected behavior from the infrared data on a large number of samples. In particular, we have found that detailed information on hybridization fractions, total hydrogen content as well as relative fractions of mono- and polyhydrides is required to correlate the measured film properties such as microhardness and optical gap.
9. Microstructural information can be unified in the average coordination number,  $m$ . In our a-C:H films values of  $m$  were found to be well correlated with the hydrogen concentration. At low hydrogen concentrations, films with high  $\text{sp}^3$  carbon content are found to be overconstrained. Network relief in such films can be achieved by the formation of mixed phases. These films can be categorized as hydrogenated tetrahedral amorphous carbon (ta-C:H).
10. Nanocrystalline phases of carbon including hexagonal diamond are observed in hard DLC films ( $V_H = 2500 \text{ kgf/mm}^2$ ) deposited at optimum ion energies ( $V_b \sim -250\text{V}$ ) at  $250^\circ\text{C}$  using acetylene diluted in hydrogen (50%). For these films, hydrogen content is quite low ( $\sim 5 \text{ at.}\%$ ).  $\text{Sp}^3$  C-C content is found to be  $\sim 71\%$ .
11. By using only one simple deposition technique of dc glow discharge, we have obtained various manifestations of the amorphous carbon microstructures by choosing the deposition parameters carefully.
12. Growth of square faceted diamond crystallites was accomplished using a simple and inexpensive oxy-acetylene flame technique. In-situ oxidation of Mo surfaces using the

oxidizing zone of the flame, just prior to diamond deposition at  $\sim 850^{\circ}\text{C}$  show the role of interfacial layers in restricting carbon diffusion in Mo and coalescence of diamond nuclei. In addition, adherent polycrystalline diamond films were obtained on stainless steel substrates without the use of external buffer layers. This was accomplished by a novel short duration pretreatment of steel surface using the oxy-acetylene flame itself.

The present work has demonstrated that highly tetrahedral amorphous carbon films can be synthesized by simple dc glow discharges at relatively low substrate temperatures. These films exhibit high optical bandgap but low hydrogen content. It would now be of interest to study the electrical transport phenomena in such films. Knowledge of density of states would help in exploring the possibility of doping. Understanding of their opto-electronic properties would make these materials useful for further technological applications.

As regards the understanding of the dc glow discharge growth process, especially substrate bias conditions, the electrical characteristics of discharge is required. One would like to find out the electric field profile (with and without bias), cathode fall voltage and sheath thickness, estimated mean free paths for elastic, dissociation and ionization at the electron energies for these discharges. Further, it would be interesting to estimate the fluxes to the substrate (neutrals, ions and electrons). These studies would also lead to the possible comparison between merits of dc arrangement with the rf discharge results.

## REFERENCES

1. F.P. Bundy, H.M. Strong, and R.J. Wentorf, *Nature*, 176, 51 (1955).
2. P.W. Bridgmann, *Sci. Am.* 193, 42 (1955).
3. R.B. Heimann, J. Kleimann and N.M. Salansky, *Carbon* 22, 147 (1984).
4. M. Frenklach, R. Kematick, D. Huang, W. Howard, K.E.Spear, A.W. Phelps and R. Koba, *J. Appl. Phys.* 66, 395 (1989).
5. See for example, H.W. Kroto, *Science* 242, 1139 (1988).
6. J.E. Field in "The Properties of Diamond" Ed. J.E. Field, p 282-324 (Academic Press, New York 1979).
7. R.E. Hanneman, H.M. Strong and F.P. Bundy, *Science* 155, 995 (1967).
8. K.L. Chopra, "Thin Film Phenomena", Mc Graw-Hill; New York (1969).
9. See for review, B.V. Dergajuin and D.B. Fedoseev, *Sci. Am.* 233, 102 (1975).
10. W.G. Eversole, U.S. patents 3030187 and 3030188 (1962).
11. J.C. Angus, H.A. Will and W.S. Stanka, *J. Appl. Phys.* 39, 2915 (1968).
12. S. Matsumoto, Y.Sato, M.Tsutsumi and N.Setaka, *J. Mater. Sci.* 17, 3106 (1982).
13. S. Matsumoto, Y. Sato, M. Kamo and N. Setaka, *Jpn. J. Appl. Phys.* 21, L183 (1982).
14. S. Matsumoto, *J. Mater. Sci. Lett.* 4, 600 (1985).
15. M. Kamo, Y. Sato, S. Matsumoto and N. Setaka, *J. Cryst. Growth* 62, 642 (1983).
16. J.C. Angus and C.C. Hayman, *Science* 241, 913 (1988).
17. K.E. Spear, *J. Am. Ceram. Soc.* 72, 171 (1989).
18. R.C. Devries, *Ann. Rev. Mater. Sci.* 17, 161 (1987).
19. J.C. Angus, Y. Wang and M. Sunkara, *Annu. Rev. Mater. Sci.* 21, 221 (1991).
20. R. Messier, A.R. Badzian, K.E. Spear, P. Bachmann and R.Roy, *Thin Solid Films* 153, 1 (1987).
21. S. Eisenberg and R.W. Chabot, *J. Appl. Phys.* 42, 2953 (1971).
22. L. Holland and S.M. Ojha, *Thin Solid Films*, 58, 107 (1979).
23. C. Weissmantel, *Thin Solid Films*, 58,101, (1979).
24. Y. Lifshitz, S.R. Kasi and J.W. Rabalais in *Properties and Characterization of Amorphous Carbon Films*, Eds. J.J.Pouch and S.A. Alterovitz, Vol. 52 &53 of *Material Science Forum*, p237 (Trans Tech Publications, Switzerland 1989).
25. W.A. Yarbrough, A. Inspektor and R. Messier in ref. 24, p151.
26. P.J. Fallon, V.S. Veerasamy, C.A. Davis, J. Robertson, G. Amaratunga, W.I. Milne, and J. Koskinen, *Phys. Rev. B* 48, 4777 (1993).
27. V.S. Veerasamy, G.A.J. Amaratunga, W.J. Mline, P.J. Fallon, D.R. McKenzie and C.H. Davis, *Diamond and Relat. Mater.* 2, 782 (1993).
28. R. Lossy, D.L. Pappas, R.A. Roy, J.J. Cuomo, and V.M. Sura, *Appl. Phys. Lett.* 54, 216 (1992).

9. M. Weiler, S. Sattel, K. Jung, H. Ehrhardt, V.S. Verrasamy, and J. Robertson, *Appl. Phys. Lett.* 64, 2797 (1994).
0. G.M. Pharr, D.L. Callhan, S.D. McAdams, T.Y. Tsui, S. Anders, A. Anders, J.W. Ager, I.G. Brown, C. Singh, S.R.P. Silva, and J. Robertson, *Appl. Phys. Lett.* 68, 779 (1996).
1. D.R. McKenzie et al., *Diamond and Related Materials* 1, 773 (1995).
2. S.Ravi, P. Silva, Shi Xu, B.X. Tay, and H.S. Tan and W.I. Milne, *Appl. Phys. Lett.* 69, 491 (1996).
3. John C. Angus, P. Koidl and S. Domitz in *Plasma Deposited Thin Films*, Eds. J. Mort and F. Jansen, Chap. 4 p89-127 (CRC Press, Boca Raton, FL 1986).
4. J.C. Angus, *Thin Solid Films* 216, 126 (1992).
5. J. Fink, Th. Muller-Heizerling, J. Pflug, J. Scheerer, B. Dischler, P. Koidl, A. Bubenzer and R.E. Sah, *Phys. Rev. B* 30, 4713 (1984).
6. F.W. Smith, *J. Appl. Phys.* 55, 764 (1984).
7. H. Efstathiadis, Z. Akkerman and F.W. Smith, *J. Appl. Physics*. 79, 2954 (1996).
8. J.C. Phillips and M.F. Thorpe, *Solid State Commun.* 53, 699 (1985).
9. J.C. Angus and Y.Wang, *NATO Advanced Study Institute on Diamond and Diamond like Materials Castel vecchio Pascoli, Italy, July22-Aug.3, 1990.*
0. J. Robertson, *Adv. Phys.* 35, (1986) 317.
1. J. Robertson and E.P. O'Reilly, *Phys. Rev. B.* 33(1986) 4034.
2. K. Kobayashi, N. Mutsukura, and Y.Machi, *Thin Solid Films* 158, 233 (1988).
3. J. W. Zou, , K. Reichelt, K. Schmidt and B. Dischler, *J. Appl. Phys.* 65, 3914 (1989).
4. J.W. Zou, K. Schmidt, K. Reichelt, and B.Dischler, *J. Appl. Phys.* 67, 487 (1990).
5. A. Bubenzer, B. Dischler, G. Brandt and P. Koidl, *J. Appl. Phys.* 54, 4590 (1983).
6. P. Couderc and Y. Catherine, *Thin Solid Films* 146, 93 (1987).
7. D. R. Mckenzie, D. A. Muller, E. Kravtchinskaria, D. Segal, D.J.H. Cockayne, G. Amaratunga and R. Silva, *Thin Solid Films* 206 (1991) 198.
8. A. Bubenzer, B. Dischler, and A. Nyaiesh, *Thin Solid Films* 91, 81 (1982).
9. B. Meyerson and F.W. Smith, *J. Non-Cryst. Solids* 35 & 36, 435 (1980).
0. O. Stenzel, R. Petrich and M. Vogel *Optical Materials* 2, 125 (1993).
1. K. Fabisiak, F. Rozploch, and J. Wiecezorek, *J. Phys. D* 21, 995 (1988).
2. R.E. Sah, B. Dischler, A. Bubenzer, and P. Koidl, *Appl. Phys. Lett.* 46, 739 (1985).
3. A. Joshi, S. A. Gangal, and S.K. Kulkarni, *J. Appl. Phys.* 62, 6668 (1988).
4. B. Dischler, A. Bubenzer, and P. Koidl, *Solid State Commun.* 48, 105 (1983).
5. J. A. Woollam, V. Natarajan, J. Lamb, A.A. Khan, G. Bu-Abbud, D. Mathine, D. Rubin and R.O. Dillon, *Thin Solid Films* 119, 121 (1984).
6. K. Kobayashi, N. Mutsukura, and Y. Machi, *J. Appl.Phys.* 59, 910 (1986).
7. M. Yoshikawa, G. Katagiri, H. Ishida, A. Ishitani and T. Akamatsu *J. Appl. Phys.* 64, 6464 (1988).

58. J. Zelez, J. Vac. Sci. Technol. A1, 305 (1983).
59. N. Savvides, J. Appl. Phys. 59 ,4133 (1986).
60. D. Duta, K.K. Chattopadhyay, J. Dutta, S. Chaudhuri and A.K. Pal. Mater. Letts. 18, 114(1993).
61. K. Rohwer, P. Hammer, J. Theile, W. Gissler, P. Blaudeck, T. Fraunheim and D. Meissner, J. Non. Cryst. Solids, 137 & 138 (1991) 843.
62. D.I. Jones and A.D. Stewart, Phil. Mag. B. 46, 423 (1982).
63. S. Craig and G. L. Harding Thin Solid Films, 97, 345 (1982)
64. J. Robertson, in ref. 24 p 125.
65. J. Seth, M.I. Chaudhry, S.V. Babu, J. Vac. Sci. Technol. A 10, 3125 (1992).
66. D.A. Anderson, Phil. Mag. 35, 17 (1977).
67. I. Laszlo and S. Kugler, J. Non Cryst. Solids 137 & 138 , 831 (1991).
68. P.N. Dixit, Sushil Kumar, D. Sarangi and R. Battacharya, preprint Solid State Commun 1995.
69. G.A.J. Amaratunga, V.S. Veerasamy, W.I. Milne, C.A. Davis, S.R. P. Silva, and H.S. Mackenzie, Appl. Phys. Lett. 63, 370 (1993).
70. V.S. Veerasamy, G.A.J. Amaratunga, C.A. Davis, W.I. Milne, P. Hewitt and M. Weiler, Solid-State Electronics 37, 319 (1994).
71. G.A.J. Amaratunga, D.E. Segal and D.R. Mckenzie, Appl. Phys. Lett. 59, 69 (1991).
72. X. Jiang, K. Reichelt, and B. Stritzker, J. Appl. Phys, 66, 5805 (1989).
73. N. Savvides and T.J. Bell, J. Appl. Phys. 72, 2791(1992).
74. E. Dunlop, J. Haupt, K. Schmidt and W.Gissler, Diamond Relat. Mat. 1, 644 (1992).
75. N. Mutsukura, S. Tomita and Y.Mizuma, Thin Solid Films, 214, 58 (1992).
76. T.M. Wang, W.J. Wang, B.L. Chen and S.H. Zhang, Phys. Rev. B 50, 5587 (1994).
77. N. Wada, P.J. Gaczi and S.A. Solin, J. Non-Cryst. Solids 35 & 36, 543 (1980).
78. R.O. Dillon, J.A. Woollam and V.Katkanant, Phys. Rev. B 29, 3482 (1984).
79. Qi Wang, D.D. Allred and J. Gonzalez-Hernandez, Phys. Rev. B 47, 6119 (1993).
80. Ch. Wild and P. Koidl, Appl. Phys. Lett., 51 (1987) 1506.
81. R. Stief, J. Schafer, J. Ristein, L. Key, and W. Beyer, J. Non. Crys. Solids 198-200, 636 (1996).
82. Y. Bounouh, M.L. Theye, A. Dehbi-Alaoui, A. Matthews and J.P. Stoquert,, Phys. Rev. B. 51 , 9597 (1995),.
83. M. Malhotra, T. Som, V.N. Kulkarni and S. Kumar, Vacuum (In Press, 1996).
84. I. Watanabe and T. Okumura, Jap. J. Appl. Phys. 25, (1986) 1851.
85. A.R. Badzian, P.K. Bachmann, T. Hartnett, T. Badzian and R. Messier, E-MRS Meeting 15, 63 June 1987.
86. M.N. Yoder, in Diamond and Diamond-Like Films and Coatings, Eds. R.E. Clausing, L.L. Horton, J.C. Angus and P.Koidl, NATOASI Series B (Physics) Vol. 266, p 1 (Plenum Press New York 1991).



7. J. M. Pinneo, in ref. 86 page 755.
8. B.V. Spitsyn, in ref. 86 page 855.
9. D.M. Grant, I.R. McColl, M.A. Golozav, J.V. Wood and N. St. J. Braithwaite, *Diamond and Related Materials* 1, 727 (1992).
0. B. Lux and R. Haubner, *Phil. Trans. R. Soc. Lond. A* 342, 297 (1993).
1. M. Seal, *Mater. Sci. Engg. B* 11, 167 (1992).
2. M.C. Costello, D.A. Tossell, D.M. Reece, C.J. Brierley and J.A. Savage, *Diamond and Related Materials*, 3 , 1137 (1994).
3. C.P. Beetz, B.Lincoln, D.R. Winn, K.Segall, M.Vasas and D. Wall, *IEEE Trans. Nuclear Science*, 38, 107 (1991).
4. M.D. Whitfield, S. SM Chan and R. B. Jackman, *Appl. Phys. Lett.* 68, 290 (1996).
5. S. Albin , L. Watkins, K. Ravi and S. Yokota, *Appl. Phys. Lett*, 54, 2728 (1989).
6. D.S. Hoover, S.Y. Lynn, D. Garg, *Solid State Technology*, 89 (1991).
7. V.K. Bazhenov, I.M. Vikulin and A.G. Gontar, *Sov. Phys. Semicond.* 19(8), 829(1985).
8. J.A. Woollam, B.N. De, S. Orzeszko, N.J. Ranno, P.G. Snyder, S.A. Alterovitz, J.J. Pouch, R.L.C. Wu and D.C. Ingram, in ref. 24 p 577.
9. A.H. Lettington, *Phil. Trans. R. Soc. Lond. A* 342, 287 (1993).
0. S. Aisenberg, *J. Vac. Sci. Technol. A*2, 369 (1984).
1. H. Tsai and D.B. Bogy, *J.Vac. Sci. Technol. A*5, 3287 (1987).
2. G.F. Zhang, L.J. Guo, Z.T. Liu, X.K. Xiu, and X.Zheng, *J. Appl. Phys.* 76, 705 (1994).
3. K. Enke, *Applied Optics*, 24, 508 (1985).
4. E. Marotta and N. Bakhru, A. Grill, V. Patel and B. Meyerson, *Thin Solid Films*, 206, 188 (1991).
5. S. Scaglione and G. Emiliani, *J. Vac. Sci. Technol. A*7, 2303 (1989).
6. C. Weissmantel, G. Reisse, H. J. Erlev, F. Henny, K. Bewilogua, U. Ebersbach and C. Schurer, *Thin Solid Films* 63, 315 (1979).
7. F. Richter, K. Bewilogua, H. Kupper, I. Muhling, B. Rare, B. Rother and D.Schumacher, in *Applications of Diamond Films and Related Materials*, Eds. Y.Tzeng, M.Yoshikawa, M.Murakawa and A. Feldman, p 819 (Elsevier, New York 1991).
8. S. Logothetidis. *Appl. Phys. Lett.* 69, 158 (1996).
9. F. Davanloo, E.M. Juengerman, D.R. Jander, T.J. Lee and C.B. Collins *J. Appl. Phys.* 67, 2081 (1990).
0. D.L. Pappas, K.L. Saenger, J. Bruely, W. Krakow, T. Gu and R.W. Collins, *J. Appl. Phys.* 71 , 5675 (1992).
1. R.K. Dwivedi and R.K. Thareja, *Surf. Coat. Tech.* 73, 170 (1995).
2. F. Davanloo, E.M. Juengerman, D.R. Jander, T.J. Lee and C.B. Collins *J. Mater. Res.* 5, 2398 (1990).
3. T. Sato, S. Iguchi, and M. Hanabusa, *Jpn. J. Appl. Phys.* A45, 35 5 (1988).

- 114 S S Wagal, E.M. Juengerman and C.B.Collins, J. Appl. Phys. 53,187 (1988)
- 115 A. Rengan, S.M.Kanetkar, J.Narayan, J.L.Park, Li Ming and S.Bedge, Mat. Sci. And Eng. B7, 2785 (1992).
- 116 T. Anthony, MRS meeting boston, 30-5 (1985).
- 117 S. Matsumoto, Y.Sato, M.Kamo and N.Setaka, Jpn. J. Appl. Phys. 21, 219 (1982).
- 118 S. Matsumoto and Y. Matsui, J. Mater. Sci. 18, 1785 (1983).
- 119 119a. E. Kondoh, T.Ohta, T.Mitomo and K.Ohtsuka, Appl. Phys. Lett. 59, 488 (1991).  
119b. E. Kondoh, K.Tanaka and T.Ohta, J. Appl. Phys. 74, 2030 (1993).
- 120 N. Dilawar, S.Sah, B.R. Mehta and V.D. Vankar, Bull. Mater. Sci. 19, 467 (1996).
- 121 A. K. Dua, V.C. George, D.D. Pruthi and P. Raj, Solid State Commun. 86, 39 (1993) .
- 122 A. Sawabe and T.Inuzuka, Thin Solid Films 35, 255 (1976).
- 123 P. Koidl, Ch. Wild, B. Dischler, J. Wagner and M. Ramsteiner, in ref. 24 p41.
- 124 N. Fourches and G. Turban, Thin Solid Films 240, 28 (1994).
- 125 C. Serra, E. Pascual, F. Maass and j. Esteve, Surf. Coat, Technol. 47, 69 (1991).
- 126 H. Ehrhardt, R. Kleber, A. Kruger, W. Dworschak, K. Jung, I. Miihling, F. Engelke and H. Metz. Diamond and Relat. Mater. 1, 316 (1992).
- 127 D. Nir, R. Kalish and G. Lewin, Thin Solid Films 117, 125 (1984).
- 128 B. Drevillon, J. Huc, A. Loret, J. Perrin, G. De Rosny and J.P.M. Schmitt, Appl. Phys. Lett. 37, 646 (1980).
- 129 K. Suzuki, A. Sawabe, H. Yasuda and E.T. Inuzuka, Appl. Phys. Lett. 50,728 (1987).
- 130 S. Nakao, M. Noda, H. Kusakabe, H. Shimizu and S. Maruno, Jap. J. Appl. Phys. 29, 1511 (1990).
- 131 M. Surendra, D.B. Graves, and L.S. Plano, in Proceedings of the Second International Conference on New Diamond Science and Technology, Washington, DC, 1990, edited by R. Messier, J.T. Glass, J.E. Butler and R. Roy. p. 347.
- 132 K.K. Chattopadhyay, J. Duta. S. Chaudhuri, A.K. Pal, Diamond Rel. Mater. 4, 122 (1995).
- 133 D.R. Mckenzie, R.C. McPhedran, N. Savvide and L.C. Botten, Philos. Mag. B48, 341 (1983).
- 134 S. Kumar, Appl. Phys. Lett. 58, 1836 (1991).
- 135 M. Ham and K.A. Lou, J. Vac. Sci. Technol. A 8, 2143 (1990).
- 136 P. Mitra, K.K. Chattopadhyay, S. Chaudhuri and A.K. Pal, Mat. Letts. 21,95 (1994).
- 137 W. Kasper, H. Bohm and B. Hirschauer, J. Appl. Phys. 71, 4168 (1992).
- 138 O.S. Panwar, D. Sarangi, S. Kumar, P.N. Dixit and R. Bhattacharya, J. Vac. Sci. Technol. A13 (1995).
- 139 M. Nakayama, A. Tsuyoshi, M. Shibbahara, K. Maruyama and K. Kamata, J. Vac. Sci. Technol. A 13 (1995) 195.
- 140 K.K. Chattopadhyay and S. Matsumoto, Appl. Phys. 67, (1995) 3972.
- 141 M. Weiler, R. Kleber, K. Jung and H. Ehrhardt, Diamond and Related Materials 1, 121 (1992).

12. W. Zhang and Y. Catherine, *Surf. Coat. Tech.* 47, 69 (1991).
13. A.R. Nyaiesh, F.F. Kirby, F.K. King and E.L. Garwin, *J. Vac. Sci. Technol.* A3, 610 (1985).
14. D. Sunil, V.D. Vankar and K.L. Chopra, *J. Appl. Phys.* 69, 3719 (1991).
15. L.P. Anderson *Thin Solid Films* 86, 193 (1981).
16. S. Matsumoto, in *Proceedings of the 7th International Symposium on Plasma Chemistry*, Endhoven, edited by C.J. Timmermann (UPAC, Oxford, (1985), Paper A-1-10, p. 79.
17. Y. Shimada, N. Mutsukura and Y. Machi, *J. Appl. Phys.* 71, 4019 (1992).
18. S. Matsumoto, *J. Mater. Sc. Lett.* 4, 600 (1985).
19. S.R. Lee and B. Gallios, *Diamond Relat. Mater* 1, 235 (1992).
20. J. Beckman, R.B. Jackman and J.S. Foord, *Diamond Relat. Mater* 3, 602 (1994).
21. M. Nakayama, A. Tsuyoshi, M. Shibahara, K. Maruyama and K. Kamata, *J. Vac. Sci. Technol.* A13 (1995) 195; and references therein.
22. J. Schwan, K. Jung, H. Ehrhardt, R. Samlenski and R. Brenn, *Diamond Films* 94. Proceeding volume.
23. T. Sharda and D.S. Mishra *Solid State Commun.* 98, 879 (1996).
24. H.C. Barshilia, R. Hariharan, B.R. Mehta and V.D. Vankar, preprint 1996.
25. Y. Liou, A. Inspektor, R. Weimer, D. Knight and R. Messier *J. Mater. Res.* 5, 2305 (1990).
26. I. Nagai, A. Ishitani H. Kuroda, M. Yoshikawa and N. Nagai, *J. Appl. Phys.* 67, 2890 (1990).
27. S.C. Kuo, E.E. Kunhardt and A.R. Srivasta, *Appl. Phys. Lett.* 59, 2532(1991).
28. G. Lucovsky, P.D. Richards, and R.J. Markura, Paper presented at the Workshop of Dielectric Systems for III-V Semiconductors, San Diego, CA, (1994).
29. T. Chonan, M. Uenura, S. Futaki and S. Nishi, *Jap. Journ. Appl. Phys.* 28 (1989) L1058.
30. F. Akatsuka, Y. Hirose and K. Kamaki, *Jap. Journ. Appl. Phys.* 27, L1600, (1988).
31. K. Kurihar, K. Sasaki, M. Kawarada and N. Koshima, *Appl. Phys. Lett.* 52, 437 (1988).
32. Y. Mitsuda, T. Yoshida and K. Akashi, *Rev. Sci. Instrum.* 60 , 249 (1989).
33. B.V. Derjaguin, D.V. Fodoseev, V.M. Lukynovich, V.M. Spitsyn, V.A. Ryabov and A.V. Lavrentev, *J. Cryst. Growth* 2, 380 (1968).
34. Angus, H.A. Will, and W.S. Stanko, *J. Appl. Phys.* 39 , 2915 (1968).
35. B. Singh, O. Mesker, A.W. Levine and Y. Arie, *Appl. Phys. Lett.* 52, 1658 (1988).
36. H. Oechsner and B. Tomcik, *Surf. Coat. Technol.* 47, 162 (1991).
37. M. Weiler, S. Sattel, K. Jung, and H. Ehrhardt *Diamond Relat. Mater.* 3, 608 (1994).
38. D.R. Meckenzie, D. Muller, B.A. Pailthorpe, *Phys. Rev. Lett.* 67, 773 (1991).
39. Hirose and N. Kondo, *Program and Book of Abstracts, Japan Applied Physics Spring Meeting* 434 (1988).
40. K.A. Snail, R.G. Vardiman, J.P. Estera, J.W. Glesener, C. Merzbacher, C.J. Craigie, C.M. Marks, R. Glosser, and J.A. Freitas, Jr., *J. Appl. Phys.* 74, 7561 (1993) and reference therein.

171. Yarbrough, M.A. Stewart and J.A. Cooper Jr., *Surf. Coat. Technol.*, 39/40, 241 (1989).
172. Hirabayashi, S. Amanuma and Y. Hirose, *appl. Phys. Lett.*, 60, 574 (1992).
173. B.D. Cullity, "Elements of X-ray Diffraction", Addison-Wesley Publishing Company, USA, (1978).
174. Powder Diffraction File, Joint Committee on Powder Diffraction Standards International Center for Diffraction Data, 1601 Park Lane, Swarthmore, Pennsylvania (1981).
175. P.J. Grundy & G.A. Jones, "Electron microscopy in the study of materials", Edward Arnold, London 1976.
176. Instruction Manual, Scanning electron microscopy, Model JSM 840, JEOL, Japan.
177. J.C. Grasselli, M.K. Snavely and B.J. Bukin, *Phys. Rep.* 65, (1980) 231.
178. Banerjee and S.S. Jha (Eds.) in *Recent Trends in Raman Spectroscopy* (World Scientific Singapore, 1989).
179. D.S. Knight and W.B. White, *J. Mater Res.* 4, 38, (1990).
180. A.R. Badzian, P.K. Bachmann, T. Hartnett, T. Badzian and R. Messier, *E-MRS Meeting* 15, 63, June 1987.
181. D. Beeman, J. Silverman, R. Lynds and M.R. Anderson *Phys. Rev. B* 30, 870 (1984).
182. S. Bhargava, Ph.D. Thesis, IIT Kanpur, (1995).
183. K.F.J. Heinrich and D.E. Newbury, "Electron Probe Microanalysis", in *Metals Handbook*, ninth Ed. (R.E. Whan, Coord.), Am. Soc. Metals, Metals Park, OH, 10, 516-535, (1986).
184. W.K. Chu, "Back scattering Spectrometry", Academic Press (1972).
185. L.C. Feldman, J.W. Mayer, "Fundamentals of Surface and Thin Film Analysis", North-Holland, (1986).
186. V.N. Kulkarni, Private Communication.
187. L.R. Doolittle, *Nucl. Instr. Meth. B* 9, 334 (1985).
188. M.H. Brodsky, M. Cardona and J.J. Cuomo, *Phys. Rev. B*, 16 (1977), 3556.
189. Reference Manual, Peakfit Version 3 (Jandel Scientific USA).
190. W.H. Press, B.P. Flannery, S.A. Teukolsky and W.T. Vetterling, *Numerical Recipes The Art of Scientific Computing*, Cambridge University Press p. 52, (1989).
191. P.A. Redhead, *Vacuum* 12, 203 (1962).
192. L.A. Petermann *Prog. Surf. Sci.* 3, 1 (1972).
193. T. Som, S. Dhar, N. Banerjee, K. Ramkrishnan and V.N. Kulkarni, *Bull. Mater. Sci.* 19, 73 (1996).
194. B.L. Doyle and P.S. Peercy, *Proceedings of a workshop summarizing developing techniques and formulating requirements for the future held at Sandia Laboratories, Albuquerque, NM* (U.S. Department of Energy, OER, Div. Of Mat. Sci. (1979).
195. B.L. Doyle and P.S. Peercy, *Appl. Phys. Lett.* 34, 811, (1979).

96. F. Besenbacher, I. Stensgaard and P. Vase, Nucl. Instrum. & Meth. B15, 459, (1986).
97. H. Wang and G.Q. Zhou, Nucl. Instrum. and Meth. B 34, 145, (1988).
98. K.E.E. Baglin, A.J. Kellock, M.A. Crockett and A.H. Shih, Nucl. Instrum. and Meth. B64, 469, (1992).
99. V. Quillet, F. Abel and M. Schott, Nucl. Instrum. and Meth. B83, 47, (1993).
00. T. Som, S.Dhar, S.N. Minwalla and V.N. Kulkarni, Nucl. Inst. Meth. B (In press)
01. Marie-Luce Theye in "Thin Film Technology and Applications", edited by K.L. Chopra and L.K. Malhotra, McGraw Hill, New Delhi .
02. R. Swanepoel, J. Phys. E: Sci. Instrum. Vol. 16, 1214, (1983).
03. G.D. Cody, C.R. Wronski, B. Abels, R.B. Stephens, and B. Brooks Solar Cells 2, 227, (1980).
04. J. Tauc, R. Grigorovici and A. Vancu, Phys. Status Solidi 15, 627, (1966).
05. J. Tauc, in 'Optical properties of solids' Ed. F. Abeles (North Holland Amsterdam, London 1972), Chap5.
06. G.D. Cody, B.G. Brooks and B. Abeles, Sol. Energy Mater, 8, 231, (1982).
07. C.R. Wronski, S. Lee, M. Hicks and S. Kumar, Phys. Rev. Lett. 63, 1420, (1989).
08. Hardness Testing, edited by Howard E. Boyer, ASM International Metals Park, OH 44073, Chap 5.
09. H.K. Pulker, Coatings on Glass, Elsevier, Amsterdam, 353, (1984).
10. B. Jonsson and S. Hogmark, Thin Solid Films 114, 257 (1984).
11. J.W. Ager and M.D. Drory, Phys. Rev. B, 48, 2601, (1993).
12. S.M. Ojha, H. Norstrom and M. McCulluch Thin Solid Films 60, 213 (1979).
13. M.H. Brodsky, Thin Solid Films 50, 57(1978).
14. P. Kocian, Thin Solid Films 80, L81, (1981).
15. B.N. Chapman, Glow Discharge Processes, (Wiley Inter Science, New York, 1980).
16. Pere Roca I Cabarrocas, THESE, University De Paris VII, U.F.R. de Physique France (1988).
17. Thin film processes, edited by Vossen and Kern, Academic Press, N.Y. 1978.
18. S. Ishihara, M. Kitagawa, T. Hirano and K. Wasa, J. Appl. Phys. 62, 485 (1987).
19. K.Tachibana, M. Nishida, H. Harima and Y. Urano, J. Phys. D. 17, 1727, (1984).
20. G.J. Varentop, M. Kawasaki, R.M. Nix, I.G. Brown, M. Salmeron and G.A. Somorjai, Phys. Rev. B 41, 3200, (1990).
21. E. Gogolides, C. Buteau, A. Rhallabi and G. Turban,, J. Phys. D. 27, 818, (1994).
22. M.J. Vasile and G. Smolinsky, Int. J. Mass Spectrum. Ion Phys. 24, 11, (1977).
23. R.P. Mota, T. Shiosawa, S.F. Durrant and M.A.B. de Moraes, J. Vac. Sci. Technol. A13, 2747, (1995).
24. L.E. Kline, W.D. Partlow and W.E. Bies, J. Appl. Phys. 65, 70, (1989).
25. D. Huang, M. Frenklach and M. Maroncelli, J. Phys. Chem. 92, 6379, (1988).

226. N. Mutsukara, S. Inoue and Y. Machi, J. Appl. Phys. 72, 43, (1992).
227. S. Naito, N. Ito, T. Hattori and T. Goto, Jpn. J. Appl. Phys. 33, 5967, (1994).
228. R.C. Ross and J. Jaklik Jr., J. Appl. Phys. 55, 3785 (1984).
229. Y. Catherine in ref. 86, p193.
230. G. Turban and Y. Catherine Thin Solid Films 48, 57 (1979).
231. H. Toyoda, M.A. Childs, K.L. Menningen, L.W. Anderson and J.E. Lawler J. Appl. Phys. 75, 3142 (1994).
232. K. Suzuki, A. Sawabe and T. Inuzuka Appl. Phys. Lett. 53, 1818 (1988).
233. S. Kaplan, F. Jansen, and M. Machomlon, Appl. Phys. Lett. 47, 750(1985) .
234. D. Boutard, B.M.U. Scherzer and W. Moller, J. Appl. Phys. 65, 3833 (1989) .
235. J.L. Bredas and G.B. Street, J. Phys. C.18, L651(1985), .
236. J. Robertson and E.P. O'Reilly, Phys. Rev. B.35, 2946(1987) .
237. G. Galli, R.M. Martin, R. Car, and M. Parrinello, Phys. Rev. Lett. 62, 555(1989) .
238. J. Tersoff, Phys. Rev. B.44, 12039(1991) .
239. P. Blaudeck, Th. Frauenheim, G. Jungnickel and U. Stephan, Solid State Commun. 85, 997(1993) .
240. P. Blaudeck, n Th. Frauenheim, D. Porezag, G. Seifert, and E. Fromm. J. Phys. 4, 6389(1992) .
241. A. Grill and V. Patel, Appl. Phys. Lett, 60, 2089, (1992).
242. W. Jacob and W. Moller, Appl. Phys Lett, 63, 1771, (1993).
243. B. Dischler, in P. Koidl and P. Oelhafen (eds.), E-MRS Symp. Proc. Vol. 17, Les Editions de Physique, Paris, p. 189 (1987).
244. Introduction to Infrared and Raman Spectroscopy, edited by N.B. Colthup, L.H. Daly and S.E. Wiberley (Academic Press, New York, 1975).
245. E.H.A. Dekempeneer, R. Jacob, J. Smeets, J. Meneve, L. Eersels, B. Blanpain, J. Roes and D.J., Oostra Thin Solid Films, 217, 56(1992) .
246. R. N. Jones and C. Sandorfy, in W. West (ed.), Chemical Applications of Spectroscopy, Interscience, New york, p. 339 ,1956.
247. E.C. Freeman and W. Paul Phys. Rev. B20, 716 (1979).
248. Weiler M., Kleber R., Sattel S., Jung K., Ehrhardt H., Jungnickel G., Deutschmann S., Stephan U., Blaudeck P. And Frauenheim T., Diamond and Related Materials 3 245 (1994),
249. C.De Martino, F. Demichelis and A. Tagliaferro, Diamond and Rel. Mat. 4, 1220 (1995).
250. F. Fujimoto, A. Ootuka, K. Komaki, Y. Watta, I. Yamane, H. Yamashita, Y. Hashimoto, Tawada, K. Nishimura, H. Okamoto and Y. Hamakawa Jap. J. Appl. Phys. 23, 810 (1984)
251. D.K. Basa and F.W. Smith, Thin Solid Films 192 , 121 (1990).
252. C.J. Fang, K.J. Gruntz, L. Ley and M. Cardona, J. Non-Cryst. Solids 35 & 36 , 255(1980).
253. B.L. Doule and P.S. Peercy, Appl. Phys. Lett. 34, 812 (1979).

4. D.C. Ingram, J.A. Woolam and G. Bu Abbud, *Thin Solid Films*, 137, 255 (1986).
5. X. Long, X. Peng, F. He, M. Liu and X. Lin. *Nucl. Inst. Meth. B68*, (1992) 266.
6. D.C. Ingram and A.W. McCormick, *Nucl. Instrum. Methods Phys. Rev. B.34*, 68 (1988).
7. R.L.C. Wu, *Surf. Coat. Technol.* 51, (1992) 258.
8. K.Tanaka, M. Okada, T. Kohno, M. Yanokura, and *Nucl. Instrum. Methods. Phys. Res. B.58*, (1991) 34.
9. D.D. Boutard and W. Moller, *J. Mater. Res.* 5, 2451 (1990).
0. T. Wang, W. Wang, and B. Chen, *Nucl. Instrum. Methds, Phys. B.* 71 ,186 (1992).
1. J. Gonzalez Hernadex, R. Asomoza, A. Reyes-Mens, J. , S.S. Chao, and D. Pawlik, *J. Vac. Sci. Technol. A6*, (1991) 1796.
2. 262a. M.E. Adel, O. Amir, R. Kalish, and L.C. Felddman, *J. Appl. Phys.* (1989)  
262b. N. Matsunami,*Nucl. Instrum. Methods B64*,800 (1992)
3. M.J. Paterson, K.G. Orman-Rossiter, S. Bhargava and A. Holfman, *J. Appl. Phys*, 74, 792 (1994) .
4. (a) D. Boutard, B.M.U Scherzer and W., J. Moller, *Phys. Rev. B* 38, 2988 (1988)  
(b) H. Baumann, T. Rupp, K. Bathge, P. Koidl and C. Wild in *Amorphous Hydrogenated Carbon Films*, E-MRS Symposia Proceedings, edited by P. Koidl and P. Oelhafen (Les Editions de Physique, Paris 1987) Vol XVII, p 343 .
5. D.K. Awasthi, D. Kabiraj, Jaipal, Mehta, G.K. Barshilia, H.C., Sah Somna, B,R.Mehta and V.D., Vankar, *Vacuum* 46 ,633(1995) .
3. W. Beyer, *Physica B*, 170(1991) 105, and references therein.
7. W.B. Jackson, N.H. Nickel, N.M. Johnson, F. Pardo and P.V. Santos, *Mater. Res. Soc. Symp. Proc.*, 336, 311 (1994) .
3. A.I. Kosarev, M. Sh. Abuduvagabov, Ju. M. Baikov, N.S. Zhdanovich and V.F. Cvetkov, *Surf. Coat. Technol.*, 50, 209 (1992) .
9. X. Jiang, W. Beyer, and K. Reichelt, *J. Appl. Phys.* 68,1378 (1990) .
0. P. Murray and J. White, *J. Trans. Brit. Ceram, Soc.* 54 , 204(1955) .
1. H.E. Kissinger, *Anal. Chem.*, 29, 1702 (1957) .
2. W. Beyer and H. Wagner, *J. Appl. Phys.* 53, 8745(1982) .
3. V.G. Raichenko, E.N. Loubnin, A.V. Popov and V.E. Strelnitsky, *Diamond and Rel. Mat.* 1 , 345 (1992)
4. K.P. Huber, in D.E. Gray (ed.). *AIP Handbook of Physics*, McGraw Hill, New York, 7-168 ,1972.
5. R.A. Street, C.C. Tsai, J. Kakalios and W.B. Jackson, *Phil. Mag. B56*, 305(1987)
6. J. Gonzalez-Hernandez, B.S. Chao and D.A. Pawlik, *J. Vac. Sci. Technol.* 7, 2332(1989)
7. M. P. Nadler, T. M. Donovan and A.K. Green, *Thin Solid Films* 116, 241(1984)
8. J. L. Akkerman, H. Efstathiadis and F. W. Smith, *J. Appl. Phys.* 80, 3068 (1996)

279. Q. Wang, D.D. Allred and J. Gonzales - Hernandez Phys. Rev. B47, 6119(1993).
280. A. Reyes-Mena, J. Gonzalez-Hernandez, R. Asomoza and B.S. Chao, J. Vac. Sci. Technol. A8, 1509(1990).
281. D. Beeman, J. Silverman, R. Lynds and M.R. Anderson, Phys. Rev. B30, 870 (1984).
282. L. H. Chou and H.W. Wang J. Appl. Phys. 74, 4673 (1993).
283. M. Weiler, S. Sattel, K. Jung and H. Ehrhardt Diamond and related Materials, 3, 608 (1994).
284. D. Revelle, L. Mulestagno, S. Lin and B.J. Feldman, Solid State Commun. 86, 235(1992).
285. S. Serra, E. Pascual, F. Maass, E. Bertran and J. Esteve, Diamond Relat. Mater 1, 538 (1992).
286. L.H. Chou, 72, 2027 (1992).
287. Ichinose, Y. and Shimokawa, F., Optical Properties of Hydrogenated Amorphous Carbon films produced by CVD of propane, presented at the 16th Biennial Conf. on Carbon San Diego, 287 (1983).
288. Munekata, H., Murasato, S., and Kukimoto, H., Appl. Phys. Lett. 37, 546 (1980).
289. D.J. Cheng, W.I. Shyy, D.H. Kuo and M.H. Hon, J. Electrochem. Soc. 134, 3145 (1987).
290. S. Lin and B.J. Feldman, Philos. Mag. B 47, 113 (1983).
291. Y. Lifshitz, s.r. Kasi and J.W. Rabalais, Phys. Rev. B 62, 1290 (1989).
292. (A) S. Bhargava, H.D. Bist, S. Sahli, M. Aslam and H.B. Tripathi Appl. Phys. Lett. 67, 1706 (1995).  
(B) H.D. Bist, S. Bhargava, T. S. Little, J. K. Gardner, Jr. and J. R. Doring, S. Sahli, and M. Aslam, J. of Raman spectroscopy, 25, 67 (1994).
293. A. M. Zaitsev, V. S. Vavilov and A. A. Gippius, Sov. Phys. Leb. Inst. Rep. 10, 15 (1981)
294. J. Nemanich, J. T. Glass, G. Lucovsky and R. E. Shroder J. Vac. Sci. Technol. A6, 1783, (1988)
295. K. Maoyama, M. Makino, N. Kikukawa and M. Shiraish J. Mater. Sci. 247, 688 (1990).
296. W.A. Yarbrough and R. Messier, Science 247, 688 (1990).
297. J.C. Wgner, C. Wild and P. Koidl Appl. Phys. Lett 59, 779 (1991).
298. S.R.P. Silva, G.A.J. Amaratunga, E.K.H. Salje and K.M. Knowles J. Mat. Sci. 29, 4962 (1994).
299. J. Perrin, J. Non Cryst., solids 138 & 139, 639 (1991).
300. J. P. M. Schmitt J. Non Cryst. Solids 59 & 60, 649 (1983).
301. S. J. Harris and A.M. Weiner, J. Appl. Phys. 67, 6520(1990); J. Appl. 70, 1385(1991).
302. T. DebRoy, K. Tankala, W. A. Yarbrough, and R. Messier, J. Appl. Phys. 68, 2424 (1990).
303. E. Kondoh, T. Ohta, T. Mimoto, and K. Ohtsuka, J. Appl. Phys. 722, 705 (1992).
304. S. J. Harris, Appl. Phys. Lett. 56, 2298 (1990).
305. M. Frenklach and K.E. Spear, J. Mater. Res. 3, 133 (1988).
306. H. N. Chu, E.A. Den Hartog, A. R. Lefkow, J. Jacobs, L. W. Anderson, M. J. Legally and J. E. Lawer, Phys. Rev. A44, 3796 (1991).



07. M.P. D'Evelyn, C.J. Chu, R.H. Hauge, and J.L. Margrave, J. Appl. Phys. 71, 15228, (1992).
08. Y. Lifshitz, S.R.Kasi, J.W.Rabalais and W.Eckstein, Phys. Rev. B, 41 10486 (1990).
09. C.E.Melton and P.S.Rudolph, J. Chem. Phys. 47 1771 (1967).
10. M. Moller, Appl. Phys. A 56, 527, (1993).
11. M.J. Kushner J. Appl. Phys. 62, 4763, (1987).
12. M.J. KMcCaughey and M.J. Kushner, Appl. Phys. Lett. 54, 1642, (1989).
13. M.F.Thorpe, J.Non-Cryst. Solids. 57, 355 (1983).
14. Y. Wang, H. Chen and R.W. Hofiman J. Mater. Res 5 (2378, (1990).
15. J.C. Angus and F. Jansen, J. Vac. Sci. Technol. A6 , 1778, (1988).
16. J. Robertson, Diamond and Relat. Mater. 2, 984, (1993).
17. (A) W. Dworschak, R.Kleber, A. Fuchs, B.Scheppat, G.Keller, K.Jung, and H.Ehrhardt, Thin Solid Films 189, 257 (1990).  
(B)R.Kleber., K.Jung, H.Ehrhardt, I.Muhling , K. Breuer , H.Metz, F. Engelke, Thin Solid Films 205, 274 (1991).
8. Koild, C. Wild, D. Dischler, J. Wagner, and M. Ramsteiner, Materials Science Forum (Trans Tech, Switzerland, 1989), Vols. 52 & 53, p. 41: R. E. Clausing, L.L. Horton, J.C. Angus and P. Koidl, Diamond and Diamond-Like Films and Coating (Plenum, New York, p. 243, (1991).
9. G.A.J. Amaratunga, S.R.P. Silva, and D.R. McKenzine, J. Appl. Phys. 70, 5374, (1991).
10. M. Nakayama, K. Ueda, M. Shibahara, K. Maruyama, and K. Kamata, Jpn. J. Appl. Phys. 30, L924, (1991).
11. M. Nakayama, M. Shibahara, K. Maruyama, and K. Kamata, J. Mater, Sci. Lett. 12, 380, (1993).
12. J.J. Chang and T.D. Mantei, J. Appl. Phys. 71, 5724, (1992).
13. Y. Hirose and N. Kondo, in Extended Abstracts, 35<sup>th</sup> Jpn. Appl. Phys. Spring Meet, March , p-434,1988
14. K.V. Ravi and C.A. Koch, Appl. Phys. Lett., 57,348 (1990) .
15. C.M. Marks, H.R. Burris, J.Grun and K.A. Snail J. Appl. Phys. 73, 755 (1993).
16. Hanssen, W.A. Carrington, J.E. Butler and K.A. Snail, Mater, Lett., 7,289 (1988) .
17. Y. Tzeng, R. Phillips, C. Cutshaw and T. Srivynunon, New diamond science and technology, edited by R. Messier, J. T. Glass, J.T. Butler and R. Roy (MRS Pittsburg, Pennsylvania 1990), p 523.
18. K.V. Ravi, C.A. Koch, H.S. Hu and A. Joshi, J. Mater, Res., 5,2356 (1990) .
19. T. Abe, M. Suemitsu, N. Miyamoto and N. Sato, J. Appl. Phys., 73,971 (1993)
20. K. Hirabayashi, T. Kimura and Y. Hirose, Appl. Phys. Lett., 62 ,354(1993)
21. K.V. Ravi and A. Joshi, Appl. Phys. Lett., 58 ,246(1991)
22. J.S. Kim, M.H. Kim, S.S. Park, and J.Y. Lee, J. Appl. Phys., 67,3354 (1990)

333. K. Hirabayashi and S. Matsumoto, J. Appl. Phys. , 75 ,1151(1994)
334. K. Hirabayashi and Y. Hirose, Diamond Relat. Mater. (1996).
335. K.A. Snail, J.A. Freitas, C.L. Vold and L.M. Hanssen, Proc. Second Int. Symp. On Diamond Materials, The Electrochemical society, Pennington, NJ, 91-98, p81, (1991)
336. K.A. Snail, J.A. Freitas, C.L. Vold and L.M. Hanssen, Proc. Second Int. Symp. On Diamond Materials, The Electrochemical society, Pennington, NJ, 91-98, p81 (1991)
337. Y. Tzeng and R. Phillips in ref. 107, p 189.
338. J.W. Glesener, A.A. Morish and K.A. Snail J. Appl. Phys. 70, 5144 (1991).
339. W. Zhu, B.H. Tan and H.S. Tan, Thin Solid Films 236 ,106 (1993) .
340. M. Murakawa, S. Takeuchi and Y. Hirose, Surf. Coat. Tech. 43/44,22 (1990)
341. Y.H. Lee, K.J. Bachmann, J.T. Glass. G.Y. Lee and R.J. Nemanich, Appl. Phys. Lett., 57,1916 (1990)
342. T.P. Ong and R.P.H. Chang, Appl. Phys. Lett., 58, 358 (1991).
343. H.C. Shih, C.P. Sung, W.L. Fan, and C.K. Lee, Surf. Coat. Technol. 57, 197 (1993).
344. P.S. Weiser, S. Praver, A. Hoffman, R.R. Manory, P.J.K. Paterson, and S.A. Stuart, J. Appl. Phys. 72, 4643 (1991).
345. P.S. Weiser, S. Praver, A. Hoffman, P.J.K. Paterson, and R.R. Manory, J. Appl. Phys. 76, 2164 (1994).
346. J. Narayan, V.P. Godbole, G. Matera, and R.K. Singh, J. Appl. Phys. 71, 966 (1992).
347. J. Ahn, F.H. Tan, and H.S. Tan, Diamond Relat. Mater. 2, 353 (1993).
348. M. Kowarada, K. Kurihara, and K. Sasaki, Diamond Relat. Mater. 2, 1083 (1993).
349. A.Fayer, O. Glotzman, and A. Hoffman, Appl. Phys. Lett., 67, 2299 (1995).
350. M.Kohzaki, K. Higuchi, S. Noda, and K. Uchida, Diamond Relat. Mater. 2, 612 (1993).
351. V.G. Ralchenko, A.A. Smolin, V.G. Pereverzev, E.D. Obraztsova, K.G. Korotouschenko, V.I. Konov, Yu. V. Lakhotkin, and E.N. Loubnin, Diamond Relat. Mater. 4, 754 (1995).
352. Patent on "Direct Deposition of Diamond Thin Films on stainless steel substrates without any external buffer layers" (Applied for No., 1365/Del/95) by Satyendra Kumar and Manju Malhotra.
353. M.A. Cappelli and P.H. Paul, J. Appl. Phys. 67,2596 (1990)
354. R.S. Yalamanchi and K.S. Harshvardhanm J. Appl. Phys. 68,5941 (1990)
355. Y. Matsui, A.Yuuki, M.Sahara and Y. Hirose, Jap. J. Appl. Phys. 28, 1718 (1989).
356. Allan Williams and D.B. Smith, Chemical Review 1969.

- J.E. Butler, F.G. Warrington and K.A. Snail, High Temp. Sci. 27, 165 (1990).
- W.A. Carrington, L.M. Hanssen, K.A. Snail, D.B. Oakes and J.E. Butler, Metall. Trans 20A, 1282(1989)
- J.S. Kim and M.A. Cappelli Appl. Phys. Lett. 65, 2786 (1994).
- J.S. Kim and M.A. Cappelli Appl. Phys. Lett. 67, 1081 (1995).
- L. Glassman, Combustion, 2nd ed. (Academic Orlando, FL, 1987).
- D.N. Belton and S.J. Schmieg, J. Appl. Phys. 66,4223 (1989)
- (a) L.M. Hanssen, K.A. Snail, W.A. Warrington, J.E. Butler, S. Kellog and D.B. Oakes, Thin Solid Films 196 ,271(1991) (b) K.A. Snail, D.B. Oakes, J.E. Butler and L.M. Hanssen, New Diamond Science and Technology, edited by R. Messier, J.T. Glass, J.E. Butler and R. Roy (MRS Pittsburg, Pennsylvania)p. 503, 1990
- K.E. Spear and M. Frenklach, Pure & Appl. Chem. 66,1773 (1994)
- B.B. Pate, Surf. Sci. 165,83 (1986)
- B.V. Spitsyn, L.L. Bouilov and B.V. Derjaguin J. Cryst. Growth 52, 219 (1981).
- R. Kapil, B.R. Mehta and V.D. Vankar, Appl. Phys. Lett. 68, 2520 (1996).
- M. Malhotra, S.C. Agarwal and Satyendra Kumar Bull. Mater. Sci. 19, 455 (1996).
- R.E. Thomas, R.A. Rudder and R.J. Markunas J. Vac. Sci. Technol. 10, 2451 (1992).
- M.F. Chung and Y.K. Lim, Scripta Metall. 20 ,807(1986)
- W.S. Basca, Nature 266, 1256 (1994) and references therein.
- V.P. Godbole, K. Jagannadham and J. Narayan, Appl. Phys. Lett., 67,1332 (1995)
- W. Zhu, P.C. Yang and J.T. Glass, Appl. Phys. Lett., 63 ,1640(1993)
- F. Akatsuka and F. Shimura, Application of diamond films and related materials, edited by Y. Tzeng, M. Yoshikawa, M. Murakawa and A. Feldman (Elsevier, Amsterdam)p. 379, 1991
- B.E. Williams, B.R. Stoner, D.A. Asburg and J.T. Glass, Diamond and diamond-like films and coatings, edited by R.E. Clausing, L.L. Horton, J. C. Angus and P. Koidl, (Plenum Press, New York)p.737, 1991
- S.S. Perry and G.A. Somorjai, J. Vac. Sci. Tech. 12 ,1513(1994)

PHY-1996-D-MAL-GRO



125699



125699

## Date Slip

This book is to be returned on the  
date last stamped.

This image shows a full page of primary-ruled paper. It features a central vertical solid line that divides the page into two equal halves. On both sides of this line, there are ten horizontal dotted lines, creating a total of twenty rows for writing. The paper is otherwise blank, with no margins or additional markings.